Small-scale modeling of dispersion and chemistry of ship plumes in urban areas

Dissertation

zur Erlangung des Doktorgrades der Naturwissenschaften
an der Fakultät für Mathematik, Informatik und Naturwissenschaften
Fachbereich Geowissenschaften
der Universität Hamburg

vorgelegt von

Ronny Badeke

geboren in Chemnitz
Deutschland

Hamburg, 2022

Datum der Disputation:

06.09.2022

Gutachter:

Prof. Dr. Kay-Christian Emeis

Dr. Volker Matthias

Mitglieder der Prüfungskommission:

Prof. Dr. Kay-Christian Emeis

Dr. Volker Matthias

Dr. David Grawe

Prof. Dr. Birgit Gaye

Prof. Dr. Martina Neuburger

Vorsitzender des Fachpromotionsausschusses Geowissenschaften:

Prof. Dr. Hermann Held

Dekan der Fakultät MIN:

Prof. Dr. Heinrich Graener

Eidesstattliche Versicherung

Hiermit erkläre ich an Eides statt, dass ich die vorliegende Dissertationsschrift selbst verfasst und keine anderen als die angegebenen Quellen und Hilfsmittel benutzt habe.

Hamburg, den 04.06.2022 Ronny Badeke

Ich versichere, dass das gebundene Exemplar der Dissertation, das in elektronischer Form eingereichte Dissertationsexemplar und das bei der Fakultät Mathematik, Informatik und Naturwissenschaften zur Archivierung eingereichte gedruckte gebundene Exemplar der Dissertationsschrift identisch sind.

Hamburg, den 04.06.2022 Ronny Badeke

The following two papers were created as part of this dissertation. They represent the contents of Chapter 4 and Chapter 5.

Badeke, R., Matthias, V., and Grawe, D.: Parameterizing the vertical downward dispersion of ship exhaust gas in the near field, Atmos. Chem. Phys., 21, 5935–5951, https://doi.org/10.5194/acp-21-5935-2021, 2021.

Badeke, R., Matthias, V., Karl, M., and Grawe, D.: Effects of vertical ship exhaust plume distributions on urban pollutant concentration – a sensitivity study with MITRAS v2.0 and EPISODE-CityChem v1.4, Geosci. Model Dev. 4077–4103, https://doi.org/10.5194/gmd-15-4077-2022, 2022.

Short summary

Shipping connects the world and promotes globalization. However, due to the steadily increasing shipping traffic, ship exhaust gases are also a growing problem for the climate, the environment and the health of people in coastal regions and port cities. Of particular interest here are the concentrations of nitrogen oxides and ozone, which are subject to legal limit values. In order to precisely assess the air quality in port cities, direct measurements are complemented by chemical transport model simulations. Models provide an extended insight into the situation: they calculate concentrations at any position in the city and allow scenarios to be simulated, for example to determine how air quality would change if the pollutant input from the shipping sector decreased.

The modeling of ship emissions poses a particular challenge because ships are mobile sources that combust exhaust gases at high temperatures but at the same time have a short stack. Their design influences the wind field and creates turbulence. As a result, the spatial propagation of ship exhaust gases sometimes deviates significantly from a classic Gaussian distribution. This variability has not yet been captured and quantified in models.

Two model systems were used in this work: the microscale model MITRAS and the city-scale model EPISODE-CityChem. The prototype of a cruise ship was simulated with the object-resolving model MITRAS. The influence of various meteorological and ship-technical parameters on the plume rise and the turbulent downward dispersion in the near field of the ship was examined and parameterized. During high wind speeds, up to 55% of the exhaust gas is transported to areas below the stack height. In comparison, the downward dispersion for a narrow chimney of the same height was only 31%. A correspondingly increased level of pollution can be expected in port areas.

The vertical distribution of ship exhaust gases was also determined and parameterized using MITRAS calculations. The derived formulas were used in the city-scale model EPOSIDE-CityChem to distribute the ship emissions more realistically. The influence of various complex parameterizations on the pollutant concentration in the city area was simulated with EPISODE-CityChem. At high wind speeds, the use of a Gaussian parameterization turned out to be sufficiently accurate, while the pollutant distribution in the case of low wind speeds with strong plume rise can be better represented by an exponentially modified Gaussian distribution. This distinction plays a role in the small-scale modeling of city centers in particular.

In the third part of the work, the developed flexible ship exhaust gas distribution ("Flexplume") was used in a complex chemical transport modeling study and compared with a conventional equal distribution ("Fixplume") and real measurements. The new method performed significantly better for the simulation of nitrogen monoxide (NO) and for the simulation of nitrogen dioxide (NO_2) and ozone (O_3) it reached a similar level of accuracy as the conventional method. This is of great relevance for the assessment of air quality in inner cities, since these three substances interact through complex, non-linear chemical reactions. It was also shown that a reduction in ship emissions in

Hamburg would lead to a significant reduction in NO_2 pollution, but at the same time causes increased ozone concentrations. In relative terms, ship traffic in Hamburg's city center accounts for up to 50% of NO pollution and 18% of NO_2 pollution, but it significantly reduces ozone pollution by up to 20%, especially in the summer.

Zusammenfassung

Die Schifffahrt ist ein bedeutendes Bindeglied der globalisierten Welt. Doch durch den stetig steigenden Schiffsverkehr stellen Schiffsabgase auch ein wachsendes Problem für das Klima, die Umwelt und die Gesundheit von Menschen in Küstenregionen und Hafenstädten dar. Von besonderem Interesse sind hierbei die Konzentrationen von Stickoxiden und Ozon, welche gesetzlichen Grenzwerten unterliegen. Um die Luftqualität in Hafenstädten präzise zu bewerten, werden direkte Messungen durch Chemietransportmodelle ergänzt. Modelle geben dabei einen erweiterten Einblick auf die Situation: sie berechnen Konzentrationen an beliebigen Positionen im Stadtgebiet und erlauben die Simulation von Szenarien, um so beispielsweise zu ermitteln, wie sich die Luftqualität verändern würde, wenn der Schadstoffeintrag durch Schiffe sinkt.

Die Modellierung von Schiffsemissionen stellt eine besondere Herausforderung dar, da es sich bei Schiffen um mobile Quellen handelt, welche Abgase bei hohen Temperaturen verbrennen, aber zugleich einen kurzen Schlot besitzen. Durch ihre Bauform beeinflussen sie das Windfeld und erzeugen Turbulenzen. Dadurch weicht die räumliche Ausbreitung von Schiffsabgasen manchmal deutlich von einer klassischen Gauß-Verteilung ab. Diese Variabilität wurde in Modellen noch nicht erfasst und beziffert.

In Rahmen dieser Arbeit wurden zwei Modellsysteme verwendet: das mikroskalige Modell MITRAS und das stadtskalige Modell EPISODE-CityChem. Durch Simulationen mit dem objektauflösenden Modell MITRAS wurde der Prototyp eines Kreuzfahrtschiffs simuliert. Dabei wurde der Einfluss verschiedener meteorologischer und schiffstechnischer Parameter auf den Fahnenaufstieg und die turbulente Abwärtsdispersion im Nahfeld des Schiffes untersucht und parametrisiert. Während hoher Windgeschwindigkeiten werden bis zu 55 % des Abgases in Bereiche unterhalb der Schlothöhe transportiert. Im Vergleich dazu betrug die Abwärtsdispersion bei einem gleichhohen schmalen Schornstein lediglich 31 %. Eine dementsprechend erhöhte Schadstoffbelastung kann in Hafenbereichen erwartet werden.

Auch die vertikale Verteilung von Schiffsabgasen wurde mit MITRAS-Rechnungen ermittelt und parametrisiert. Die abgeleiteten Formeln wurden schließlich in dem stadtskaligen Modell EPOSIDE-CityChem verwendet, um die Schiffsemissionen realistischer zu verteilen. Der Einfluss verschiedener komplexer Parametrisierungen auf die Schadstoffkonzentration im Stadtgebiet wurde mit EPISODE-CityChem simuliert. Unter hohen Windgeschwindigkeiten stellte sich die Verwendung einer Gauß-Parametrisierung für hinreichend genau heraus, während die Schadstoffverteilung im Fall von niedrigen Windgeschwindigkeiten starkem Fahnenaufstieg besser durch eine exponentiell modifizierte Gauß-Verteilung abgebildet werden kann. Diese Unterscheidung spielt insbesondere bei der feinskaligen Modellierungen von Stadtzentren eine Rolle.

Im dritten Teil der Arbeit wurde die entwickelte flexible Schiffsabgasverteilung („Flexplume“) in einer komplexen Chemietransportstudie verwendet und mit einer konventionellen Gleichverteilung („Fixplume“) und realen Messungen verglichen. Die

neue Methode schnitt dabei für die Simulation von Stickstoffmonoxid (NO) deutlich besser und für die Simulation von Stickstoffdioxid (NO_2) und Ozon (O_3) ähnlich gut wie die konventionelle Methode. Dies ist für die Beurteilung der Luftqualität in Innenstädten von hoher Relevanz, da die drei genannten Stoffe durch komplexe, nichtlineare chemische Reaktionen aufeinander einwirken. Es konnte auch gezeigt werden, dass eine Reduktion von Schiffsemissionen in Hamburg zwar zu einer deutlichen Verringerung der Belastung durch NO_2 beiträgt, aber gleichzeitig erhöhte Ozonkonzentrationen verursacht. Relativ betrachtet trägt der Schiffsverkehr in der Hamburger Innenstadt zu bis zu 50 % der Belastung durch NO und 18 % der Belastung durch NO_2 bei, reduziert aber die Belastung durch Ozon, besonders im Sommer, um bis zu 20 %.

Table of contents

List of acronyms

Acronym	Explanation
AIS	Automatic Identification System
BImSchV	Bundes-Immissionsschutzverordnung
BSH	Budesamt für Seeschifffahrt und Hydrographie (Federal Maritime and Hydrographic Agency of Germany)
BUE	Behörde für Umwelt und Energie
BUKEA	Behörde für Umwelt, Klima, Energie und Agrarwirtschaft
BVM	Behörde für Verkehr und Mobilitätswende
c	Concentration
CLF	Cloud fraction
CMAQ	Community Multiscale Air Quality Modeling System
CSIRO	Commonwealth Scientific and Industrial Research Organization
d	Draught
dd	Wind direction
D	Downward dispersion
DEM	Digital Elevation Model
DFG	Deutsche Forschungsgemeinschaft (German Research Foundation)
erfc	Complementary error function
E	Energy consumption
ECMWF	European Centre for Medium-Range Weather Forecasts
EF	Emission factor
EMEP	European Monitoring and Evaluation Programme
EMSA	European Maritime Safety Agency
Expgauss	Exponentially modified Gaussian function
F	Sub-grid-scale turbulent fluxes
FAC2	Fraction of the modeled values within a factor of 2 to the observed values
GT	Gross tons
h	Planck constant (-6.62607015 × 10^{-34} m^2 kg s^{-1})
h_e	Effective stack height
h_{fleet}	Fleet height
$h_{keel\text{-}to\text{-}mast}$	Keel-to-mast height
h_r	Reference height
h_s	Stack height
h_{top}	Altitude of highest model layer
h_{up}	Upper plume boundary height
Δh	Plume rise
HBEFA	Handbook For Emission Factors for street traffic
ICDC	Integrated Climate Data Center
IMO	International Maritime Organization
IOA	Index of agreement
J	Photolysis rate

Acronym	Explanation
k	Rate coefficient for chemical reactions
K_{ij}	Eddy diffusivity
l_{ship}	Ship length
L	Monin-Obukhov length
LNG	Liquified Natural Gas
m	Mass
m_p	Mass of pollutant
MARPOL	International Convention for the Prevention of Pollution from Ships
MEPC	Marine Environment Protection Committee
MITRAS	Microscale transport and stream model
MoSES	Modular Ship Emission modeling System
n	Amount of substance (mole)
N_d	Number concentration of dry air ($2.46 * 10^{13}$ molecules cm^{-3})
NECA	Nitrogen emission control area
NILU	Norwegian Institute for Air Research
NMB	Normalized mean bias
NO_x	Oxides of nitrogen
NMHC	Non-methane hydrocarbon
NMVOC	Non-methane volatile organic compounds
OCD	Offshore and Coastal dispersion model
p	Pressure
PM	Particulate matter
ppb	Parts per billion (10^{-9})
ppm	Parts per million (10^{-6})
r	Effective range
R	Ideal gas constant (8.314 J $(K\ mol)^{-1}$) (in chemical context)
	Pearson regression coefficient (in statistical context)
RMSE	Root mean square error
sgn	Sign function
S	Sources and sinks
SCE	Single cell emission
SECA	Sulfur emission control area
SSCM	Simplified Street Canyon Model
STD	Standard deviation
STEAM	Ship Traffic Emission Assessment model
T	Temperature
T_{exh}	Exhaust temperature
TAPM	The Air Pollution Model
u_*	Friction velocity
UECT	Urban Emission Conversion Tool
UNCTAD	United Nations Conference on Trade and Development
UTM	Universal Transverse Mercator projection
v_{exit}	Stack exit velocity

Acronym	Explanation
v_{rel}	Relative wind speed
v_{ship}	Ship speed
v_{wind}	Wind speed
w_{ship}	Ship width
V	Volume
VOC	Volatile organic compounds
WGS	World Geodetic System
WHO	World Health Organization
z_0	Surface roughness length
z_1	Lowest model layer height
α^*	Grid volume
ζ	Scalar quantity
Γ	Lapse rate / Stability
Γ_d	Dry adiabatic lapse rate
Γ_e	Environmental lapse rate
κ	Kármán's constant
λ	Wavelength
λ_1, λ_2, λ_3	Shape parameters for the Expgauss function
μ	Mean of a Gaussian distribution
σ	Standard deviation of a Gaussian distribution
τ	Surface shear stress
ν	Photon frequency (in chemical reactions) or kinematic viscosity
ρ	Density
ϕ	Flow angle
χ	Volume mixing ratio

1 Introduction

Shipping is the anchor of a globalized world.

Almost the entire world population benefits from shipping. It allows the cost-effective transport of enormous quantities of goods across the world's oceans. Fishing is one of the most important sources of food and work for many coastal residents. The cruise-shipping sector represents one of the cornerstones of tourism.

Nevertheless, shipping also poses a growing problem for the climate, health and the environment (Fig. 1.1). This Chapter gives an overview of the impacts of air emissions (gases and particles) on the air quality, climate and the environment. E.g., Byrnes and Dunn (2020) and Jägerbrandt et al. (2019) give a good general overview on shipping impacts on the environment.

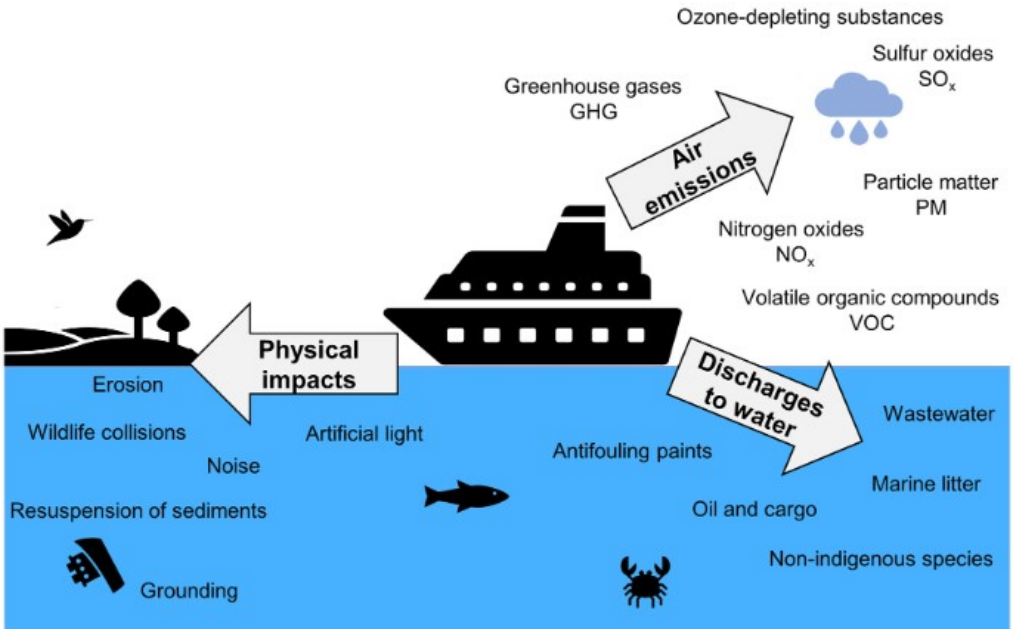

Figure 1.1: Overview of environmental impacts of shipping (adapted from Jägerbrandt et al., 2019).

1.1 The role of ship emissions from an air quality perspective

The urge to quantify ship emissions has attracted much international attention due to the fast growth in shipping activity during recent decades (Brandt et al., 2013). Despite a slowing international maritime trade in 2020 as a result of the coronavirus disease, the global commercial shipping fleet grew by 4.1% over the course of the year, representing the highest growth rate since 2014 (UNCTAD, 2020).

The negative impacts of shipping emissions on human health and the environment remain an ongoing problem in coastal cities. Ship emissions include various pollutants that are relevant to air quality. The most important pollutants are oxides of nitrogen (NO_x = NO + NO_2), oxides of sulfur (SO_x), carbon monoxide (CO), volatile organic compounds (VOC) and particulate matter (PM).

The quantitative composition depends on the type of fuel, the ship engine and the exhaust gas cleaning measures (Fridell et al., 2008; Moldanová et al., 2009).

Globally, ships are known to emit 5.0–7.0 · 10^9 kg yr^{-1} of NO_x, 4.7–6.0 · 10^9 kg yr^{-1} of sulfur dioxide (SO_2) and 1.2–1.6 · 10^9 kg yr^{-1} of PM into the atmosphere (Corbett and Koehler, 2003; Eyring et al., 2005). According to the 3rd Greenhouse Gas Study from the International Maritime Organization (Smith et al., 2015), this translates to 15% NO_x and 13% SO_x of all global emissions.

Seventy percent of ship emissions occur near coastlines and therefore contribute to air pollution in both coastal areas and harbor cities (Andersson et al., 2009; Corbett et al., 1999; Endresen, 2003).

In the North Sea region, the relative contribution of shipping to NO_2 emissions reaches up to 25% during summer and 15% in winter (Aulinger et al., 2016). Increasing trends in ship emissions in northern Europe have been modeled for the North Sea (Matthias et al., 2016) and Baltic Sea (Karl et al., 2019a).

Huszar et al. (2010) described that the contribution of ship-induced surface NO_x reaches 10–30% near coastal regions.

Andersson et al. (2009) found an average contribution of shipping emissions to population exposure across Europe of approximately 16.5% NO_x and 11% SO_x.

On the city-scale and according to Merico et al. (2017, 2019), NO_x due to ship and harbor activities could be of a comparable rate to that of road traffic in medium-sized harbor cities, i.e., up to 40%.

Ledoux et al. (2018) described that harbor emissions contribute to 51% SO_2, 35% NO and 15% NO_2 of the average pollutant concentration in the city of Calais, France.

In the Hamburg harbor area, Ramacher et al. (2020) modeled an impact of shipping on the NO_2 concentration of approximately 50% and between 3 and 30% in the other parts of the city. They modeled maximum concentrations of up to 75 µg m^{-3} NO_2 close to the port.

Regarding the distribution in a harbor city, Bai et al. (2020) described an affected area of 4 to 26 km² from ship emissions in Yantian port in the southeastern part of China. Cohan et al. (2011) found an affected area to be within 2–6 km of the port in San Pedro Bay, California.

Despite not running at full engine power inside of the harbor, ocean-going ships still consume large amounts of fuel for heat and electricity generation and therefore emit atmospheric pollutants while at berth (Hulskotte and Denier van der Gon, 2010).

These have been found to be up to 5 times higher compared to other activities such as maneuvering or cruising during the course of a year, as ships spend more time at berth and have a high auxiliary engine power demand for hotel services (Tzannatos, 2010). This can lead to severe air quality problems in harbor areas.

1.2 Ship emission effects on health and the environment

1.2.1 Health effects

Corbett et al. (2007) presented a study on the global effect of ship-related particulate matter emissions on human health and found that they are at least partially responsible for approximately 60000 cardiopulmonary and lung cancer deaths annually, mainly in coastal regions of Europe and South and East Asia. The harmful effects of ship emissions include asthma, lung diseases and cardiovascular problems. Particulate matter is a significant cause of these diseases (Anderson et al., 2012; Martinelli et al., 2013), especially at sizes smaller than 2.5 µm ($PM_{2.5}$), since these particles can penetrate deep into the lungs and bronchi. A large proportion of particulate matter is also formed from precursor substances such as SO_2 and NO_x by gas-to-particle conversion (Khoder, 2002).

Despite numerous measures to reduce these impacts, such as the International Maritime Organization's global sulfur cap to 0.5% maximum sulfur content in marine fuels since 1 January 2020 (IMO, 2022), research on the impacts of ship emissions on human health and air quality remains an ongoing topic (e.g., Barregard et al., 2019; Ramacher et al., 2019; Zhang et al., 2019).

1.2.2 Eutrophication and acidification

Shipping emissions also contribute to the enrichment of nutrients in coastal waters by the deposition of nitrogen and sulfur compounds (Aksoyoglu et al., 2016; Hunter et al., 2011). This can cause excessive growth of plants and algae (eutrophication), which may result in oxygen deprivation of the water body with detrimental effects for the plants and animals. Complete food chain dynamics may be disrupted.

Nitrogen oxide emissions in combination with volatile organic compounds can cause the formation of ozone (O_3) during summer smog events.

Nitrogen oxides also cause necrosis of plant leaves.

NO_x and SO_2 can be oxidized in the atmosphere and then dissolve in water to form sulfuric acid and nitric acid, respectively. This acidification of droplets can lead to the formation of acid rain. Acid rain damages forests, kills insects, corrodes steel structures and causes weathering of stone buildings and statues (e.g., Seinfeld and Pandis, 2006, Chapter 20.5).

1.2.3 Radiative forcing

Ship emissions also alter the radiative budget of the atmosphere. For example, SO_2 is a toxic gas that can be oxidized to non-sea-salt sulfates that act as cloud condensation nuclei and cause a negative global radiative forcing, therefore cooling the atmosphere (e.g., Capaldo et al., 1999; Langley et al., 2010; Saxena and Seigneur, 1987). On the other hand, ship emissions of the greenhouse gas CO_2 and soot particles cause an absorption of solar energy and a warming of the atmosphere.

1.3 Legislative efforts to reduce shipping emissions

To reduce the harmful effects of air pollutants on human health and the environment, several regional and global guidelines exist. They provide information on the effects of air pollution as well as thresholds for harmful pollution levels.

Most of the EU guidelines for air pollutants are legally binding limit values, whereas the values from the World Health Organization (WHO) are only target values (recommendations) that are not legally binding but offer guidance in reducing health impacts on air pollution (Table 1.1, European Union, 2008; World Health Organization, 2021). In 2019, 99% of the world population was living in places where the WHO air quality guideline levels were not met.

Specific legislative efforts have been made to curb atmospheric pollutant emissions from the shipping sector. On January 1st, 2020, the International Maritime Organization (IMO) enforced the Global Sulfur Cap 2020, according to the revised International Convention for the Prevention of Pollution from Ships (MARPOL) Annex VI, which allows a maximum of 0.5% mass sulfur per mass oil outside of sulfur emission control areas (SECAs). Inside a SECA, a maximum of 0.1% mass sulfur per mass oil was already enforced from 2015 onward (MEPC, 2008). The goals can be met, for example, by using cleaner fuels or exhaust scrubbers. Sulfur dioxide emissions are therefore expected to develop in a beneficial way regarding health and air pollution levels.

Regarding NO_x, the North and Baltic Seas have been declared nitrogen emission control areas (NECAs) since January 1st, 2021. The regulation enforces a reduction of NO_x emissions by 80% compared to the present emission level for newly built ships. This can be achieved by using catalysts (= selective catalytic reduction) or liquefied natural gas (LNG) as a fuel. Karl et al. (2019a) estimated an 80% reduction for the entire maritime transport sector to be reached by 2040.

Table 1.1: EU and WHO guideline values for ambient air pollution concentrations. The peak season is defined as the average daily maximum 8-hour mean O_3 concentration in the six consecutive months with the highest six-month running average O_3 concentration.

Substance	EU guidelines	WHO guidelines
PM_{10}	**24-hour mean:** 50 µg m^{-3} not more than 35 times per year **annual mean:** 40 µg m^{-3}	**24-hour mean:** 45 µg m^{-3} **annual mean:** 15 µg m^{-3}
$PM_{2.5}$	**annual mean:** 20 µg m^{-3}	**24-hour mean:** 15 µg m^{-3} **annual mean:** 5 µg m^{-3}
NO_2	**24-hour mean:** 200 µg m^{-3} not more than 18 times per year **annual mean**: 40 µg m^{-3}	**24-hour mean:** 25 µg m^{-3} **annual mean:** 10 µg m^{-3}
O_3	**maximum 8-hour daily mean:** 120 µg m^{-3} not more than 25 days per year (as a mean over 3 years) *(target value)*	**maximum 8-hour daily mean:** 100 µg m^{-3} and not more than 4 exceedances per year **8-hour daily mean:** 60 µg m^{-3}, peak season
SO_2	**24-hour mean**: 350 µg m^{-3} not more than 24 times per year **daily**: 125 µg m^{-3} not more than 3 times per year	**24-hour mean:** 40 µg m^{-3}
CO	**8-hour daily mean:** 10 mg m^{-3}	**24-hour mean:** 4 mg m^{-3}

The emissions will decrease gradually because nitrogen reduction requirements are only valid for new built ships, and an almost full fleet replacement could take more than 30 years. Sofiev et al. (2018) stated that the implementation of the IMO-2020 policy will cause a global decrease in premature deaths and morbidity due to shipping of 34% and 54%, respectively. Additional measures for reducing emissions include optimizing cruising speed and switching to hydrogen, electricity and wind-assisted propulsion (e.g., Comer, 2019; Kotrikla et al., 2017; McKinlay et al., 2020; Ramacher et al., 2020).

Specific measures to reduce air pollution in the **Hamburg** harbor area that are currently available or planned include (1) the use of PowerPacs (containers with liquefied natural gas), which are used for ship energy supply instead of diesel engines, (2) additional onshore electrical power supply systems, (3) the fitting of ferries with filters and low-emission drives, (4) discounts for cleaner ships on harbor dues, and (5) electrification at the port railway. Moreover, to stop the exceedance of NO_2 limit values and to protect human health, the senate of the city of Hamburg decided to impose diesel transit restrictions for cars under emission standard Euro 6 and trucks under Euro VI norm (e.g., Williams and Minjares, 2016). This applies on two road sections in the inner city of Hamburg: Max-Brauer-Allee and Stresemannstraße, beginning on June 1st, 2018 (BUE, 2017).

1.4 Approach and thesis aim

This work was conducted as part of the DFG-funded project *"ShipCHEM – Regional air quality impacts of ship emissions from megaports in the Yangtze River Delta, China, and in Northern Europe"* in a cooperation between Helmholtz-Zentrum Hereon and the Fudan University of Shanghai, China.

The project aims to improve ship emissions estimates in megaports and coastal areas from regional to local scales. This thesis covers results for the inner-city domain of the port city of Hamburg, Germany.

Chapter 2 provides the scientific foundation of this work. It covers the basics of atmospheric physics and chemistry that are important to analyze ship plumes in this work. It also gives a basic overview on plume modeling methods and the modeling uncertainties.

A general overview on the two main models that were used in this work is given in Chapter 3.

This is followed by a set of three detailed studies on dispersion and chemical transformation in exhaust gas plumes for ships, that are the core of this work.

In the first study (Chapter 4), the microscale model MITRAS is used to derive parameterizations for the downward dispersion of pollutant concentrations in the near field of a medium-sized cruise vessel. The influence of meteorological parameters (wind speed, wind direction and atmospheric stability) as well as the effects of technical parameters (stack exit velocity and exhaust temperature) on the pollutant downward dispersion is examined. The effect of the ship as an obstacle on the wind field is compared to the effect of an ordinary stack. Finally, conditions of strong pollution (i.e., strong downward dispersion) are described, which are crucial for the health conditions of people working in harbor areas.

In the second study (Chapter 5), a similar approach is used to find a parameterization for vertical plume profiles with MITRAS. This is used to derive vertical emission distributions for ship emissions that can be used in the city-scale model EPISODE-CityChem. In this way, the effects of plume rise and downward dispersion are then included in the larger-scale model. Three different parameterization functions for the vertical emission profile are then tested in EPISODE-CityChem, and the effect of different distributions on the plume concentrations several kilometers downwind, i.e., inside the city, are compared. The sensitivity of concentrations on meteorology and the surface roughness inside the city are evaluated. Recommendations are given for which vertical plume parameterization should be used under which meteorological conditions.

Finally, in the third study (Chapter 6), the newly developed plume profiles ("Flexplume") are used in a complex urban air quality study, including realistic meteorology, chemical reactions, multiple ships and other sources such as traffic and industrial emissions. The new Flexplume approach will be compared against a static approach ("Fixplume")

and local measurement values. The model performance is evaluated, and it is shown which areas of the city of Hamburg are affected by ship emissions.

Some key questions answered in the overarching conclusions (Chapter 7) are as follows:

1. What effects do ship emissions have on the pollutant concentration and urban chemistry?
2. Which relevance does ship emissions have for air quality regulations?
3. What benefits did this work bring and what is needed to improve ship plume modeling in the future?

2 Scientific fundamentals

2.1 Atmospheric physics

This chapter will give an overview of relevant physical processes that affect the concentration of pollutants in the boundary layer.

2.1.1 Ideal gas law

This section is based on Chapter 3.4 in Jacobson (2002).

The ideal gas law is the equation of state of a (hypothetical) ideal gas. It can be used to relate the partial pressure exerted by a gas to its number concentration.

$$pV = nRT, \tag{2.1}$$

where p is the pressure, V is the volume, n is the number of gas molecules in moles and R is the ideal gas constant (8.314 J (K mol)$^{-1}$). With the definition of molar mass M and density ρ:

$$M = \frac{m}{n} \tag{2.2}$$

$$\rho = \frac{m}{V}, \tag{2.3}$$

where m is the mass, the ideal gas law can be rewritten as:

$$c = \frac{pM}{RT}, \tag{2.4}$$

where c is the concentration.

Therefore, the general gas equation is the compact summary of various laws, e.g.:

- Avogadro's theorem: Equal volumes of ideal gases contain the same number of molecules at the same pressure and temperature.
- Boyle−Mariotte law: At constant temperature, the pressure is inversely proportional to the volume.
- Law of Amontons: At constant volume, the pressure increases like the absolute temperature.
- Gay−Lussac's law: At constant pressure, the volume increases like the absolute temperature.

In the atmosphere, air parcels change temperature as they respond to a change in pressure as they move vertically. The Ideal gas law is used to calculate how much the density, volume, and temperature change as air parcels rise and sink.

Equation (2.4) also allows a quick conversion from mass concentration [µg m^{-3}] to volume mixing ratio χ in parts per billion [ppb] and vice versa:

$$c = 0.001 \frac{\chi p M}{R T}, \tag{2.5}$$

The factor 0.001 is necessary since M is usually given in [g mol^{-1}] and not in [kg mol^{-1}]. The volume mixing ratio of 1 ppb equals a value of 1 molecule of a certain gas per 10^9 molecules of dry air. This is a basic equation in atmospheric modeling for converting input data given in different formats.

2.1.2 Boundary layer

This section covers basics of the boundary layer theory relevant for this thesis. It is summarized from Carruthers (2003), Jacobson (2002 Chapter 3.3), and Seinfeld and Pandis (2006, Chapter 16.4).

All air pollution from ships and most of the anthropogenic pollution in general occurs inside the planetary boundary layer. This part of the atmosphere extends from the ground surface to a height of between 500 and 3000 m. The upper boundary is characterized by a statically stable temperature inversion.

The temperature profile in the boundary layer responds to ground temperature changes over a period of less than one hour (Stull, 1988, Chapter 1.6).

The boundary layer temperature has a marked diurnal cycle, especially during fair weather over land (Fig. 2.1).

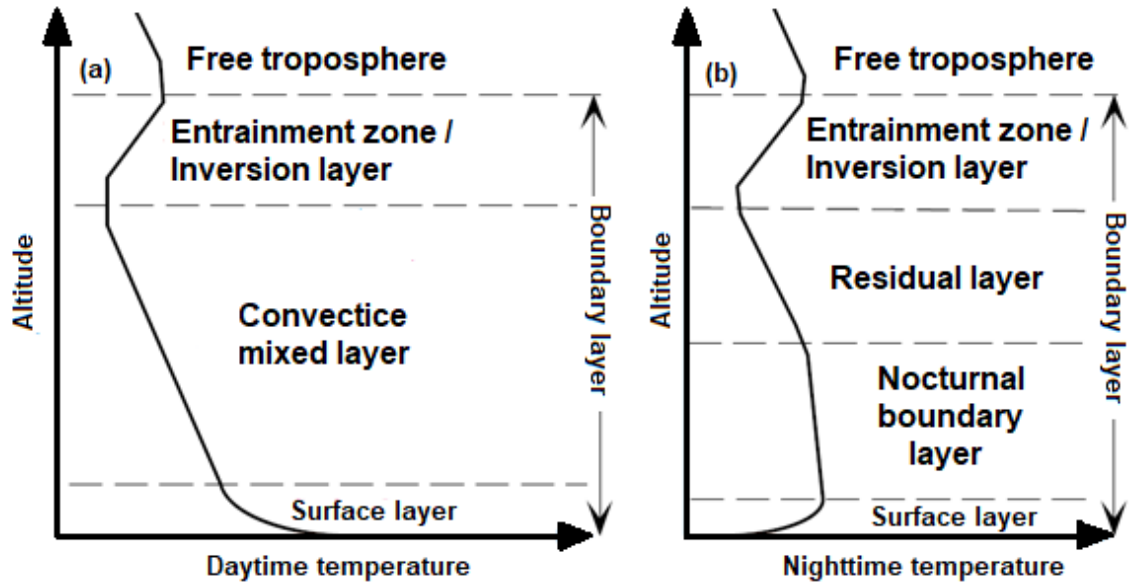

Figure 2.1: Variation in temperature with height in the atmospheric boundary layer during (a) day and (b) night over land under a high-pressure system. Adapted from Jacobson (2002, Chapter 3.3) and Stull (1988, Chapter 1.6).

During daytime, the boundary layer consists of a surface layer, a convective mixed layer and an entrainment zone. The surface layer is characterized by strong changes in wind speed with height and is approximately 50 to 300 m thick. The sun heats the ground and the air just above it. This warm air rises as due to being less dense than the cold air above. This process is called free convection. It displaces cool air aloft downward and causes an often turbulent mixing in the convective mixed layer. This also causes a mixing of pollutants into a wider area. The inversion above inhibits a further rise in the thermals, but some mixing between the inversion and mixed layer occurs (entrainment). Pollutant concentrations are higher when the inversion occurs closer to the ground.

Turbulence decays near sunset, and convective processes slowly cease. During the night, the bottom of the convective mixed layer is transformed into a statically stable nocturnal boundary layer. The surface cools by longwave radiation at night, creating a surface inversion, which traps pollutants close to the ground. The air above remains a residual layer where weak turbulent motions are still active. The temperature inversion above also remains at night.

If the surface is very smooth (e.g., on a calm water body), a laminar sublayer can establish inside the surface layer.

The mean velocity profile over a **smooth surface** and under adiabatic conditions is

$$\overline{u_x} = u_* \left(\frac{1}{\kappa} \ln \left(\frac{u_* z}{\nu} \right) + 5.5 \right), \tag{2.6}$$

where κ is Kármán's constant (= 0.4), ν is the kinematic viscosity and u_* is the friction velocity (defined below).

Over a **rough surface**, no laminar sublayer is formed, and therefore, no kinematic viscosity is necessary for the wind profile calculation. However, the effects of roughness elements on the wind field now need to be considered.

One defines a roughness length z_0 as the height above the surface, where the mean wind speed is zero. It has been experimentally found to be approximately the average height of obstacles divided by 30.

An overview of different surface roughness lengths is given in Table 2.1.

The friction velocity expresses the magnitude of shear stress and is calculated as:

$$u_* = \sqrt{\frac{\tau}{\rho}}, \tag{2.7}$$

where τ is the surface shear stress and ρ is the air density.

Table 2.1: Roughness lengths for various surfaces, according to McRae et al. (1982).

Surface	z_0 [m]
Very smooth (ice, mud flats)	10^{-5}
Snow	10^{-3}
Smooth sea	10^{-3}
Level desert	10^{-3}
Lawn	10^{-2}
Uncut grass	0.05
Full-grown root crops	0.1
Tree covered	1
Low-density residential	2
Central business district	5−10

Since measurements of surface shear stress are often not available, an alternative to determine u_* is to derive it from wind speed measurements at a reference height (h_r, often 10 m):

$$u_* = \frac{\kappa \overline{u_x} h_r}{\ln\left(\frac{h_r}{z_0}\right)} \tag{2.8}$$

The vertical wind velocity profile then becomes:

$$\overline{u_x}(z) = \frac{u_*}{\kappa} \ln\left(\frac{z}{z_0}\right) \quad \text{if} \quad z > z_0 \tag{2.9}$$

This profile is valid for heights significantly greater than the roughness length and under adiabatic conditions.

To find velocity profiles under more frequently encountered nonadiabatic conditions, the Monin-Obukhov similarity theory is employed (Monin and Obukhov, 1954; Foken, 2006).

The Monin-Obukhov length L is the height at which the production of turbulence by mechanical and buoyancy forces is equal. This provides a measure of surface layer stability. A detailed derivation of L is found in Seinfeld and Pandis (2006, Chapter 16.4).

Golder (1972) presented a simplified relation between L, surface roughness and stability:

$$\frac{1}{L} = a + b \log(z_0) \tag{2.10}$$

The coefficients a and b depend on the atmospheric stability, more precisely on the Pasquill Stability Classes (Pasquill and Smith, 1983). Values are given in Table 2.2.

Table 2.2: Correlation parameters for the estimation of L using Eq. (2.10), after Golder (1972)

Pasquill stability class	a	b
A (extremely unstable)	-0.096	0.029
B (moderately unstable)	-0.037	0.029
C (slightly unstable)	-0.002	0.018
D (neutral)	0	0
E (slightly stable)	0.004	-0.018
F (moderately stable)	0.035	-0.036

Pasquills stability classes can be derived by simple measurements of surface wind speed, incoming radiation and cloud cover. Table 2.3 gives an overview of the classes according to Turner (1969).

Finally, with the derived Monin-Obukhov length L, additional equations are available for the calculation of the mean wind profile.

For a stable atmosphere:

$$\overline{u_x}(z) = \frac{u_*}{\kappa}\ln\left(\frac{z}{z_0}\right) + 4.7\frac{u_*}{\kappa}\frac{z - z_0}{L} \tag{2.11}$$

And for an unstable atmosphere:

$$\overline{u_x}(z) = \frac{u_*}{\kappa}\int_{\frac{z_0}{L}}^{\frac{z}{L}} \frac{d\xi}{\xi(1-15\xi)^{\frac{1}{4}}}, \tag{2.12}$$

where ξ *is a* dimensionless length in the surface layer ($\xi = z\,L^{-1}$).

More details on stability are given in Chapter 2.1.3.3.

When investigating urban systems, it is helpful to specify the characteristics of an urban boundary layer. This is generally done at different length scales: the street scale, neighborhood scale and city-scale (Britter and Hanna, 2003).

Table 2.3: Estimation of Pasquill stability classes according to Turner (1969).

	Daytime			Nighttime	
	incoming solar radiation			Cloud cover fraction	
Surface wind speed (10 m) [m s^{-1}]	**> 700 W m^{-2}**	**350−700 W m^{-2}**	**< 350 W m^{-2}**	$\geq \frac{4}{8}$	$\leq \frac{3}{8}$
< 2	A	A−B	B	−	−
2−3	A−B	B	C	E	F
3−5	B	B−C	C	D	E
5−6	C	C−D	D	D	F
> 6	C	D	D	D	D

The street scale covers the flow around single obstacles (e.g., buildings or ships), divergence around and displacement above it. Vortices in front and in the wake of the obstacle are formed. The wake extends several obstacle heights downstream, and the flow there tends to be highly turbulent.

The neighborhood scale extends to approximately 1−2 km. It may have the size of the Hamburg harbor area. Groups of buildings can be treated collectively with similar surface roughness assumptions. Vertically, it covers the surface layer and can be divided into two sublayers: a roughness sublayer and an inertial sublayer above. In the roughness sublayer, fluxes and mean profiles are spatially variable, and wind velocities are different upwind and downwind of a building. In the inertial sublayer, they are homogeneous.

The city-scale extends to the size of a whole city. It comprises several surface roughness classes that affect the wind profile. Differences between air flow in the rural areas upwind and downwind of the city need to be covered, as well as increased surface heating and convectively rising air masses in urban areas.

Another important feature of the boundary layer is the turning of wind direction at heights between approximately 100 and 1000 m. In the free troposphere, wind moves almost parallel to the isobars, i.e., the lines of equal pressure. This is caused by an equilibrium of pressure gradient force and Coriolis force (i.e., the inertial force caused by Earth's rotation). Close to the ground, the friction force causes an imbalance and a spiral turning of wind direction, the **Ekman spiral**.

For a plume emitted on a near-surface position in the Northern Hemisphere and under north wind conditions at the ground, the Ekman spiral causes the plume to turn to the east (clockwise) with increasing height until it (theoretically) reaches the free troposphere.

2.1.3 Factors affecting concentrations

The most important factors controlling the plume concentration are the emission rate, wind speed and atmospheric stability. The emission height, exhaust temperature and location of atmospheric inversion layers determine whether pollutants are trapped close to the ground. Deposition processes remove pollutants from the atmosphere.

The underlying mechanics are presented in the following subchapters, following the meteorological basics from Jacobson (2002, Chapter 3.3 and Chapter 6.6).

2.1.3.1 Emission rate

Increasing the **emission rate** (i.e., mass of emitted substance per hour), significantly impacts the chemical transformation. NO_x promotes highly nonlinear chemistry, where increases in emissions can lead to even larger increases in its loss rate. The NO_x lifetime inside a plume is shorter than that under clean ambient conditions, such as the marine boundary layer. The chemical transformation rate is further affected by the strength of solar radiation and background levels of O_3, CO and volatile organic compounds (VOCs).

Typical emission rates for NO_x from ships range between 4 and 20 g s^{-1} (Hobbs et al., 2000; Song et al., 2003).

For rather passive gases such as CO_2, an increase in emission rate directly translates into a concentration increase (see Chapter 2.2 for more information on atmospheric and plume chemistry).

2.1.3.2 Advection and convection

Advection is the horizontal movement of energy, gases and particles by wind and results in the mass movement of molecules. The **wind speed** determines the advective transport of pollutants away from the source. This means that higher wind speeds result in lower pollutant accumulation and therefore a lower local concentration. In case of a moving ship, it is important to take the relative movement of the ship into account. Concentrations are highest if the ship moves in the same direction as the wind and lowest if it moves counter to the wind. One can use relative wind speeds to account for ship movements. The relative wind speed can be calculated with the trigonometric law of cosines:

$$v_{rel} = \sqrt{v_{wind}^2 + v_{ship}^2 - 2\, v_{wind} v_{ship} \cos(\phi)}, \qquad (2.13)$$

where ϕ is the angle between vectors of wind speed v_{wind} and ship speed v_{ship} (e.g., 0° means frontal wind, 90° and 270° means lateral wind and 180° means tailwind).

Convection describes the transfer of energy, gases and particles by vertical movement of the air. A distinction is made between free and forced convection.

Free convection describes thermal turbulence, which is predominantly produced when the sun heats different areas of the ground differently and has been explained in Chapter 2.1.2.

Forced convection is caused by mechanical means, e.g., due to a topographic barrier or obstacles, which create turbulent swirling air motions (**eddies**).

2.1.3.3 Lapse rates and stability

Adiabatic expansion describes the process of expansion by a change in air pressure. The kinetic energy of air molecules is thereby converted to expand the air. The temperature of the air is proportional to the kinetic energy of air molecules. Therefore, a parcel of rising air (e.g., a plume) cools during adiabatic expansion.

The lapse rate describes this rate of temperature changes with an increase in altitude.

The dry adiabatic lapse rate of this air parcel is $\Gamma_d = -9.8\ K\ km^{-1}$.

Note: Throughout this work, a negative lapse rate indicates decreasing temperatures with height, whereas a positive lapse rate indicates increasing temperatures with height.

Water vapor in the atmosphere reduces the lapse rate since cooling air decreases the saturation vapor pressure of water, causing a condensation and release of latent heat.

The environmental lapse rate Γ_e describes the actual change in air temperature outside of the specific air parcel.

The **stability** of the air is a measure of whether pollutants emitted will convectively rise and disperse or stay close to the emission height.

Three basic states of the atmospheric surface layer can be distinguished: stable, neutral and unstable. The adjectives describe how a parcel of air, which can be an emitted plume, reacts when displaced adiabatically in the vertical direction.

The emitted plume will move along the gray line of Γ_d in Figure 2.2. Whether it rises or sinks depends on the current environmental lapse rate.

If the surrounding atmosphere is **stable** ($\Gamma_e > \Gamma_d$), the plume will move neither upward nor downward. A perturbed plume will quickly decelerate and move back to the original height. Stable atmospheres can cause near-surface pollution buildup when sources are close to the ground. When sources are elevated, they cause a typical **fanning** behavior, i.e., the plume remains at the emission height.

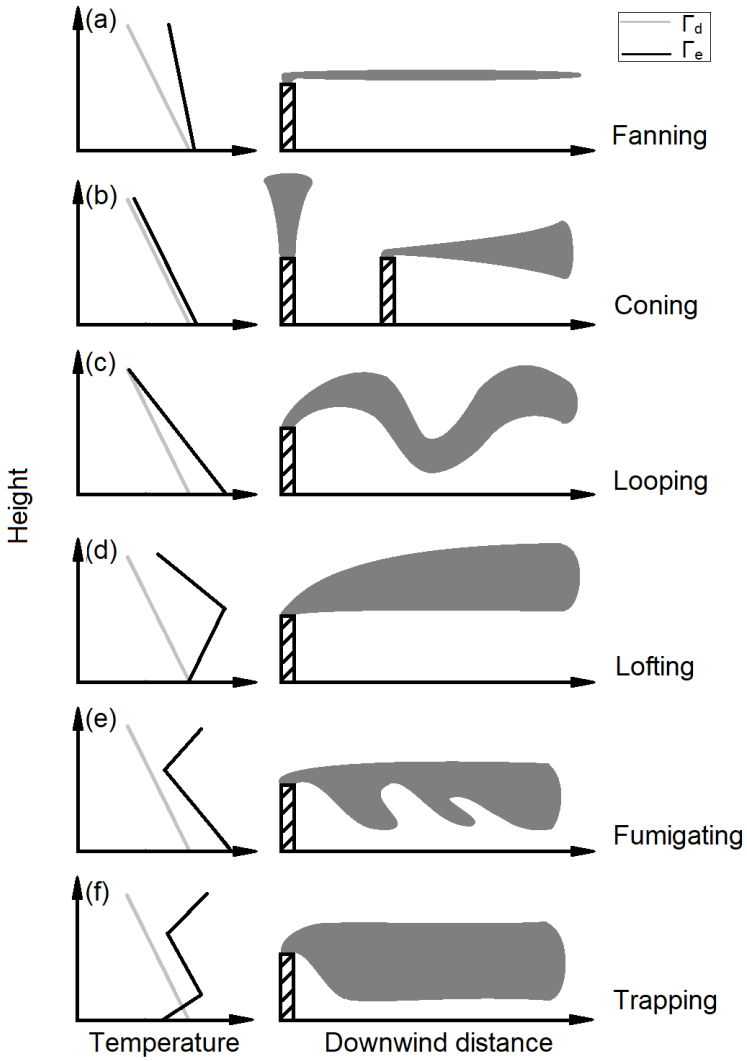

Figure 2.2: Scheme of different plume types depending on the ambient temperature profile. The gray line corresponds to the dry adiabatic lapse rate of the plume (Γ_d = -9.8 K km^{-1}), and the black line is the environmental lapse rate (Γ_e).

In a **neutral** atmosphere, the environmental lapse rate is equal to the dry adiabatic lapse rate ($\Gamma_e = \Gamma_d$ = -9.8 K km^{-1}). A perturbed plume will neither accelerate nor decelerate, but continues to move along the direction of the initial perturbation at a constant velocity. Neutral atmospheres occur on windy and cloudy days or nights. Over the open ocean, the most likely stability condition is neutral, caused by the similar temperature between the ocean and the lower troposphere (Frick and Hoppel, 2000).

The typical plume shape of a neutral atmosphere is **coning**. Slight turbulence and random movement spread the plume shape far from the source. Under calm conditions, the plume rises vertically until it reaches an inversion layer (see explanation in Chapter 2.1.3.4).

For **unstable** conditions, the environmental lapse rate is smaller than the dry adiabatic lapse rate ($\Gamma_e < \Gamma_d$). A perturbed plume is accelerated in the direction of perturbation.

The plume stops accelerating only when encountering air with the same temperature and density, i.e., a new environmental lapse rate. Unstable conditions typically occur in the lowest 100 m of the surface during a sunny day driven by thermals in the convective mixed layer (Hanna et al., 1982). Different sized eddies often cause a **looping** shape of the plume.

2.1.3.4 Inversions and mixing height

A special case of strong atmospheric stability is inversions, i.e., increases in air temperature with increasing height. They can occur both near the ground and at higher altitudes and strongly affect plume movement.

The **mixing height** is the height from the ground to the bottom of the inversion. It is an estimated height to which pollutants that are released from the surface mix. However, depending on the initial temperature of the polluted air parcel, some plumes can break through the inversion.

Figure 2.3 shows how the initial plume temperature determines whether trapping by an inversion layer occurs. The scheme shows how plumes with higher exhaust temperatures have an increased capability to break through inversions and reach higher altitudes, which reduces the danger of near-ground pollution.

Concerning plume classifications, the consideration of inversions adds more types of plumes depending on the location of the inversion.

The already mentioned fanning plume also exists when the inversion reaches from the ground until above the stack, since it is just a special case of a very stable atmosphere.

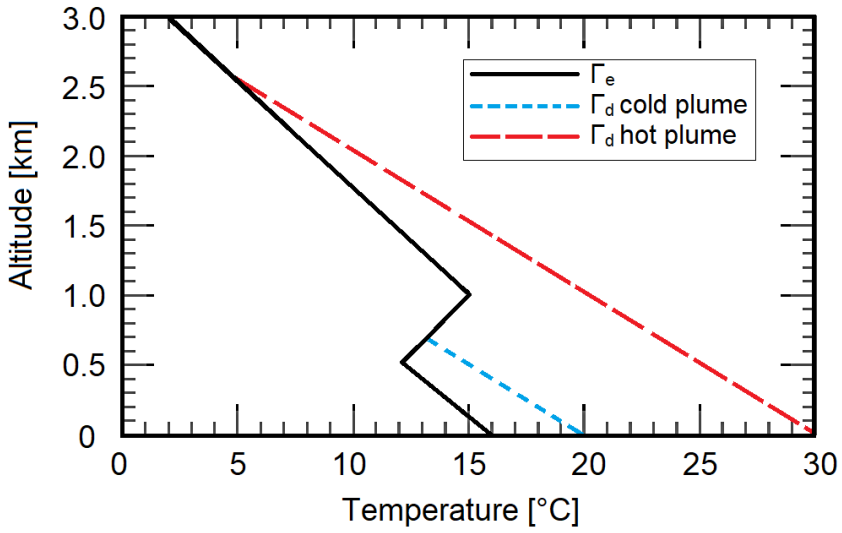

Figure 2.3: Scheme of idealized plumes trapped by an inversion and by stable stratified air. The cold plume (blue) released at 20 °C rises at a dry adiabatic lapse rate (-9.8 K km^{-1}) until its temperature equals that of the environment. This plume is trapped by the inversion. The hot plume (red) released at 30 °C also rises at -9.8 K km^{-1}. It breaks through the inversion but stops rising in stable free-tropospheric air, where the environmental lapse rate is -6.5 K km^{-1}. Adjusted from Jacobson (2002, Chapter 6.6).

The lofting plume occurs when a ground inversion occurs but does not reach the stack height. The plume therefore always stays above the stack height.

A **fumigating** plume occurs when the inversion lies above the stack height and an unstable atmosphere occurs below, creating turbulent mixing of pollutants toward the ground.

Finally, if two inversions occur, one below the stack and one above it, this is called a **trapping** condition. The plume will then remain between the two inversions.

Whether an inversion occurs close to the ground or at greater altitudes depends on the formation mechanism. Common inversion types include radiation inversion, subsidence inversion, marine inversion and frontal inversion. Most of them are formed due to differences in atmospheric pressure above and/or temperature above different regions. For example, radiation inversion often occurs at night when land surfaces cool down by emitting thermal infrared radiation. The air is then warmer than the ground below, creating a near-surface inversion.

2.1.3.5 Sink mechanisms for atmospheric gases

A variety of chemical and physical mechanisms causes the concentration of atmospheric pollutants to decrease.

Chemical reactions such as oxidation by OH radicals or photolysis can transform a pollutant into another substance, thereby reducing its concentration. The most important chemical reactions affecting ship plume emissions are covered in Chapter 2.2.

From a physical perspective, the most important removal mechanisms are dry and wet deposition (Carruthers, 2003).

Dry deposition covers the removal of pollutants from the atmosphere to the ground or onto surfaces by gravitational sedimentation, diffusion or turbulence.

Increasing deposition rates are caused by higher concentration; therefore, the strength of the pollution directly impacts the deposition (World Meteorological Organization, 2022). Typical dry deposition velocities are between 0.1 and 1 cm s^{-1}.

Wet deposition occurs when atmospheric pollutants mix with suspended water in the atmosphere and are then washed out through rain, fog or snow.

Molecules of higher polarity are more soluble. In particular, gases containing a high fraction of oxygen atoms, such as HNO_3 and H_2SO_4, are easily soluble and undergo dissociation in the aqueous phase, e.g., $HNO_3 \longrightarrow H^+ + NO_3^-$.

The free H^+ ions reduce the pH value of the droplets, creating acid rain or fog.

2.2 Atmospheric chemistry

The following section describes the relevant chemical features for an urban atmosphere that is affected by ship plumes.

2.2.1 Background chemistry

The background ozone concentration is determined by a set of three reactions with nitrogen oxides (e.g., Jacobson, 2002, Chapter 4.2).

$$NO + O_3 \longrightarrow NO_2 + O_2 \quad (2.14)$$

$$NO_2 + h\nu\ (\lambda < 420\ nm) \longrightarrow NO + O(^3P) \quad (2.15)$$

$$O(^3P) + O_2 + M \longrightarrow O_3 + M \quad (2.16)$$

The first reaction is NO titration. This reaction transforms NO emissions into NO_2 and causes a loss of O_3. The second reaction is the NO_2 **photolysis**, i.e., a chemical process by which molecules are broken up through light absorption. M is a neutral collision partner (usually molecular nitrogen or oxygen) that absorbs parts of the reaction energy.

NO_2 photolysis creates O_3 during the daytime at a wavelength $\lambda < 420$ nm. The rate-limiting step for the production of ozone is the creation of ground-state oxygen atoms by NO2 photolysis. The atomic oxygen is so reactive that it disappears as fast as it is formed. These reactions alone create a steady-state equilibrium over a long time (photostationary state). The volume mixing ratio of ozone (χ_{O_3}) formed in this equilibrium can be calculated as:

$$\chi_{O_3} = \frac{J_{NO_2}}{N_d k_1} \frac{\chi_{NO_2}}{\chi_{NO}}, \quad (2.17)$$

where J_{NO2} is the photolysis rate coefficient of Eq. (2.15), k_1 is the rate coefficient of Eq. (2.14) and N_d is the concentration of dry air ($2.46 \cdot 10^{13}$ molecules cm^{-3}). The photolysis rate coefficient is depending on the strength of radiation ($\lambda < 420$ nm) and k_1 depends on temperature.

In a clean atmosphere, e.g., marine background air, the **hydroxyl radical** (OH) - the main chemical species controlling the oxidizing capacity of the troposphere - is formed during the daytime by photolysis of O_3 and further reaction of atomic oxygen with water vapor:

$$O_3 + h\nu\ (\lambda < 310\ nm) \longrightarrow O_2 + O(^1D) \quad (2.18)$$

$$O(^1D) + H_2O \longrightarrow 2\ OH \quad (2.19)$$

$O(^1D)$ is the atomic oxygen in the excited state.

2.2.2 NO_x- and VOC-limited regimes and smog

The NO_x-O_3 cycle in a photostationary state has been explained before. However, the formation of NO_2 from NO is also possible without O_3. This process requires the HO_2 or another peroxy radical and can lead to a net formation of O_3.

HO_2 is created by the oxidation of CO or volatile organic compounds (VOCs = CH_4 and non-methane hydrocarbons (NMHCs), including biogenic VOCs such as isoprene and terpenes) with OH radicals.

Sources for OH radicals are the already presented photolysis of ozone (2.18 and 2.19) and, in the urban atmosphere, it can also be created, e.g., by photolysis of nitrous acid and formaldehyde or the reaction of NO with HO_2 radical (see Fig. 2.4):

$$NO + HO_2 \longrightarrow NO_2 + OH \qquad (2.20)$$

This indicates that high concentrations of CO or VOCs can cause increased O_3 formation. Due to its longer atmospheric lifetime of approximately 2 months, CO concentrations mainly affect the background ozone concentration. To reach peak concentrations, ozone production is either NO_x-limited or VOC-limited (Fig. 2.4).

Conditions of high mixing ratios of both VOC and NO_x, combined with stable sunny weather can lead to the formation of **summer smog**, a mixture of gases and aerosol particles that is typically heavier than background air due to heavier organic compounds (e.g., aromatics).

Under smog conditions, high ozone concentrations are possible, especially at a concentration ratio of VOC:NO_x of 8:1. This is visualized by ozone isopleths (i.e., lines of equal ozone concentrations) in an EKMA (empirical kinetic modeling approach) diagram (Fig. 2.5; Dodge, 1977).

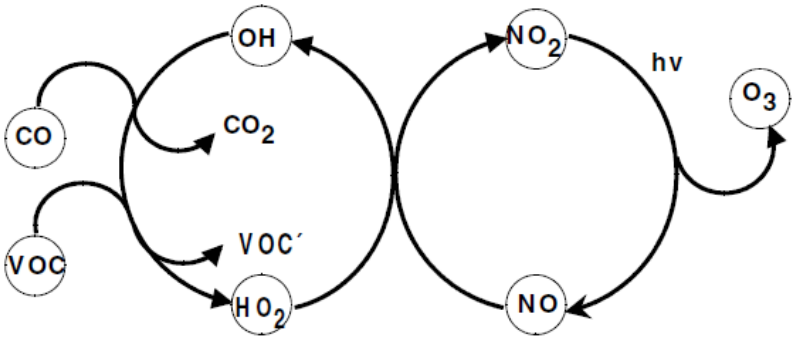

Figure 2.4: Cycle of ozone formation from precursors and the role of NO_x, CO and VOCs.

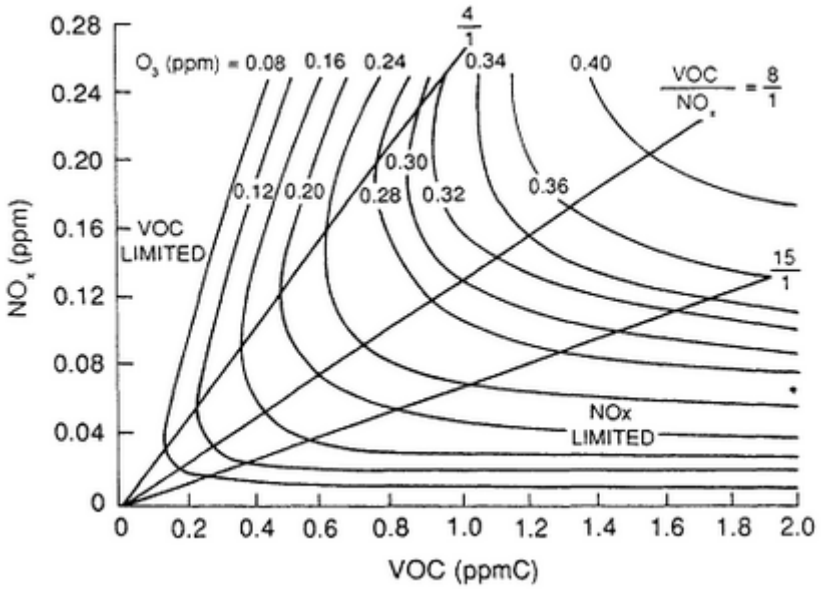

Figure 2.5: Typical ozone isopleths showing NO_x- and VOC-limited regimes for ozone production. Adapted from Dodge (1977).

The ozone isopleths are lines of equal ozone concentration.

In many polluted urban areas, the ratio is lower than 8:1, indicating that limiting VOC emissions should be the most effective method of controlling ozone. A net O_3 formation occurs downwind of city centers rather than inside. Urban areas are generally VOC-limited.

In a NOx-limited regime, more HO_2 radicals are formed than react with NO to NO_2. In this regime, the absolute amount of formed O_3 over a longer period of time can only be reduced by reducing NO_x emissions. This is typical for rural areas.

2.2.3 Plume O_3 and NO_x chemistry

Adding an emission source, e.g., a ship that emits a pollutant plume, disturbs the steady-state equilibrium of O_3. For detailed insights into ship plume chemistry, it is useful to distinguish three phases of plume evolution (Karamchandani et al., 1998, 2000; Song et al., 2003):

1) Early plume dispersion (i.e., χ_{NO_x} > 1 ppm and O_3 depletion)

2) Mid-range dispersion (i.e., χ_{NO_x} ~ several ppb and O_3 recovery)

3) Long-range dispersion (i.e., χ_{NO_x} < 1 ppb and net O_3 production)

Furthermore, it is important to distinguish between daytime and nighttime chemistry due to several photochemical reactions that are only active during daytime.

NO is formed in a thermal combustion reaction at high temperatures from molecular nitrogen (N_2) and molecular oxygen (O_2).

$$N_2 + O_2 \longrightarrow 2\ NO \tag{2.21}$$

The early stage of plume dispersion is similar during the day and night. Titration of ambient O_3 by NO emissions (Eq. 2.14) is the dominating process, reducing O_3 often to values close to zero (Song et al., 2003). The back-reactions (Eq. 2.15 and 2.16) happen later, depending mainly on the initial NO_x emission rate, relative wind speed and atmospheric stability. During the night, there is no photolysis of NO_2 due to the absence of shortwave radiation.

During the day, the strong depletion of O_3 causes a suppression of OH production in the early stage of the plume. The O_3 concentration recovers to background values after plume aging of approximately 30 to 100 minutes (Song et al., 2003). In this **second stage** of the plume evolution, OH formation is reactivated (Eq. 2.18 and 2.19).

Additional OH formation can occur with NO and available HO_2 (Eq. 2.20) or the methylperoxy radical (CH_3O_2):

$$NO + CH_3O_2 \longrightarrow NO_2 + CH_3O \tag{2.22}$$

These reactions convert NO to NO_2 without O_3 and are followed by NO_2 photolysis (Eq. 2.15 and 2.16), therefore causing net O_3 formation in the third stage of the plume. Reactions with hydroxyl radicals (OH) can also remove NO_2 from the photostationary state. The formed HNO_3 can be scavenged by water droplets and underlie wet deposition.

$$NO_2 + OH + M \longrightarrow HNO_3 + M \tag{2.23}$$

M represents a non-reacting molecule (often O_2 or N_2) that absorbs a portion of the reaction energy to produce a stable reaction product. The nitrate radical (NO_3) and dinitrogen pentoxide (N_2O_5) are considered nighttime species. NO_3 formation is possible via:

$$NO_2 + O_3 \longrightarrow NO_3 + O_2 \tag{2.24}$$

At night it further reacts with NO_2 to form N_2O_5. The three nitrogen oxides exist in a dynamic equilibrium.

$$NO_2 + NO_3 + M \rightleftharpoons N_2O_5 + M \tag{2.25}$$

During the night, NO_3 takes over as the major reactive oxidant in the troposphere.

During the day, NO_3 is photolyzed.

$$NO_3 + h\nu\ (420\ nm < \lambda < 690\ nm) \longrightarrow NO_2 + O(^3P) \tag{2.26}$$

N_2O_5 can react with water in the aqueous phase to form nitric acid.

$$N_2O_5 + H_2O \longrightarrow 2\ HNO_3 \tag{2.27}$$

This reaction occurs on aerosol or hydrometeor particle surfaces.

2.2.4 Sulfur chemistry

Sulfur dioxide (SO_2) is a gaseous and predominantly anthropogenic air pollutant, as it is the byproduct of burning fossil fuels that are contaminated with sulfur compounds such as heavy diesel oil (HDO).

$$S + O_2 \longrightarrow SO_2 \tag{2.28}$$

Stockwell and Calvert (1983) derived the following gas-phase reaction with the OH radical to form the hydroxysulfonyl radical ($HOSO_2$):

$$SO_2 + OH + M \longrightarrow HOSO_2 + M \tag{2.29}$$

This is followed by the regeneration of the chain-carrying HO_2 radical:

$$HOSO_2 + O_2 \longrightarrow HO_2 + SO_3 \tag{2.30}$$

In the presence of water vapor, sulfur trioxide (SO_3) is converted rapidly into sulfuric acid (H_2SO_4):

$$SO_3 + H_2O + M \longrightarrow H_2SO_4 + M \tag{2.31}$$

This is a precursor to acid rain and atmospheric particles. It may also combine with ammonia (e.g., from agricultural emissions) to form ammonium sulfate particles.

Capaldo et al. (1999) showed that ship emissions of SO_2 can lead to enhanced rates of cloud condensation particle formation.

2.3 Plume modeling

When modeling air pollutant concentrations, one must distinguish between Eulerian and Lagrangian approaches. In Eulerian approaches, the behavior of a species is described relative to a fixed coordinate system. In Lagrangian approaches, the concentration changes are described relative to a moving fluid. This work applies the Eulerian models MITRAS and EPISODE-CityChem (Chapter 3). However, since many single-plume studies are based on (Lagrangian) Gaussian plume calculations, an overview of this approach is also given.

This chapter further describes the important data that are necessary for ship plume modeling, gives a slight overview of previous ship plume modeling studies and describes the causes of uncertainties.

2.3.1 Eulerian diffusion modeling

This section is based on the general description of Eulerian modeling from Seinfeld and Pandis (2006, Chapter 16.4).

Diffusion is the mixing of substances in contact with each other due to their thermal molecular motion (Brownian motion). This explains the net flux of molecules from a region of higher concentration to one of lower concentration.

When no or only little external energy is added (e.g., in a laminar flow), the process is called **molecular diffusion**. This can occur due to differences in concentration, pressure and temperature.

Molecular diffusion for gases at normal densities occurs when the mean free path of a molecule is many orders of magnitude smaller than the distances over which gas properties such as velocity or temperature vary. It rarely occurs in the boundary-layer atmosphere, as there are usually turbulent eddies of the same size as the characteristic length scale for changes in the mean fields of velocity, temperature or concentration.

Diffusion caused by turbulent motions is called **turbulent diffusion** or eddy diffusion. It occurs as a combination of steep concentration gradients, density gradients and high velocities. It occurs more rapidly than molecular diffusion.

The strength of diffusion depends on the atmospheric stability. In the case of a stable atmosphere, the horizontal scale of turbulence is much greater than the vertical scale of turbulence. In the case of instability and buoyancy, the vertical diffusion may be greater than the horizontal diffusion.

To calculate the concentration changes over a volume element, the **continuity equation** must be satisfied. This means, that the sum of the concentration change over time and transport out of the volume element must be equal to the sum of concentration change entering by diffusion, production by chemical reactions and sources inside the volume element.

$$\frac{\partial c_i}{\partial t} + \frac{\partial}{\partial x_j}\left[\left(\overline{u_j} + u_j'\right)c_i\right] = D_i \frac{\partial^2 c_i}{\partial x_j \partial x_j} + R_i(c_1, \ldots, c_N) + S_i(\boldsymbol{x}, t)\,, \tag{2.32}$$

where u_j is the j^{th} component of the fluid velocity, D_i is the molecular diffusivity of species i in the carrier fluid, R_i is the rate of generation of species i by chemical reactions and S_i is the rate of addition of species i at a certain location $\mathbf{x} = (x_1, x_2, x_3)$ at time t due to local sources. The wind velocities u_j are the sum of a deterministic ($\overline{u_j}$) and a stochastic (u_j') component.

Solving this equation leads to a closure problem, i.e., more dependent variables than independent variables in the equation. Therefore, an **Eulerian description** of turbulent diffusion cannot permit an exact solution for the concentration c_i as a function of space and time. This is why solutions are usually based on the mean concentration ($\bar{c}$) and underly several assumptions. Solving this problem is the basis of the mixing length theory or K-theory. One replaces $\overline{u_j' c'}$ with the eddy diffusivity K_{jj}, i.e. the exchange coefficient for the diffusion of a conservative property by eddies in a turbulent flow:

$$\overline{u_j' c'} = -K_{jj} \frac{\partial \overline{c}}{\partial x_j} \tag{2.33}$$

Under the assumptions that (1) molecular diffusion is negligible compared to turbulent diffusion and (2) the atmosphere is incompressible ($\frac{\partial \overline{u_j}}{\partial x_j} = 0$), the atmospheric turbulent diffusion equation becomes:

$$\frac{\partial \overline{c_i}}{\partial t} + \overline{u_j} \frac{\partial \overline{c_i}}{\partial x_j} = \frac{\partial}{\partial x_j}\left(K_{jj} \frac{\partial \overline{c}}{\partial x_j}\right) + R_i(\overline{c_1}, \ldots, \overline{c_N}) + S_i(\mathbf{x}, t) \tag{2.34}$$

This is a valid description of turbulent diffusion and chemical reactions as long as the reaction processes are slow compared to turbulent transport.

2.3.2 Gaussian plume modeling

One simple approach to describe plume shape and concentration mathematically is by a Gaussian plume model (e.g., Briggs, 1982; Hanna et al., 1985, 2001; Janicke and Janicke, 2001; Schatzmann, 1979). This can be seen as the Lagrangian counterpart to the Eulerian diffusion equations of Chapter 2.3.1 and is the most commonly used approach for single-plume calculations.

Combustion processes such as fuel burning on a ship usually create emissions at higher temperatures than the surrounding atmosphere. The emission is positively buoyant and may be lifted further upward by an accelerated volume flow. This first stage of plume movement is called plume rise and is active as long as the emitted substance is not traveling with the velocity of the surrounding airflow and as long as the plume temperature is higher than the surrounding temperature. Figure 2.6 shows the scheme of a Gaussian plume.

A small layer surrounding the emitted plume is formed due to the different velocities of the released gas and surrounding airflow. Wind shear across this layer leads to small-scale turbulent mixing and an entrainment of cleaner air into the plume. This mixing causes the loss of buoyancy and cooling of the plume.

The plume rise (Δh) is defined as the difference between the effective plume height (h_e), i.e., the height of the plume concentration centerline after the plume temperature reaches ambient temperature and stack height (h_s). It can be calculated by Briggs equations (Briggs, 1982), which offer different solutions for hot and cold plumes in either stable, neutral or unstable ambient atmospheres.

As soon as the temperature of the exhaust plume equals the ambient temperature, the pollutant is transported downwind with the mean wind field (advection) and diffuses laterally and vertically by turbulent eddies.

The expected pollutant concentration is expressed as a function of time and space.

$$\langle C(x,y,z,t)\rangle = \frac{q}{2\pi\bar{U}\sigma_y\sigma_z}\exp\left[-\frac{y^2}{2\sigma_y^2}-\frac{z^2}{2\sigma_z^2}\right], \tag{2.35}$$

where $\langle C(x,y,z,t)\rangle$ is the expected concentration value at coordinates (x, y, z) at time t, q is the source emission rate, $\bar{U}$ is the mean wind speed and σ_y and σ_z represent mixing in the lateral and vertical directions, respectively, in the form of standard deviations of Gaussian distributions. The mixing coefficients are a function of x, i.e., they increase with distance from the source and cause spreading of the plume. Streamwise mixing is neglected, as advective transport usually dominates. The coordinates (x, y, z) are defined relative to the coordinates of the emission point. Parameterizations for σ_y and σ_z that depend on the stability class (Pasquill and Smith, 1983) account for varying stability and height up to a certain degree. Further adjustments of this equation are possible to account for various other features, e.g., reflections from the ground or inversion layers above.

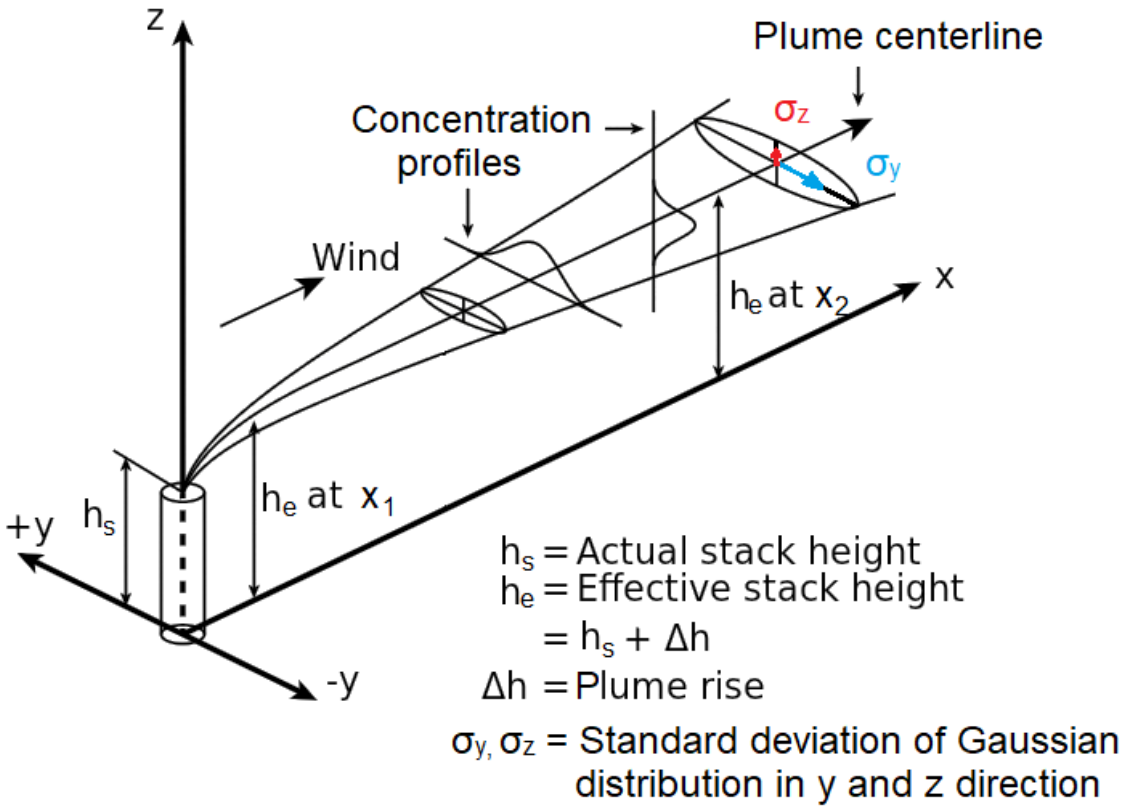

Figure 2.6: Visualization of a buoyant Gaussian air pollutant dispersion plume.

In a convective boundary layer, the σ_z can become significantly non-Gaussian due to strong thermal updraughts and otherwise weak downdraughts (Carruthers, 2003). Then, the height of the maximum concentration will decrease with increasing distance and will not be constant.

Despite all possible adjustments, Eq. (2.35) assumes steady-state conditions, i.e., that the atmosphere behaves the same over several hours. In reality, fast changes in wind speed, stability and turbulence reduce the accuracy of this equation. This is especially the case for emissions close to the ground, e.g., ship plumes that occur under complex and spatiotemporally changing conditions. The effects of large obstacles on the wind field, such as the flow around it, pollution downward dispersion behind it and the formation of downstream wakes, need to be accounted for. A simple Gaussian approach is not sufficient to adequately represent large ships in a complex chemical transport model study.

2.3.3 Ship emission estimation

The ship **activity** can be derived from data from the Automatic Identification System (AIS) (e.g., Jalkanen et al., 2009, 2012; IMO, 2015; Aulinger et al., 2016). These transceivers are mandatory to be used on all ships larger than 300 gross tons to avoid collisions.

AIS data include information on the ship identification number, type, position, course, speed and other safety-relevant information. Positional signals are reported at a temporal resolution depending on the ship speed (e.g., every 10 s for ships moving with a speed between 0 and 14 knots) (IMO, 2015).

From the speed, ship type and available data on engine power, fuel type and loading, energy use in kWh can be derived. Emission factors for specific chemical compounds are typically measured on test beds (e.g., Aulinger et al., 2016). They are given in [g kW h^{-1}]. Multiplying energy use and emission factor yields the total emission in [g].

Emission inventories are integrated datasets of emission data combined from many sources and cover different scales, i.e., from global and international to local and national. They are usually created in a bottom-up approach, which combines activity data with source-specific emission factors.

Some important emission inventories based on ship emissions extracted from AIS data were published by Johansson et al. (2017), who created a global shipping emission inventory, Jalkanen et al. (2009, 2012) and Aulinger et al. (2016) for the Baltic Sea and the North Sea and Ramacher et al. (2018) for a ship emission inventory in Hamburg.

The recently developed modular ship emission modeling system (MoSES, Schwarzkopf et al., 2021) will be applied in Chapter 6.

2.3.4 State-of-the-art ship emission modeling and uncertainties

Many ship plume modeling studies focus on global- or regional-scale plume dispersion, chemistry and their parametrization (e.g., Aksoyoglu et al., 2016; Huszar et al., 2010; Vinken et al., 2011).

On the urban and microscale, a large variety of modeling options for ship emissions exist. Most commonly used for plumes in general are Gaussian dispersion models, where the pollutant distribution corresponds to a normal probability distribution. An example is the offshore and coastal dispersion (OCD) algorithm of Hanna et al. (1985).

Their computational costs are low; however, they often assume a steady-state solution, spatially uniform meteorology and straight-line trajectories (Bluett et al., 2004), making them less suitable for complex air quality modeling studies.

More advanced models used in ship plume studies include large eddy simulations (e.g., Chosson et al., 2008), unsteady Gaussian puff models such as CALPUFF (e.g., Bai et al., 2020; Jahangiri et al., 2018; Murena et al., 2018; Poplawski et al., 2011) or Eulerian grid models such as EPISODE-CityChem (e.g., Karl et al., 2019b, 2020; Pan et al., 2021; Ramacher et al. 2020).

All model studies show a certain degree of over- or underestimations regarding ship emissions. Various studies describe that overestimations and underestimates of modeled emission and concentration values can cancel each other out and assume a general uncertainty of ~30% in their studies (Broome et al., 2016; Merico et al., 2016, 2017).

A certain degree of uncertainty is caused by assumptions of emission rates when exact engine values are not available as well as inaccurate spatial and temporal emission distributions (Matthias et al., 2018). The distribution depends strongly on data availability, interpolation procedures and initial assumptions.

For example, an emission overestimation for single ships can occur if ship emissions are diluted instantaneously and equally into a large grid (Vinken et al., 2011; von Glasow et al., 2003). Due to highly nonlinear NO_x chemistry, this can lead to enhanced lifetimes and higher estimated background NO_x levels. This error can be reduced by using high-resolution numerical models or by adjusting the initial emission factors.

In the Hamburg Harbor study from Ramacher et al. (2020), a comparison with measurements revealed an overprediction of modeled NO_2 close to the port area. In their study, all shipping emissions were released into the lowest vertical layer of the model (10 m) as area sources on a 1 km × 1 km grid without including the effects of plume rise, which might have led to the overprediction.

A common way to include plume rise effects into models that are not obstacle-resolving is to use effective emission heights where emissions are placed into the model at the effective stack height, i.e., after accounting for plume rise effects (see Fig. 2.6). This can either be a fixed height or a distribution of heights to cover different meteorological conditions. Most commonly, a Gaussian distribution is assumed.

The Gaussian vertical emission profile is a good representation for large industrial stacks that are not strongly affected by turbulent motions. However, this approximation might not be valid for large ships that clearly affect the wind field and have a comparatively short stack. The ship stack characteristics must also be accounted for. The exhaust gas leaves the stack with a certain exit velocity and a temperature of several hundred °C. These quantities depend on the technical parameters of the individual ship, which are often unknown.

Based on a large eddy simulation study, Chosson et al. (2008) pointed out that Gaussian plume dispersion models might not be well suited for the early ship plume development. Although the OCD model of Hanna et al. (1985) includes the effects of pollutant downward dispersion behind the obstacle, i.e., the vessel, by lowering the effective plume height and adjusting dilution parameters in the model, this effect has yet to be applied to large ships.

Many studies distribute ship emissions vertically into an Eulerian grid model by using the results of the Ship Traffic Emission Assessment Model STEAM (Jalkanen et al., 2009, 2012; Johansson et al., 2017). However, it does not include plume rise and has mainly been used for regional studies with large grid cells where the effects of plume rise were neglected and emissions were roughly distributed in the lowest layers (e.g., Karl et al., 2019c; Nunes et al., 2020).

An accurate representation of plume rise and downward dispersion processes in the near field under different meteorological conditions is therefore important, since it changes the effective emission height and may cause the vertical concentration profile to deviate from a Gaussian shape (Bieser et al., 2011; Brunner et al., 2019). A correct assessment of the downward dispersion processes is particularly important because it may lead to an increased health burden for port workers.

The vertical emission distribution also has a large effect on modeled concentration values further downwind of the source, as it influences chemical reaction rates and transport processes (Pozzer et al., 2009). The sensitivity of an Eulerian model to different initial concentration profile assumptions has not been described, and its impact on urban air pollution is still not well described.

3 Fundamentals of the applied models

3.1 MITRAS

In this work, the microscale transport and stream model MITRAS v2.0 is used to account for micrometeorological effects. MITRAS is developed at the University of Hamburg and is part of the M-SYS model system (Schatzmann et al., 2006; Schlünzen et al., 2003, 2018; Trukenmüller et al., 2004), which is designed to investigate atmospheric phenomena in the boundary layer, particularly air quality. MITRAS calculates wind, temperature, pressure, precipitation and pollutant transport within the obstacle layer. The following short model description covers the essential parts of MITRAS used in this work and is based on the general model description paper of Salim et al. (2018).

The basic physical conservation equations that are solved in MITRAS are the Navier−Stokes equations, the continuity equation and the conservation equation for scalar quantities, e.g., temperature and concentrations. The equations are solved in a terrain-following coordinate system, and Reynolds averaging is used to filter the equations after coordinate transformation. Using Reynolds averaging creates mean results and leads to the closure problem presented in Chapter 2.3.1.

MITRAS calculates fields of wind, concentration, temperature, etc. in a prognostic way, i.e. it predicts the future based on the present or past. Detailed equations for the three wind components and any scalar quantity are given in Salim et al. (2018).

The prognostic equation for the mean of a scalar quantity ($\bar{\zeta}$) such as temperature or concentration reads:

$$\frac{\partial \rho_0 \alpha^* \bar{\zeta}}{\partial t} = -\frac{\partial}{\partial \dot{x}^1}\left(\bar{u}\dot{x}_x^1 \rho_0 \alpha^* \bar{\zeta}\right) - \frac{\partial}{\partial \dot{x}^2}\left(\bar{v}\dot{x}_y^2 \rho_0 \alpha^* \bar{\zeta}\right) - \frac{\partial}{\partial \dot{x}^3}\left(\overline{\dot{u}^3} \rho_0 \alpha^* \bar{\zeta}\right) + \rho_0 \alpha^* \bar{S}_{\bar{\zeta}} - \bar{F}_{\bar{\zeta}}, \qquad (3.1)$$

where ρ_0 is the large-scale part of the air density, α* denotes a grid volume, and ($\dot{x}^1, \dot{x}^2, \dot{x}^3$) are the coordinates of the terrain-following coordinate system. $\bar{u}$ and $\bar{v}$ are the mean horizontal wind components. $\overline{\dot{u}^3}$ is the vertical component of the wind vector in the terrain-following coordinate system. $\overline{S_{\bar{\zeta}}}$ are sources and sinks of the scalar quantity, and $\overline{F_{\bar{\zeta}}}$ are sub-grid-scale turbulent scalar fluxes that emerge from filtering the equations.

Equation (3.1) simply reads that the change of a mean scalar quantity over time $\left(\frac{\partial \rho_0 \alpha^* \bar{\zeta}}{\partial t}\right)$ depends on the advection in three directions $\left(-\frac{\partial}{\partial \dot{x}^1}\left(\bar{u}\dot{x}_x^1 \rho_0 \alpha^* \bar{\zeta}\right) - \frac{\partial}{\partial \dot{x}^2}\left(\bar{v}\dot{x}_y^2 \rho_0 \alpha^* \bar{\zeta}\right) - \frac{\partial}{\partial \dot{x}^3}\left(\overline{\dot{u}^3} \rho_0 \alpha^* \bar{\zeta}\right)\right)$, changes due to sources and sinks $\left(\rho_0 \alpha^* \bar{S}_{\bar{\zeta}}\right)$ and sub-grid-scale turbulent fluxes $\left(-\bar{F}_{\bar{\zeta}}\right)$.

The model equations are solved on a staggered Arakawa C grid (Arakawa and Lamb, 1977), where scalar variables are defined at the cell center and velocity components are defined on their respective normal cell faces. The discretized 3-D model domain

allows for grid stretching in both the vertical and horizontal directions. MITRAS is usually used for grid sizes in the order of 1−10 m.

A one-dimensional model prepares meteorological information and creates physically consistent conditions (initialization). It imposes frictional effects and wind rotation with height and calculates initial scalar values, wind inflow profiles (at fixed boundaries) and top boundary values.

To solve the closure problems, Monin-Obukhov similarity theory is assumed at the lowermost layer (Foken, 2006; Monin and Obukhov, 1954). In the layers above, first-order closures are used to derive sub-grid-scale momentum and scalar quantity fluxes. The exchange coefficients are calculated using the Prandtl-Kolmogorov closure in this work (López, 2002).

MITRAS furthermore applies the Boussinesq approximation, which means that density variations in the Navier−Stokes equations are neglected except for the buoyancy term.

Advection and diffusion terms are solved using the Adam-Bashforth scheme (e.g., Durran, 1991) in time and centered differences in space. Vertical diffusion is determined with the Crank-Nicolson implicit scheme (Crank and Nicolson, 1947). Advection of scalar quantities is solved forward in time with the upstream scheme.

Different boundary conditions are used on the surface boundary, the lateral boundary and the top boundary.

On the surface, the vertical wind is set to zero (= no slip boundary condition). The temperature values of the ground (ground soil heat flux) and obstacle surfaces are accounted for. Mean scalar quantities (e.g., for concentration) and dissipation are calculated as a function of local friction velocity.

On the inlet lateral boundary the wind profiles are kept fixed at the initial values. At the outflow the lateral boundary is open and wind velocities can vary.

The vertical wind is defined at the **top boundary**. For other quantities, the gradients normal to the top boundary are set to zero.

Obstacles are explicitly resolved by employing the concept of the mask method (Briscolini and Santangelo, 1989). Grid cells in a domain are either free atmospheric cells, obstacle-adjacent cells or impermeable obstacle cells. Wind velocities vanish at the obstacle boundaries, and wall functions are used to account for the effects of friction and obstacle temperature.

The **surface cover class** that was used in this work was set to water for the whole MITRAS domain. The roughness length for water depends on the wind speed (Fischereit et al., 2016).

3.2 EPISODE-CityChem

The three-dimensional Eulerian grid model EPISODE-CityChem (Hamer et al., 2020; Karl et al., 2019b) is used to simulate the emission, transport, dispersion, photochemical transformation and deposition of pollutants on a city-scale.

The model uses a terrain-following sigma coordinate system defined from an idealized hydrostatic pressure distribution.

The topography input consists of a 2-dimensional static field of terrain heights that is created using the terrain preprocessor AERMAP (EPA-454/B-03-003) of the U.S. EPA air dispersion model AERMOD (US-EPA, 2004). It coordinates the allocation of terrain elevation data from several digitized databases to a user-specified model grid. From the database of NASA's Shuttle Radar Topography Mission (SRTM, Rodriguez et al., 2006), digital elevation data are used. They have a spatial resolution of approximately 100 m and WGS 84 as the reference geoid. The Universal Transverse Mercator (UTM) conformal projection is used to set the geographic dimensions for the research domain.

Two different options for the creation of the meteorological field are applied in this work. In Chapter 4, the meteorological preprocessor MCWIND v1.2 (Hamer et al., 2020) is used. This software produces a diagnostic wind field based on observational or synthetic data. MCWIND adjusts a first guess wind field to a given topography in such a way that it becomes non-divergent and mass-consistent. The 3D fields are calculated internally by applying surface similarity profiles according to Monin-Obukhov theory (Monin and Obukhov, 1954; Foken, 2006).

In Chapter 5, meteorological fields are generated by the meteorological component of the Australian air quality model TAPM (The Air Pollution Model) (Hurley, 2008; Hurley et al., 2005).

Horizontal advection is considered using a positive 4^{th} degree Bott scheme (Bott, 1989, 1992, 1993), which calculates flux between grid cells, describing the concentration fluctuations locally. A time-splitting method is employed to solve advection separately in the x and y directions.

Vertical advection is solved with an upstream scheme (Byun et al., 1999), which implicitly assumes that the 3D wind field is free of divergence. Vertical motion is therefore either convergence or divergence in the input horizontal wind fields. This allows mass conservation.

Both horizontal and vertical eddy diffusivities are calculated on the Eulerian grid using parameterizations. The horizontal diffusion is calculated using a fully explicit forward Euler scheme (Smith, 1985).

The vertical diffusion is solved according to the mixing length theory (Monin-Obukhov similarity theory) by a semi-implicit Crank-Nicolson scheme.

Eddy diffusion coefficients are calculated by the urban K(z) method presented in Hamer et al. (2020).

The transport of pollutants in and out of the model domain is implicitly considered within the 3D advection equations.

The effect of dry deposition is included, whereas the effect of wet deposition is not.

The dry deposition is calculated based on the resistance analogy (Simpson et al., 2003).

The EPISODE-CityChem chemistry options on the Eulerian grid include a dispersion without photochemistry (applied in Chapter 5), a solution for basic NO_x-O_3 photochemical equilibrium, a detailed two-step urban chemistry solver with 45 gas-phase species (EmChem03-mod) and an urban chemistry scheme including heterogeneous gas-phase reactions EmChem09-HET (Karl et al., 2019b; Simpson et al., 2012). The latter includes 70 compounds, 67 thermal reactions and 25 photolysis reactions and is used in Chapter 6.

Secondary aerosol formation is not considered in the model (Karl et al., 2019b).

A simplified street canyon model (SSCM) is used for a better treatment of NOx at traffic stations.

All emission input data, except for the specifically generated ship emissions, were preprocessed with the Urban Emission Conversion Tool (UECT; Hamer et al., 2020).

Chemical boundary conditions can be either a constant value for each pollutant, an hourly list of variable values (e.g., from a measurement station) or 3-D boundary concentrations from simulations with a regional air quality model.

EPISODE-CityChem can create pollutant concentration fields for an entire city on a horizontal resolution of 100 m or even finer.

4 Parameterizing the vertical downward dispersion of ship exhaust gas in the near field

Badeke, R., Matthias, V., and Grawe, D.: Parameterizing the vertical downward dispersion of ship exhaust gas in the near field, Atmos. Chem. Phys., 21, 5935–5951, https://doi.org/10.5194/acp-21-5935-2021, 2021.

Abstract

Estimating the impact of ship emissions on local air quality is a topic of high relevance, especially in large harbor cities. For chemistry-transport modeling studies, the initial plume rise and dispersion play a crucial role for the distribution of pollutants into vertical model layers. This study aims at parameterizing the vertical downward dispersion in the near field of a prototype cruise ship, depending on several meteorological and technical input parameters. By using the microscale chemistry, transport and stream model (MITRAS), a parameterization scheme was developed to calculate the downward dispersion, i.e., the fraction of emissions, which will be dispersed below stack height. This represents the local concentration in the vicinity of the ship. Cases with and without considering the obstacle effect of the ship have been compared. Wind speed and ship size were found to be the strongest factors influencing the downward dispersion, which can reach values up to 55% at high wind speed and lateral wind. This compares to 31% in the case where the obstacle effect was not considered and shows the importance of obstacle effects when assessing the ground-level pollution situation in ports.

Note:

This chapter consists of the manuscript published as declared before by me as lead author for the purpose of this thesis. The introduction and MITRAS model description have been omitted and incorporated into Chapters 1−3 to avoid duplication. For Internet sources, the years of the last access have been updated. Numbering of chapters, equations, figures and tables have been adapted to this document. Minor adjustments have been made to the acronyms to match with the other publications and the thesis document.

4.1 Methodology

The dispersion of an exhaust plume is affected by several meteorological and technical parameters (Fig. 4.1). The upward movement, i.e., the plume rise, is mainly determined by the initial temperature of the exhaust and its exit velocity, which can be calculated by dividing the gas volume flow by the stack diameter. The stack angle describes whether the exhaust flow is directed vertically, horizontally or at an angle. The stack height only has an indirect effect on the plume rise, as higher emitted gases experience a stronger wind speed inside the boundary layer.

Turbulence enhances the plume dispersion, leading to dilution of the embedded gases by entrainment of ambient air into the plume. The dispersion increases with the wind speed. It depends also on the ship geometry and the flow direction of the wind towards the vessel. Furthermore, a stronger turbulence occurs in case of higher surface roughness.

The ambient vertical temperature profile determines the atmospheric stability. The presence of an inversion can strongly decrease the strength of the plume dispersion, as it thermodynamically hinders the vertical movement of air masses. Depending on the altitude of the inversion and the exhaust temperature, the plume may or may not break through the inversion.

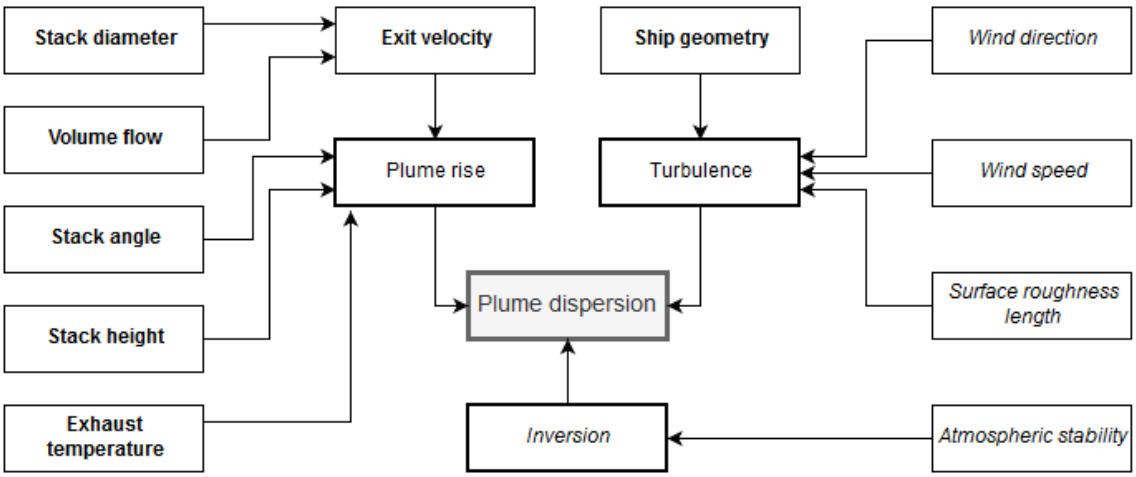

Figure 4.1: Conceptual model of parameters affecting the shape and movement of a ship plume (bold: technical parameters, italic: ambient parameters).

4.1.1 MITRAS

In this study, a non-equidistant grid is used with the highest resolution of 2 m × 2 m × 2 m close to the ship. The chosen domain has an overall size of around 1 km × 1 km horizontally and 500 m vertically. The surface cover for the whole domain is water and the roughness length is calculated from the wind speed (see Schlünzen et al., 2018, for detailed equations). Its values are close to zero.

The emission occurs continuously in one model cell right above the ship stack, which is an impenetrable obstacle cell (Fig. 4.2). The emitted gas is as a passive trace gas (e.g., CO_2 or non-reactive SO_2). No chemical reactions occur in the simulations. The emission cell has a constant temperature, which corresponds to a given exhaust temperature and a vertically directed exhaust velocity. The wind field is affected by Coriolis force and friction force, which cause the wind to slightly turn counterclockwise according to an Ekman spiral. Furthermore, the flow field is modified by the obstacle itself, the high temperature of the exhaust and the exit velocity. No deposition occurs in the model domain, the surface is a mirror source which reflects the concentration when the lowest model layer is reached.

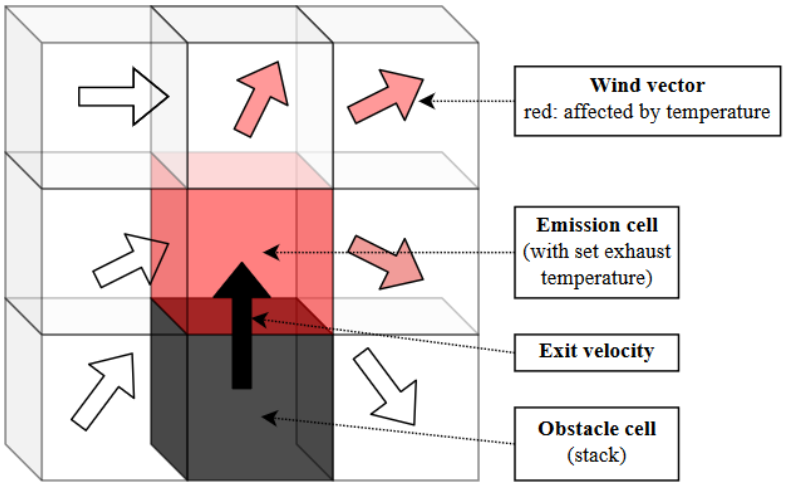

Figure 4.2: Visualization of the stack emission for wind direction from left to right. Passive trace gas emission occurs in the cell above the stack, which has a constant exhaust temperature and a vertically directed exhaust velocity. The arrows indicate the change of the ambient wind field due to the obstacle and the plume temperature.

4.1.2 Meteorological data

Idealized meteorological conditions are used to investigate effects of single variations of input parameters on the dispersion process. The range of input values is listed in Table 4.1. One input parameter per model run was varied while the other meteorological and technical parameters were fixed at predefined default values.

The ambient temperature is set to 15 °C at the surface. It changes with altitude according to the given ambient temperature gradient, which represents the atmospheric stability. The value of ambient temperature itself has a negligible small effect on the plume dispersion compared to the plume temperature and was therefore not varied in this study.

The atmospheric stability is varied in a range of different lapse rates, covering one unstable condition (-1.2 K · 100 m^{-1}), one neutral condition (-0.98 K · 100 m^{-1}) and several stable conditions including inversions (up to +0.5 K · 100 m^{-1}).

The wind speed is investigated in a range of 2–15 m s^{-1}. The limits were chosen according to hourly wind speed data from Hamburg weather mast in 2018 (see Appendix A.1) and can also be seen as representative for other large North Europe ports including Rotterdam and Antwerp. The value 2 m s^{-1} is close to the 5th percentile and 15 m s^{-1} corresponds to the 95th percentile at 280 m measurement height. This covers most of the naturally occurring scenarios. The selected default value is 5 m s^{-1} which fits well with the mean wind speed in Hamburg at a height of 50 m, which is close to the stack height.

The effect of wind direction is relevant in correspondence to the orientation of the ship. Frontal wind is herein defined at an angle of 0° and lateral wind at 90°. Oblique wind conditions lie between these values.

Table 4.1: Input parameters for this study. While varying one single input parameter in the investigation range, all others remain at default setting.

Input parameter	Default setting	Investigation range
Ambient temperature at surface	15 °C	None
Ambient temperature gradient	-0.65 K · 100 m^{-1}	-1.2–0.5 K · 100 m^{-1}
Wind speed at upper model boundary	5 m s^{-1}	2–15 m s^{-1}
Wind direction	0° (= frontal wind)	0–90°
Ship length	246 m	None
Ship width	30 m	None
Stack height	52 m	None
Exit velocity	10 m s^{-1}	4–12 m s^{-1}
Exhaust temperature	300 °C	200–400 °C

4.1.3 Ship characteristics

This study represents a cruise ship prototype. From an online database (Port of Hamburg, 2022) the average length and width of cruise ships that were visiting Hamburg harbor during the years 2018 to 2019 has been calculated. The stack height was approximated from freely available photos (e.g., Vesseltracker, 2022). The ship prototype has a length of 246 m, a width of 30 m and a stack height of 52 m (see Table 4.1 and Fig. 4.3). This corresponds to a typical cruise ship that can carry between 1000 and 2500 passengers. A non-moving source is assumed, i.e., a hoteling ship at berth.

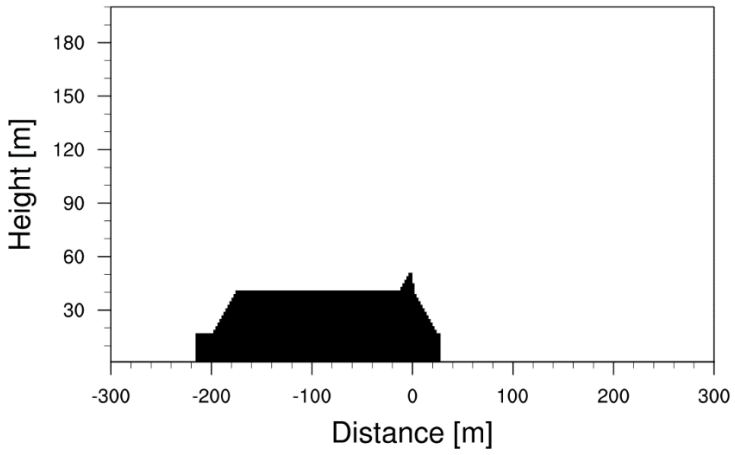

Figure 4.3: Side view of the prototype cruise ship in the MITRAS domain with the x-axis located at the stack position.

The study goes beyond a case study. A loaded container ship of similar size and exhaust characteristics would deliver similar results because its shape is comparable. On top of that, for all investigated input characteristics, the results of stack-only cases are presented as well. Therefore, one can assume that results for smaller ships lie between these two cases.

The exhaust gas temperature depends on technical parameters of the ship's engine and can be found in engine data sheets provided by manufacturers like Caterpillar (CAT, 2022), Wärtsilä (Wärtsilä, 2022) and MAN (MAN, 2022) on their websites. For large cruise vessels, it ranges between approximately 300 °C and 400 °C, depending on the used engine power. However, the exhaust temperature can be lowered by 75–100 °C when a heat exchanger which generates electric energy from the excess heat is in operation (Murphy et al., 2009). Therefore, the temperature effects are investigated for 200 °C, 300 °C and 400 °C plumes to cover a realistic spectrum. Similarly, the exit velocity was assumed from these data sheets. It depends on the engine type (main engine or auxiliary engine) and the used engine power and was investigated in a range of 4–12 m s^{-1}.

4.1.4 Plume dispersion in different regimes

When investigating plume dispersion, one needs to separate two regimes: the momentum-driven regime and the buoyancy-driven regime. In the momentum-driven regime the movement of the plume is affected by (a) the initial plume rise due to both, the exit velocity and the high-temperature convective upward transport and (b) the dispersion due to turbulence generated by the obstacle (i.e., the ship) inside the wind field. In the buoyancy-driven regime, the movement of the plume is determined by the wind field and turbulence generated by the ambient conditions (e.g., orography effects and surface roughness). Here, the plume temperature is equal to the ambient temperature. The microscale model MITRAS can investigate plume behavior in both regimes on a high resolution.

MITRAS is used to capture the initial plume rise and turbulence effects in the momentum driven regime. The vertical concentration profiles are calculated at a distance outside of the momentum-driven regime, i.e., when the buoyancy-driven regime is reached. Then, the concentration profiles are calculated on a 100 m × 100 m area column with layer-mean values (Fig. 4.4). The calculation of these column values has two benefits. First, it covers the mean behavior of the whole plume better than single values of 2 m × 2 m × 2 m grid sizes, since the movement of the plume can be highly variable. Second, the concentration profiles can then also be transferred into larger-scale models which usually have a much coarser grid (e.g., 100 m × 100 m horizontally). However, the coupling of MITRAS results into a larger-scale model will be part of a future study and is not covered here.

Since the plume needs to have cooled down to ambient temperatures to be considered outside the momentum-driven regime, test simulations have been performed to find a distance at which this condition is met (see Appendix A.2). This was the case at a distance of 100 m downwind of the ship. Therefore, all concentration profiles are calculated as 100 m × 100 m columns with average concentration per layer at a distance of 100 m downwind of the ship.

In the following, the term **downward dispersion D** is defined as the relative proportion of the total concentration column in the layers below the stack height.

$$\mathrm{D} = \frac{\int_0^{\mathrm{h_s}} \mathrm{c}}{\int_0^{\mathrm{h_{top}}} \mathrm{c}} \cdot 100\%, \tag{4.1}$$

where h_{top} is the altitude of the highest model layer (500 m), h_s is the stack height (52 m) and c is the total concentration. A mean downward dispersion is calculated for the described 100 m × 100 m column at a distance of 100 m downwind from the stack. From an application perspective, this downward dispersion parameter is an indicator for the pollution situation in the vicinity of the ship and useful to evaluate the level of pollution inside of a harbor.

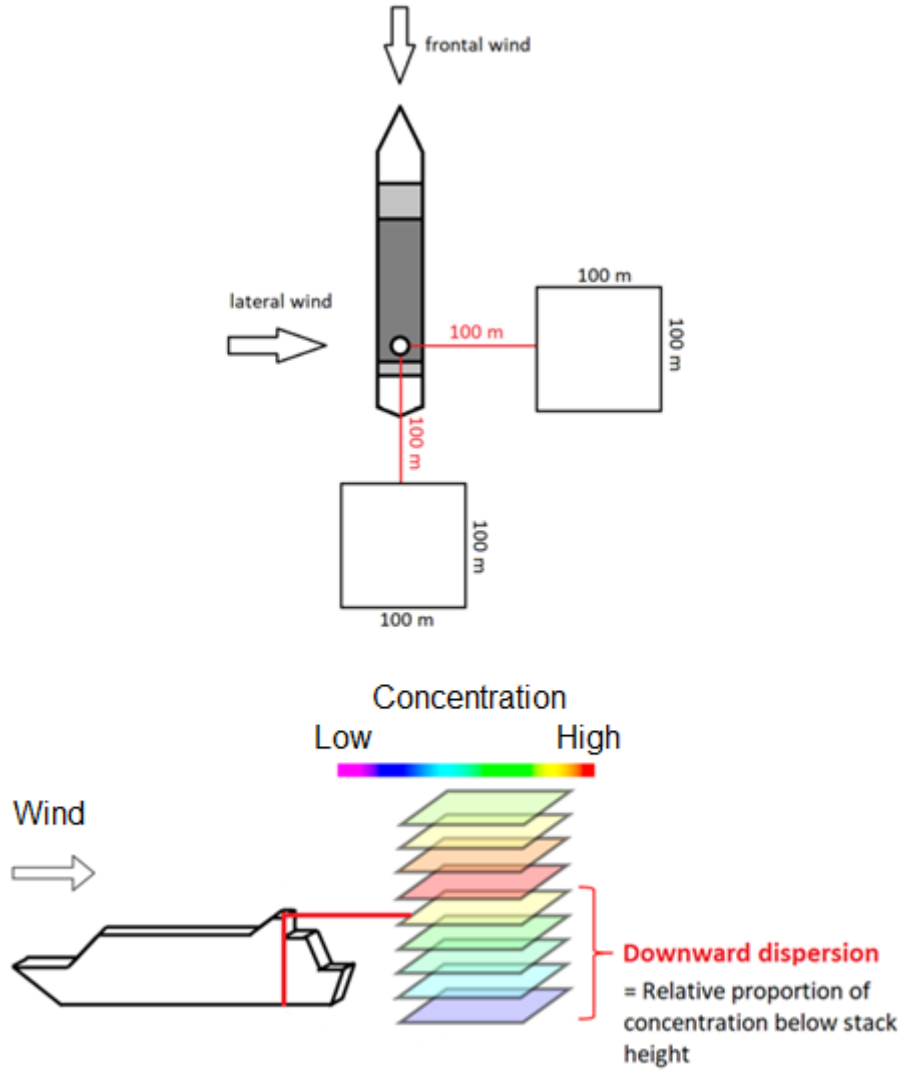

Figure 4.4: Schematic sketches of the investigation area. Vertical concentration profiles are evaluated at a distance of 100 m downwind of the ship for layers of 100 m × 100 m.

For single regression analyses, downward dispersion values are investigated depending on the variation of one single input parameter at a time while the others remain at default settings (Table 4.1). To assess the sensitivity of the downward dispersion to each input parameter, an **effective range r** is calculated. It is defined as the difference between the highest and the lowest downward dispersion value for one regression:

$$r_i = D(max)_i - D(min)_i \,, \tag{4.2}$$

where i is the individual input parameter that is varied while the other remain at default setting. The effective range describes how strongly one parameter can change the downward dispersion and helps to evaluate which input parameter has the strongest impact in the given range of values.

4.2 Results and discussion

Figure 4.5 presents an exemplary output of the MITRAS model for the default conditions, i.e., frontal wind at 5 m s^{-1}, exit velocity of 10 m s^{-1}, exhaust temperature of 300 °C and an ambient temperature gradient of -0.65 K · 100 m^{-1}. The concentration values result from an emission of 50 kg trace gas per hour.

The following subsections describe the results of single- and multi-parameter regressions that were performed in order to describe the relationship between the downward dispersion and the input parameters. From the multi-parameter regression, a parameterization is derived that covers all input parameters in the investigation range. A bootstrapping procedure is presented to test how well the parameterization results match with the MITRAS model results. The obstacle effect is evaluated and, finally, some limitations of the modeling approach are discussed.

4.2.1 Results of single-parameter regressions

Single-parameter regressions are performed after basic statistic formulae (see Appendix A.3) to investigate the impact of individual input parameters, i.e., wind speed, exit velocity, wind direction, plume temperature and atmospheric stability on the downward dispersion.

4.2.1.1 Effect of wind speed and exit velocity

The dependence of the downward dispersion from wind speed was modeled in the range of 2–15 m s^{-1} at the uppermost model layer, which is set as the input parameter. It is slightly lower at stack height following the logarithmic vertical wind profile. See Table A.2 for the exact values at stack height.

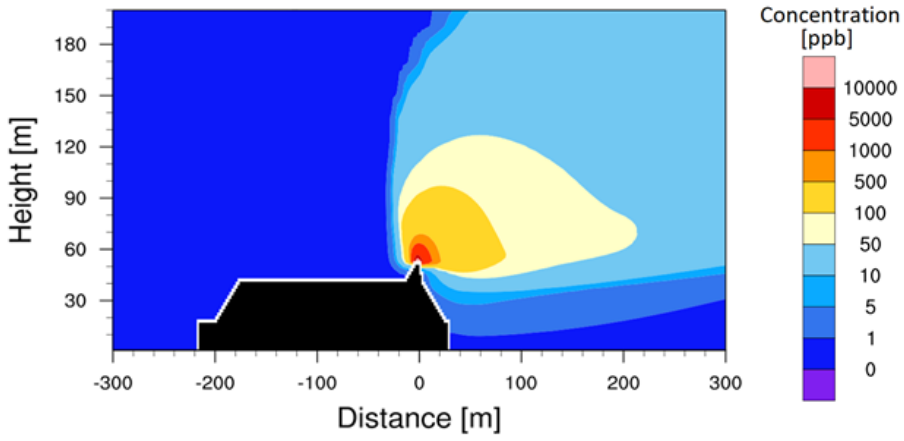

Figure 4.5: MITRAS model results for default conditions (frontal wind at 5 m s^{-1}, exit velocity 10 m s^{-1}, exhaust temperature of 300 °C and an ambient temperature gradient of -0.65 K · 100 m^{-1}).

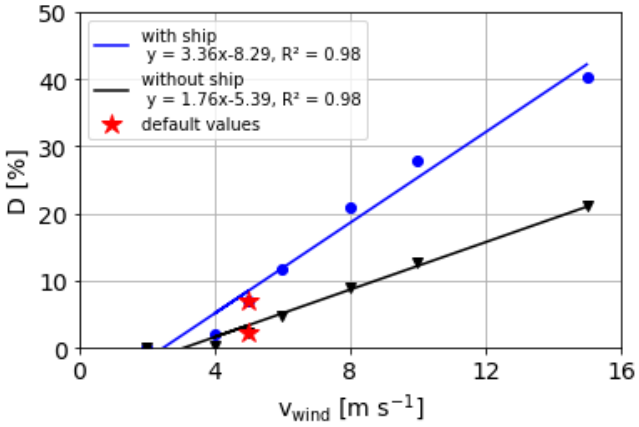

Figure 4.6: Dependence of the downward dispersion D on different wind speeds v_{wind} with and without the obstacle effect.

Figure 4.6 presents results of a single linear regression for the dependence of downward dispersion on varying wind speeds with and without obstacle effect. Other input parameters remained constant at default values (Table 4.1). A linear relationship with correlation coefficients R^2 of 0.98 was found for both runs with and without ship, respectively. At high wind speeds, the turbulence behind the obstacle causes strong downward dispersion. Under these settings, the wind speed has an effective range on the downward dispersion of 40.3% with and 21.1% without ship, making the wind speed a crucial factor influencing the downward dispersion (Fig. 4.6 and Table 4.2).

A similarly strong linear relationship has been found between the exit velocity of the exhaust gas and the downward dispersion (Fig. 4.7 and Table 4.2) with regression R^2 of 1.00 for cases with and without obstacle. It is, however, a negative dependence, because higher exit velocities transport the plume into higher altitudes and consequently the downward dispersion is lower. The effective range is much smaller than for the wind speed with only 3.7% with and 2.1% without obstacle, respectively.

Table 4.2: Effective ranges of investigated input parameters on the downward dispersion under default settings.

Input parameter	Investigated range	Default value	Effective range with ship	Effective range without ship
Wind speed	2–15 m s^{-1}	5 m s^{-1}	40.3%	21.1%
Exit velocity	4–12 m s^{-1}	10 m s^{-1}	3.7%	2.1%
Wind direction	0–90°	0° (frontal)	9.7%	None
Exhaust temperature	200–400 °C	300 °C	6.9%	2.9%
Atmospheric stability	-1.2−0.5 K · 100 m^{-1}	-0.65 K · 100 m^{-1}	6.6%	3.8%

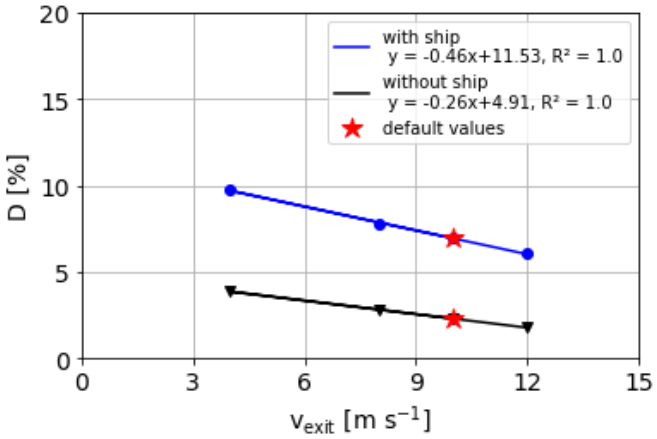

Figure 4.7: Dependence of the downward dispersion D on different exit velocities v_{exit} with and without the obstacle effect.

4.2.1.2 Effect of wind direction

The strength of the downward dispersion was investigated depending on different wind directions in relation to the orientation of the ship. Frontal wind (angle 0°) hits the short side of the vessel, which has a width of 30 m, whereas lateral wind (angle 90°) has to be lifted over the 246 m length of the ship. Therefore, a stronger distortion of the flow during lateral wind has been observed.

The downward dispersion correlates linearly with the cosine of the flow angle ϕ (Fig. 4.8). A regression coefficient R^2 of 0.98 was calculated. At default settings a downward dispersion ratio of 7.0% and 16.6% was found under frontal and lateral wind conditions, respectively. This results in an effective range of 9.6%. The corresponding downward dispersion under no obstacle condition is 2.3%. There is no effective range for no-obstacle conditions, because here a single symmetrical stack is assumed, where the downward dispersion values are the same for both, frontal and lateral wind.

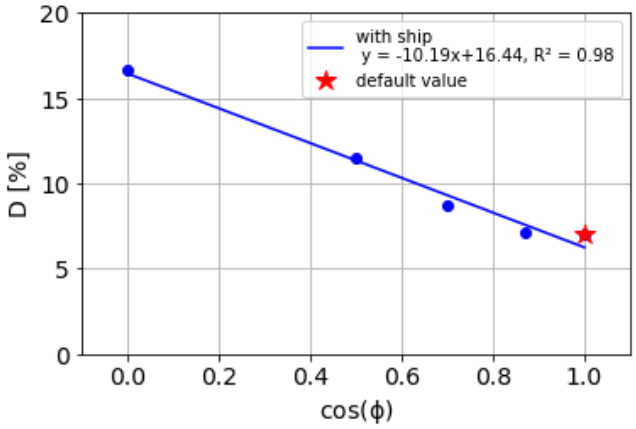

Figure 4.8: Dependence of the downward dispersion D on the cosine of different wind flow angles (ϕ) towards the ship. 0° = frontal wind, 90° = lateral wind.

However, very small differences between these conditions can occur during the modeling (see Table A.2), which result from an asymmetry in the numerical grid.

4.2.1.3 Effect of exhaust plume temperature

The exhaust plume temperature depends on technical parameters like the engine power and the use of a heat exchanger and, therefore, a range of possible temperatures (200 °C–400 °C) was investigated. Figure 4.9 presents results of the single linear regression for the downward dispersion at varying exhaust temperatures with and without obstacle effect.

Once again, a strong linear relationship with correlation coefficients R^2 of 0.98 and 0.99 was found for results with and without ship, respectively. At higher exhaust temperatures, the plume reaches higher altitudes by convective upward movement, which results in lower downward dispersion ratios. The effective range under default settings is 6.9% with and 2.9% without obstacle effect (Table 4.2).

4.2.1.4 Effect of atmospheric stability

The effect of atmospheric stability Γ on the downward dispersion was investigated in a range from unstable (-1.2 K · 100 m^{-1}) to very stable (+0.5 K · 100 m^{-1}) vertical temperature gradients. Under default settings, linear regression resulted in correlation coefficients of R^2 = 0.90 and 0.94 with and without ship, respectively (Fig. 4.10a). Since the R^2 coefficient was low compared to the other investigated input parameters, a linear dependence would deliver poorer results for this parameter. Therefore, a quadratic dependence was calculated as well.

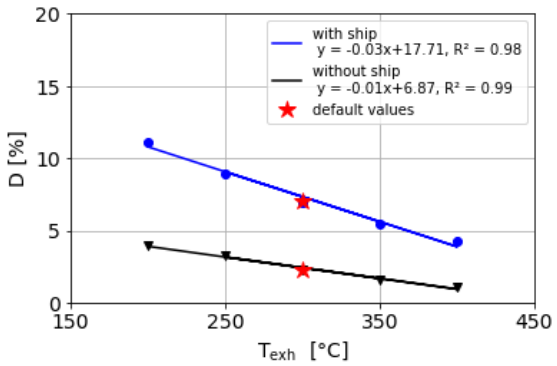

Figure 4.9: Dependence of the downward dispersion D on different exhaust temperatures T_{exh} with and without the obstacle effect.

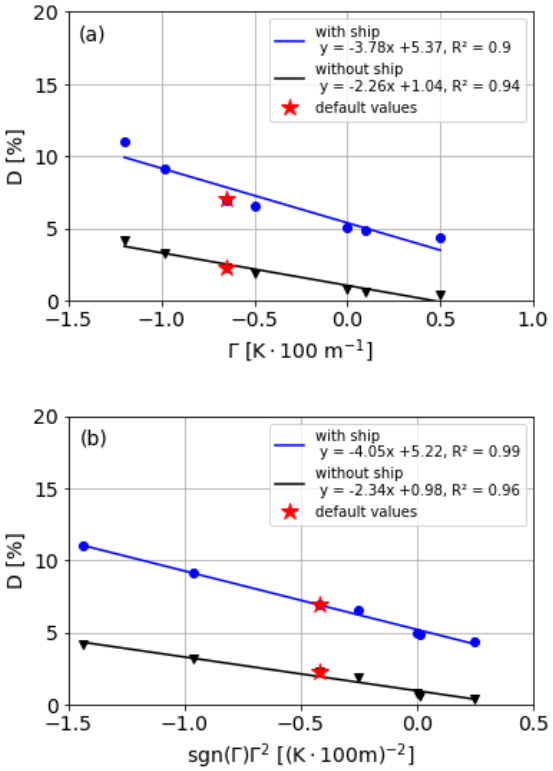

Figure 4.10: Dependence of the downward dispersion D on different vertical temperature gradients Γ with and without the obstacle effect. Linear regressions of the downward dispersion against Γ (panel a) and sgn(Γ)Γ² (panel b) are shown.

Since the square of a negative vertical temperature gradient would result in a positive value, a sign function was applied. The mathematical expression is:

$$\mathrm{sgn}(x) := \begin{cases} -1 \; if \; x < 0 \\ 0 \;\; if \; x = 0 \\ 1 \;\; if \; x > 0 \end{cases} \tag{4.3}$$

Then, the correlation between downward dispersion and sgn(Γ)Γ² is calculated (Fig. 4.10b). It shows better agreement in the cases considering obstacle effects ($R^2 = 0.99$) and slightly better agreement in cases without ship ($R^2 = 0.96$), as well. It is a negative correlation, because higher temperature gradients correspond to a higher stability which thermodynamically prevents the plume to disperse vertically and therefore lowers the downward dispersion ratio. The effective range of the temperature gradient on the downward dispersion is 6.6% for ship cases and 3.8% for stack-only cases.

4.2.2 Result of the multiple regression

Multiple regression is performed according to the equations in Appendix A.3. The downward dispersion ratio depends linearly on all investigated input parameters, their cosine (in case of the angle of wind direction) or their squares (in case of atmospheric stability). With that in mind, a training data set for the multiple regression was created. Here, all independent input parameters are varied at the same time (but in the given range) and the downward dispersion ratio is calculated with MITRAS. For a set of 39 different combinations (Table A.2) of input parameters with obstacle effect and 27 without, the estimation coefficients $\hat{\beta}_i$ for individual parameters i (wind speed, exit velocity, etc.) are calculated with the multiple regression. The number of simulated cases without obstacle effects are lower, because in these cases the wind direction has been varied which will not show differences in case of stack-only conditions. The resulting formulae for the parameterization read

$$\mathrm{D}\,[\%] = 13.03 + 3.45\,\mathrm{v_{wind}} - 1.01\,\mathrm{v_{exit}} - 0.026\,\mathrm{T_{exh}} - 3.81\ \mathrm{sgn}(\Gamma)\Gamma^2 + 6.13\cos(\phi), \quad (4.4)$$

with ship and

$$\mathrm{D}\,[\%] = 4.55 + 1.78\,\mathrm{v_{wind}} - 0.64\,\mathrm{v_{exit}} - 0.018\,\mathrm{T_{exh}} - 3.40\mathrm{sgn}(\Gamma)\Gamma^2, \quad (4.5)$$

without ship (i.e., stack-only).

Here, v_{wind} and v_{exh} are given in [m s^{-1}], T_{exh} in [°C], Γ in [K · 100 m^{-1}] and ϕ in [°], where 0° refers to frontal wind and 90° to lateral wind.

4.2.3 Bootstrapping

A bootstrapping procedure is applied to estimate how well the parameterization can represent the model data. For this purpose, downward dispersion ratios were calculated with the parameterization formulae (Eq. 4.4 and 4.5) and compared to the original MITRAS results for all investigated cases and ranges. Results of the individual parameterization results are listed in Table A.2 and Table 4.3 gives the overall results of the bootstrapping procedure.

With a mean absolute error of 1.9 ± 1.6% for cases with ship and 1.2% ± 0.9% without ship the parameterization delivers very similar results to the model runs. The maximum absolute errors were found to be 6.1% in cases with ship and 4.0% in cases without ship.

Table 4.3: Results of the bootstrapping procedure for cases with and without considering the ship-induced obstacle effect.

	With Ship	Without Ship
Number of training cases	39	27
Mean absolute error	1.9%	1.2%
Standard deviation	1.6%	0.9%
Maximum absolute error	6.1%	4.0%

4.2.4 Assessment of the obstacle effect

Another aim was to investigate under which conditions the strongest downward dispersion occurs and which effect the consideration of the obstacle has on the downward dispersion.

From the single-parameter regressions, it is assumed that the strongest downward dispersion occurs at high wind speed (15 m s^{-1}) with lateral wind (90°), low exit velocity (4 m s^{-1}), low plume temperature (200 °C) and during unstable atmospheric conditions (-1.2 K · 100 m^{-1}). This is displayed in Fig. 4.11 with the ship as an obstacle (panel a) and under stack-only conditions (panel b).

The calculated downward dispersion ratio for this condition is 54.9% and 31.1% with and without obstacle effect, respectively. This means that a significant proportion of nearly 25% of the emission can be dispersed downwards only by taking into account the turbulence caused by the ship.

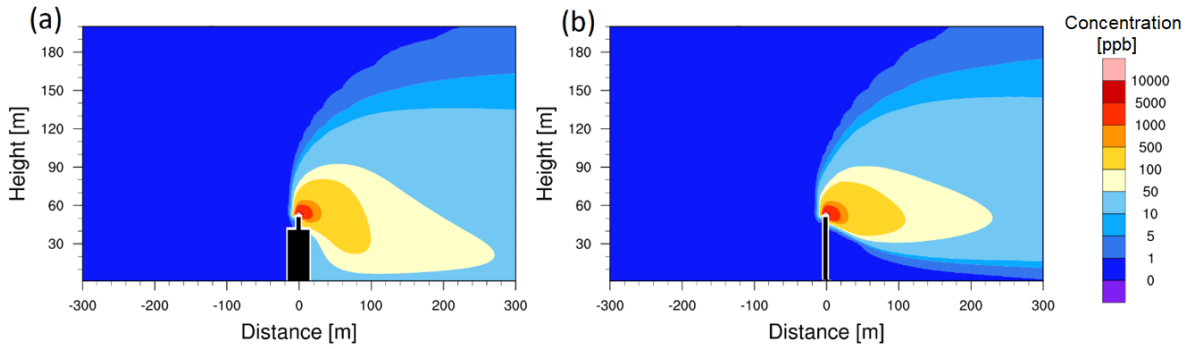

Figure 4.11: Visualization of the obstacle effect in MITRAS. Examples for lateral wind with v_{wind} = 15 m s^{-1}, v_{exit} = 4 m s^{-1}, T_{exh} = 200 °C and Γ = -1.2 K · 100 m^{-1} are presented. Concentration fields are displayed with ship, pointing towards the viewer (a) and under stack-only conditions (b).

4.2.5 Discussion of limitations

Despite efforts to represent real conditions as best as possible, the results are subject to a few limitations or uncertainties that will be discussed in the following section. For a general comparison of our MITRAS results with a common dispersion model, see Appendix A.4.

One factor that is not considered in this study is relative humidity. Here, a distinction must be made between the relative humidity of the ambient air and the relative humidity of the exhaust. By using the Lagrangian concept based on the so-called projected area entrainment (Lee and Cheung, 1990), Affad et al. (2006) stated that the relative humidity of the ambient air has only a slight impact on the plume rise, diameter and temperature for values between 20% and 90%. It can have an impact on particle growth, but as this study focusses on a passive gaseous tracer, this effect is neglected. On the other hand, the humidity of the exhaust gas might have a larger impact on the plume rise. Since water vapor has a lower density than air, an exhaust gas mixture of high humidity will show a stronger plume rise. Furthermore, as the gas will quickly condense, it will release latent heat and rise further. However, the data base on humidity of ship exhaust is sparse. It could play a role in case of vessels using a scrubber to wash out SO_2 from the exhaust. During this process, the exhaust is cooled down significantly and therefore will show a weaker plume rise (Murphy et al., 2009). It is unclear, if the additional buoyancy can compensate for the lower exhaust temperatures. Due to these uncertainties and lack of data, the relative humidity has not been included in this study.

Second, the emission is assumed to occur in the grid cell above the stack, which has a size of 2 m × 2 m × 2 m. This corresponds to a stack with a square cross section of 4 m² and is a limitation connected to the chosen grid size. Real stacks are usually round and have a smaller diameter. However, Bai et al. (2020) reported about plume modeling for container vessels with measured funnel diameters in the range of 1.38 to 3.0 m, so the selected value is inside a reasonable range. Furthermore, many ships operate multiple smaller stacks that might in sum lead to a similar exhaust behavior. Based on the selected diameter, the real exit velocity could differ slightly. However, by comparing the effective ranges for exit velocity against all other input factors (Table 4.2), it can be seen that this parameter has the smallest overall impact of the downward dispersion and therefore, this uncertainty factor has a low impact on the overall performance.

Another assumption was that the ship has been considered as a non-moving source, i.e., a hoteling ship. However, the results can be applied to a moving ship by calculating the vector sum of the wind and the vessel speed. It is difficult to account for complex maneuvers, though, as the resulting wind vector may change quickly and the technical conditions like exhaust temperature and exit velocity may also vary with the speed of the ship.

The shape of the vessel and the location of the stack are additional parameters that can influence the exact value of downward dispersion. Parameterizing them is beyond the scope of this study as the shape was chosen to investigate the average effect of a cruise-ship sized vessel on pollutant concentrations close to ground. However, to get

an impression, an exemplary comparison of MITRAS results for a cruise ship and container vessel can be found in Table A.4.

The chosen model surface is water but assuming a hoteling ship, the land surface effects may play a role for the dispersion. This effect has not been part of this study, as this is a highly variable parameter that depends on the structure of the harbor, the city and the orography. These effects need to be covered by a larger scale model.

4.3 Conclusion

A ship plume modeling study was performed with the microscale numerical model MITRAS to investigate the downward dispersion of the exhaust in close vicinity to a modeled cruise ship (i.e., in the momentum-driven regime). A set of 39 different scenarios with varying meteorological and technical input parameters were analyzed. A multiple regression algorithm was used to estimate a parameterization function for the downward dispersion. This parameterization has been tested against the MITRAS model results through a bootstrapping procedure.

From single-parameter regressions a positive linear relationship of the downward dispersion from wind speed and negative linear relationships from exit velocity, plume temperature and the cosine of the angle of wind direction was found. The downward dispersion ratio was larger in case of lateral wind than in case of frontal wind. In case of atmospheric stability, the downward dispersion showed a squared dependence from the vertical temperature gradient multiplied by the sign function. From all these input parameters, the wind speed shows the largest effect on the downward dispersion in the investigated range (2–15 m s^{-1}).

A comparison of the model results and the parameterization from multiple regression shows a good agreement with a mean absolute error of 1.9% ± 1.6% for cases with ship and 1.2% ± 0.9% without ship. For the case of strongest downward dispersion, the difference was calculated between downward dispersion with (54.9%) and without considering the obstacle effect (31.1%), which was almost 25%. This shows how important it is to consider the effects of the downward dispersion in the momentum-driven regime when one wants to evaluate the air pollution situation in harbor areas.

The parameterization functions can also be used for container ships of similar size. It may also be applied to different emission situations like industrial stacks.

In a future study, other plume parameters will be derived from the vertical concentration profiles in a similar way as the downward dispersion. This includes the height of the plume axis and the shape of the vertical plume profile, which may deviate from the often assumed Gaussian distribution. These results can further be used in a city-scale model, which only calculates the plume dispersion inside the buoyancy-driven regime.

5 Effects of vertical ship exhaust plume distributions on urban pollutant concentration – a sensitivity study with MITRAS v2.0 and EPISODE-CityChem v1.4

Badeke, R., Matthias, V., Karl, M., and Grawe, D.: Effects of vertical ship exhaust plume distributions on urban pollutant concentration – a sensitivity study with MITRAS v2.0 and EPISODE-CityChem v1.4, Geosci. Model Dev. 4077–4103, https://doi.org/10.5194/gmd-15-4077-2022, 2022.

Abstract

The modeling of ship emissions in port areas involves several uncertainties and approximations. In Eulerian grid models, the vertical distribution of emissions plays a decisive role for the ground-level pollutant concentration. In this study, model results of a microscale model, which takes thermal plume rise and turbulence into account, are derived for the parameterization of vertical ship exhaust plume distributions. This is done considering various meteorological and ship-technical conditions. The influence of three different approximated parameterizations (Gaussian distribution, single-cell emission and exponential Gaussian distribution) on the ground-level concentration are then evaluated in a city-scale model. Choosing a Gaussian distribution is particularly suitable for high wind speeds (> 5 m s^{-1}) and a stable atmosphere, while at low wind speeds or unstable atmospheric conditions the plume rise can be more closely approximated by an exponential Gaussian distribution. While Gaussian and exponential Gaussian distributions lead to ground level concentration maxima close to the source, with single-cell emission assumptions the maxima ground-level concentration occurs at a distance of about 1500 m from the source. Particularly high-resolution city-scale studies should therefore consider ship emissions with a suitable Gaussian or exponential Gaussian distribution. From a distance of around 4 km, the selected initial distribution no longer shows significant differences for the pollutant concentration near the ground; therefore, model studies with lower resolution can reasonably approximate ship plumes with a single-cell emission.

Note:

This chapter consists of the manuscript published as declared before by me as lead author for the purpose of this thesis. The introduction and general parts of MITRAS and EPISODE-CityChem model description have been omitted and incorporated into Chapters 1−3 to avoid duplication. For Internet sources, the years of the last access have been updated. Numbering of chapters, equations, figures and tables have been adapted to this document. Minor adjustments have been made to the acronyms to match with the other publications and the thesis document.

5.1 Methodology

The schematic concept of this study is presented in Fig. 5.1. It is composed of three major parts. First, the obstacle-resolving microscale model MITRAS v2.0 (Grawe et al., 2013; Salim et al., 2018) is used to generate a set of synthetic ship plumes based on technical and meteorological input parameters. This allows studying the impact of obstacle-induced turbulence and thermal plume rise on the shape of the vertical concentration profile. The shape of these profiles is then parameterized depending on different meteorological and technical input parameters (Fig. 5.1; Chapter 5.2). In a second step, the parameterized profiles are used in the city-scale model EPISODE-CityChem v1.4 (Karl et al., 2019b; Karl and Ramacher, 2020) with various meteorological settings and additional terrain information (Chapter 5.3). Finally, pollution ground-level concentration values at different distances from the source are calculated and the impacts of different plume parameterizations as well as meteorological input parameters and the surface roughness are compared (Chapter 5.4).

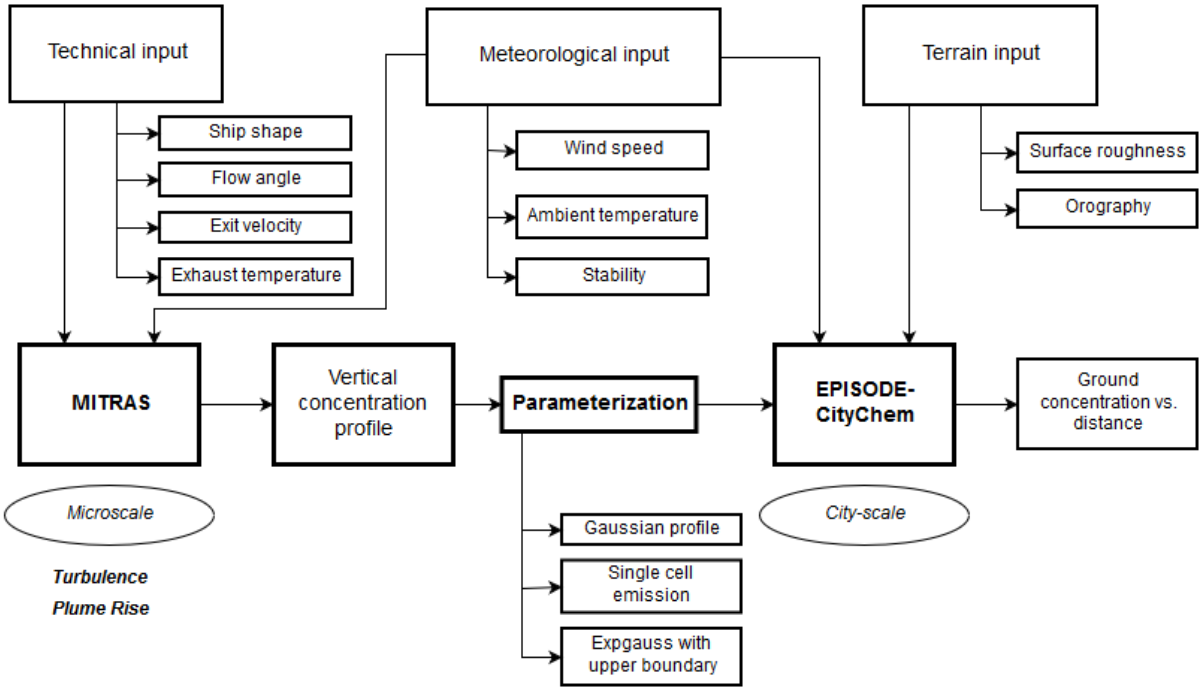

Figure 5.1: Schematic concept of the second study.

5.2 Plume parameterization

To better represent microscale effects in the near field of the ship in city-scale models, it is necessary to include the effects of plume rise and turbulence into the vertical emission profile. The first step of this work is to find a good parameterization for the vertical concentration profile at a point where the plume movement is no longer affected by thermal plume rise or ship-induced turbulence, as these factors are usually not covered in larger-scale models. This is the case at a distance of around 100 m from the source (see Chapter 4). At this distance, the vertical concentration profile is calculated with the microscale model MITRAS (Chapter 5.2.1). The resulting profiles are parameterized in three different ways, i.e., with a classical Gaussian fit (Chapter 5.2.2), a very simple single-cell emission assumption (Chapter 5.2.3) and a rather complex exponentially modified Gaussian fit with an upper plume boundary (Chapter 5.2.4).

5.2.1 MITRAS

Plume rise and turbulence effects of the source (i.e., the ship) are resolved by running a set of modeling runs with MITRAS. A general MITRAS model description is given in Chapter 3.1. The model configuration is the same as in Chapter 4. In short, the highest resolution is 2 m × 2 m × 2 m close to the ship in a domain of roughly 1 km × 1 km horizontally and 500 m vertically. The bottom boundary of the domain is water for which the surface roughness is calculated from the wind speed and for the presented cases is near zero. No chemical reactions occur in the simulations. A constant high temperature and a vertically directed exhaust velocity is added to the emission cell (i.e., the grid cell above the stack).

The input data for ship characteristics and meteorology are presented in Table 4.1. Default values are constant while for all regression analysis one input parameter at a time is varied along the investigation range. In total, 39 different cases have been calculated in MITRAS. The corresponding input values are presented in Tables B.1 and B.2 in the Appendix.

Vertical concentration profiles are derived at a distance of 100 m away from the ship as the mean of a column with 100 m × 100 m cell sizes (see Appendix B.1 for the concept). While in Chapter 4, a formula for the downward dispersion, i.e., the fraction of concentration that is found below ship stack height, was derived, in this study, parameterizations for the whole vertical concentration profiles are calculated that account for near field effects (thermal plume rise and obstacle-induced turbulence).

5.2.2 Gaussian scheme

One common way to describe the vertical dilution of a ship plume is to assume a concentration reduction according to a Gaussian curve where the mean value μ corresponds to the height of the central plume axis and the standard deviation σ describes the vertical strength of diffusion. In this way, high values of σ correspond to

a plume with strong vertical diffusion that might be caused by high plume rise mainly due to high exhaust temperatures, low wind speed and/or an unstable atmosphere.

The general formula for a vertical Gaussian profile is:

$$c(h) = \frac{1}{\sqrt{2\pi\sigma^2}} \exp\left(-\frac{(h-\mu)^2}{2\sigma^2}\right), \tag{5.1}$$

where c is a dimensionless concentration value and h is the height given dimensionless in [m].

A Gaussian curve was fitted to the results according to a least square minimization with the Levenberg-Marquardt Algorithm (Moré, 1977). From that, individual values for μ and σ were found.

To parameterize the Gaussian curve, the dependency of μ and σ on meteorological and technical input parameters needs to be investigated. Therefore, single regression analyses have been performed.

To estimate the effect that one single input parameter has on the value of μ or σ, all values but the one of interest for a single regression remain constant at a predefined value. These values were selected according to Chapter 4; see Table 4.1.

In the single regressions in Fig. 5.2, the value of default setting is highlighted with a red asterisk.

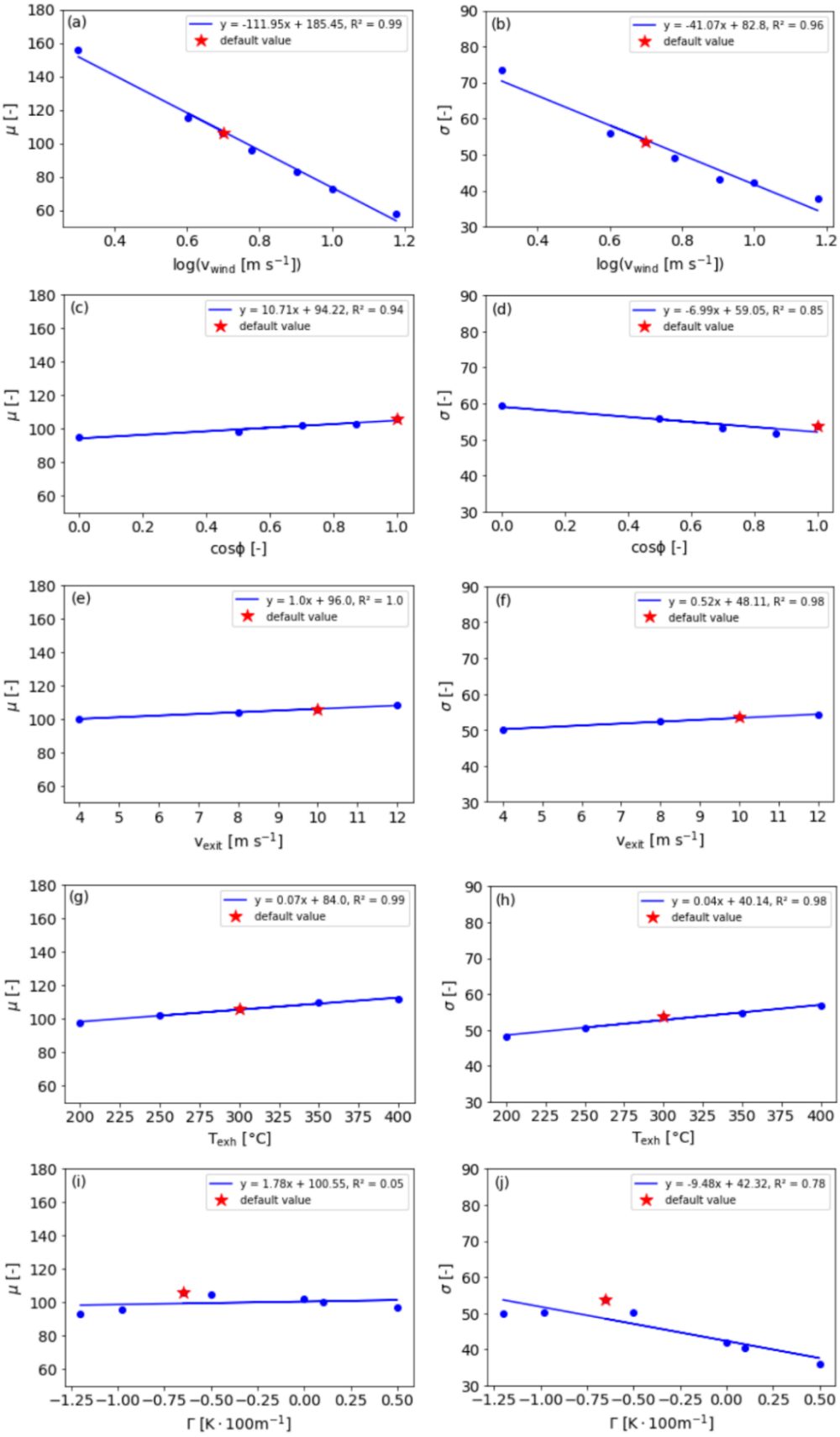

Figure 5.2: Single regression analysis of μ and σ against the input variables wind speed (v_{wind}), flow angle (ϕ), exit velocity (v_{exit}), exhaust temperature (T_{exh}) and atmospheric stability (Γ).

As visualized in the regression figures, μ and σ depend on most of the input parameters in an approximately linear way. For the wind speed, a linear correlation for μ and σ has been found against the logarithmic value of v_{wind}, which accounts for the natural logarithmic wind profile close to the ground (Prandtl layer). The negative correlation can be interpreted as follows: Higher wind speed causes the plume to remain at lower altitudes (low plume rise, low μ) and also cause a weaker vertical diffusion (lower σ). The wind speed has the strongest effect on both, μ and σ, within the investigated range of the input parameters.

A different type of linear correlation has been found for the wind angle, which describes the effect of the obstacle (i.e., the ship) orientation towards the wind direction. It ranges from 0° (frontal wind) to 90° (lateral wind). A positive linear dependency has been found for cos(ϕ) against μ and a negative dependency for cos(ϕ) against σ. This means that frontal wind allows for a higher plume rise (larger value of μ) but a weaker vertical dispersion (lower value of σ) than lateral wind, which can be explained by the stronger turbulent eddies that are created in case of lateral wind (larger obstacle effect). Strong turbulence leads to a strong dispersion but at the same time weakens the plume rise.

Positive linear dependencies have been found for μ and σ against exit velocity and exhaust temperature, which both affect the initial plume rise.

No clear correlation was found for μ against the atmospheric stability (Fig. 5.2i). This means that, under otherwise default conditions, the atmospheric stability does not show a significant influence on the mean plume height. A negative dependency has been found for stability against σ. This means that the plume does show stronger vertical dispersion in the case of an unstable or neutral atmosphere. In a stable atmosphere (i.e., at higher values of Γ), the plume remains narrow as during very stable fanning conditions.

By applying multiple regression analysis (for a more detailed insight into the procedure for ship plume studies see Appendix A.3.2), two functions have been determined to parameterize μ and σ based on the meteorological and technical parameters with all cases in Table B.1 in the Appendix.

$$\mu = 153.54 - 19.48 \log_{10}(v_{wind}) + 4.79 \cos(\phi) + 0.60\, v_{exit} + 0.075\, T_{exh} \quad (5.2)$$

$$\sigma = 57.7 - 41.02 \log_{10}(v_{wind}) - 5.0 \cos(\phi) + 0.41\, v_{exit} + 0.053\, T_{exh} - 13.21\, \Gamma, \quad (5.3)$$

where v_{wind} and v_{exit} are given dimensionless in [m s^{-1}], T_{exh} is given dimensionless in [K] and Γ is given dimensionless in [K · 100 m^{-1}].

By inserting μ and σ into the Gaussian distribution equation (Eq. 5.1), individual Gaussian profiles can be determined and used in larger-scale Eulerian grid models for ship plumes under different meteorological and technical conditions.

The quality of this parameterization has been tested in two steps. In the first step, the fitting of a Gaussian curve to the original model with the Levenberg-Marquardt Algorithm (Moré, 1977) has been evaluated. An average fitting quality of $R^2 = 0.92$ has been found. Especially in cases of strong winds and stable atmospheric conditions, the simple Gaussian distribution delivers good results. However, in cases of strong plume rise at neutral or unstable atmospheric conditions, fitting concentration profiles with a

simple Gaussian distribution can result in a poorer fitting quality of $R^2 = 0.8$ (e.g., case no. 6 in Table B.1 in the Appendix).

In a second step, the quality of the parameterization was tested against the fitting results, which reached an average of $R^2 = 0.99$. The parameterization can reproduce the fitted curves very well.

For a complete comparison of all investigated cases see Table B.1 and Table B.3 in the Appendix.

5.2.3 Single cell emission

A much simpler assumption is that all emission occurs in one emission height. This may be the stack height itself or an effective emission height, the latter being the case in many simple Gaussian dispersion models that solve plume rise and downward dispersion analytically.

In Eulerian grid models, the emission height equals the stack height only when the model can account for plume rise due to hot sources and turbulence due to obstacles, e.g., when using the MITRAS model.

The single cell emission (SCE) assumption used in this model assumes all emission to enter the larger model domain (EPISODE-CityChem) at the height μ that was calculated by the Gaussian parameterization (Chapter 5.2.2) from MITRAS results. In this way, it accounts for plume rise and downward dispersion in a minimalistic way, since the position of the central plume axis is represented but not the initial dispersion in the first 100−200 m.

5.2.4 Exponentially modified Gaussian scheme with upper plume boundary

The exponentially modified Gaussian distribution (Expgauss) adds an exponential feature to the upper end on the Gaussian distribution, thereby allowing the curve to be asymmetrical. The concentration function applied here is

$$c(h) = \frac{\lambda_1}{2} \exp\left(\frac{\lambda_1}{2}(2\lambda_2 + \lambda_1\lambda_3^2 - 2h)\right) \cdot \operatorname{erfc}\left(\frac{\lambda_2 + \lambda_1\lambda_3^2 - h}{\sqrt{2}\lambda_3}\right), \tag{5.4}$$

where c is a dimensionless concentration value and h is the height given dimensionless in [m].

It contains three shape parameters (λ_1, λ_2 and λ_3), as well as the complementary error function erfc(x):

$$\operatorname{erfc}(x) = \frac{2}{\sqrt{\pi}} \int_x^{\infty} e^{-t^2}\, dt \tag{5.5}$$

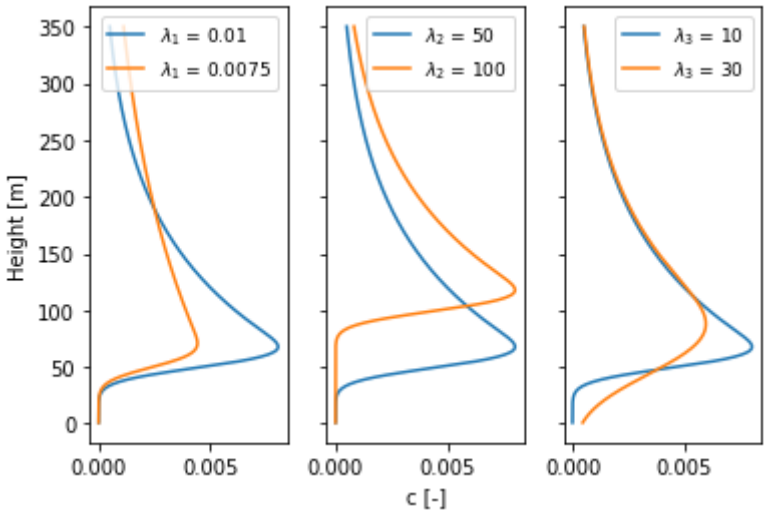

Figure 5.3: Visualization of the effect of different shape parameters on the exponentially modified Gaussian distribution. Blue profiles are the same with $\lambda_1 = 0.01$, $\lambda_2 = 50$ and $\lambda_3 = 10$, while in the orange profiles one shape parameter is varied in each panel. The concentration profile is dimensionless and needs to be normalized to serve as an initial emission input profile in EPISODE-CityChem.

This density function is derived by a convolution of the normal and the exponential probability density functions. Figure 5.3 gives an impression on how the different shape parameters affect the curve.

λ_1 is the exponential decay parameter. At $\lambda_1 = 1$ the function resembles an ideal Gauss curve with $\lambda_2 + 1$ as mean and λ_3 as standard deviation. $\lambda_1 = 0$ results in a constant line. λ_2 affects the height of the maximum concentration and moves the curve along the y-axis. It resembles the mean value of an ideal Gaussian curve when $\lambda_1 = 1$. λ_3 determines how steep the non-exponentially modified part (i.e., heights below the maximum concentration) rises. It also slightly affects the position of the concentration maximum.

As in the case of the Gaussian fit, the Expgauss curve was fitted to the results of the MITRAS simulations according to a least square minimization with the Levenberg-Marquardt Algorithm (Moré, 1977). From that, individual values for λ_1, λ_2 and λ_3 were determined. Next, the meteorological and technical input parameters were plotted against the individual shape parameters to determine which input affects which shape parameter. Figure 5.4 shows the corresponding single regressions for the ranges presented in Table 4.1.

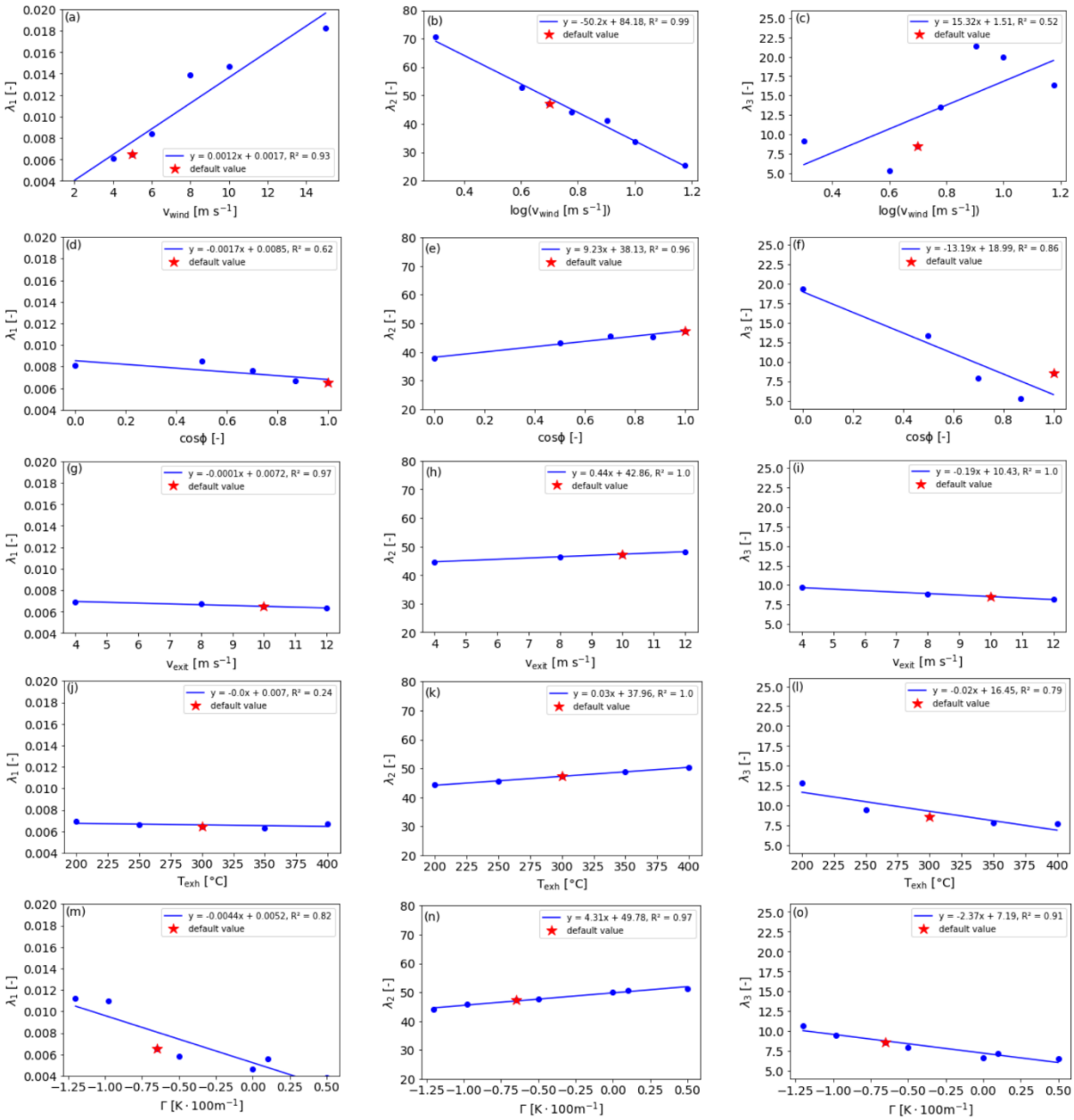

Figure 5.4: Single regression analysis of λ_1, λ_2 and λ_3 against the input variables wind speed (v_{wind}), flow angle (ϕ), exit velocity (v_{exit}), exhaust temperature (T_{exh}) and atmospheric stability (Γ).

By applying multiple regression analysis based on the results of the strongest single regressions (see Table B.3 in the Appendix for a comparison of effective ranges), the following parameterizations were found for the shape parameters:

$$\lambda_1 = -0.00445 + 0.002\, v_{wind} - 0.00575\, \Gamma \tag{5.6}$$

$$\lambda_2 = 77.6 - 52.7 \log_{10}(v_{wind}) + 2.86 \cos(\phi) + 0.023\, T_{exh} + 3.86\, \Gamma \tag{5.7}$$

$$\lambda_3 = 20.4 - 8.28 \cos(\phi) - 0.0135\, T_{exh} - 6.0\, \Gamma, \tag{5.8}$$

where v_{wind} is given dimensionless in [m s^{-1}], T_{exh} is given dimensionless in [K], and Γ is given dimensionless in [K · 100 m^{-1}].

These parameterizations can then be used in Eq. (5.4) to calculate the vertical plume profile.

Particularly in cases of a stable atmosphere, the plume rise in the near field tends to be overestimated when fitting with an exponentially modified Gaussian function. MITRAS results show a rather sharp reduction in vertical concentration as soon as the plume temperature decreases down to ambient temperature. The height at which the plume temperature equals the ambient temperature is herein defined as upper plume boundary height h_{up}. It was calculated based on the MITRAS model results and parameterized similar to the concentration profile functions. It can cause sharp concentration gradients in cases of a stable surrounding atmosphere.

A strong logarithmic dependency of the upper plume boundary on wind speed was found (see Fig. 5.5a). Larger wind speeds lead to lower maximum elevations that the plume could reach in the near field. A linear dependency was found for the upper plume boundary against the exhaust temperature (Fig. 5.5b) and against the function sgn(Γ)Γ² (Fig. 5.5c), which is the square of the vertical temperature gradient (i.e., stability) where the sign is retained (sign function). See also Chapter 4.2.1.4 for comparable correlations for the stability.

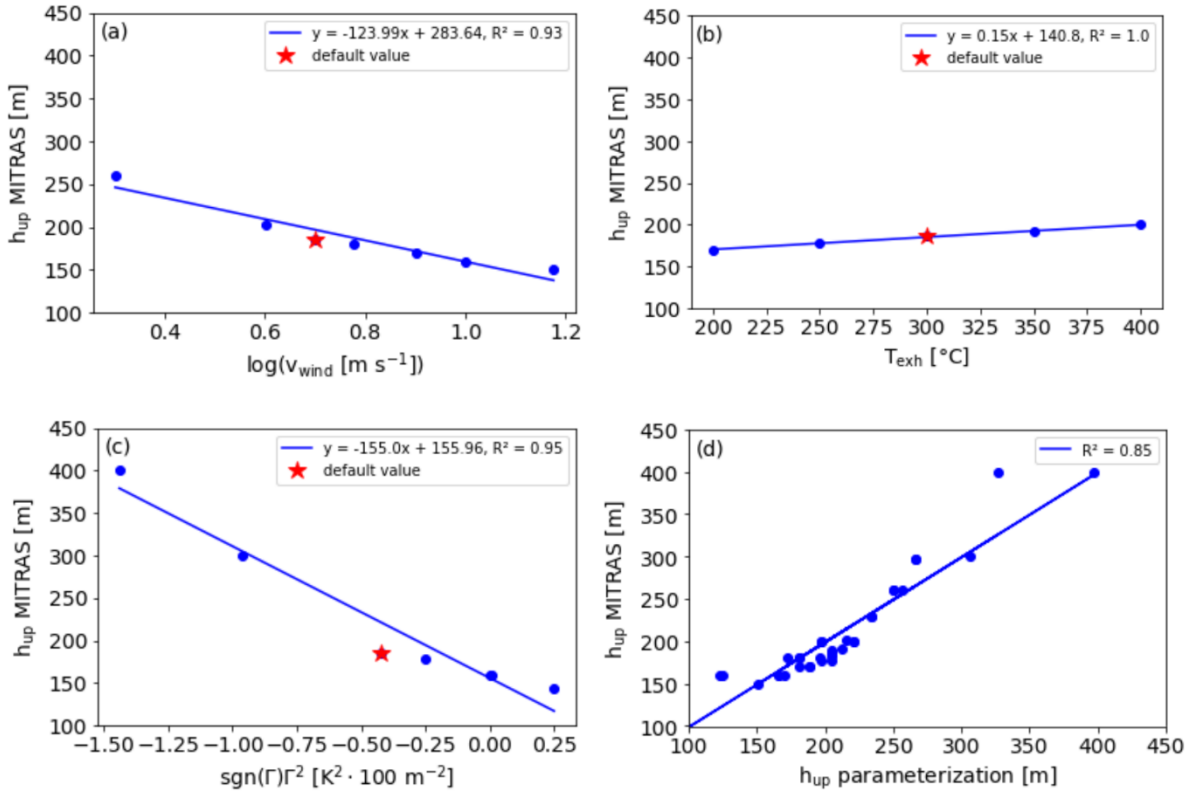

Figure 5.5: Regression analysis for upper plume boundary heights calculated with MITRAS against (a) wind speed (v_{wind}), (b) exhaust temperature (T_{exh}) and (c) atmospheric stability (Γ). Panel (d) shows the regression of the upper plume boundary from MITRAS results against the parameterization.

From these regressions, a multiple regression formula was calculated to parameterize the upper plume boundary:

$$h_{up} = 154.09 - 114.0 \log(v_{wind}) + 0.164\, T_{exh} - 189.0\, \mathrm{sgn}(\Gamma)\Gamma^2, \quad (5.9)$$

where v_{wind} is given dimensionless in [m s^{-1}], T_{exh} is given dimensionless in [K], and Γ is given dimensionless in [K · 100m^{-1}]. h_{up} results in [m].

This parameterization was tested against MITRAS model results for a variety of 39 different scenarios (see Table B.2 in the Appendix). A correlation of $R^2 = 0.85$ for upper boundary calculation with MITRAS and the parameterization formula was found (Fig. 5.5d). The performance is weakest under scenarios of very low plume rise, mainly at high wind speeds (> 10 m s^{-1}). Under these conditions, one can either ignore the upper boundary condition or use the classical Gaussian profile.

Finally, the quality of the Expgauss parameterization from ground to upper plume boundary has been tested in two steps. The fitting of the Expgauss curve to the original MITRAS results delivered a mean fitting quality of $R^2 = 0.99$ for all 39 investigated cases, which is better than the Gaussian fit. Furthermore, the quality of the parameterization was tested against the fitting results, which reached an average of $R^2 = 0.96$. The parameterization can reproduce the fitted curves very well and only shows weaker results at high wind speeds.

For a complete comparison of all investigated cases see Table B.3 in the Appendix.

Results from the Expgauss parameterization were included into further EPISODE-CityChem calculations from the ground up to the parameterized upper boundary.

5.3 EPISODE-CityChem

The resulting parameterization for the vertical concentration profile is integrated in the city-scale model system EPISODE-CityChem (Hamer et al., 2020; Karl et al., 2019b).

In this study, the focus lies on investigating the dilution of ship plumes under varying initial emission profiles. Chemical reactions are deactivated in this study, to make it applicable to any passive tracer gas. Also, the highly nonlinear NO_x–O_3 chemistry would need an inclusion of background chemistry, diurnal differences for photochemistry and other sources to model NOx concentrations precisely. This was beyond the scope of this study. Therefore, gases are modeled as passive tracers.

Table 5.1: Overview of the EPISODE-CityChem setup.

Horizontal domain size	8 × 8 km²
Horizontal domain resolution	100 m
Model grid coordinate system	WGS1984 Universal Transverse Mercator (UTM) Zone 32N
Vertical dimension	30 layers Lowest 20 layers: 10 m Layers 21−30: step-wise increasing resolution up to 250 m Vertical top height: 1000 m
Meteorological inputs for MCWINDv1.2	Ground temperature: 15 °C Wind direction: 180° Wind speed at stack height (50 m): 1−12 m s^{-1} Atmospheric stability: -1.2−0.0 K · 100 m^{-1} Cloud coverage: 100%
Technical parameters of the ship (used for parameterization formulae)	Exhaust temperature: 300 °C Exit velocity: 10 m s^{-1} Flow angle: 0° (frontal wind)
Surface roughness water	0.001 m
Surface roughness land	0.1−1.0 m
Emission rate	1 g s^{-1}
Emitted substance	NO_x (95% NO, 5% NO_2) No reactions
Background chemistry	None
Emission type	Area emission
Vertical emission distribution	Gaussian profile Single-cell emission Exponentially modified Gaussian profile

5.3.1 Model setup

This section describes the specific setup and inputs selected for this study. A summary is given in Table 5.1.

The inner part of the city of Hamburg is simulated, representing a northern European harbor city. A horizontal resolution of 100 m × 100 m is used. The overall horizontal domain size is 8 km × 8 km.

30 vertical layers are used with increasing vertical expansion. In the lowest 200 m the vertical resolution is fixed at 10 m. Above this height, it increases up to a vertical resolution of 250 m. A total height of approximately 1 km is covered. Due to the terrain-following coordinate system used, this upper limit may vary slightly.

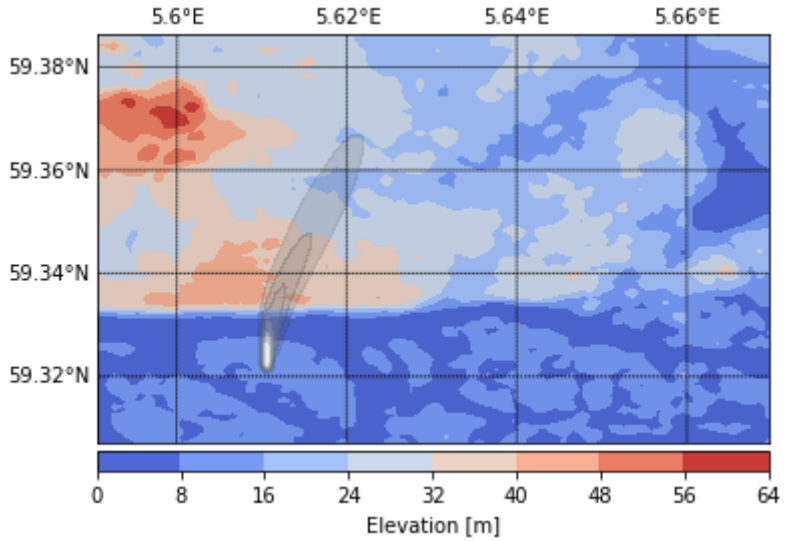

Figure 5.6: Elevation map of the inner city of Hamburg in the EPISODE-CityChem model domain of 8 km × 8 km. An example ship plume is shown in grayscale.

Digital Elevation Data SRTM3 for the region of Hamburg have been used with Universal Transverse Mercator (UTM) coordinates of south west corner of the model domain being x = 559064 and y = 5930727 (UTM zone 32N), which corresponds to 9.89091° E and 53.52215° N, respectively, in Cartesian coordinates.

Topography information is converted into landuse classes and surface roughness values distinguishing only two different landuse classes: water and land. Figure 5.6 shows the investigation area with elevation information and an example plume.

The surface roughness is the height above the displacement plane at which the mean wind becomes zero when extrapolating the logarithmic wind speed profile downward through the surface layer. For water surfaces, in Chapter 4, a value close to 0 m was used, depending on the wind speed (Schlünzen et al., 2018). Here, a fixed value of 0.001 m is used, which is reasonable, as the focus lies in the investigation of the behavior of the plume over land. The surface roughness of the land area is varied between 0.1 m and 1.0 m, corresponding to different structures, from low crops to medium-sized building areas (e.g., Wieringa, 1992). It plays a major role in the computation of the friction velocity, the turbulent mixing in the vertical diffusion scheme and the dry deposition.

In this study, the meteorological field is created by the meteorological preprocessor MCWIND v1.2 (Hamer et al., 2020).

The EPISODE-CityChem chemistry options on the Eulerian grid include a dispersion without photochemistry, which is applied here. More general information on the EPISODE-CityChem modeling system is given in Chapter 3.2.

5.3.2 Emission characteristics

Ship emissions are treated by EPISODE-CityChem as an area source. This means that concentrations are diluted instantaneously into the corresponding emission grid cells and emitted pollutants are then subject to advection, diffusion, deposition and chemistry (if activated) in the model grid. The vertical emission distribution corresponds to a parameterized profile derived from MITRAS results (see Fig. B.1 in the Appendix) for a column of 100 m × 100 m × 10 m downwind from the ship to account for thermal plume rise and obstacle-induced turbulence in the near field. Three different parameterization schemes are applied.

The first scheme will be standard Gaussian parameterization described in Chapter 5.2.2. The vertical emission profile was normalized and distributed into the corresponding cells of a vertical column.

In the single cell assumption, the whole emission will be inserted into one single cell of the model. This will be the cell at the height of the mean value in the standard Gaussian parameterization (Chapter 5.2.3).

The third profile is calculated with the Expgauss parameterization (Chapter 5.2.4).

A normalized emission rate of 1 g s^{-1} NO_x was selected to easier compare different effects (e.g., different concentration distribution, different meteorology or different surface roughness) on the dispersion.

A NO_x split of 95% NO and 5% NO_2 is used. However, in this study chemical transformations are not considered and therefore, the ratio will not change, as they will behave as passive tracer gas.

The differences of the chosen parameterization and their effect on the ground-level concentration depending on meteorological conditions and surface roughness will be evaluated. Therefore, the concentration will be calculated with increasing distance from the source along the path of highest ground-level concentration (see Fig. B.2 in the Appendix for an exemplary scheme).

5.4 Results and discussion

This section presents pollution ground-level concentration values at different distances from the source. The impacts of different plume parameterizations as well as meteorological input parameters and the surface roughness on the concentration values are compared and uncertainties are discussed.

5.4.1 Input profile

Three different methods for the initial distribution of vertical plume profiles were presented in Chapter 5.2. Now the differences of the resulting ground-level concentrations in dependence of the distance to the source will be examined.

As an example, Fig. 5.7 shows the initial emission profiles for the Gaussian and Expgauss profiles based on default input parameters, i.e., a wind speed of 5 m s^{-1} with frontal direction, exit velocity of 10 m s^{-1}, exhaust temperature of 300 °C and an atmospheric stability of -0.65 K · 100 m^{-1}.

The concentration values in Fig. 5.7 are normalized, i.e., the vertically integrated emission is 1. In the case of single-cell emission, the normalized concentration value is 1 at the height of mean Gaussian distribution. For the exponential Gaussian profile the upper plume boundary of the near field lies at around 200 m. However, this upper boundary is only used for the initial emission distribution. In further EPISODE-CityChem calculations, parts of the plume might rise higher.

These normalized curves are used as initial emission profiles in EPISODE-CityChem according to the vertical resolution of the cells.

As can be seen in Fig. 5.7, the Gaussian profile tends to distribute a part of the emission to the lowest model layer already in the near field. Therefore, high ground-level concentration values close to the source are to be expected. The exponential Gaussian profile can better represent the plume rise. Therefore, ground-level concentrations will have a maximum at a farther distance. In the case of SCE, all emissions occur at the mean height of the Gaussian profile, i.e., with no proportion in the lowest model layer. Therefore, the peak ground-level concentration for the SCE approach occurs several 100 m downwind of the source position.

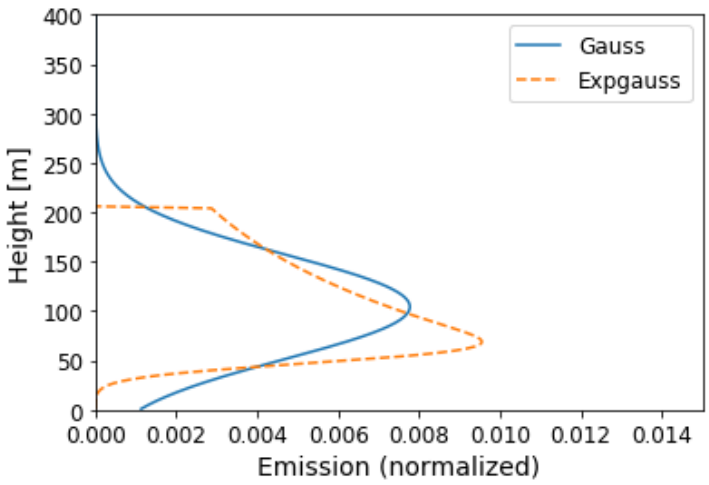

Figure 5.7: Initial vertical emission profiles for Gaussian and exponential Gaussian emissions under default conditions (see Table 4.1). The single-cell emission profile lies at the mean height of the Gaussian profile with a normalized emission of 1.0 (not shown).

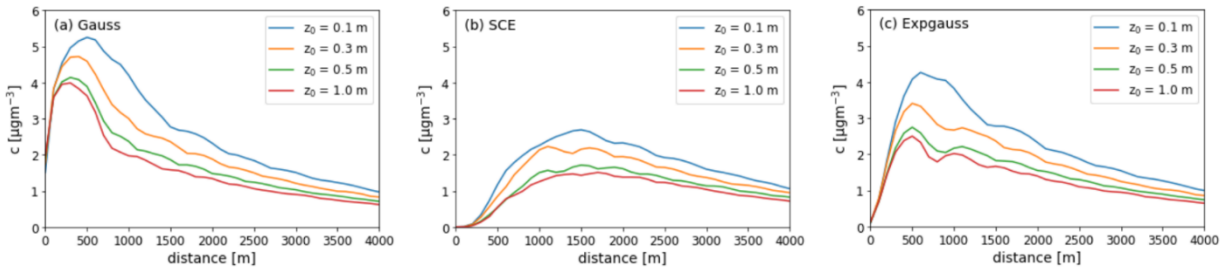

Figure 5.8: Ground-level concentration profiles depending on the distance to the source for different roughness lengths and initial emission distribution.

Variations of these input profiles can be found in Fig. B.3 in the Appendix for several different initial conditions.

5.4.2 Effect of surface roughness

To evaluate the impact of surface roughness on pollutant ground-level concentration, the roughness value for land areas was varied between 0.1 m (grassland) and 1.0 m (urban area), which was assumed to be the range of surface roughness that can occur in the harbor area. All the remaining input values were kept at default conditions (Table 4.1). It is important to mention that surface roughness was not included in the calculation of initial vertical plume profiles.

Therefore, the initial profiles are all the same as in Fig. 5.7.

Figure 5.8 shows the ground-level concentration depending on the distance from the source, the roughness length and the effect of different initial plume profiles. For all investigated cases, the surface roughness shows larger ground-level concentration values in cases of lower surface roughness. In the case of the Gaussian profile, the highest differences occur at a distance of 700 m, where z_0 = 0.1 m causes 2.72 µg m^{-3} (113%) higher ground-level concentration than z_0 = 1.0 m. For the SCE assumption, the maximum difference is 1.26 µg m^{-3} (88%) at 1400 m distance. Finally, for the Expgauss assumption, the highest difference is 2.29 µg m^{-3} (128%) at 700 m distance.

Decreasing ground-level concentrations in areas of increased roughness lengths (city centers) have also been reported in a model study from Barnes et al. (2014). In their study, the lowest model layer experienced localized high ground-level concentration values of NO_x in a city center where the main source of NO_x is traffic. They expected a low ground-level concentration at high surface roughness due to weaker horizontal ventilation but the turbulent mixing effect dominated, thus causing lower ground-level concentrations when modeling with higher surface roughness. In our study, increased dilution also causes lower concentration values when the surface roughness is high.

When comparing the effect of initial plume profile, it can be seen that the highest ground-level concentrations occur close to the source when assuming a Gaussian distribution (see also Fig. B.4 in the Appendix). The SCE assumption shows a rather

flat maximum between 1000 m and 2000 m, while the Expgauss distribution shows a similar behavior as Gaussian distribution but with a smaller maximum close to the source. This can all be attributed to the ratio of emission that is initially distributed into the lower modeling layers (see Fig. 5.7). In case of SCE, all emissions enter the modeling domain at a height of around 100 m and need a much longer distance to be transported downward. At a distance of around 1500 m, the ground-level concentration becomes independent of the initial plume profile.

5.4.3 Effects of stability

Stability effects on the ground-level concentration were tested in EPISODE-CityChem for three different temperature profiles: the standard atmosphere stability (-0.65 K · 100 m^{-1}), a very stable atmosphere (0.0 K · 100 m^{-1}) and an unstable atmosphere (-1.2 K · 100 m^{-1}). Again, all the remaining input values were kept at default conditions (Table 4.1).

Figure 5.9 displays the effect of stability on the ground-level concentration for the different input concentration assumptions. For all cases, the highest ground-level concentrations are reached in the case of unstable atmospheres. This is especially strong in the nearest 1000 m. Here, the obstacle effect of the ship causes stronger turbulent mixing at high instability and more downward dispersion. Under stable conditions, the downward transport is weak and the largest proportion of the concentration remains at emission height.

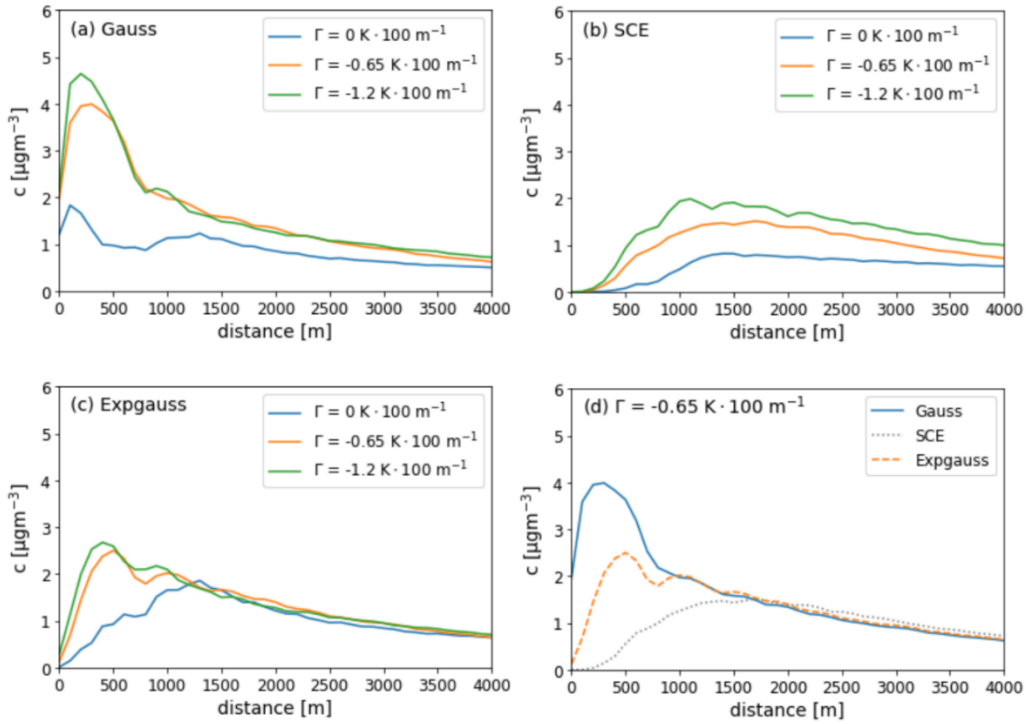

Figure 5.9: (a–c) Ground-level concentration profiles depending on the distance to the source for different stabilities and initial emission distribution; (d) direct comparison of the effect of different emission distribution at Γ = -0.65 K · 100 m^{-1}.

For Gaussian and Expgauss profiles the strongest absolute difference of 3.16 µg m^{-3} (241%) and 2.00 µg m^{-3} (378%), respectively, occurs at a distance of 200 m from the source when comparing the unstable and the very stable cases. For the SCE assumption, the highest absolute difference of 1.45 µg m^{-3} (302%) occurs at a farther distance of 900 m when comparing unstable and very stable case.

At a distance of more than 3 km, the difference in ground-level concentration between different stabilities and input profiles are almost negligible. This is caused by turbulent mixing, which is a factor of wind speed and surface roughness. Note that this distance can vary when changing the values for wind speed and surface roughness.

5.4.4 Effects of wind speed

EPISODE-CityChem simulations with six different wind speeds have been performed: 1, 2, 3, 5, 8 and 12 m s^{-1}. This covers a typical range of values in Northern European harbor cities (see Appendix A.1). All the remaining input values were kept at default conditions (Table 4.1).

Results of ground-level concentration simulations are presented in Fig. 5.10. The effect of different wind speeds on the ground-level concentration is a complex phenomenon in this study. Highest concentration values are found at 1 m s^{-1}, then there are minimum values between 3 and 5 m s^{-1} while at higher wind speeds, the ground-level concentration rises again.

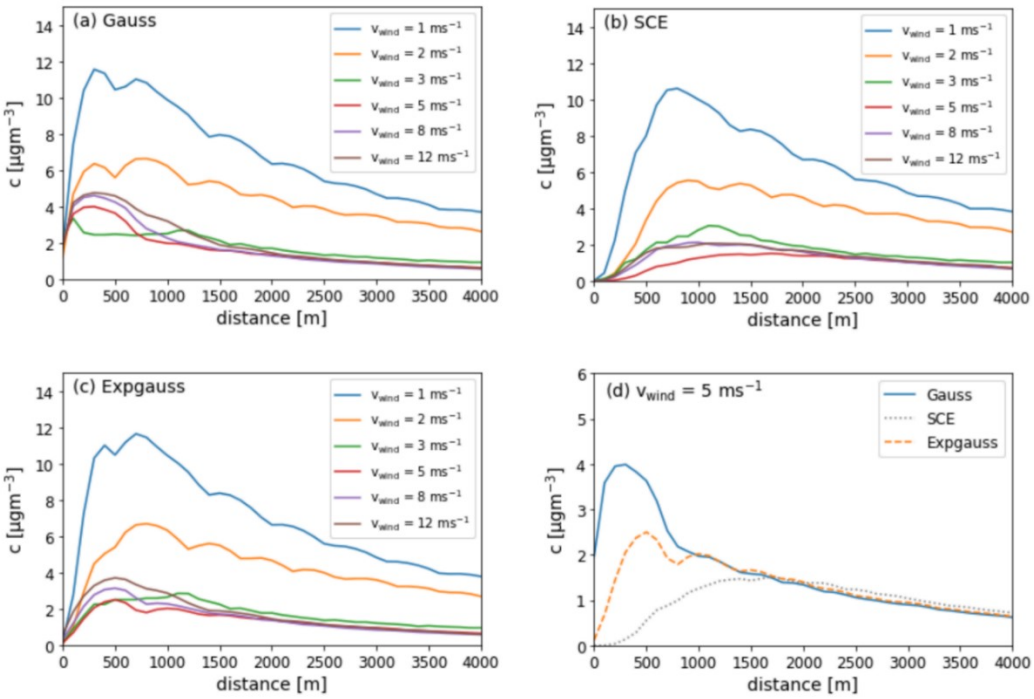

Figure 5.10: (a−c) Ground-level concentration profiles depending on the distance to the source for different wind speeds and initial emission distribution; (d) direct comparison of the effect of different emission distribution at v_{wind} = 5 m s^{-1}.

Two different effects cause this behavior. For slow wind speeds, advective transport is low and the pollutants accumulate to a higher rate. This alone would lead to the impression that ground-level concentration are lowest at high wind speeds. However, a second effect increases the ground-level concentration with increasing wind speed. This is caused by the input emission profile, which shows a weaker plume rise and a stronger obstacle-induced downward dispersion at high wind speeds (see Fig. B.3 in the Appendix for different input profiles depending on wind speed). In Chapter 4, high wind speed was described as the most important factor for downward dispersion of the plume. This is caused by (a) strong turbulent eddies formed in the wake of the ship which dilutes it and (b) a weaker thermal plume rise at higher wind speeds, as the plume is transported faster and thus cools down more quickly.

Ledoux et al. (2018) also found higher concentrations with increased wind speed and described that low wind speeds rather lead to a vertical dispersion and lower concentrations.

Comparing the different parameterizations, the Gaussian profile shows the strongest differences of 9.12 µg m^{-3} (374%) when comparing 1 m s^{-1} and 3 m s^{-1} wind speed at a distance of 200 m. The SCE assumption shows a similar maximum absolute difference of 9.63 µg m^{-3} but with a much larger corresponding relative difference (1095%) when comparing 1 m s^{-1} and 5 m s^{-1} at a distance of 600 m. Finally, the Expgauss profile shows a maximum absolute difference of 9.73 µg m^{-3} (506%) at 600 m when comparing 1 m s^{-1} and 5 m s^{-1}.

At a distance of more than 1500 m, the individual plume profiles show very similar results.

5.4.5 Comparison of the effects

Table B.4 summarizes the results of Chapters 5.4.2 to 5.4.4 and allows a comparison of the effect of different input variables on the ground-level concentration. Under default conditions, the strongest effect was found for wind speed variations, causing differences > 9 µg m^{-3} or up to over 1000%. Stability and roughness length can both cause differences in the range of 1 to 3 µg m^{-3} under default conditions. The strongest differences between the different input parameterizations occur in the first 1500 m from the source. Gaussian profiles give the best representation at high wind speeds and when downward dispersion near the source are strong. Expgauss profiles can better account for unstable atmospheres and strong plume rise. The SCE approach is simple but always leads to a ground-level concentration maximum at a larger distance from the source (i.e., around 1000 m downwind). This approach is certainly not optimal when measurements close to the source are underestimated.

5.4.6 Discussion of uncertainties

The performance of MITRAS has been verified before with quality-ensured wind tunnel data, including simple obstacle configurations and results showed a very good agreement of the wind field for most test cases (Grawe et al., 2013). The plume rise effects have been compared to the integral plume rise model IBS-PLURIS (Janicke and Janicke, 2001) in Chapter 4. The initial plume rise was generally some meters higher in the MITRAS study, as MITRAS accounts for the change in the thermodynamic field and the heat balance equation creates additional buoyancy that is not accounted for in simple Gaussian approaches.

The performance of EPISODE-CityChem has been evaluated in Karl et al. (2019b) with a series of statistical tests, including comparisons against the standard EPISODE model, the air pollution model (TAPM; Hurley et al., 2005; Hurley, 2008) and measurements in the city of Hamburg. It fulfils the model performance objectives set for the air quality directive, which qualifies it for use in policy applications. From these previous performance evaluations, it is assumed that the model setup in this study is capable of reproducing ship plume scenarios in a realistic manner.

In the EPISODE-CityChem part of this study, the ship plume is classified as an area source and not a point source as in the majority of plume model studies (e.g., Bai et al., 2020; Merico et al., 2019; Pan et al., 2021; Poplawski et al., 2011). This can lead to a poorer performance at lower grid resolutions when the emission is instantaneous diluted equally into the corresponding emission cells (e.g., Huszar et al., 2010; Jonson et al. 2015; Vinken et al., 2011). Studies that treat ship emissions as area sources are rather rare (Abrutytė et al., 2014; Kotrikla et al., 2013). However, in this study the emission profile is adjusted based on MITRAS parameterizations of the initial plume distribution, accounting for plume rise and obstacle-induced turbulence in the near field. The MITRAS results are based on a point source approach, where emissions enter the grid in a 2 m × 2 m × 2 m grid (Chapter 4). Afterwards the plume concentration profile is used for the vertical emission distribution in the EPISODE-CityChem model. At a distance of roughly 100 m from the source, a dilution of the plume to a 100 m × 100 m area source can be considered acceptable and the equally dilution error is further reduced when applying Gaussian or Expgauss vertical distribution.

Applying Monin-Obukhov similarity theory for the vertical wind profile in the surface layer has a limitation for models with a high vertical resolution. The logarithmic wind profile is inaccurate inside the surface roughness layer in cases where the surface roughness is not considerably smaller than the lowest model layer height and the wind speed then tends to be overestimated (e.g., Lee et al., 2020). Basu and Lacser (2017) presented an overview of this issue recommending the modeling community to follows a guideline of $z_1 > 50\ z_0$, where z_1 corresponds to the lowest model layer height. This condition is not fully satisfied in some of the EPISODE-CityChem simulations with higher surface roughness. However, EPISODE-CityChem includes empirical stability correction functions for the surface layer wind profile that address this problem (Holtslag, 1984; Holtslag and de Bruin, 1988) and from the results herein, no evidence of inaccuracies in the plume dispersion even at higher surface roughness was found.

Input assumptions are based on a medium-sized cruise ship with a stack height of approximately 50 m. The selected range of input values such as exit velocity and exhaust temperature have already been discussed in Chapter 4. For smaller ships the distribution curves can vary. An adjustment to different stack heights is possible and in a first approximation done by shifting the emission distribution by the difference of the chimney heights.

A complete validation of the vertical profiles is only possible by comparing them with real measurements that also need the inclusion of correct emission factors, other sources and chemistry effects. A precise estimation of emission factors of moored ships includes a further uncertainty, namely the inaccurate data basis for the use of auxiliary engines that are used during hoteling. Most studies investigate emissions of main engines, while only a few specifically measured or modeled auxiliary engines (e.g., Abrutytė et al., 2014; Cooper 2003; Eyring et al., 2005; Moreno-Gutiérrez et al., 2015; Tzannatos, 2010). Large ships have generally between three and seven auxiliary engines (Jayaram et al., 2011) and uncertainties arise from individual engine operating days, engine load, the specific fuel consumption and the kind of performed operation, e.g., hoteling or loading (Cooper 2003; Moreno-Gutiérrez et al., 2015).

The authors assume that besides the variety of uncertainties, the results of this study have a relevant practical implication in real cases, most importantly due to including the wind speed as a variable into the calculation of vertical emission profiles, which has the largest impact on the emission distribution and resulting concentrations. Since wind speed measurements are widely available, an inclusion of wind speeds into the distribution function is possible in any real case scenario. Further uncertainties like technical parameters can be extracted from engine data sheets for individual ships and, if not available, be extrapolated from similar ships or engines. An important tool to derive this information for individual ships is the recently developed modular ship emission modeling system MoSES (Schwarzkopf et al., 2021).

Including all of this was beyond the scope of this study but the inclusion of the new emission profiles into a more complex chemistry transport model study is planned for the future (Chapter 6).

5.5 Conclusion

This study served to improve the modeling of ship exhaust gases on the city-scale with regard to the vertical pollutant distribution. In a first step, vertical concentration profiles were calculated using the microscale MITRAS model, which takes into account plume rise and obstacle turbulence. This was done for various meteorological and ship-technical conditions to cover a variety of possible scenarios in northern Europe harbor cities. From the MITRAS results, three different parameterizations for the emission distribution in the city-scale model EPISODE-CityChem were derived. Their effect on the urban ground-level concentration have been compared under conditions of varying urban surface roughness, wind speed and atmospheric stability.

Based on the model results of this study, the authors would like to make recommendations for which vertical plume parameterization should be used and when. A general differentiation is recommended for studies with horizontal resolutions ≤ 4 km, i.e. especially on the city-scale. At a larger distance from the source, the profiles deliver approximately the same results for pollution close to the ground. Therefore, a simple single-cell emission is sufficient for open-ocean or regional studies with horizontal resolutions > 4 km. Note that the emissions should still be inserted into the correct vertical cell. Equation (5.2) is then used to calculate the emission height.

At smaller scales, authors recommend the use of a Gaussian profile in case of moderate or strong wind speeds (> 5 m s^{-1}) and neutral to stable atmosphere (Γ > -1.0 K · 100 m^{-1}). Regression results for the parameterization were close to R^2 = 1.0 in these cases. A vertical Gaussian distribution for stable boundary layers has also been applied for a ship emission study with AERMOD (Cohan et al., 2011). Gaussian parameterization can also be recommended in case of moving ship studies, e.g., Pan et al. (2021) since ship speed and wind speed often sum up to a higher effective wind speed, which should then be used in the parameterization formulae.

For calm wind situations or unstable atmospheres, which can occur in harbors under hoteling situations, the Expgauss parameterization can better account for the initial plume rise and is recommended. A comparable result is expected by applying the bi-Gaussian distribution, which is used in case of convective boundary layers in AERMOD (e.g., Cohan et al., 2011). The Expgauss parameterization is of special interest for air quality studies, since pollutant accumulation usually occurs at low wind speeds. To the authors' knowledge, this approach is the first of its kind to develop a dynamic vertical emission profile for ship emissions, including effects of plume rise and downward dispersion and it allows an adjustment of the emission profile for each time step. This is especially useful in cases of moving sources where the ship orientation and flow angle change frequently. A future study is planned to combine results of this study with the moving point source approach from Pan et al. (2021) for the EPISODE-CityChem modeling system. This will allow a time-flexible variation of the vertical profile of shipping emissions with either the Gaussian or Expgauss profiles derived here.

6 Application of the flexible plume approach for ship emissions in a city-scale air quality model

Abstract:

Precise horizontal and vertical positioning of ship emissions is one of the key drivers for accurate air quality modeling in harbor cities. This study presents the application of an advanced method for ship emission distribution inside the inner city of Hamburg, based on a complex chemistry transport modeling study.

Ship emissions are distributed with an exponentially modified Gaussian profile (Flexplume) and compared against a static assumption, where ship emissions are evenly distributed into the lowest four model layers (Fixplume), and measurements. The Flexplume method takes into account wind speed and atmospheric stability, ship height, flow angle and exhaust temperature, and thus captures the effects of turbulence and thermal plume rise. The horizontal distribution of the ship emissions is based on AIS position data and the application of the recently developed modular ship emissions modeling system MoSES on an hourly basis.

Results show a strong improvement of modeled nitrogen oxide (NO) values with the Flexplume assumption. At the representative station close to the Elbe River, mean hourly biases of NO are reduced from 11.35 µg m^{-3} to 1.57 µg m^{-3} and from 13.36 µg m^{-3} to 6.69 µg m^{-3} in January and August 2018, respectively. Comparisons with previous studies show that the Flexplume approach results in similar or better statistical results for NO_2 and O_3 as well. Therefore, it allows for a better representation of air quality, exposure and health effects for the shipping sector.

Note:

This chapter consists of a preliminary manuscript that will be submitted in the near future. The introduction and general parts of the EPISODE-CityChem model description have been omitted and incorporated into Chapters 1−3 to avoid duplication.

6.1 Methodology

In this chapter, the new vertical ship emission profile (Expgauss profile) is implemented into the EPISODE-CityChem model (Chapter 6.1.1). To investigate its performance under real conditions, a complex real-case setup for the city of Hamburg is modeled (6.1.2). This includes city-specific meteorological fields (6.1.3), regional background concentrations (6.1.4), inclusion of AIS-based ship movement and emission data (6.1.5), as well other land-based emission sources to simulate pollutant concentrations (6.1.6). These modeled concentrations are then compared with measured concentrations (6.1.7). The comparison is done using various statistical indicators (6.1.8).

The aim of the study is to first compare the sectorial emission contribution (6.2.1) for NO_x emissions. The concentrations calculated with the new Expgauss profile assumption for mobile ship emissions (Flexplume) are compared against concentrations modeled based on a static assumption (Fixplume) and measurements (6.2.2). The results are evaluated depending on wind directions (6.2.3). Finally, the model performance is discussed based on similar studies (6.2.4).

6.1.1 Flexible Plume in EPISODE-CityChem

Previous model setups with EPISODE-CityChem used a static vertical ship emission distribution into the model domain (Ramacher et al., 2019). Emissions were distributed evenly into the lowest four model layers, i.e., 25% each layer. This is referred here as “Fixplume”.

In this study, the Fixplume assumption is compared against a flexible plume, in which the vertical ship emission distribution corresponds to the newly implemented Expgauss function (Chapter 5.2.4). This function and the shape parameters therein were based on a parameterization with a medium-sized cruise ship. In this study, an adjustment was made to make it useable for an average fleet height (h_{fleet}).

To do this, a simple adjustment of the second shape parameter was made, which shifts the plume profile along the vertical axis.

$$\lambda_2 = 27.6 + h_{fleet} - 52.7 \log_{10}(v_{wind}) + 2.86 \cos(\phi) + 0.023 T_{exh} + 3.86 \Gamma \quad (6.1)$$

Currently, all ships in the EPISODE-CityChem model have the same height, exhaust temperature and flow angle. These were set to 25 m, 300°C and 0°, respectively. The 25 m average fleet height was derived from MoSES data (Schwarzkopf et al., 2021), based on IHS Markit 2020 ship database information (see Chapter 6.1.5 and Appendix C.2 for details). The exhaust temperature and flow angle values was selected from Table 4.1 for default conditions.

With the update of EPISODE-CityChem v1.6 (Karl, 2022), it is now possible to include the effects of wind speed and stability on the vertical ship emission distribution. EPISODE-CityChem calculates the ship emission distribution at every x-y position inside the domain where ship emissions occur and generates individual Expgauss

emission profiles. Therefore, the vertical ship emission distribution becomes very flexible in space and time.

6.1.2 General model setup

General information on the EPISODE-CityChem model were presented in Chapter 3.2. Figure 6.1 and Table 6.1 present an overview of the specific model setup of this study. The investigated domain is the same as in Chapter 5. Results are calculated for two months, January and August 2018, to cover seasonal differences. The year 2018 was selected, because new traffic emission data were available for 2018, including several updated features such as more different traffic situations and an updated vehicle database (see Chapter 6.1.6).

Also, there was no overlapping effect of the Corona pandemic in 2018, which had a strong impact on air pollution of later years (Matthias et al., 2021), which would add another level of complexity and uncertainty onto the model results. The results are presented on an hourly resolution, which is the same as available from measurements. This means the model calculates the sum of plume concentrations for the actual fleet of ships inside the modeled Hamburg harbor area.

The horizontal resolution was set to 250 m × 250 m to match with the resolution of the meteorological input data from the Australian air quality model TAPM (The Air Pollution Model) (Hurley, 2008; Hurley et al., 2005, see Chapter 6.1.3). Results from Chapter 5 suggest that the effect of plume rise and turbulence, that is covered by the Expgauss vertical emission distribution are still valid, since significant differences to other distributions occur up to 1500 m distance from the source.

The simplified street canyon model (SSCM) is activated for a better treatment of NO_x at traffic stations. All emission input data, except for the specifically generated ship emissions, were preprocessed with the Urban Emission Conversion Tool (UECT; Hamer et al., 2020).

The applied chemical scheme in this study is EmChem09-mod, an urban chemistry scheme including heterogeneous gas-phase reactions (Karl et al., 2019b; Simpson et al., 2012). 70 compounds, 67 thermal reactions and 25 photolysis reactions are included.

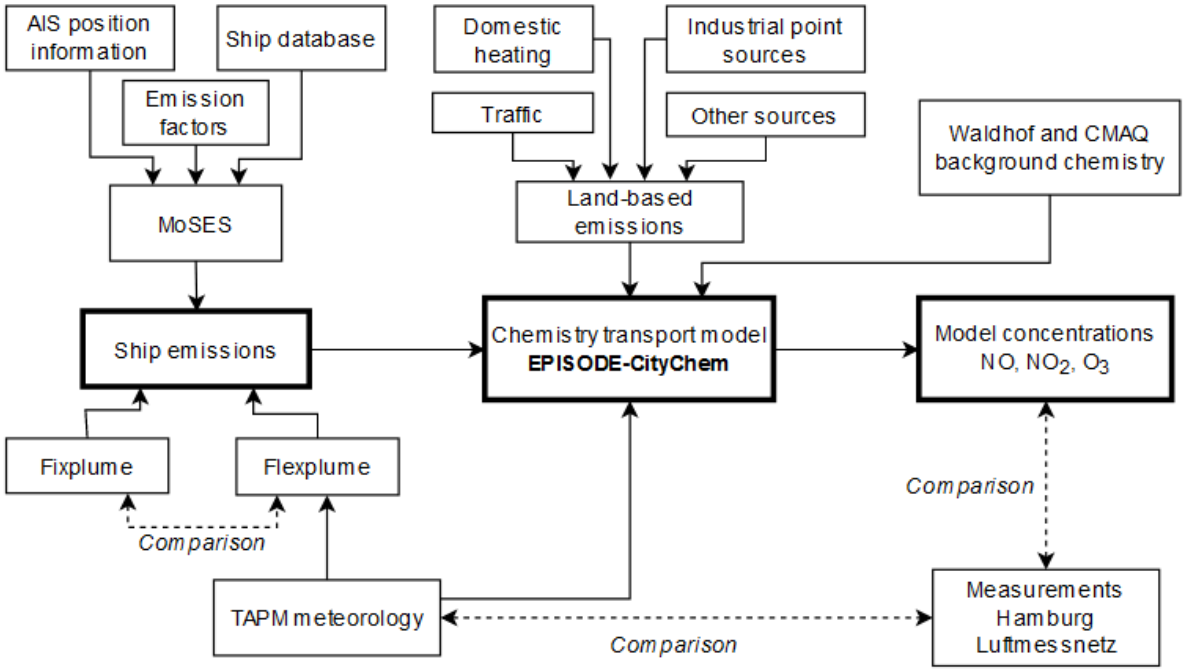

Figure 6.1: Schematic overview of the model setup for this study.

Table 6.1: Overview of the EPISODE-CityChem setup.

Investigation period	January and August 2018
Temporal resolution	hourly
Horizontal domain size	8 × 8 km²
Horizontal domain resolution	250 m
Vertical dimension	24 layers Lowest layer: 17.5 m, step-wise increasing resolution up to 500 m Vertical top height: 3750 m
Meteorological input	TAPM (Hurley, 2008; Hurley et al., 2005)
Background concentrations	Rural measurement site Waldhof and CMAQ model outputs from Matthias et al. (2021)
Area emission sources	CAMS 2016 REG-AP v3.1 (Granier et al., 2019; Kuenen et al., 2022)
Shipping emission	MoSES (Schwarzkopf et al., 2021)
Technical parameters of the ships (used for parameterization formulae)	Exhaust temperature: 300 °C Height: 25 m Flow angle: 0° (frontal wind)
Line sources (traffic)	HBEFA 4.1 (Umweltbundesamt, 2019)
Land cover classes	Corine Land Cover database (Copernicus Land Monitoring Service, 2018)
Terrain height	EU-DEM (EEA, 2017)

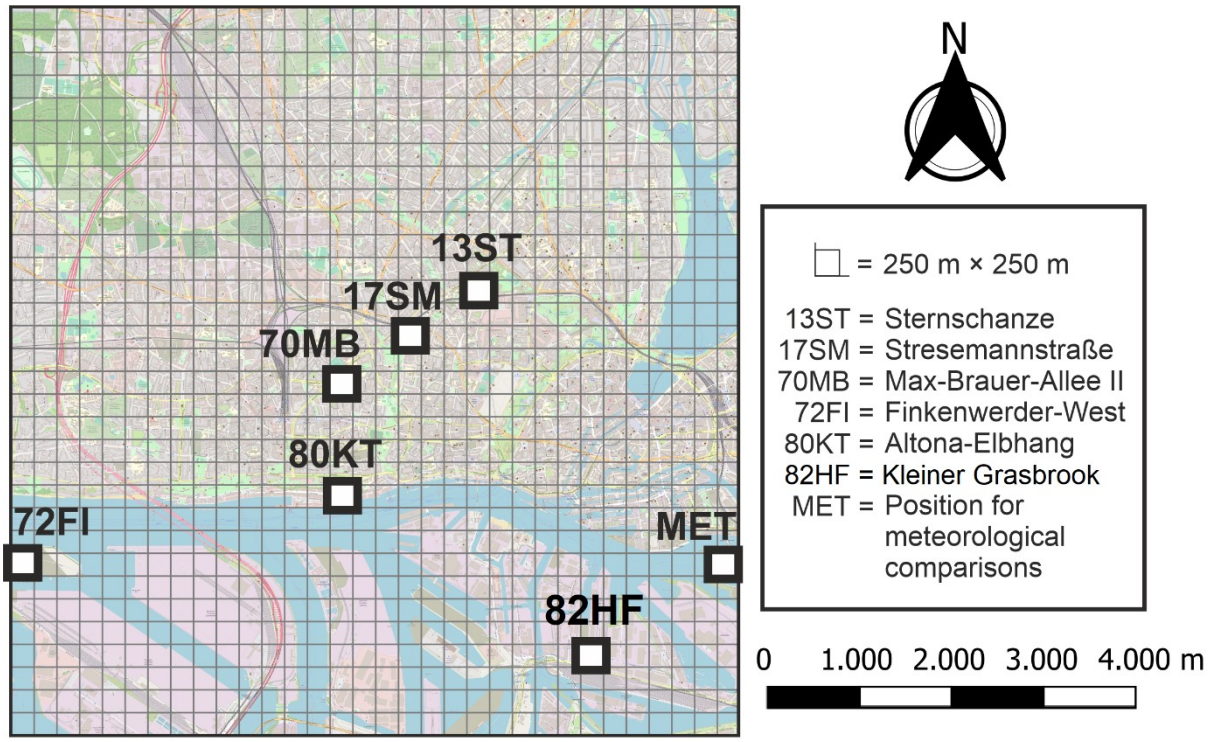

Figure 6.2: The model domain of inner-city Hamburg with the available measurement stations. Each grid cell has a horizontal dimension of 250 m × 250 m. Created using © QGIS-Version 3.22.1-Białowieża with a topographic base map by © OpenStreetMap contributors 2022 and © Copernicus Urban Atlas 2012 land use and land cover data. Distributed under a Creative Commons BY-SA License.

Figure 6.2 presents the modeled inner-city domain together with the locations for the measurement stations. More details on the measurement stations from the air quality monitoring network (Hamburger Luftmessnetz, 2022) are found in Chapter 6.1.7.

6.1.3 TAPM and weather mast

The city-specific meteorological fields are based on the coupled meteorological and chemical model TAPM (The Air Pollution Model), developed by the Commonwealth Scientific and Industrial Research Organization (CSIRO, Hurley, 2008; Hurley et al., 2005). The predicted three-dimensional meteorology is based on a non-hydrostatic, incompressible and primitive equation model. It includes a terrain-following vertical coordinate for three-dimensional simulations.

TAPM solves the momentum equations for horizontal wind components and the incompressible continuity equation for the vertical wind component. It also solves the scalar equation for potential virtual temperature and specific humidity, cloud water and ice, rain water and snow (Hurley, 2008).

At the surface a vegetative canopy, soil scheme and urban scheme are used. Radiative fluxes are included.

In this study, the synoptic scale data for outer domain forcing are 3-hourly synoptic-scale reanalysis ensemble means from the European Centre for Medium-Range Weather Forecasts from the fifth generation (ECMWF ERA5). They are given on a longitude-latitude grid at 0.3° grid spacing.

By a multiple one-way nesting procedure, the meteorological reanalysis data are downscaled. Four nesting steps allow the calculation of meteorological data in a resolution of 250 m (Table 6.1).

Land cover is classified according to the Corine Land Cover database (Copernicus Land Monitoring Service, 2018). Terrain height is gathered from the Digital Elevation Model over Europe (EU-DEM) (EEA, 2017).

The TAPM wind speed and wind direction are compared against data from the Hamburg weather mast (ICDC, 2022). The weather mast was not exactly inside the investigation area (Fig. 6.2); therefore, the closest model position at the edge (MET) is taken for comparisons. Figure 6.3 presents comparisons for wind speed (v_{wind}) and wind direction (dd) for January and August, which show an overall good agreement. The mean modeled wind speed is 3.71 m s^{-1} and 2.58 m s^{-1} in January and August, respectively. The mean observed wind speed is 3.43 and 2.70 m s^{-1} in January and August, respectively.

See Appendix C.1 for the complete statistical comparison based on statistical indicators of Chapter 6.1.8.

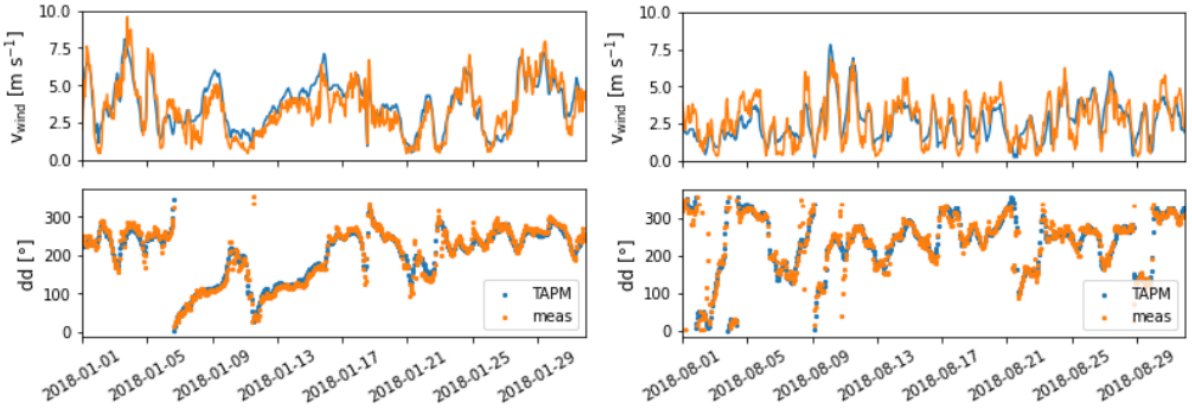

Figure 6.3: Comparison of wind speed (v_{wind}) in 10 m height and wind direction (dd) in 280 m height from TAPM and the measurement data from Hamburg weather mast in January (left) and August (right).

6.1.4 Background concentrations

Regional background concentrations were gathered from two sources.

The primary source are measurements at the station Waldhof, which is part of the European Monitoring and Evaluation Programme (EMEP, 2022). Data are stored in the EBAS database (EBAS, 2022), developed and operated by the Norwegian Institute for Air Research (NILU). Waldhof is located just a few hundred meters from the state border with Saxony-Anhalt in the east of the Lüneburg Heath in Lower Saxony. Air masses are representative for background pollution of the northern Germany plains (Umweltbundesamt, 2022).

Most important pollutant concentrations like those from NO_2, O_3 and PM species were gathered from Waldhof data. Since some trace substances are not measured at the station but can be added into the EPISODE-CityChem EmChem09-mod chemical scheme, additional data were collected from a study of Matthias et al. (2021). They calculated regional air pollutant concentrations with the Community Multiscale Air Quality Modeling System CMAQ for the year 2020. Since this is a different year than the one investigated in this study (2018), only mean monthly concentrations from Matthias et al. (2021) at the location of Waldhof were used to represent general seasonal differences, e.g., for carbon monoxide (CO) concentrations. A complete list of included background concentration pollutants and their source is given in Table 6.2.

The model input are hourly background concentrations, evenly distributed for the whole domain.

Table 6.2: Overview of background concentration substances and their sources, included in the EPISODE-CityChem modeling run.

Substance	Source
O_3	Waldhof measurement
NO_2	Waldhof measurement
H_2O_2 (hydrogen peroxide)	CMAQ
N_2O_5 (dinitrogen pentoxide)	CMAQ
HNO_3 (nitric acid)	Waldhof measurement
HONO (nitrous acid)	CMAQ
SO_2	Waldhof measurement
Sulphate (H_2SO_4)	CMAQ
CO	CMAQ
C_2H_6 (ethane)	Waldhof measurement
HCHO (formaldehyde)	CMAQ
CH_3CHO	CMAQ
C_2H_4 (ethene)	Waldhof measurement
nC_4H_{10} (butane and 2-methylbutane)	Waldhof measurement
$CH_3COC_2H_5$ (ethyl acetate)	CMAQ
o-xylene	Waldhof measurement
isoprene	Waldhof measurement
$PM_{2.5}$	Waldhof measurement
PM_{10}	Waldhof measurement

6.1.5 Ship emission data

Ship emissions are calculated with the recently developed modular ship emission modeling system (MoSES, Schwarzkopf et al., 2021).

It is a bottom-up model for ship emissions that can create temporally and spatially high-resolved emission inventories. The emission calculation is based on information about the ship (e.g., ship type, fuel type, engine power) that is gathered from the IHS Markit 2020 ship database. Navigational information such as speed and location as well as ship identification data are transferred as AIS data and used in an hourly resolution in this study. MoSES enables differentiation between the use of main and auxiliary engines; the latter is important for berthing ships.

AIS data in this study were collected by the European Maritime Safety Agency (EMSA) and acquired from the Federal Maritime and Hydrographic Agency of Germany (BSH) for the months January and August 2018.

Emission data are updated hourly based on the AIS track of all individual ships in the model domain. Figure 6.4 presents the number of ships within the model domain in January and August per hour (ship density). Higher ship numbers in August can be attributed to passenger-related ships and pleasure craft, as many ships stay inside the domain at night and leave it during daytime.

Emission factors are substance-specific. For example, NO_x emission factors depend on IMO MEPC Tier regulations for nitrogen oxides (MEPC, 2008; Smith et al., 2015), the fuel type and engine characteristics. The emission is then calculated as a mass of pollutant (m_p) as product of emission factor EF in [g kW h^{-1}] and energy consumption E in [kW h^{-1}].

$$m_p = EF \cdot E \tag{6.2}$$

The created pollutant-specific hourly emission data from CO, non-methane volatile organic compounds (NMVOC), NO_x, $PM_{2.5}$ and SO_2 were used as input in the EPISODE-CityChem calculations. A NO_x split of 95% NO to 5% was applied, according to the guideline from the International Council on Combustion Engines (CIMAC, 2008).

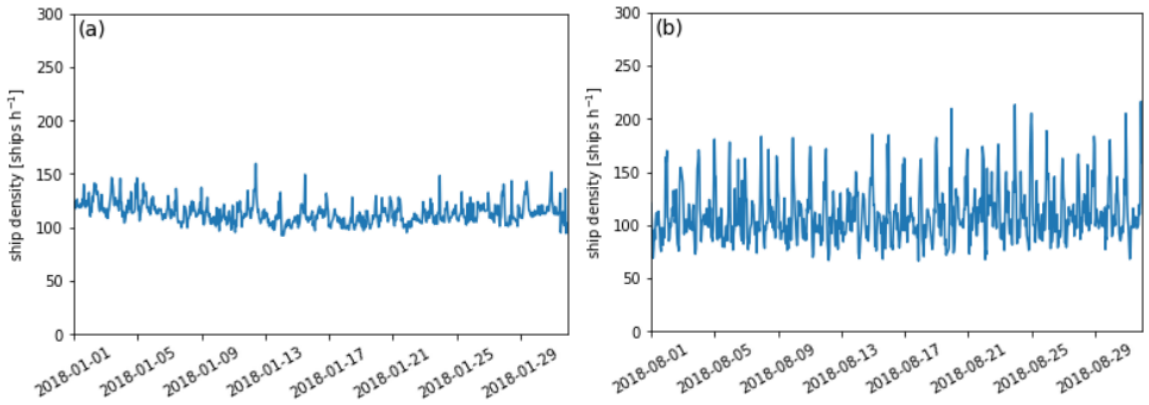

Figure 6.4: Ship density in the investigated domain (Fig. 6.2) in (a) January and (b) August 2018.The ship density for all ships is calculated based on AIS data and considers the time each ship actually spends in the harbor.

The modular and flexible nature of MoSES allows the extraction and compilation of ship characteristics of the vessels identified in the processed data. Missing data is thereby estimated by implemented methods. For this work the ship height is an important input factor for calculating the shape parameter λ_2 for the Expgauss vertical emission distribution function (Eq. 6.2).

From the IHS database, the ship height, i.e., the effective height of the ship over the sea surface can be derived by subtracting the draught (d) from the keel-to-mast height.

$$h_{ship} = h_{keel\text{-}to\text{-}mast} - d \quad (6.3)$$

However, since these information are only available for approximately 34% of the ships in the domain, parameterization formulae have been derived to approximate the ship height based on only the keel-to-mast height, the length and/or width of the ship (Appendix C.2). After applying these parameterizations for the missing ships, the coverage of available ship heights reached 91%. Since EPISODE-CityChem treats all ships with the same height, the mean height of this dataset was calculated. A value of 25 m was derived (Table 6.1).

6.1.6 Land-based emissions

To account for industrial **point sources** a dataset from the Behörde für Umwelt, Klima, Energie und Agrarwirtschaft (BUKEA), formerly known as Behörde für Umwelt und Energie (BUE) was used (BUE, 2017). This data accounts mainly for facilities subject to mandatory permission under the 11th Bundes-Immissionsschutzverordnung (BImSchV) reported in the year 2016 in Hamburg. Besides exact locations, the applied dataset contains information about annual emission totals for different pollutants and several stack parameters (stack height, exit velocity and temperature) for each of the 746 reported stacks. In addition, we included emissions from road traffic of the highway in the Elbe Tunnel, which are routed to the surface via two central ventilation systems,

in the inventory of point sources and removed them from the inventory of line sources accordingly.

To account for **road traffic emissions**, a bottom-up road traffic emission inventory for the city of Hamburg was applied. The bottom-up approach is based on daily traffic densities for the main road network (13270 road segments) in Hamburg in the year 2018 provided by the Behörde für Verkehr und Mobilitätswende Hamburg (BVM). In combination with fleet characteristics for Hamburg and the most recent version of the Handbook For Emission Factors for street traffic (HBEFA 4.1) (Umweltbundesamt, 2019) road segment specific traffic annual emissions for different pollutants were calculated, based on the results of Wagner (2022). The updates of this database covers e.g., more different traffic situations, a better calculation of catalysts, temperature corrections for emissions depending on outside temperature, inclusion of aging effects and an updated database of registered vehicles.

An NO:NO_2 split of 70:30 was applied, according to Karl et al., (2019b), accounting for high ratios from diesel passenger cars (Carslaw and Rhys-Tyler, 2012; Grice et al., 2009).

Land-based **area emissions** for commercial and industrial combustion processes, domestic heating, agriculture, waste and solvent emissions are preprocessed with the UrbEm framework, which is a hybrid method to derive high-resolved emissions for city-scale air quality modeling studies (Ramacher et al., 2021). An exception in the industrial sector are sources that have been classified as point sources (see above). In the UrbEm framework regional-scale area emissions of the CAMS 2016 REG-AP v3.1 regional emission inventory (Granier et al., 2019; Kuenen et al., 2022) are downscaled to the urban-scale domain definition in this study under application of sector-specific proxies, given in Ramacher et al. (2021).

6.1.7 Measurement stations

Modeled concentrations for NO, NO_2 and O_3 are compared against measurements from stations of the air quality measurement network (Hamburger Luftmessnetz, 2022). Table 6.3 gives a general overview on the stations (e.g., station type and measured pollutants) and Figure 6.2 shows their positions on the map of inner-city Hamburg.

The stations Altona-Elbhang, Finkenwerder-West and Kleiner Grasbrook are located close to the river Elbe and are therefore affected by ship emissions. However, Finkenwerder-West and Kleiner Grasbrook are near the model boundaries and cannot account accurately for other sources from outside of the modeled domain. Therefore, the evaluation is mainly based on Altona-Elbhang.

The station Sternschanze is an urban background station and the only one available for model-measurement comparisons of O_3.

Finally, the stations Max-Brauer-Allee II and Stresemannstraße are classified as traffic stations and allow a comparison of traffic effects on urban NO_x concentrations with ship effects.

Table 6.3: Overview of the measurement stations in the modeled Hamburg inner-city domain.

Station name	Short	Coordinates (UTM 32)	Measurement height above ground	Station type	Measured pollutants (selection)
Altona-Elbhang	80KT	562611 E, 5933342 N	3.50 m	background, shipping	SO_2, NO, NO_2, PM_{10}
Finkenwerder-West	72FI	555949 E, 5932255 N	3.50 m	background, shipping	NO, NO_2, PM_{10}
Kleiner Grasbrook	82HF	565068 E, 5931587 N	3.50 m	background, shipping	SO_2, NO, NO_2
Sternschanze	13ST	564134 E, 5935504 N	3.50 m	background	SO_2, NO, NO_2, O_3, PM_{10}, $PM_{2.5}$
Max-Brauer-Allee II	70MB	562473 E, 5934507 N	4.00 m	traffic	NO, NO_2, PM_{10}
Stresemann-straße	17SM	563414 E, 5935091 N	4.00 m	traffic	NO, NO_2, PM_{10}

6.1.8 Statistical indicators

Different statistical indicators are applied to evaluate the model performance against measurements.

The bias describes the difference between mean model $\overline{M}$ and mean observation $\overline{O}$ data.

$$\mathrm{Bias} = \overline{M} - \overline{O} \tag{6.4}$$

A positive bias corresponds to a model overestimation and a negative value to an underestimation.

The normalized mean bias (NMB) describes the ratio of over- or underestimation. It is presented as a relative value in this work.

$$\mathrm{NMB} = \frac{\overline{M} - \overline{O}}{\overline{O}} \cdot 100\% \tag{6.5}$$

The root mean square error (RMSE) combines the magnitudes of the errors in model predictions for various times into one single measure.

$$\mathrm{RMSE} = \sqrt{\frac{1}{N}\sum_{i=1}^{N}(M_i - O_i)^2} \tag{6.6}$$

The subscript i indicates the time step and N the total number of time steps, e.g., 744 (31 days × 24 hours) for hourly resolution of a complete dataset in January or August.

The standard deviation for model (STD_m) and observation (STD_o) is calculated as:

$$\mathrm{STD_M} = \sqrt{\frac{1}{\mathrm{N}-1}\sum_{\mathrm{i}=1}^{\mathrm{N}}(\mathrm{M_i}-\overline{\mathrm{M}})^2} \tag{6.7}$$

$$\mathrm{STD_O} = \sqrt{\frac{1}{\mathrm{N}-1}\sum_{\mathrm{i}=1}^{\mathrm{N}}(\mathrm{O_i}-\overline{\mathrm{O}})^2} \tag{6.8}$$

The index of agreement (IOA) is calculated following the refined definition by Willmott et al. (2012) as:

$$\mathrm{IOA} = \begin{cases} 1-\frac{\sum_{\mathrm{i}=1}^{\mathrm{N}}|\mathrm{M_i}-\mathrm{O_i}|}{2\sum_{\mathrm{i}=1}^{\mathrm{N}}|\mathrm{O_i}-\overline{\mathrm{O}}|}, \mathrm{if}\sum_{\mathrm{i}=1}^{\mathrm{N}}|\mathrm{M_i}-\mathrm{O_i}| \le 2\sum_{\mathrm{i}=1}^{\mathrm{N}}|\mathrm{O_i}-\overline{\mathrm{O}}| \\ \frac{2\sum_{\mathrm{i}=1}^{\mathrm{N}}|\mathrm{O_i}-\overline{\mathrm{O}}|}{\sum_{\mathrm{i}=1}^{\mathrm{N}}|\mathrm{M_i}-\mathrm{O_i}|}-1, \mathrm{if}\sum_{\mathrm{i}=1}^{\mathrm{N}}|\mathrm{M_i}-\mathrm{O_i}| > 2\sum_{\mathrm{i}=1}^{\mathrm{N}}|\mathrm{O_i}-\overline{\mathrm{O}}| \end{cases} \tag{6.9}$$

It ranges between -1 and 1, where 1 indicates an ideal model to measurement agreement. Exemplary, a value of 0.5 indicates that the sum of error-magnitudes is half the sum of the perfect-model-deviation and observed-deviation magnitudes and a value of -0.5 indicates that the sum of the error-magnitudes is twice the sum of the perfect-model-deviation and observed-deviation magnitudes. Values close to -1 can mean that the estimated deviations about $\bar{O}$ are poor estimates of the observed deviations or that there is little variability in the observation.

The Pearson correlation coefficient R for the temporal correlation is defined as:

$$\mathrm{R} = \frac{\sum_{\mathrm{i}=1}^{\mathrm{N}}(\mathrm{O_i}-\overline{\mathrm{O}})\cdot(\mathrm{M_i}-\overline{\mathrm{M}})}{\sqrt{\sum_{\mathrm{i}=1}^{\mathrm{N}}(\mathrm{O_i}-\overline{\mathrm{O}})^2\cdot\sum_{\mathrm{i}=1}^{\mathrm{N}}(\mathrm{M_i}-\overline{\mathrm{M}})^2}} \tag{6.10}$$

Finally, the fraction of modeled values within a factor of 2 to the observed values (FAC2) is defined as proportion of values inside:

$$\mathrm{FAC2} = \frac{1}{\mathrm{N}}\sum_{\mathrm{i}=1}^{\mathrm{N}}\mathrm{n_i}\ \mathrm{with}\begin{cases}\mathrm{n_i}=1, \mathrm{if}\ 0.5 \le \frac{\mathrm{M_i}}{\mathrm{O_i}} \le 2.0 \\ \mathrm{n_i}=0, \mathrm{else}\end{cases}, \tag{6.11}$$

where N is the total number of model-measurement couples.

Hanna and Chang (2012) consider a FAC2 ≥ 0.3 an acceptable value for modeled concentrations in urban areas.

6.2 Results and discussion

6.2.1 Sectorial emission contribution

Figure 6.5 presents the modeled NO and NO_2 emissions based for the major source sectors in January and August in the defined domain. NO emissions are dominated by the shipping and traffic sectors, which are in a comparable range between 30% and 50%. Large industrial point sources account for approximately 10% of NO emissions in the domain.

For NO_2 traffic emissions are the dominant source (primary emission), accounting for approximately 70−80% of emissions. This is caused by the different NO:NO_2 emission split for ships and traffic sector (95:5 for ships and 70:30 for traffic).

A seasonal difference can be seen for all sectors and both NO and NO_2. January NO and NO_2 emission were higher for domestic heating and point sources, probably caused by a larger energy consumption due to heating. The higher emissions for shipping may be caused by a different fleet composition (e.g., a larger proportion of container vessels). For the traffic sector, slightly larger emissions were found for August, which might be caused by more and longer activities during the daytime and holiday traffic.

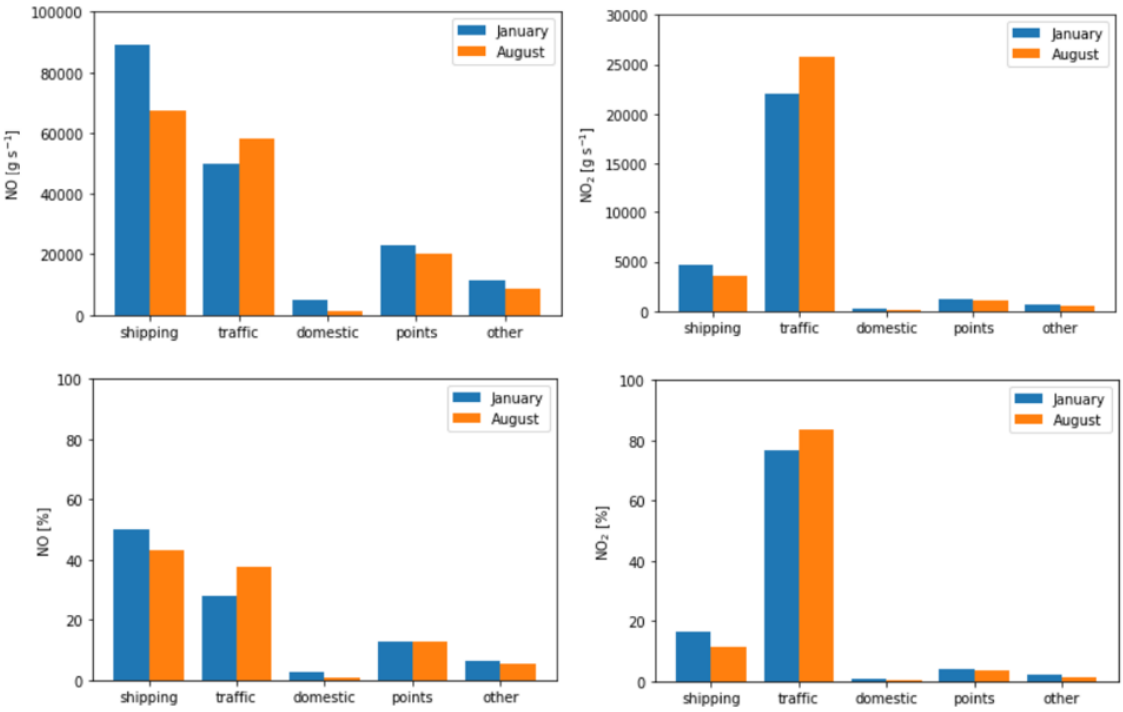

Figure 6.5: Sectorial emission contribution in the whole model domain for January and August 2018 and pollutants NO (left) and NO_2 (right). Absolute (upper) and relative (lower) emissions are shown.

6.2.2 Flexplume versus Fixplume

For modeled NO concentrations compared to measured concentrations, almost all statistical parameters show improvements for the new Flexplume algorithm compared to the Fixplume, both on an hourly and daily scale. An exception are model results in January at the station Grasbrook, which will be discussed below. A comprehensive overview of the comparison is given in the Tables C.2 to C.7 in the Appendix.

The largest improvement is found at the stations Altona-Elbhang and Finkenwerder West as expected since they are closest to the river Elbe and not dominated by traffic emissions. Figure 6.6 presents the corresponding time series for Altona-Elbhang, based on **daily trimmed mean values**. Trimmed means that only values from percentile 10 to percentile 90 (i.e., 20 hours per day) are used for the calculation of daily means to reduce the effect of outliers that cannot be captured by the model. Outliers may be caused by local activity, e.g., people smoking close to the instruments or short-time construction works nearby. Trimming was done for both measured and modeled values to maintain consistency and work with the same amount of data.

For hourly data in January, the bias in Altona-Elbhang is reduced from 11.35 µg m^{-3} to 1.57 µg m^{-3} compared to the Fixplume (Table C.2). The RMSE improves from 45.34 µg m^{-3} to 19.99 µg m^{-3}. The correlation coefficient R increases from 0.76 to 0.86 (based on daily trimmed mean data). In August, the NO model performance is lower, but still an improvement can be seen when comparing Flexplume to Fixplume. The bias is reduced from 13.36 µg m^{-3} to 6.89 µg m^{-3} (hourly data). However, correlation does not show a significant improvement in Altona-Elbhang in August and lies at approximately R = 0.45 (daily trimmed mean).

The station Grasbrook shows a stronger NO underestimation in January caused by the Flexplume compared to the Fixplume (bias of -8.99 µg m^3 and -1.53 µg m^{-3}, respectively). Yet, regression and RMSE slightly improve in January. In August, the results improve (e.g., bias of 0.07 µg m^{-3} in Flexplume compared to 12.65 µg m^{-3} for the Fixplume). The reason for the lower performance of the Flexplume algorithm in NO in January at the station Grasbrook is probably caused by nearby industrial activities will be discussed in Chapter 6.2.3.

For NO_2 in January, the Flexplume algorithm shows an overall worse statistical agreement with measurements compared to the Fixplume assumption. However, the positive change in bias and negative impact on regression bias are small. The highest additional absolute bias is ~3.0 µg m^{-3} more compared to the Fixplume in Finkenwerder-West (from -3.3 to -6.14 with hourly data). The strongest loss in correlation is -0.03 points, also in Finkenwerder West (from 0.89 to 0.86 based on daily trimmed mean data). In August, NO_2 model results improve statistically. The bias from Altona-Elbhang is reduced from 5.81 µg m^{-3} to 3.05 µg m^{-3} for the Flexplume algorithm.

Overall the positive effect for NO modeling outweigh the loss in model performance for NO_2 in January.

The improvements are generally best in Finkenwerder West, although these data must be viewed with caution, as the station lies at the western edge of the model domain and does not receive effects of local pollution for winds from the western sector.

Other stations show only slight differences, as they are not strongly affected by ship plumes. Therefore, in case of O_3, no clear statistical differences can be derived by comparing the two plume approaches with measurements at the O_3 measurement station Sternschanze (Fig. 6.6e and f).

The differences of Flexplume and Fixplume algorithms are clearly located in the harbor area (Fig. 6.7). For NO the highest differences between the algorithms occur close to the shipping lanes and at the shipping terminals, since NO is quickly oxidized. For NO_2 and O_3, the differences occur more evenly distributed over the whole harbor area.

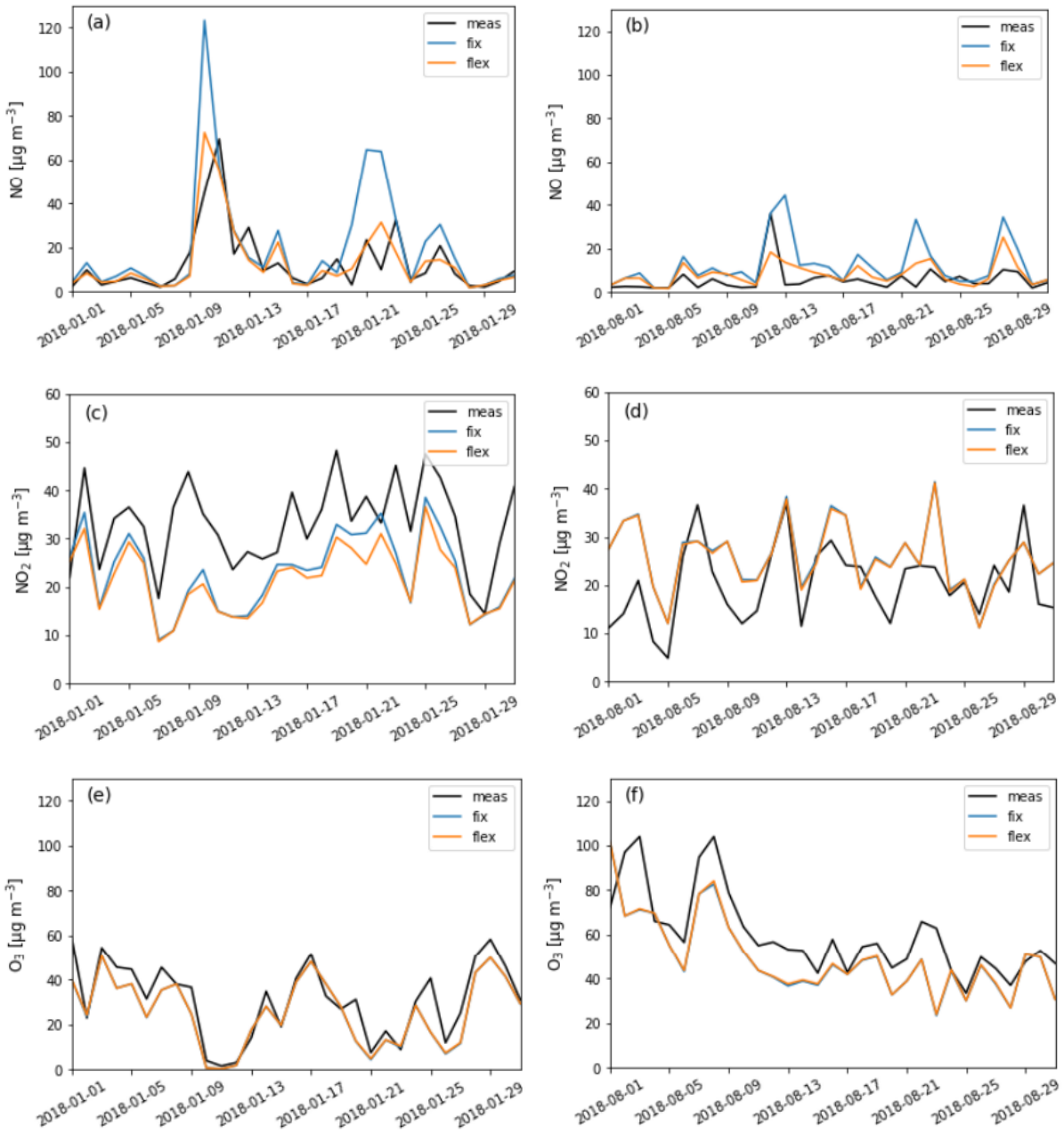

Figure 6.6: Time series (daily, trimmed mean) for the station Altona-Elbhang (NO, NO_2) and Sternschanze (O_3) in January (left) and August (right) 2018. Comparison of measurements with the Fixplume and Flexplume model algorithm for ship emissions.

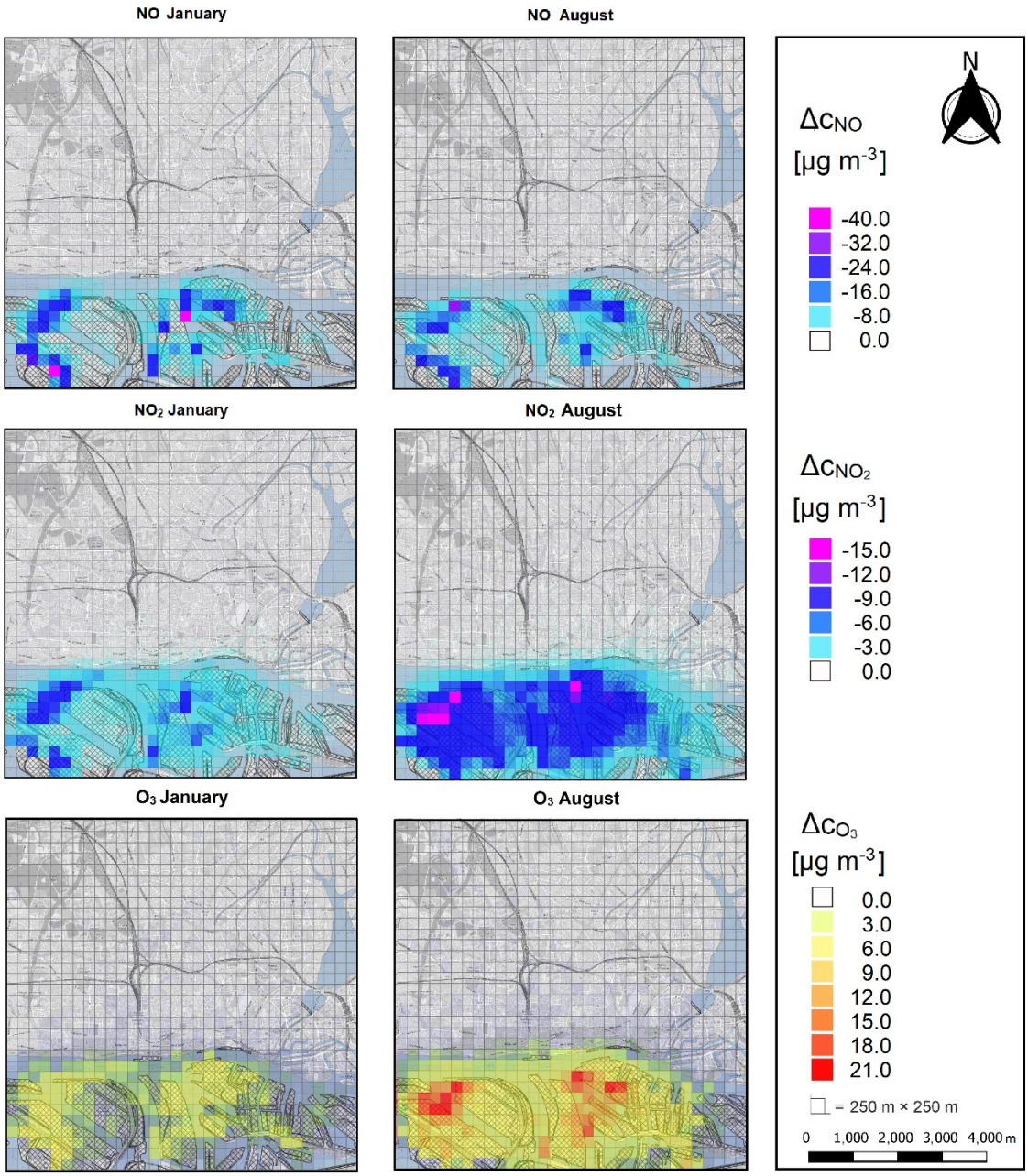

Figure 6.7: Concentration maps of the investigated domain showing the difference of the Flexplume approach to the Fixplume ($\Delta c = c_{Flex} - c_{Fix}$) for mean monthly concentrations of NO, NO_2 and O_3. Maps were created using © QGIS-Version 3.22.1-Białowieża with a topographic base map by © OpenStreetMap contributors 2022 and © Copernicus Urban Atlas 2012 land use and land cover data. Distributed under a Creative Commons BY-SA License.

6.2.3 Effect of wind direction

In the following section, wind direction effects are analyzed based on the Flexplume setup results. The sectors NE, SE, SW and NW cover the wind directions 0−89°, 90−179°, 180−269° and 270−359°, respectively.

In January, the main wind sector was southwest with 51.1% of the time followed by southeast and northwest. Wind from northeast occurred only 6.8% of the time (see Fig. 6.8).

In August the main wind sector was southwest with 40.0% of the time followed closely by northwest with 37.5%. The rarest wind sector was also northeast with 5.1% relative occurrence.

An overview on the model performance based on the modeled bias is presented in Fig. 6.9 for the Flexplume approach and in Fig. C.2 in the Appendix for the Fixplume approach. A comprehensive statistical overview of the comparison of different wind sector effects given in the Tables C.2 to C.7 in the Appendix.

For NO modeling at **Altona-Elbhang (80 KT)** the best results compared to measurement data were found for wind conditions from the southwest sector (e.g., bias -0.07 µg m^{-3} in January and 2.38 µg m^{-3} in August). In comparison, the lowest model performance at this station were found for winds from the northeast sector with biases of 7.82 µg m^{-3} in January and a large bias of 47.18 µg m^{-3} in August.

NO_2 results show the best performance for winds from the northeast sector (bias: -8.64 µg m^{-3}) in January and from the southeast (0.35 µg m^{-3}) and southwest (-0.35 µg m^{-3}) in August. The largest biases occurred from the southeast sector in January (-11.95 µg m^{-3}) and from the northeast sector in August (15.21 µg m^{-3}).

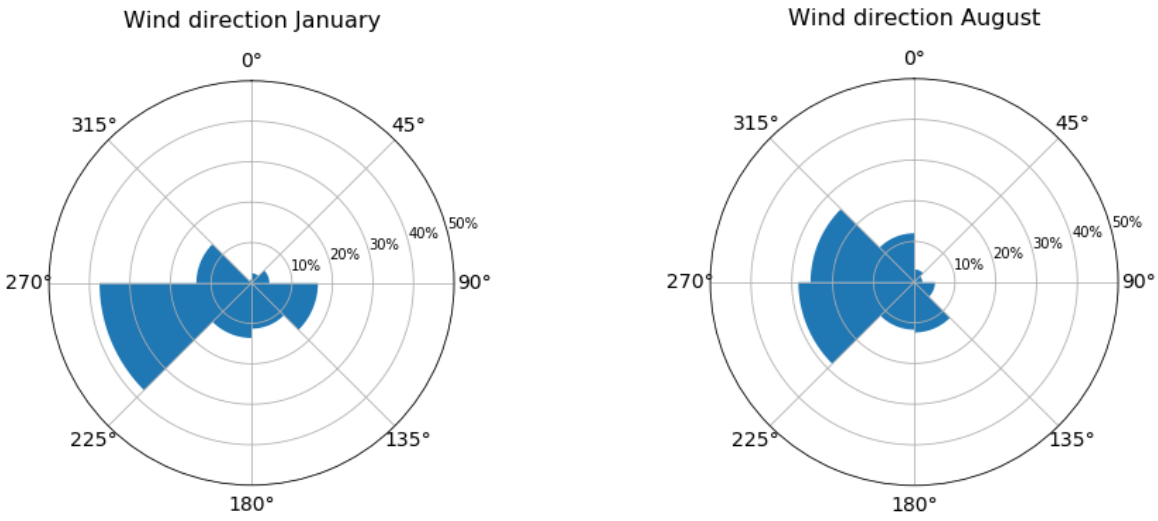

Figure 6.8: Windroses of measured wind directions in Hamburg in January and August 2018 at 280 m height.

Notably, northeast conditions showed the best regression results for NO_2 (R = 0.72 in January and 0.52 in August).

Since the station Altona-Elbhang lies close to the Elbe at the northern shore, good performance for winds from the southern sectors are attributed to good representation of shipping emissions in this study. Air masses from the northwest represent mainly urban background conditions, which are also well represented. The larger errors from the northeast sector are attributed to strong traffic emissions. The low model performance can also be attributed to the low occurrence of winds from this sector (Fig. 6.8). In this way, few very strong peaks can raise the model error very high.

The NO model results for **Finkenwerder West (72 FI)** show best performance for wind from the northwest and southwest sector, e.g., a regression of R = 0.76 from NW and bias of -0.76 µg m^{-3} from SW in January. The January results are statistically closer to the measurements than the August results. All August NO regressions are below R = 0.2. The bias is also particularly high with values of 32.02 µg m^{-3} from the southeast sector for August results.

NO_2 modeling shows generally better results than NO at the station Finkenwerder-West. Again, better results are found for winds from the westerly sectors, e.g., a bias of only 1.98 µg m^{-3} for winds from the northwest sector in August.

Due to the station Finkenwerder-West being located at the western border of the model, the model results does only take background concentrations into account for winds from the western sector and statistical results should be viewed with caution. Notably, this produces good statistical agreements, probably because there are no large anthropogenic sources west of Finkenwerder-West and, therefore, the background concentrations deliver sufficient results. Winds from the northeast are affected by ship plumes and inner-city traffic and heating emission. The same arguments as for the station Altona-Elbhang apply for winds from northeast. Winds from southeast are especially affected by near industrial emissions that are not ideally represented in this study.

At the station **Kleiner Grasbrook (82 HF)**, the best model results for NO and NO_2 were found for winds from the northwest sector, i.e., from which most effect of ship emission on this station is to be expected. The bias of NO for the Flexplume assumption from the northwest sector in January reads -5.82 µg m^{-3} compared to a bias of 12.03 µg m^{-3} for the Fixplume. The Flexplume approach delivers larger errors from the southern wind directions compared to the Fixplume approach (e.g., a bias of -8.33 µg m^{-3} compared to -0.62 µg m^{-3} for Flexplume and Fixplume, respectively, from the southwestern sector). However, it is very likely that the good results from the Fixplume at this station are not caused by a specifically good ship plume representation. It is rather assumed that overestimations of shipping emissions are outweighing underestimations of other sectors at this location. The station Grasbrook lies in the southeastern part of the investigation domain. There is a large industry located south of this station, e.g., the power plant Moorburg, which was still active in 2018. Large parts of this industrial activity in southern Hamburg are not accounted for in the small

inner-city model domain (boundary conditions cover only the background atmosphere in this study); however, they have probably reached station Grasbrook. This is indicated by the fact that underestimations in NO occurred mainly in winter, when industrial and heating emissions were stronger. It is therefore still assumed that the Flexplume approach delivers an improved representation for the shipping sector at this station.

The urban background station **Sternschanze (13 ST)** is the only available station inside the model domain that measures O_3, next to NO_x.

For NO modeling, similarly good statistical results are found for winds from the sectors northwest, southwest and southeast both in January and August. Again, the January simulation shows better statistical agreement than the August simulation with bias values as low as 0.15 µg m^{-3} and regressions up to R = 0.64. Winds from the northeast show again lowest model performances for NO modeling.

NO_2 concentrations are slightly underestimated in January and overestimated in August. In January, statistical indicators show similar good performances for all wind sectors (e.g., biases as low as -6.84 µg m^{-3}), while in August there are clearly better results from the southwest sector and lower performance from the northeast sector. Notably, the absolute biases in August are lower than in January for southern sectors.

Ozone is underestimated by the model. The underestimation lies in a similar range for all sectors in January (biases around -5.0 µg m^{-3}), while in August, a lower performance is found for the northeast sector (bias of -21.63 µg m^{-3}). Regressions are generally very good, notably for the often critical northeast sector, where R reach up to 0.92 in January and 0.82 in August. Also notably, winds from the southwest sector show poorest performance in January, but best in August.

The urban background influence is found for all sectors at the station Sternschanze. Overall, winds from southeast show the best performance, since there are no larger street sources in this sector. Winds from the western sector might bring larger traffic emissions from the street “Ring 2”. For the northeast sector, the same arguments can be made as for the previous stations.

The NO model results at the traffic station **Max-Brauer-Allee II (70 MB)** show overestimations both in January and August. January estimates are better with the best overall statistical agreement for winds from the southeast sector (e.g., correlation of 0.8 and bias of 14.18 µg m^{-3}). In January, largest model overestimations occur for conditions from the northwest sector and in August form the northeast. Biases can be very large for model results for winds from the northeast sector in August (83.56 µg m^{-3}).

For NO_2 an overall good model performance was found for all sectors. Largest biases were again found for winds from the northeast in August. However, biases were much lower than for NO, since NO_2 distributes further away from the sources and is stronger affected by background conditions. Best overall NO_2 model statistics for this station are found for winds from the southwest sector.

The street Max-Brauer-Allee II runs from southwest to northeast, causing wind channeling along this axis and potentially additional concentration accumulation from the traffic. Winds from southeast represent rather urban background pollution, which show better statistical agreement.

At the second traffic station **Stresemannstraße (17 SM),** some different model results are observed compared to Max-Brauer-Allee II. NO is underestimated for winds from eastern sectors and overestimated for winds from western sectors. The absolute bias is lower than in Max-Brauer-Allee II and occurs also from wind from the northwest sector (17.87 µg m^{-3}). Correlation coefficients are ≥ 0.5 for all wind directions and best from northeast wind (0.70). In August, model results show only overestimations. These are larger than in January, but not as large as in Max-Brauer-Allee II. Again, wind conditions from northeast causes high biases. However, regression is notably good for this wind sector (R = 0.71). Winds from the southeast sector deliver the best statistical agreements for NO in August at this station.

NO_2 is underestimated in January for all wind directions, but the biases are comparatively low (up to -12.05 µg m^{-3}). Best model performance is found for winds from the southwest sector, similar to Max-Brauer-Allee II. Regression is overall good (up to 0.76). In August, best model statistic is found for the southwest sector and worst for the northeast sector. The model overestimates, except for winds from the southeast sector, similarly as to Max-Brauer-Allee II. The absolute biases are much lower than for NO.

The measurement station Stresemannstraße lies close to the Bundesstraße 4, which runs from northwest to southeast. In the southwest sector, urban background air dominates, which is modeled appropriately. Overall, traffic emissions show a good regression, which means that they follow diurnal patterns correctly. The amount of emission and ratio of NO to NO_2 for traffic emission could be adjusted in a future study.

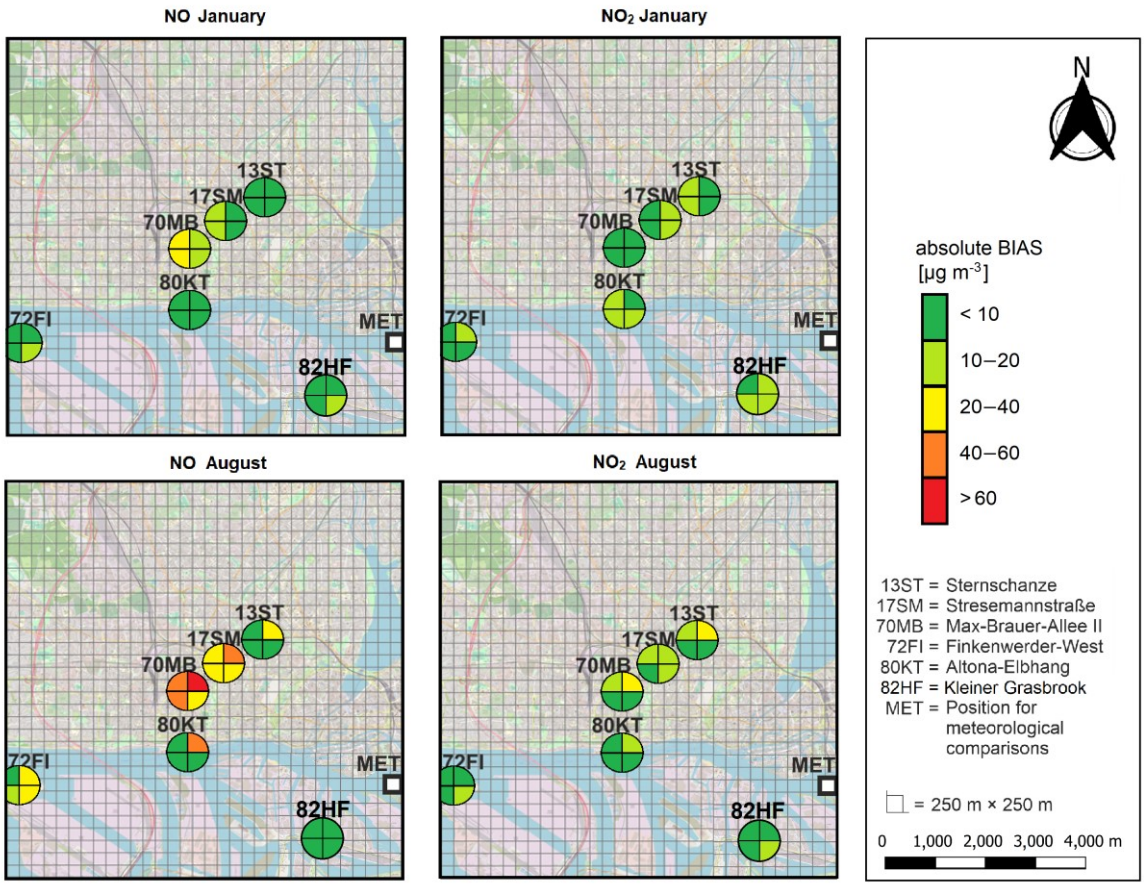

Figure 6.9: Overview on the EPISODE-CityChem performance (bias) in NO_2 and NO depending on the wind sector in January and August based on the Flexplume approach. Maps were created using © QGIS-Version 3.22.1-Białowieża with a topographic base map by © OpenStreetMap contributors 2022 and © Copernicus Urban Atlas 2012 land use and land cover data. Distributed under a Creative Commons BY-SA License.

6.2.4 Comparison with similar studies

Statistical results of this study were compared against previous model calculations with EPISODE-CityChem from Ramacher et al. (2019) and Ramacher et al. (2021).

Ramacher et al. (2019) investigated the ship emission impact in three Baltic Sea cities, Rostock (Germany), Riga (Latvia) and Gdánsk-Gdynia (Poland) for 2012. They simulated NO_2, O_3 and PM concentrations to study the population exposure.

Ramacher et al. (2021) presented the new downscaling approach for gridded emission inventories (UrbEm), which is based on regional anthropogenic emissions from the Copernicus Atmospheric Monitoring Service (CAMS), that are disaggregated based on proxies for the European area (such as population data, Urban Atlas 2012, Corine and OpenStreetMap) and compared it to a CAMS no proxy approach (= uniform spatial disaggregation of the original annual emission rates). They simulated NO_2 in Hamburg and Athens. This study compares the statistical indicators of their Hamburg data from the year 2012 to the presented data herein.

An overview on the compared statistical indicators is given in Tables 6.4 to 6.6.

For **NO_2 in urban background stations** (Altona-Elbhang, Finkenwerder-West, Grasbrook and Sternschanze), mean observed and modeled data are in a similar order of magnitude compared to Ramacher et al. (2019, 2021) (Table 6.4). The NMB in this study shows a significantly larger range, reaching up to +36% overestimation, while in the compared studies mainly underestimations were found. This might be due to the fact that compared studies averaged over the whole year, while in this study only two months were investigated. The overestimation occurred in August, while in January, the concentrations were underestimated in this study as well. Overestimations of this study were even larger for the Fixplume assumption (up to +75%, not shown here), indicating that the Flexplume reduced this error significantly. Another reason for the deviations from the UrbEm results from Ramacher et al. (2021) might be the different ship emission algorithm that have been applied. Ramacher et al. (2021) used global shipping lanes from CAMS-REG, taking AIS ship movement information into account (Jalkanen et al., 2016), on a bigger domain, but with a coarser grid resolution (1 km²) and by applying a fixed vertical ship emission distribution. They also used hourly changing CAMS background concentrations, while this study relies mainly on Waldhof measurement data. This study also found comparatively good correlation up to 0.72 and a good range of FAC2 values of 0.55−0.69.

Table 6.4: Comparison of hourly mean NO_2 concentrations at urban background statistics with similar studies.

	This study (Flexplume) Hamburg	Ramacher et al. (2019) Rostock, Riga and Gdánsk-Gdynia	Ramacher et al. (2021) CAMS no proxy Hamburg	Ramacher et al. (2021) UrbEm Hamburg
$Mean_{model}$ [µg m^{-3}]	12.50 − 28.55	10.14 − 32.50	14.37	19.95
$Mean_{obs}$ [µg m^{-3}]	16.31 − 33.00	13.75 − 34.18	21.57	21.57
NMB [%]	-44 − +36	-31.95 − +4.36	-33	-12
RMSE [µg m^{-3}]	11.11 − 20.77	14.13 − 21.86	15.05	15.44
STD_{model} [µg m^{-3}]	9.37 − 23.78	10.53 − 20.61	11.18	16.10
STD_{obs} [µg m^{-3}]	12.35 − 17.13	11.09 − 20.75	15.23	15.23
IOA [-]	0.37 − 0.58	0.45 − 0.67	0.55	0.54
R [-]	0.22 − 0.72	0.23 − 0.46	0.39	0.43
FAC2 [-]	0.55 − 0.69	0.36 − 0.74	0.59	0.64

For **NO_2 at traffic stations** (Max-Brauer-Allee II, Stresemannstraße), mean observed and modeled data are best comparable to the UrbEm approach from Ramacher et al. (2021), which is expected, because the underlying data is most similar (Table 6.5).

Again, the NMB shows noticeably low values, even with overestimations, mainly in some cases in August. Another good performance is seen in the low RMSE values and the high FAC2 ratios reaching up to 0.89. The same argumentation as for NO_2 at background stations can be applied, although at traffic stations, the effect of the Flexplume algorithm in comparison to the Fixplume algorithm is negligible.

Table 6.5: Comparison of hourly mean NO_2 concentrations at urban traffic stations with similar studies.

	This study (Flexplume) Hamburg	Ramacher et al. (2019) Rostock, Riga and Gdánsk-Gdynia	Ramacher et al. (2021) CAMS no proxy Hamburg	Ramacher et al. (2021) UrbEm Hamburg
$Mean_{model}$ [µg m^{-3}]	29.48 − 52.7	14.12 − 20.52	15.50	33.82
$Mean_{obs}$ [µg m^{-3}]	37.66 − 44.33	32.26 − 44.06	54.38	54.38
NMB [%]	-22 − 19	-53 − -60	-71	-38
RMSE [µg m^{-3}]	15.67 − 26.6	25.12 − 35.38	47.43	32.71
STD_{model} [µg m^{-3}]	17.59 − 27.07	11.37 − 19.10	11.15	20.82
STD_{obs} [µg m^{-3}]	16.26 − 23.30	17.42 − 26.59	27.88	27.88
IOA [-]	0.43 − 0.59	0.53 − 0.55	0.11	0.41
R [-]	0.48 − 0.75	0.32 − 0.50	0.26	0.41
FAC2 [-]	0.79 − 0.89	0.19 − 0.35	0.19	0.58

Table 6.6: Comparison of hourly mean and 8-hour moving average O_3 concentrations at urban background stations with similar studies.

	This study Flexplume Hamburg	This study Flexplume Hamburg	Ramacher et al. (2019) Rostock, Riga and Gdánsk-Gdynia
Statistical measure	Hourly mean	8-hour moving average	8-hour moving average
$Mean_{model}$ [µg m^{-3}]	25.72 − 48.63	25.50 − 48.80	27.72 − 46.14
$Mean_{obs}$ [µg m^{-3}]	31.25 − 59.42	30.94 − 59.60	41.66 − 53.17
NMB [%]	-18	-18	-12 − -33
RMSE [µg m^{-3}]	12.49 − 25.68	9.96 − 20.58	25.58 − 28.48
STD_{model} [µg m^{-3}]	18.52 − 35.18	17.24 − 29.22	16.58 − 22.31
STD_{obs} [µg m^{-3}]	21.10 − 31.70	19.49 − 27.60	20.59 − 24.53
IOA [-]	0.58 − 0.74	0.62 − 0.77	0.52 − 0.67
R [-]	0.76 − 0.85	0.81 − 0.90	0.20 − 0.45
FAC2 [-]	0.68 − 0.71	0.76 − 0.82	0.53 − 0.72

Finally, for **urban background O_3 concentration**, a comparison with results from Ramacher et al. (2019) is possible. Since Ramacher et al. (2019) based their results on 8-hour moving averages for the mean O_3 concentrations, this measure was also added here. The moving average is calculated for a value at time t based on the mean of this value and the seven previous hours.

The resulting statistical indicators are in a similar range (Table 6.6). Notably, the correlation for O_3 reaches up to 0.9 in our study, indicating that the measured Waldhof O_3 concentrations are very suitable as boundary conditions for this study.

6.3 Conclusion

This study presented the results of the newly developed Flexplume approach for the ship emission distribution in the inner city of Hamburg, Germany. Ship emissions were vertically distributed according to the exponentially modified Gaussian profile. The shape of the distribution function depends on local wind speed and stability.

This approach was compared against a static approach for emissions (Fixplume), which distributes emissions evenly into the lowest four model layers, and against measurements.

Results were presented in a complex chemistry transport modeling study with the EPISODE-CityChem model system, including the effects of realistic meteorology, other sources like traffic and industry, background chemistry and chemical transformations. Contrary to the previous studies, this setup also includes emission data for a complete fleet of ships that were present in the Hamburg harbor area based on AIS information calculated with the MoSES system (Schwarzkopf et al., 2021). An average ship height of 25 m was derived and implemented into the Expgauss profile function.

Two months of model results were presented, January and August, 2018.

The results show that ship emissions are the dominant source of NO (up to 50%) in the inner city of Hamburg and the second strongest source of NO_2 (up to 18%). Shipping emissions were around 5-10% higher in winter than in summer, which may have been caused by the different fleet composition (more container vessels) in winter.

The Flexplume distribution showed an improved model accuracy, especially for NO close to the shipping lanes. The model bias was reduced by up to ~10 µg m^{-3} NO based on hourly data. The modeled NO_2 concentrations showed slightly lower statistical accuracy with the new Flexplume approach in January, but better results in August. The model results also indicate that the effect of the new Flexplume approach mainly affects the harbor area and approximately 2 km around it. Due to the lower modeled NO concentrations, the modeled O_3 concentrations are up to 20 µg m^{-3} higher in the harbor area than with the Fixplume approach.

The model improvement for shipping emissions was further shown by analyzing model biases depending on the wind direction, showing that for most measurement stations the modeled bias in NO and NO_2 now lies below 10 µg m^{-3} when the wind transported air from the harbor area to the measurement instrument. This often delivered better results than from other sectors (e.g., when the wind blows from traffic or industrial areas).

Finally, a comparison with similar studies of Ramacher et al. (2019, 2021) showed that the model results in this setup delivered comparable results for NO_2 and good results for O_3, indicating that the Flexplume approach overall preserved the modeling accuracy for NO_2 and O_3 while improving it for NO.

The results of this study have strong implications on the chemical feedback and a high relevance for compliance with air quality regulations. This will be examined in the final chapter of this thesis.

7 Overarching conclusions and outlook

This final chapter shall answer the initial questions raised in Chapter 1.4 and give some concluding remarks from the author as well as an outlook on future challenges of ship plume modeling.

Chapter 7.1 will examine the shipping effect on various pollutant concentrations in the inner-city of Hamburg. It also includes an investigation of the main chemical reactions that are affected by ship emissions. Chapter 7.2 will provide insights into the relevance of the herein modeled ship emissions for air quality regulations. Finally, Chapter 7.3 will conclude the benefits of this work and discuss remaining sources of uncertainties.

7.1 Shipping effect on the pollutant concentration and chemical feedback

The contribution of shipping emissions to the total modeled concentration of air pollutants was determined based on the zero-out method, i.e., the difference between model runs including all emissions (= with ships) and runs without ship emissions.

Figure 7.1 presents concentration maps of the effect of ship emissions on the concentrations of NO, NO_2 and O_3 in the investigated domain as monthly mean differences in each grid cell ($\Delta c = \bar{c}_{\text{with ships}} - \bar{c}_{\text{without ships}}$). Calculations with ships are based on the Flexplume approach.

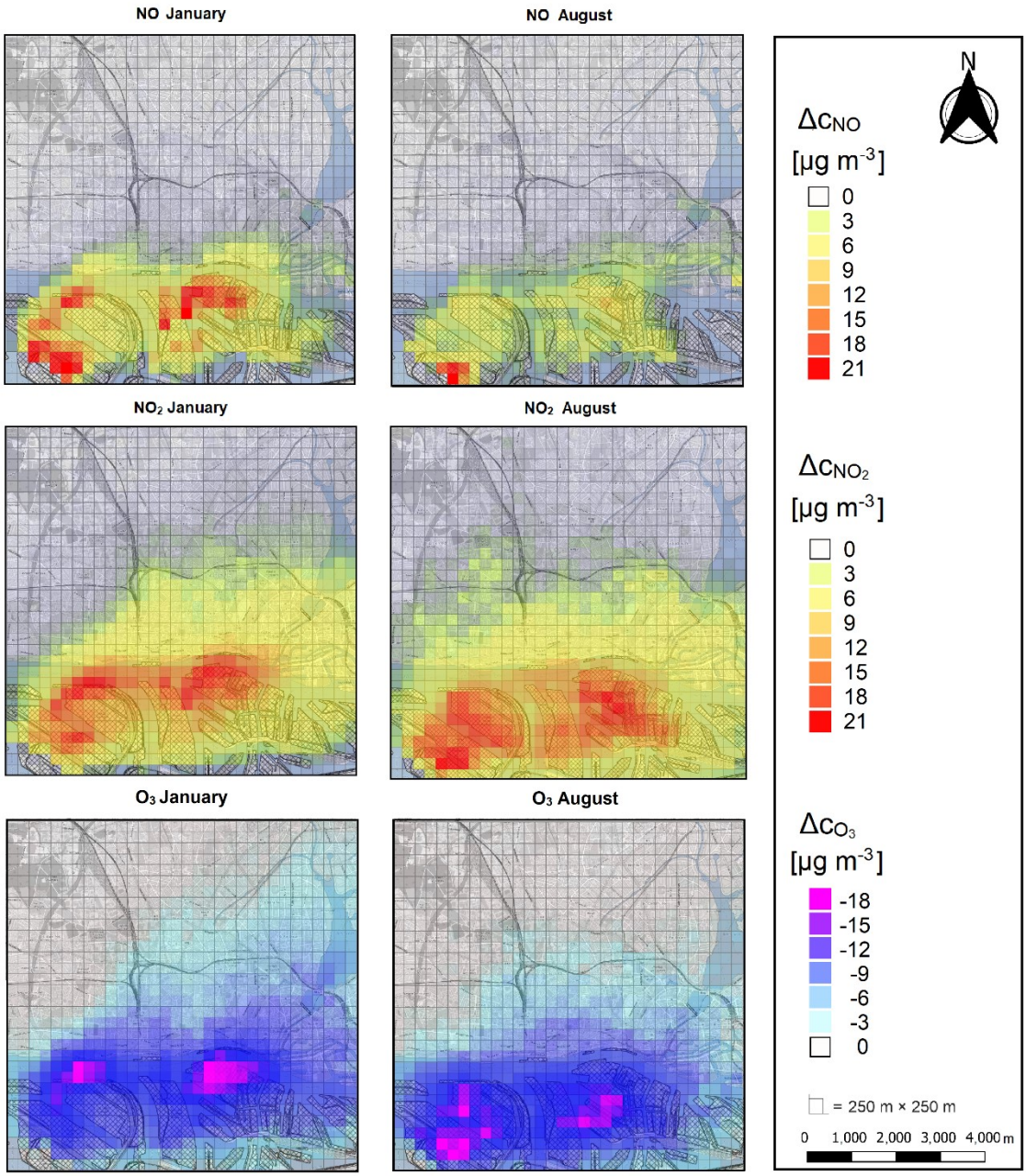

Figure 7.1: Concentration maps of the investigated domain showing the effect of ship emissions on mean monthly concentrations of NO, NO_2 and O_3 based on a difference to the situation without ships. Maps were created using © QGIS-Version 3.22.1-Białowieża with a topographic base map by © OpenStreetMap contributors 2022 and © Copernicus Urban Atlas 2012 land use and land cover data. Distributed under a Creative Commons BY-SA License.

Monthly mean NO concentrations show differences up to 30 µg m^{-3} in January and 24 µg m^{-3} in August. The highest values occur very close to the source, e.g., at the ship terminals, since NO quickly reacts with available O_3 to form NO_2 (Eq. 2.14).

Table 7.1: Overview on shipping effect on mean monthly concentration of various chemical substances, modeled for the position of Altona-Elbhang. Absolute ship effect is calculated as $\Delta c = \bar{c}_{\text{with ships}} - \bar{c}_{\text{without ships}}$, and relative ship effect is calculated as $c_{\text{rel}} = (\bar{c}_{\text{with ships}} - \bar{c}_{\text{without ships}})/\bar{c}_{\text{without ships}} \cdot 100\%$. EX corresponds to factor 10^X.

Substance	Month	$\bar{c}_{\text{with ships}}$	$\bar{c}_{\text{without ships}}$	Δc	c_{rel}
NO	January	14.6	7.0	7.6	109%
[µg m^{-3}]	August	12.4	5.8	6.6	114%
NO_2	January	21.8	12.3	9.5	77%
[µg m^{-3}]	August	27.7	19.2	8.5	44%
O_3	January	23.0	32.1	-9.1	-28%
[µg m^{-3}]	August	46.4	54.7	-8.7	-16%
N_2O_5	January	0.040	0.050	-0.010	-20%
[µg m^{-3}]	August	0.015	0.022	-0.007	-32%
SO_2	January	2.0	1.6	0.4	25%
[µg m^{-3}]	August	1.4	1.1	0.3	27%
CO	January	135.6	134.9	0.7	0.5%
[µg m^{-3}]	August	92.0	91.4	0.6	0.7%
HONO	January	0.11	0.09	0.02	22%
[µg m^{-3}]	August	0.46	0.34	0.12	35%
CH_3CHO	January	0.12	0.10	0.02	20%
[µg m^{-3}]	August	0.47	0.45	0.02	4%
C_3H_6	January	0.20	0.15	0.05	33%
[µg m^{-3}]	August	0.20	0.15	0.05	33%
CH_3O_2	January	2.2E3	5.0E3	-2.8E3	-56%
[molecules cm^{-3}]	August	2.2E5	4.2E5	-2.0E5	-48%
NO_3	January	1.0E6	1.8E6	-0.8E6	-44%
[molecules cm^{-3}]	August	3.9E6	5.5E6	-1.6E6	-29%
OH	January	1.5E4	2.3E4	-7.7E3	-33%
[molecules cm^{-3}]	August	2.3E6	2.7E6	-3.9E5	-14%
HO_2	January	3.8E4	9.2E4	-5.3E4	-58%
[molecules cm^{-3}]	August	3.9E6	7.5E6	-3.6E6	-47%

NO_2 concentrations show differences up to 15 and 19 µg m^{-3} in January and August, respectively. O_3 shows a maximum in decrease of -18 µg m^{-3} both in January and August. High differences are not as localized as for NO concentration, but reach further into the city center.

To gain a deeper insight into the chemical mechanisms that are affected by ship emissions, the following discussion is based on daily mean values at the station Altona-Elbhang, i.e. the reference station close to the harbor. Results are based on a comparison between calculations with ships (using the Flexplume approach) and without ships (Table 7.1).

The ship emission contribution to mean daily **NO concentration** is 7.0 µg m^{-3} and 5.8 µg m^{-3} in January and August, respectively. This is an increase of 109−114%

compared to a situation without ships. The main contribution is from direct NO emission by ships, which form 95% of their total NO_x emission. Another source for NO concentrations is NO_2 photolysis during daytime (Eq. 2.15), which also intensifies due to direct ship emission of NO_2. A sink for NO is the oxidation with HO_2, CH_3O_2 or other peroxy radicals to form NO_2 (Eq. 2.20).

Mean daily **NO_2 concentration** contribution by ships is 9.5 µg m^{-3} and 8.5 µg m^{-3} for January and August, respectively, which corresponds to an increase of 77% and 44%, respectively. The main reaction for increased NO_2 by ship emissions are the production from NO and O_3 (Eq. 2.14), as well as reactions of NO with peroxy radicals like HO_2 and CH_3O_2 (Eq. 2.20). The higher modeled NO_2 concentration in summer is not caused by higher ship emissions, but rather by the higher emissions from the traffic sector (Fig. 6.5). The seasonal difference in mean concentrations might also be caused by the underestimation of NO_2 concentrations in winter, which may be caused by uncertain numbers for NO_2 emissions from domestic or industrial heating in winter.

O_3 concentrations are reduced by reaction with NO emissions by ships. In January and August the mean reduction due to ship emissions on a daily basis is -9.1 µg m^{-3} and -8.7 µg m^{-3}, respectively. This corresponds to -28% in January and -16% in August compared to a situation without ships. Similar to NO_2 the relative effect of ships is larger in January. The effect of the direct NO emission from ships on O_3 concentration is similar in both months, as emissions of NO are also very similar. During daytime, O_3 can be photolyzed (Eq. 2.18), which is an important sink reaction. However, this is part of the photostationary equilibrium, which means, that O_3 is also formed by reaction of atomic oxygen $O(^3P)$ with O_2 (Eq. 2.16). Based on the photostationary state relationship (Eq. 2.17), background O_3 concentrations directly depend on the photolysis rate coefficient J_{NO2}, which is much higher in summer (monthly mean of ~0.0025 s^{-1}) than winter (~0.0002 s^{-1}) due to stronger radiation. In this study, the cloud cover fraction was also found to be higher in January than in August, reducing the available radiation in winter and, following this, the mean O_3 concentration, further (see Appendix D). Therefore, a stronger relative reduction of O_3 due to ships in winter is caused by the lower background O_3 concentrations in winter (Fig. 6.6e and f). The fact that no O_3 increase was detected has to do with urban areas typically being VOC-limited. In a NO_x-limited regime, adding NO_x by ships could cause an additional production of O_3.

N_2O_5 is a product of nighttime chemistry and results from oxidation of NO_2 to NO_3 and further reaction of NO_2 with NO_3 (Eq. 2.24 and 2.25). These three nitrogen species remain in a dynamic equilibrium at night. During day, NO_3 is quickly destroyed by photolysis (Eq. 2.26). Since nights are shorter during summer, less N_2O_5 is created. Shipping emissions reduce the formation of N_2O_5 by reducing the available O_3 that is necessary to oxidize NO_2 to NO_3.

The substances SO_2, CO, formaldehyde (HONO), acetaldehyde (CH_3CHO) and propene (C_3H_6) are directly emitted from ships. The relative increase in concentration in the harbor area varies strongly for the individual substances. Most notably, SO_2, HONO and C_3H_6 concentrations increase by around 20−30% compared to the simulation without ships. The concentration increase of CO is below 1%. The main

sources of CO are emissions from vehicles and incomplete combustion processes (Fenger, 1999) and these clearly dominate over emissions from ships in the city. Acetaldehyde are an intermediate product in respiration of higher plants and, therefore, part of the natural occurring VOCs (Fidler, 1968; Luecken et al., 2012). Higher plant activity in summer cause the seasonal differences.

Shipping emissions also affect the local radical concentrations. OH, HO_2, CH_3O_2 and NO_3 are all reduced by various reactions with directly emitted NO, NO_2, CO and VOCs or secondary effects due to decreased O_3 concentrations (Fig. 2.4).

A complete overview on the daily mean concentration of the different chemical substances and various meteorological parameters is given in the Appendix D.

7.2 Ship emission relevance for air quality regulations

The relevant EU and WHO guideline values for urban air pollutants have been presented in Chapter 1.3 and Table 1.1. With the results of this work, the number of exceedances of these values can be calculated. Based on comparisons with the zero-out method, it is also possible to estimate to which degree a reduction or elimination of ship emissions can help to keep air quality below threshold values.

This work focuses on the exceedance of NO_2 and O_3 guideline values at the station Altona-Elbhang.

For NO_2, the EU limit value for 24-hour mean concentrations is 200 µg m^{-3}, that shall not be exceeded more than 18 times per year. The corresponding WHO recommendation is 25 µg m^{-3}.

The EU limit value is never exceeded at the station Altona-Elbhang and daily mean NO_2 concentrations stay below 50 µg m^{-3} both in January and August. This is probably because Altona-Elbhang is not strongly affected by traffic emissions. However, the WHO recommendation value is often exceeded (Table 7.2).

Results from Table 7.2 show that in January, the number of exceedances lies significantly lower for modeled values than for measured values. In August, the model performance is better. Reasons for the underestimation in January are not caused by inaccurate ship emission estimations, since the underestimation occurs also at the station Sternschanze, which is barely affected by ship emissions. The underestimation may be caused by uncertain numbers for NO_2 emissions from domestic or industrial heating in winter.

Since the WHO recommendation value lies in the same order of magnitude as the modeled RMSE values (7.26−13.12 µg m^{-3} for daily mean NO_2), it is very difficult to predict the exact number of WHO recommendation value exceedances with the current model accuracy. Nevertheless, model calculations with the zero-out method indicate the strong potential of reducing the number of exceedances when eliminating NO_x emissions from ships. The number of exceedances reduces by 12 days (August) to up to 25 days (without considering the modeling bias in January). When considering the modeling bias in January, exceedances might reduce by at least around 11−14 days.

Table 7.2: Monthly mean NO_2 concentrations and number of exceedances for WHO recommendations (24-hour mean NO_2 ≤ 25 µg m^{-3}) at the station Altona-Elbhang.

	Monthly mean concentration [µg m^{-3}]		**Number of exceedances**	
Month	January	August	January	August
Measurement	33.0	25.5	25	16
Fixplume	23.1	30.6	14	22
Flexplume	21.6	27.9	11	18
No ships	12.2	19.3	0	4

For O_3, the EU guidelines state that a maximum 8-hour daily mean value of 120 µg m^{-3} shall not be exceeded on more than 25 days per year as a mean over 3 years. For the WHO recommendation, the value is 100 µg m^{-3} and the number of exceedances shall not be larger than 4 days per year.

The maximum 8-hour daily mean value is calculated as following: First, an 8-hr moving average is calculated for a value at time t based on the mean of this value and the seven previous hours. From this smoothed hourly time series the daily maximum value is selected.

Resulting values lie below 100 µg m^{-3} for the entire January, when photochemical background ozone production is low. Some exceedances occur in August and are presented in Table 7.3 for Altona-Elbhang. No measurement values are given, since O_3 is only measured at the station Sternschanze. There, model results show slight underestimations of ~5−10 µg m^{-3} (see Fig. 6.6f).

Independent of the selected ship emission distribution, the model values give the same number of exceedances in August: 1 regarding the EU guideline value and 7 for the WHO recommendation. For the latter it shows that the maximum of 4 allowed exceedances for the whole year is already exceeded in one single month of the summer. Moreover, the exclusion of ship emissions would lead to a further increase in O_3 exceedance number, caused by the reduced O_3 destruction by NO titration (Eq. 2.14). From these model results, it can be concluded that ships cause a reduction of O_3 concentrations of approximately 20% in August.

In a VOC-limited regime like inner-city Hamburg, a reduction in NO_x emission always leads to an additional production of O_3 (see Fig. 2.5). To achieve a reduction in both NO_2 and O_3 it would be also necessary to reduce urban VOC concentrations.

These urban VOCs occur both from natural as well as from anthropogenic sources. Examples for naturally occurring VOCs are isoprene, methanol and ethanol that are produced by plants (Lewis et al., 2000; Simpson and Volosciuk, 2019). Acetylene, propane, butane and ethene are examples for mainly anthropogenic emissions. Their main sources are traffic, industry, solvents and waste burning. Although the use of catalytic converters has reduced their emission significantly during the last decades (Parrish et al., 2016), a further reduction can be reached by switching to more electro mobility (in both the traffic and the shipping sector). This could finally lead to a more efficient reduction of both NO_x and O_3.

Table 7.3: Monthly mean and maximum concentrations of O_3 (after applying an 8 hour moving average) and number of exceedances for the EU limit value (120 µg m^{-3}) and the WHO recommendations (100 µg m^{-3}) at the station Altona-Elbhang.

	Monthly mean concentration [µg m^{-3}]	Monthly max concentration [µg m^{-3}]	Number of exceedances	
			EU limit	WHO recommendation
Fixplume	42.8	121.9	1	7
Flexplume	45.3	123.8	1	7
No ships	53.7	144.2	4	9

7.3 Concluding remarks and outlook

This work represents a comprehensive, coherent study aiming to improve the representation of ship emissions on the small-scale: from a single ship to an urban center. Based on the results from MITRAS, a new detailed representation of microscale effects like plume rise and turbulent downward dispersion in the urban-scale model EPISODE-CityChem was achieved. The new Flexplume approach is capable of calculating variable ship emission profiles depending on the local meteorological situation. This allows for an improved representation of ship emissions close to the ship, especially for nitrogen monoxide. With the model setup, it was possible to investigate the impact of ship emissions on the urban atmospheric chemistry and for air quality regulations. The derived parameterizations for downward dispersion and vertical emission profiles can be applied to any Eulerian grid model in any harbor city, but also be used for investigating effects of single ships on the local pollutant situation. This works especially well when it is combined with the results of the modular ship emission modeling system MoSES, developed by Daniel Schwarzkopf, a partner in the ShipCHEM project.

Despite all the advances made in this and other works in recent years, there are still many challenges in improving ship emissions modeling and remaining sources of uncertainties.

One problem in the small-scale studies is the resolution. It is often very difficult to combine input data of different resolutions into a working model setup. For example, the results of Chapter 5 allowed for a city-scale modeling at a horizontal resolution of 100 m × 100 m. This was possible with the static meteorological preprocessor MCWIND. The more realistic TAPM meteorology used in Chapter 6 could only be resolved on a 250 m × 250 m without implementing an additional interpolation scheme.

Similar problems occur for the temporal resolution, e.g., for emission sources that are only given as yearly totals downscaled to mean hourly values. This is a problem of e.g., traffic emissions, which could be improved by using actual real-time road intensities. In case of ship emissions, the use of AIS data improved their spatial and temporal representation. However, an uncertainty due to missing ship characteristic data introduces additional approximations for the emission totals. It is therefore important to collect more data on ship engines, height and stack properties to better represent

emissions based on individual ships. A future task on this could be the introduction of different ship types (e.g., container ships, cruise ships and ferries) into the EPISODE-CityChem modeling system to account even better for the effect of different ship shapes and sizes on the vertical emission distribution.

The introduced Gaussian, SCE and Expgauss parameterization covers typical meteorological conditions occurring in northern Europe. They might need to be adjusted when used in other regions like the Mediterranean area.

It will also be important to adjust emissions based on new fuels (e.g., LNG, ammonia, or hybrid approaches) in future studies.

Finally, I would like to give an outlook on my personal future plans regarding ship emission modeling.

As already mentioned in Chapter 5.5, an improved representation of the actual movement of ships could be achieved by combining results of this work with the moving point source approach from Pan et al. (2021). This is planned for the near future.

The results of this work showed, that ship emissions mainly cause ozone loss in urban areas. However, in rural areas they can act as ozone source (e.g., Huszar et al., 2010). A study on the German coast of the Baltic Sea is planned to investigate the transition of ozone sink and ozone source regions for ship emissions in the context of stricter ozone target concentrations from WHO.

One important pollutant that has not been evaluated in this work is particulate matter. From an air pollutant perspective, the formation of ultrafine particles and secondary aerosols are of high concern. Future studies on this topic are planned, based on the community aerosols dynamic model MAFOR (Karl et al., 2022). The aim of this work is the short-time forecast of ship plume particle events as part of the Dtec-LUKAS project.

References

Abrutytė, E., Žukauskaitė, A., Mickevičienė, R., Zabukas, V., and Paulauskienė, T.: Evaluation of NO_x emission and dispersion from marine ships in Klaipeda Sea port, J. Environ. Eng. Landsc., 22, 264–273, https://doi.org/10.3846/16486897.2014.892009, 2014.

Affad, E., Saadeddine, S., Assou, M. and Sbaibi, A.: Effect of the relative humidity on an industrial plume behavior, Glob. NEST J., 8(3), 297–305, https://doi.org/10.30955/gnj.000294, 2006.

Aksoyoglu, S., Baltensperger, U., and Prévôt, A. S. H.: Contribution of ship emissions to the concentration and deposition of air pollutants in Europe, Atmos. Chem. Phys., 16, 1895–1906, https://doi.org/10.5194/acp-16-1895-2016, 2016.

Anderson, J. O., Thundiyil, J. G., and Stolbach, A.: Clearing the air: A review of the effects of particulate matter air pollution on human health, J. Med. Toxicol., 8, 166−175, https://doi.org/10.1007/s13181-011-0203-1, 2012.

Andersson, C., Bergström, R., and Johansson, C.: Population exposure and mortality due to regional background PM in Europe - Long-term simulations of source region and shipping contributions, Atmos. Environ., 43, 3614–3620, https://doi.org/10.1016/j.atmosenv.2009.03.040, 2009.

Arakawa, A. and Vivian, R. L.: Computational design of the basic dynamical processes of the UCLA general circulation model, Method. Comput. Phys., 17, 173–265, 1977.

Aulinger, A., Matthias, V., Zeretzke, M., Bieser, J., Quante, M. and Backes, A.: The impact of shipping emissions on air pollution in the Greater North Sea region - Part 1: Current emissions and concentrations, Atmos. Chem. Phys. Discuss., 15(8), 11277–11323, https://doi.org/10.5194/acpd-15-11277-2015, 2016.

Badeke, R., Matthias, V., and Grawe, D.: Parameterizing the vertical downward dispersion of ship exhaust gas in the near field, Atmos. Chem. Phys., 21, 5935–5951, https://doi.org/10.5194/acp-21-5935-2021, 2021.

Badeke, R., Matthias, V., Karl, M., and Grawe, D.: Effects of vertical ship exhaust plume distributions on urban pollutant concentration – a sensitivity study with MITRAS v2.0 and EPISODE-CityChem v1.4, Geosci. Model Dev. 4077–4103, https://doi.org/10.5194/gmd-15-4077-2022, 2022.

Bai, S., Wen, Y., He, L., Liu, Y., Zhang, Y., Yu, Q., and Ma, W.: Single-vessel plume dispersion simulation: Method and a case study using CALPUFF in the Yantian port area, Shenzhen (China). Int. J. Environ. Res. Pub. He., 17, 7831, https://doi.org/10.3390/ijerph17217831, 2020.

Barnes, M. J., Brade, T. K., MacKenzie, A. R., Whyatt, J. D., Carruthers, D. J., Stocker, J., Cai, X., and Hewitt, C. N.: Spatially-varying surface roughness and ground-level

air quality in an operational dispersion model, Environ. Pollut., 185, 44–51, https://doi.org/10.1016/j.envpol.2013.09.039, 2014.

Barregard, L., Molnár, P., Jonson, J. E. and Stockfelt, L.: Impact on population health of baltic shipping emissions, Int. J. Environ. Res. Public Health, 16(11), https://doi.org/10.3390/ijerph16111954, 2019.

Basu, S., and Lacser, A.: A cautionary note on the use of Monin-Obukhov similarity theory in very high-resolution Large-Eddy-Simulations, Bound.-Lay. Meteorol., 163, 351–355, https://doi.org/10.1007/s10546-016-0225-y, 2017.

Bieser, J., Aulinger, A., Matthias, V., Quante, M., and van der Gon, H. A. C. D.: Vertical emission profiles for Europe based on plume rise calculations, Environ. Pollut., 159, 2935–2946, https://doi.org/10.1016/j.envpol.2011.04.030, 2011.

Bluett, J., Gimson, N., Fisher, G., Heydenrych, C., Freeman, T., and Godfrey, J.: Good practice guide for atmospheric dispersion modelling, Ministry for the Environment, Wellington, New Zealand, ISBN: 0478189419, 2004.

Bott, A.: A positive definite advection scheme obtained by nonlinear renormalization of the advective fluxes, Mon. Weather Rev., 117, 1006–1016, https://doi.org/10.1175/1520-0493(1989)117<1006:APDASO>2.0.CO;2, 1989.

Bott, A.: Monotone flux limitation in the area-preserving flux-form advection algorithm, Mon. Weather Rev., 120, 2592–2602, https://doi.org/10.1175/1520-0493(1992)120<2592:MFLITA>2.0.CO;2, 1992.

Bott, A.: The monotone area-preserving flux-form advection algorithm: Reducing the time-splitting error in two-dimensional flow fields, Mon. Weather Rev., 121, https://doi.org/10.1175/1520-0493(1993)121<2637:TMAPFF>2.0.CO;2, 2638–2641, 1993.

Brandt, J., Silver, J. D., Christensen, J. H., Andersen, M. S., Bønløkke, J. H., Sigsgaard, T., Geels, C., Gross, A., Hansen, A. B., Hansen, K. M., Hedegaard, G. B., Kaas, E., and Frohn, L. M.: Assessment of past, present and future health-cost externalities of air pollution in Europe and the contribution from international ship traffic using the EVA model system. Atmos. Chem. Phys., 13, 7747–7764, https://doi.org/10.5194/acp-13-7747-2013, 2013.

Briggs, G.: Plume rise predictions, Plume rise predictions, in: Lectures on air pollution and environmental impact analyses, American Meteorological Society, Boston, MA, https://doi.org/10.1007/978-1-935704-23-2_3, 1982.

Briscolini, M., and Santangelo, P.: Development of the mask method for incompressible unsteady flows, J. Comput. Phys., 84, 57–75, https://doi.org/10.1016/0021-9991(89)90181-2, 1989.

Britter, R. and Hanna, S.: Flow and dispersion in urban areas, Annu. Rev. Fluid Mech., 35, 469–496, https://doi.org/10.1146/annurev.fluid.35.101101.161147, 2003.

Broome, R. A., Cope, M. E., Goldsworthy, B., Goldsworthy, L., Emmerson, K., Jegasothy, E., and Morgan, G. G.: The mortality effect of ship-related fine particulate

matter in the Sydney greater metropolitan region of NSW, Australia, Environ. Int., 87, 85–93, https://doi.org/10.1016/j.envint.2015.11.012, 2016.

Brunner, D., Kuhlmann, G., Marshall, J., Clément, V., Fuhrer, O., Broquet, G., Löscher, A., and Meijer, Y.: Accounting for the vertical distribution of emissions in atmospheric CO_2 simulations, Atmos. Chem. Phys., 19, 4541–4559, https://doi.org/10.5194/acp-19-4541-2019, 2019.

BUE: Luftreinhalteplan für Hamburg (2. Fortschreibung), https://www.hamburg.de/contentblob/9024022/7dde37bb04244521442fab91910fa39c/data/d-lrp-2017.pdf, (last access: 21 May 2022), 2017.

Byrnes, T. A., and Dunn, R. J. K.: Boating- and shipping-related environmental impacts and example management measures: A review, J. Mar. Sci. Eng., 8(11), 908, https://doi.org/10.3390/jmse8110908, 2020.

Byun, D. W., Young, J., Pleim, J., Odman, M. T., and Alapaty, K.: Numerical transport algorithms for the community multiscale air quality (CMAQ) chemical transport model in generalized coordinates, in: Science Algorithms of the EPA Models-3 Community Multiscale Air Quality (CMAQ) Modeling System, edited by: Byun, D. W. and Ching, J. K. S., National Exposure Research Laboratory, U.S. EPA, Research Triangle Park, NC, Chap. 7, EPA/600/R-99/030, https://nepis.epa.gov/Exe/ZyPDF.cgi?Dockey=30003R9Y.PDF (last access: 24 May 2022), 1999.

Capaldo, K., Corbett, J. J., Kasibhatla, P., Fischbeck, P., and Pandis, S. N.: Effects of ship emissions on sulphur cycling and radiative climate forcing over the ocean, Nature, 400, 743–746, https://doi.org/10.1038/23438, 1999.

Carruthers, D.: Atmospheric dispersion and air pollution meteorology, in: Handbook of Atmospheric Science: Principles and Applications, edited by C. N. Hewitt and A. V. Jackson, 255–274, Blackwell Sci., Malden, Mass, ISBN: 0632052864, 2003.

Carslaw, D. and Rhys-Tyler, G.: New insights from comprehensive on-road measurements of NO_x, NO_2 and NH_3 from vehicle emission remote sensing in London, UK, Atmos. Environ., 81, 339–347, https://doi.org/10.1016/j.atmosenv.2013.09.026, 2013.

CAT: Marine power systems, https://www.cat.com/en_GB/products/new/power-systems/marine-power-systems.html (last access: 27 May 2022), 2022.

Chosson, F., Paoli, R., and Cuenot, B.: Ship plume dispersion rates in convective boundary layers for chemistry models, Atmos. Chem. Phys., 8, 4841–4853, https://doi.org/10.5194/acp-8-4841-2008, 2008.

CIMAC: Guide to diesel exhaust emissions control of NO_X, SO_X, particulates, smoke and CO_2 − Seagoing ships and big stationary diesel power plants; Recommendation No. 28; International Council on Combustion Engines: Frankfurt, Germany, https://www.cimac.com/cms/upload/Publication_Press/Recommendations/Recommendation_28.pdf (last access: 26 May 2022), 2008.

Cohan, A., Wu, J. and Dabdub, D.: High-resolution pollutant transport in the San Pedro Bay of California, Atmos. Pollut. Res., 2, 237-246, https://doi.org/10.5094/APR.2011.030, 2011.

Comer, A. B., Chen, C., Stolz, D., and Rutherford, D.: Rotors and bubbles: Route-based assessment of innovative technologies to reduce ship fuel consumption and emissions, ICCT working paper, 1–19, https://theicct.org/sites/default/files/publications/Rotors_and_bubbles_2019_05_12.pdf (last access: 27 April 2022), 2019.

Cooper, D. A.: Exhaust emissions from ships at berth, Atmos. Environ., 37, 3817–3830, https://doi.org/10.1016/S1352-2310(03)00446-1 , 2003.

Copernicus Land Monitoring Service: Corine land cover, https://land.copernicus.eu/pan-european/corine-land-cover/clc2018 (last access: 25 May 2022), 2018.

Corbett, J. J., and H. W. Koehler: Updated emissions from ocean shipping, J. Geophys. Res., 108, 4650, https://doi.org/10.1029/2003JD003751, 2003.

Corbett, J. J., Fischbeck, P. S., and Pandis, S. N.: Global nitrogen and sulfur inventories for oceangoing ships. J. Geophys. Res., 104, 3457–3470, https://doi.org/10.1029/1998JD100040, 1999.

Corbett, J. J., Winebrake, J. J., Green, E. H., Kasibhatla, P., Eyring, V., and Lauer, A.: Mortality from ship emissions: A global assessment, Environ. Sci. Technol., 41, 8512–8518, https://doi.org/10.1021/es071686z, 2007.

Crank, J. and Nicolson, P.: A practical method for numerical evaluation of solutions of partial differential equations of the heat conduction type, Proc. Camb. Philol. Soc., 43, 50–67, https://doi.org/10.1017/S0305004100023197, 1947.

Dodge, M.: Combined use of modeling techniques and smog chamber data to derive ozone-precursor relationships, in: Proceedings of the International Conference on Photochemical Oxidant Pollution and its Control, US Environmental Protection Agency, Research Triangle Park, NC, USA, 881–889, 1977.

Durran, D. R.: The third-order Adams–Bashforth method: an attractive alternative to leapfrog time differencing, Mon. Weather Rev., 119, 702–720, https://doi.org/10.1175/1520-0493(1991)119<0702:TTOABM>2.0.CO;2, 1991.

EBAS: A database hosting observation data of atmospheric chemical composition and physical properties, http://ebas-data.nilu.no/ (last access: 25 May 2022), 2022.

EEA: Digital elevation model over Europe (EU-DEM v1.1), https://www.eea.europa.eu/data-and-maps/data/copernicus-land-monitoring-service-eu-dem (last access: 26 May 2022), 2017.

EMEP: European Monitoring and Evaluation Programme, https://www.emep.int/ (last access: 25 May 2022), 2022.

Endresen, Ø., Sørgård, E., Sundet, J. K., Dalsøren, S. B., Isaksen, I. S. A., Berglen, T. F., and Gravir, G.: Emission from international sea transportation and environmental impact. J. Geophys. Res., 108, 4560, https://doi.org/10.1029/2002JD002898, 2003.

European Union: Directive 2008/50/EC of the European Parliament and of the Council of 21 May 2008 on ambient air quality and cleaner air for Europe. Off. J. Eur. Union 51, 1–44, https://eur-lex.europa.eu/legal-content/EN/TXT/PDF/?uri=OJ:L:2008:152:FULL&from=EN (last access: 24 May 2022), 2008.

Eyring, V., Köhler, H. W., van Aardenne, J., and Lauer, A.: Emissions from international shipping: 1. The last 50 years. J. Geophys. Res., 110, https://doi.org/10.1029/2004JD005619, 2005.

Fenger, J.: Urban air quality, Atmos. Environ., 33, 4877–4900, https://doi.org/10.1016/S1352-2310(99)00290-3, 1999.

Fidler, J.C.: The metabolism of acetaldehyde by plant tissues. J. Exp. Bot. 19, 1–51, https://doi.org/10.1093/jxb/19.1.41, 1968.

Fischereit, J., Schlünzen, K. H., Gierisch, A. M. U., Grawe, D., and Petrik, R.: Modelling tidal influence on sea breezes with models of different complexity, Meteorol. Z., 25, 343–355, https://doi.org/10.1127/metz/2016/0703, 2016.

Foken, T.: 50 years of the Monin-Obukhov similarity theory, Bound.-Lay. Meteor., 119, 431–437, 2006.

Frick, G. M. and Hoppel, W. A.: Airship measurements of ship's exhaust plumes and their effect on marine boundary layer clouds, J. Atmos. Sci., 57, 2625–2648, https://doi.org/10.1175/1520-0469(2000)057<2625:AMOSSE>2.0.CO;2, 2000.

Fridell, E., Steen, E., and Peterson, K.: Primary particles in ship emissions, Atmos. Environ., 42, 1160–1168, https://doi.org/10.1016/j.atmosenv.2007.10.042, 2008.

Golder, D.: Relations among stability parameters in the surface layer, Bound.-Lay. Meteorol., 3, 47–58, https://doi.org/10.1007/BF00769106, 1972.

Granier, C., Darras, S., Denier van der Gon, H., Doubalova, J., Elguindi, N., Galle, B., Gauss, M., Guevara, M., Jalkanen, J.-P., Kuenen, J., Liousse, C., Quack, B., Simpson, D., and Sindelarova, K.: Copernicus Atmosphere Monitoring Service global and regional emissions (April 2019 version), Copernicus Atmosphere Monitoring Service (CAMS) report, https://doi.org/10.24380/d0bn-kx16, 2019.

Grawe, D., Schlünzen, K. H., and Pascheke, F.: Comparison of results of an obstacle resolving microscale model with wind tunnel data, Atmos. Environ., 79, 495–509, https://doi.org/10.1016/j.atmosenv.2013.06.039, 2013.

Grice, S., Stedman, J., Kent, A., Hobson, M., Norris, J., Abbott, J., and Cooke, S.: Recent trends and projections of primary NO_2 emissions in Europe, Atmos. Environ., 43, 2154–2167, https://doi.org/10.1016/j.atmosenv.2009.01.019, 2009.

Hamburger Luftmessnetz: Messstationen, https://luft.hamburg.de/ (last access: 01 June 2022), 2022.

Hamer, P. D., Walker, S.-E., Sousa-Santos, G., Vogt, M., Vo-Thanh, D., Lopez-Aparicio, S., Schneider, P., Ramacher, M. O. P., and Karl, M.: The urban dispersion model EPISODE v10.0 - Part 1: An Eulerian and sub-grid-scale air quality model and its application in Nordic winter conditions, Geosci. Model Dev., 13, 4323–4353, https://doi.org/10.5194/gmd-13-4323-2020, 2020.

Hanna, S. and Chang, J.: Acceptance criteria for urban dispersion model evaluation, Meteorol. Atmos. Phys., 116, 133–146, https://doi.org/10.1007/s00703-011-0177-1, 2012.

Hanna, S. R., Briggs, G. A., and Hosker Jr., R. P.: Handbook on Atmospheric Diffusion, Technical Information Center, U.S. Department of Energy, 102, 1982.

Hanna, S. R., Schulman, L. L., Paine, R. J., Pleim, J. E., and Baer, M.: Development and evaluation of the offshore and coastal dispersion model, J. Air Pollut. Control Assoc., 35, 1039–1047, https://doi.org/10.1080/00022470.1985.10466003, 1985.

Hanna, S. R., Egan, B. A., Purdum, J., and Wagler, J.: Evaluation of the ADMS, AERMOD and ISC3 dispersion models with the OPTEX, Duke Forest, Kincaid, Indianapolis and Lovett field datasets, Int. J. Environ. Pollut., 16, 301–314, https://doi.org/10.1504/IJEP.2001.000626, 2001.

Hobbs, P. V., Garrett, T. J., Ferek, R. J., et al.: Emissions from ships with respect to their effects on clouds, J. Atmos. Sci., 57, 2570–2590, https://doi.org/10.1175/1520-0469(2000)057<2570:EFSWRT>2.0.CO;2, 2000.

Holtslag A. A. M.: Estimates of diabatic wind speed profiles from near-surface weather observations. Bound.-Lay. Meteorol., 29, 225–250, https://doi.org/10.1007/BF00119790, 1984.

Holtslag, A. A. M., and de Bruin, H. A. R.: Applied modeling of the nighttime surface energy balance over land, J. Appl. Meteorol., 27, 689–704, https://doi.org/10.1175/1520-0450(1988)027<0689:AMOTNS>2.0.CO;2, 1988.

Hulskotte, J. H. J., and Denier van der Gon, H. A. C.: Fuel consumption and associated emissions from seagoing ships at berth derived from an on-board survey, Atmos. Environ., 44, 1229–1236, https://doi.org/10.1016/j.atmosenv.2009.10.018, 2010.

Hunter, K. A., Liss, P. A., Surapipith, V., Dentener, F., Duce, R., Kanakidou, M., Kubilay, N., Mahowald, N., Okin, G., Sarin, M., Uematsu, M., and Zhu, T.: Impacts of anthropogenic SO_x, NO_x and NH_3 on acidification of coastal waters and shipping lanes, Geophys. Res. Lett., 38, 13, https://doi.org/10.1029/2011GL047720, 2011.

Hurley, P.: TAPM v.4. Part 1: Technical Description. CSIRO Marine and Atmospheric Research Paper No. 25, Aspendale, Vic., Australia, ISBN: 9781921424717, https://www.cmar.csiro.au/research/tapm/docs/tapm_v4_technical_paper_part1.pdf (last access: 24 May 2022), 2008.

Hurley, P. J., Physick, W. L., and Luhar, A. K.: TAPM – A practical approach to prognostic meteorological and air pollution modelling, Environ. Modell. Softw., 20, 737–752, https://doi.org/10.1016/j.envsoft.2004.04.006, 2005.

Huszar, P., Cariolle, D., Paoli, R., Halenka, T., Belda, M., Schlager, H., Miksovsky, J. and Pisoft, P.: Modeling the regional impact of ship emissions on NO_x and ozone levels over the Eastern Atlantic and Western Europe using ship plume parameterization, Atmos. Chem. Phys., 10, 6645–6660, https://doi.org/10.5194/acp-10-6645–2010, 2010.

ICDC: Daten, https://www.cen.uni-hamburg.de/icdc/data/atmosphere/weathermast-hamburg.html (last access: 19 May 2022), 2022.

IMO: Revised Guidelines for the Onboard Operational Use of Shipborne Automatic Identification Systems (AIS), IMO: London, UK, https://wwwcdn.imo.org/localresources/en/OurWork/Safety/Documents/AIS/Resolution%20A.1106(29).pdf (last access: 03 June 2022), 2015.

IMO: Sulphur oxides (SO_x) and particulate matter (PM) – Regulation 14, https://www.imo.org/en/OurWork/Environment/Pages/Sulphur-oxides-(SOx)-%E2%80%93-Regulation-14.aspx (last access: 27 April 2022), 2022.

Jacobson, M. Z.: Atmospheric Pollution: history, science and regulation, Cambridge University Press, Cambridge, United Kingdom and New York, NY, USA, ISBN: 9780511802287, https://doi.org/10.1017/CBO9780511802287, 2002.

Jägerbrand, A. K., Brutemark, A., Barthel Svedén, J., and Gren, I.-M.: A review on the environmental impacts of shipping on aquatic and nearshore ecosystems, Sci. Total Environ., 695, 133637, https://doi.org/10.1016/j.scitotenv.2019.133637, 2019.

Jahangiri, S., Nikolova, N., and Tenekedjiev, K.: Application of a developed dispersion model to port of Brisbane, American J. Environ. Sci., 14, 156–169, https://doi.org/10.3844/ajessp.2018.156.169, 2018.

Jalkanen, J.-P., Brink, A., Kalli, J., Pettersson, H., Kukkonen, J., and Stipa, T.: A modelling system for the exhaust emissions of marine traffic and its application in the Baltic Sea area, Atmos. Chem. Phys., 9, 9209–9223, https://doi.org/10.5194/acp-9-9209-2009, 2009.

Jalkanen, J.-P., Johansson, L., Kukkonen, J., Brink, A., Kalli, J., and Stipa, T.: Extension of an assessment model of ship traffic exhaust emissions for particulate matter and carbon monoxide, Atmos. Chem. Phys., 12, 2641–2659, https://doi.org/10.5194/acp-12-2641-2012, 2012.

Jalkanen, J.-P., Johansson, L., and Kukkonen, J.: A comprehensive inventory of ship traffic exhaust emissions in the European sea areas in 2011, Atmos. Chem. Phys., 16, 71–84, https://doi.org/10.5194/acp-16-71-2016, 2016.

Janicke, U. and Janicke, L.: A three-dimensional plume rise model for dry and wet plumes, Atmos. Environ., 35, 877–890, https://doi.org/10.1016/S13522310(00)00372-1, 2001.

Jayaram, V., Nigam, A., Welch, W. A., Miller, J. W., and Cocker III, D. R.: Effectiveness of emission control technologies for auxiliary engines on ocean-going vessels, J. Air. Waste Manage., 61:1, 14–21, https://doi.org/10.3155/1047-3289.61.1.14, 2011.

Johansson, L., Jalkanen, J. P., and Kukkonen, J.: Global assessment of shipping emissions in 2015 on a high spatial and temporal resolution, Atmos. Environ., 167, 403–415, https://doi.org/10.1016/j.atmosenv.2017.08.042, 2017.

Jonson, J. E., Jalkanen, J. P., Johansson, L., Gauss, M., and Denier van der Gon, H. A. C.: Model calculations of the effects of present and future emissions of air pollutants from shipping in the Baltic Sea and the North Sea, Atmos. Chem. Phys., 15, 783–798, https://doi.org/10.5194/acp-15-783-2015, 2015.

Karamchandani, P., Koo, A., and Seigneur, C.: Reduced gas-phase kinetic Mechanism for atmospheric plume chemistry, Environ. Sci. Technol., 32, 1709–1720, https://doi.org/10.1021/es970707u, 1998.

Karamchandani, P., Santos, L., Sykes, I., Zhang, Y., Tonne, C., and Seigneur, C.: Development and evaluation of a state-of-the-science reactive plume model, Environ. Sci. Technol., 34, 870–880, https://doi.org/10.1021/es990611v, 2000.

Karl, M.: City-scale Chemistry Transport Model EPISODE-CityChem (Release version 1.6), Zenodo [code], https://doi.org/10.5281/zenodo.6573059, 2022.

Karl, M. and Ramacher, M.: City-scale Chemistry Transport Model EPISODE-CityChem (Release version 1.4), Zenodo [code], https://doi.org/10.5281/zenodo.3862264, 2020.

Karl, M., Bieser, J., Geyer, B., Matthias, V., Jalkanen, J.-P., Johansson, L., and Fridell, E.: Impact of a nitrogen emission control area (NECA) on the future air quality and nitrogen deposition to seawater in the Baltic Sea region, Atmos. Chem. Phys., 19, 1721–1752, https://doi.org/10.5194/acp-19-1721-2019, 2019a.

Karl, M., Walker, S.-E., Solberg, S., and Ramacher, M. O. P.: The Eulerian urban dispersion model EPISODE - Part 2: Extensions to the source dispersion and photochemistry for EPISODE-CityChem v1.2 and its application to the city of Hamburg, Geosci. Model Dev., 12, 3357–3399, https://doi.org/10.5194/gmd-12-3357-2019, 2019b.

Karl, M., Jonson, J. E., Uppstu, A., Aulinger, A., Prank, M., Sofiev, M., Jalkanen, J.-P., Johansson, L., Quante, M., and Matthias, V.: Effects of ship emissions on air quality in the Baltic Sea region simulated with three different chemistry transport models, Atmos. Chem. Phys., 19, 7019–7053, https://doi.org/10.5194/acp-19-7019-2019, 2019c.

Karl, M., Pirjola, L., Karppinen, A., Jalkanen, J.-P., Ramacher, M. O. P., and Kukkonen, J.: Modeling of the concentrations of ultrafine particles in the plumes of ships in the vicinity of major harbors, Int. J. Environ. Res. Pu., 17, 777, https://doi.org/10.3390/ijerph17030777, 2020.

Karl, M., Pirjola, L., Grönholm, T., Kurppa, M., Anand, S., Zhang, X., Held, A., Sander, R., Maso, M. D., Topping, D., Jiang, S., Kangas, L., and Kukkonen, J.: Description and evaluation of the community aerosol dynamics model MAFOR v2.0, Geosci. Model Dev., 15, 3969–4026, https://doi.org/10.5194/gmd-15-3969-2022, 2022.

Khoder, M.I.: Atmospheric conversion of sulfur dioxide to particulate sulfate and nitrogen dioxide to particulate nitrate and gaseous nitric acid in an urban area, Chemosphere, 49, 675–684, https://doi.org/10.1016/S0045-6535(02)00391-0, 2002.

Kotrikla, A., Dimou, K., Korras-Carraca, M., and Biskos, G.: Air quality modelling in The city of Mytilene, Greece, in: Proceedings of the 13th International Conference on Environmental Science and Technology, Athens, Greece, 5–7 September 2013, https://hero.epa.gov/hero/index.cfm/reference/details/reference_id/6682759 (last access: 24 May 2022), 2013.

Kotrikla, A. M., Lilas, T., and Nikitakos, N.: Abatement of air pollution at an Aegean island port utilizing shore side electricity and renewable energy, Mar. Policy, 75, 238–248, https://doi.org/10.1016/j.marpol.2016.01.026, 2017.

Kuenen, J., Dellaert, S., Visschedijk, A., Jalkanen, J.-P., Super, I., and van der Gon, H. D.: CAMS-REG-v4: a state-of-the-art high-resolution European emission inventory for air quality modelling, Earth Syst. Sci. Data, 14, 491−515, https://doi.org/10.5194/essd-14-491-2022, 2022.

Langley, L., Leaitch, W. R., Lohmann, U., Shantz, N. C., and Worsnop, D. R.: Contributions from DMS and ship emissions to CCN observed over the summertime North Pacific, Atmos. Chem. Phys., 10, 1287–1314, https://doi.org/10.5194/acp-10-1287-2010, 2010.

Ledoux, F., Roche, C., Cazier, F., Beaugard, C., and Courcot, D.: Influence of ship emissions on NO_x, SO_2, O_3 and PM concentrations in a North-Sea harbor in France, J. Environ. Sci., 71, 56–66, https://doi.org/10.1016/j.jes.2018.03.030, 2018.

Lee, J. H. W. and Cheung, V.: Generalized lagrangian model for buoyant jets in current, J. Environ. Eng. (United States), 116, 1085–1106, https://doi.irg/10.1061/(ASCE)0733-9372(1990)116:6(1085), 1990.

Lee, J., Hong, J., Noh, Y., and Jiménez, P. A.: Implementation of a roughness sublayer parameterization in the Weather Research and Forecasting model (WRF version 3.7.1) and its evaluation for regional climate simulations, Geosci. Model Dev., 13, 521–536, https://doi.org/10.5194/gmd-13-521-2020, 2020.

Lewis, A. C., Carslaw, N., Marriott, P. J., Kinghorn, R. M., Morrison, P., Lee, A. L., Bartle, K. D., and Pilling, M. J.: A larger pool of ozone-forming carbon compounds in urban atmospheres, Nature, 405(6), 778–781, https://doi.org/10.1038/35015540, 2000.

López, S. D.: Numerische Modellierung Turbulenter Umströmungen von Gebäuden = = Numerical modelling of turbulent flow around buildings, Berichte zur Polar-und Meeresforschung (Reports on Polar and Marine Research), Bremerhaven, Alfred Wegener Institute for Polar and Marine Research, 418, 93 p., https://doi.org/10.2312/BzPM_0418_2002, 2002.

Luecken, D. J., Hutzell, W. T., Strum, M. L., and Pouliot, G. A.: Regional sources of atmospheric formaldehyde and acetaldehyde, and implications for atmospheric

modeling, Atmos. Environ., 47, 477–490, https://doi.org/10.1016/j.atmosenv.2011.10.005, 2012.

MAN: Two-stroke project guides, https://marine.man-es.com/two-stroke/project-guides (last access: 27 May 2022), 2022.

Martinelli, N., Olivieri, O., and Gierlli, D.: Air particulate matter and cardiovascular disease: A narrative review, Eur. J. Intern Med., 24, 295–302, https://doi.org/10.1016/j.ejim.2013.04.001, 2013.

Matthias, V., Aulinger, A., Backes, A., Bieser, J., Geyer, B., Quante, M., and Zeretzke, M.: The impact of shipping emissions on air pollution in the greater North Sea region – Part 2: Scenarios for 2030, Atmos. Chem. Phys., 16, 759–776, https://doi.org/10.5194/acp-16-759-2016, 2016.

Matthias, V., Arndt, J. A., Aulinger, A., Bieser, J., Denier van der Gon, H., Kranenburg, R., Kuenen, J., Neumann, D., Pouliot, G. and Quante, M.: Modeling emissions for three-dimensional atmospheric chemistry transport models, J. Air Waste Manage., 68, 763–800, https://doi.org/10.1080/10962247.2018.1424057, 2018.

Matthias, V., Quante, M., Arndt, J. A., Badeke, R., Fink, L., Petrik, R., Feldner, J., Schwarzkopf, D., Link, E.-M., Ramacher, M. O., et al.: The role of emission reductions and the meteorological situation for air quality improvements during the COVID-19 lockdown period in Central Europe, Atmospheric Chemistry and Physics, 21, 13 931–13 971, 2021.

McKinlay, C. J., Turnock, S. R., and Hudson, D. A.: A comparison of hydrogen and ammonia for future long distance shipping fuels, In: Proceedings of the LNG/LPG and Alternative Fuels Ships Conference, London, UK, 29–30 January 2020, https://eprints.soton.ac.uk/437555/ (last access: 24 May 2022), 2020.

McRae, G., Goodin, W., and Seinfeld, J.: Development of a second generation mathematical model for urban air pollution: I. model formulation, Atmos. Environ., 16, 679–696, 1982.

MEPC: Report of the Marine Environment Protection Committee on its fifty-eighth session, https://www.mpa.gov.sg/web/wcm/connect/www/0e3d48a6-97b3-4c6b9dee-ea6f773897ad/mepc58-23-final-report.pdf?MOD=AJPERES (last access: 27 May 2022), 2008.

Merico, E., Donateo, A., Gambaro, A., Cesari, D., Gregoris, E., Barbaro, E., Dinoi, A., Giovanelli, G., Masieri, S., and Contini, D.: Influence of in-port ships emissions to gaseous atmospheric pollutants and to particulate matter of different sizes in a Mediterranean harbour in Italy, Atmos. Environ., 136, 1–10, http://doi.org/10.1016/j.atmosenv.2016.05.024, 2016.

Merico, E., Gambaro, A., Argiriou, A., Alebic-Juretic, A., Barbaro, E., Cesari, D., Chasapidis, L., Dimopolous, S., Dinoi, A., Donateo, A., Giannaros, C., Gregoris, E., Karagiannidis, A., Konstandopoulos, A. G., Ivošević, T., Liora, N., Melas, D., Mifka, B., Orlić, I., Poupkou, A., Sarovic, K., Tsakis, A., Giua, R., Pastore, T., Nocioni, A., and Contini, D.: Atmospheric impact of ship traffic in four Adriatic-Ionian port-cities:

Comparison and harmonization of different approaches, Transp. Res. D.-Tr. E., 50, 431−445, http://doi.org/10.1016/j.trd.2016.11.016, 2017.

Merico, E., Dinoi, A., and Contini, D.: Development of an integrated modelling-measurement system for near-real-time estimates of harbour activity impact to atmospheric pollution in coastal cities, Transp. Res. D.-Tr. E., 73, 108−119, https://doi.org/10.1016/j.trd.2019.06.009, 2019.

Moldanová, J., Fridell, E., Popovicheva, O., Demirdjian, B., Tishkova, V., Faccinetto, A., and Focsa, C.: Characterisation of particulate matter and gaseous emissions from a large ship diesel engine, Atmos. Environ., 43, 2632–2641, https://doi.org/10.1016/j.atmosenv.2009.02.008, 2009.

Monin, A. S. and Obukhov, A.: Basic laws of turbulent mixing in the surface layer of the atmosphere, Contrib. Geophys. Inst. Acad. Sci. USSR, 151, 163–187, 1954.

Moré, J. J.: The Levenberg-Marquardt algorithm: Implementation and theory, in: Numerical Analysis, edited by: Watson, G. A., Springer, Heidelberg, 105–116, ISBN: 3540085386, https://www.osti.gov/servlets/purl/7256021-WWC9hw/ (last access: 24 May 2022), 1977.

Moreno-Gutiérrez, J., Calderay, F., Saborido, N., Boile, M., Valero, R. R., and Durán-Grados, V.: Methodologies for estimating shipping emissions and energy consumption: A comparative analysis of current methods, Energy, 86, 603–616, https://doi.org/10.1016/j.energy.2015.04.083, 2015.

Murena, F., Mocerino, L., Quaranta, F., and Toscano, D.: Impact on air quality of cruise ship emissions in Naples, Italy, Atmos. Environ., 187, 70–83, https://doi.org/10.1016/j.atmosenv.2018.05.056, 2018.

Murphy, S., Agrawal, H., Sorooshian, A., Padró, L. T., Gates, H., Hersey, S., Welch, W. A., Jung, H., Miller, J. W., Cocker, D. R., Nenes, A., Jonsson, H. H., Flagan, R. C. and Seinfeld, J. H.: Comprehensive simultaneous shipboard and airborne characterization of exhaust from a modern container ship at sea, Environ. Sci. Technol., 43, 4626–4640, https://doi.org/10.1021/es802413j, 2009.

Nunes, R. A. O., Alvim-Ferraz, M. C. M., Martins, F. G., Calderay-Cayetano, F., Durán-Grados, V., Moreno-Gutiérrez, J., Jalkanen, J.-P., Hannuniemi, H., and Sousa, S. I. V.: Shipping emissions in the Iberian Peninsula and the impacts on air quality, Atmos. Chem. Phys., 20, 9473-9489, https://doi.org/10.5194/acp-20-9473-2020, 2020.

Pan, K., Lim, M. Q., Kraft, M., and Mastorakos, E.: Development of a moving point source model for shipping emission dispersion modeling in EPISODE-CityChem v1.3, Geosci. Model Dev., 14, 4509−4534, https://doi.org/10.5194/gmd-14-4509-2021, 2021.

Parrish, D. D., Xu, J., Croes, B., and Shao, M.: Air quality improvement in Los Angeles-perspectives for developing cities, Front. Env. Sci. Eng., 10, 11, https://doi.org/10.1007/s11783-016-0859-5, 2016.

Pasquill, F. and Smith, F. B.: Atmospheric Diffusion, Ellis Horwood Limited, 3rd edn., J. Wiley and Sons, New York, USA, ISBN: 9780470668924, 1983.

Poplawski, K., Setton, E., McEwen, B., Hrebenyk, D., Graham, M., and Keller, P.: Impact of cruise ship emissions in Victoria, BC, Canada, Atmos. Environ., 45, 824−833, https://doi.org/10.1016/j.atmosenv.2010.11.029, 2011.

Port of Hamburg: Vessels, https://www.hafen-hamburg.de/en/vessels/ (last access: 20 May 2022), 2022.

Pozzer, A., Jöckel, P., and Van Aardanne, J.: The influence of the vertical distribution of emissions on tropospheric chemistry, Atmos. Chem. Phys., 9, 9417−9432, https://doi.org/10.5194/acp-9-9417-2009, 2009.

Ramacher, M. O. P., Karl, M., Aulinger, A., Bieser, J., Matthias, V., and Quante, M.: The impact of emissions from ships in ports on regional and urban scale air quality, in: Air Pollution Modeling and its Application XXV, edited by: Mensink, C. and Kallos, G., Springer Proceedings in Complexity, Springer International Publishing, Imprint, Springer, Cham, Switzerland, 309–316, 2018.

Ramacher, M. O. P., Karl, M., Bieser, J., Jalkanen, J.-P., and Johansson, L.: Urban population exposure to NO_x emissions from local shipping in three Baltic Sea harbour cities - a generic approach, Atmos. Chem. Phys., 19, 9153–9179, https://doi.org/10.5194/acp-19-9153-2019, 2019.

Ramacher, M. O. P., Matthias, V., Aulinger, A., Quante, M., Bieser, J., and Karl, M.: Contributions of traffic and shipping emissions to city-scale NO_x and $PM_{2.5}$ exposure in Hamburg, Atmos. Environ., 237, https://doi.org/10.1016/j.atmosenv.2020. 117674, 2020.

Ramacher, M.O.P., Kakouri, A., Speyer, O., Feldner, J., Karl, M., Timmermans, R., van der Gon, H.D., Kuenen, J., Gerasopoulos, E., and Athanasopoulou, E.: The UrbEm Hybrid Method to Derive High-Resolution Emissions for City-Scale Air Quality Modeling, Atmosphere, 12, 1404, https://doi.org/10.3390/atmos12111404, 2021.

Rodriguez, E., Morris, C. S., and Belz, J. E.: A global assessment of the SRTM performance, Photogramm. Eng. Rem. S., 72, 249–260, https://doi.org/10.14358/ PERS.72.3.249, 2006.

Salim, M. H., Schlünzen, K. H., Grawe, D., Boettcher, M., Gierisch, A. M. U., and Fock, B. H.: The microscale obstacle-resolving meteorological model MITRAS v2.0: model theory, Geosci. Model Dev., 11, 3427–3445, https://doi.org/10.5194/gmd-11- 3427-2018, 2018.

Saxena, P. and Seigneur, C.: On the oxidation of SO2 to sulfate in atmospheric aerosols, Atmos. Environ., 21(4), 807–812, https://doi.org/10.1016/ 0004-6981(87)90077-1, 1987.

Schatzmann, M.: An Integral Model of Plume Rise, Atmos. Environ., 13, 721–731, https://doi.org/10.1016/0004-6981(79)90202-6, 1979.

Schatzmann, M., Bächlin, W., Emeis, S., Kühlwein, J., Leitl, B., Müller, W. J., Schäfer, K., and Schlünzen, H.: Development and validation of tools for the implementation of european air quality policy in Germany (Project VALIUM), Atmos. Chem. Phys., 6, 3077–3083, https://doi.org/10.5194/acp-6-3077-2006, 2006.

Schlünzen, K. H., Hinneburg, D., Knoth, O., Lambrecht, M., Leitl, B., López, S., Lüpkes, C., Panskus, H., Renner, E., Schatzmann, M., Schoenemeyer, T., Trepte, S., and Wolke, R.: Flow and transport in the obstacle layer: First results of the micro-scale model MITRAS, J. Atmos. Chem., 44, 113–130, https://doi.org/10.1023/A:1022420130032, 2003.

Schlünzen, K. H., Boettcher, M., Fock, B. H., Gierisch, A., Grawe, D., and Salim, M.: Scientific documentation of the Multiscale Model System M-SYS, MEMI Tech. Rep. 4, CEN, Univ. Hambg., 153 p., https://www.mi.uni-hamburg.de/en/arbeitsgruppen/memi/modelle/dokumentation/msys-scientific-documentation-20180706.pdf (last access: 24 May 2022), 2018.

Schwarzkopf, D. A., Petrik, R., Matthias, V., Quante, M., Majamäki, E., & Jalkanen, J. P.: A ship emission modeling system with scenario capabilities. Atm. Environment: X 12, 100132, https://doi.org/10.1016/j.aeaoa.2021.100132, 2021.

Seinfeld, J. and Pandis, S.: Atmospheric chemistry and physics: From air pollution to climate change, 2nd edition, John Wiley & Sons Inc, New York, USA, ISBN: 9780471720188, 2006.

Simpson, D., Fagerli, H., Jonson, J. E., Tsyro, S., Wind, P., and Tuovinen, J.-P.: Transboundary acidification, eutrophication and ground level ozone in Europe, Part 1: Unified EMEP model description, EMEP Report 1/2003, https://www.emep.int/publ/reports/2003/emep_report_1_part1_2003.pdf (last access: 03 June 2022), 2003.

Simpson, D., Benedictow, A., Berge, H., Bergström, R., Emberson,L. D., Fagerli, H., Flechard, C. R., Hayman, G. D., Gauss, M., Jonson, J. E., Jenkin, M. E., Nyíri, A., Richter, C., Semeena, V.S., Tsyro, S., Tuovinen, J.-P., Valdebenito, Á., and Wind, P.: The EMEP MSC-W chemical transport model – technical description, Atmos. Chem. Phys., 12, 7825–7865, https://doi.org/10.5194/acp-12-7825-2012, 2012.

Simpson, I., and Volosciuk, C.: Changing volatile organic compound emissions in urban environments: Many paths to cleaner air, WMO Bulletin n°, 68, 2, https://public.wmo.int/en/resources/bulletin/changing-volatile-organic-compound-emissions-urban-environments-many-paths (last access: 01 June 2022), 2019.

Smith, G. D.: Numerical solution of partial differential equations: finite difference methods, 3rd edn., edited by: Buxton, J. N., Churchhouse, R. F., and Tayler, A. B., Clarendon Press, Oxford, UK, ISBN: 0198596413, https://wp.kntu.ac.ir/ghoreishif/smith.pdf (last access: 24 May 2022), 1985.

Smith, T. W. P., Jalkanen, J. P., Anderson, B. A., Corbett, J. J., Faber, J., Hanayama, S., O'Keeffe, E., Parker, S., Johansson, L., Aldous, L., Raucci, C., Traut, M., Ettinger, S., Nelissen, D., Lee, D. S., Ng, S., Agrawal, A., Winebrake, J. J., Hoen,

M., Chesworth, S., and Pandey, A.: Third IMO greenhouse gas study 2014, International Maritime Organization, London, UK, https://www.imo.org/en/OurWork/Environment/Pages/Greenhouse-Gas-Studies-2014.aspx (last access: 03 June 2022), 2015.

Sofiev, M., Winebrake, J. J., Johansson, L., Carr, E. W., Prank, M., Soares, J., Vira, J., Kouznetsov, R., Jalkanen, J. P., and Corbett, J. J.: Cleaner fuels for ships provide public health benefits with climate tradeoffs, Nat. Commun., 9, 1–12, https://doi.org/10.1038/s41467-017-02774-9, 2018.

Song, C. H., Chen, G., Hanna, S. R., Crawford, J., and Davis, D. D.: Dispersion and chemical evolution of ship plumes in the marine boundary layer: Investigation of $O_3/NO_y/HO_x$ chemistry, J. Geophys. Res., 108, 4143, https://doi.org/10.1029/2002JD002216, 2003.

Stockwell, W. R. and Calvert, J. G.: The mechanism of the HO-SO_2 reaction, Atmos. Environ., 17, 2231–2235, https://doi.org/10.1016/0004-6981(83)90220-2, 1983.

Stull, R. B.: An Introduction to boundary Layer meteorology, Kluwer Academic Publishers, Dordrecht, ISBN: 9789027727688, 1988.

Trukenmüller, A., Grawe, D., and Schlünzen, K. H.: A model system for the assessment of ambient air quality conforming to EC directives, Meteorol. Z., 13, 387–394, 10.1127/0941-2948/2004/0013-0387, 2004.

Turner, D. B.: Workbook of Atmospheric Diffusion Estimates, U.S. Environmental Protection Agency Report 999-AP-26, Washington, DC 1969.

Tzannatos, E.: Ship emissions and their externalities for Greece, Atmos. Environ., 44, 2194–2202, https://doi.org/10.1016/j.atmosenv.2010.03.018, 2010.

Umweltbundesamt: Hintergrundinformationen zur Version 4.1 des Handbuchs für Emissionsfaktoren des Straßenverkehrs (HBEFA), https://www.umweltbundesamt.de/sites/default/files/medien/421/dokumente/20190920_hbefa41_release_hintergrunddokument_v2.pdf (last access: 25 May 2022), 2019.

Umweltbundesamt: Luftmessnetz des Umweltbundesamtes, https://www.umweltbundesamt.de/themen/luft/messenbeobachtenueberwachen/luftmessnetz-des-umweltbundesamtes (last access: 25 May 2022), 2022.

UNCTAD: Review of maritime transport 2019, United Nations, Geneva, https://unctad.org/en/Pages/Publications/Review-of-Maritime-Transport-(Series).aspx (last access: 27 May 2022), 2020.

US-EPA: User's guide for the AMS/EPA Regulatory Model–AERMOD. USEPA-454/B-03-001, Research Triangle Park, NC, https://nepis.epa.gov/Exe/ZyPURL.cgi?Dockey=P100OYLX.txt (last access: 24 May 2022), 2004.

Vesseltracker: Vessels, https://www.vesseltracker.com/en/vessels.html (last access: 16 May 2022), 2022.

Vinken, G. C. M., Boersma, K. F., Jacob, D. J., and Meijer, E. W.: Accounting for non-linear chemistry of ship plumes in the GEOS-Chem global chemistry transport model, Atmos. Chem. Phys., 11, 11707–11722, https://doi.org/10.5194/acp-11-11707-2011, 2011.

von Glasow, R., Lawrence, M. G., Sander, R. and Crutzen, P. J.: Modeling the chemical effects of ship exhaust in the cloud-free marine boundary layer, Atmos. Chem. Phys., 3, 233–250, https://doi.org/10.5194/acp-3-233-2003, 2003.

Wagner, T.: Elektromobilität und Schadstoffexposition in Hamburg, Master Thesis Leuphana Universität Lüneburg, 2022.

Wärtsilä: Diesel engines Reliability, efficiency, and low operating costs, https://www.wartsila.com/marine/build/engines-and-generating-sets/diesel-engines (last access: 24 May 2022), 2022.

Wieringa, J.: Updating the Davenport roughness classification, J. Wind Eng. Ind. Aerod., 41, 357−368, https://doi.org/10.1016/0167-6105(92)90434-C, 1992.

Williams, M., and Minjares, R.: A technical summary of Euro 6/VI vehicle emission standards. International Council for Clean Transportation (ICCT), Washington, DC, https://theicct.org/sites/default/files/publications/ICCT_Euro6-VI_briefing_jun2016.pdf (last access: 03 June 2022), 2016.

Willmott, C. J., Robeson, S. M., and Matsuura, K.: A refined index of model performance, Int. J. Climatol., 32, 2088–2094, https://doi.org/10.1002/joc.2419, 2012.

World Health Organization: WHO global air quality guidelines: particulate matter ($PM_{2.5}$ and PM_{10}), ozone, nitrogen dioxide, sulfur dioxide and carbon monoxide, https://apps.who.int/iris/bitstream/handle/10665/345329/9789240034228eng.pdf?sequence=1&isAllowed=y (last access: 25 March 2022), 2021.

World Meteorological Organization: Atmospheric deposition, https://public.wmo.int/en/our-mandate/focus-areas/environment/atmospheric-deposition (last access: 02 June 2022), 2022.

Zhang, Y., Feng, J., Liu, C., Zhao, J., Ma, W., Huang, C., An, J., Shen, Y., Fu, Q., Wang, S., Ding, D., Ge, W., Fung, F., Manokaran, K., Patton, A. P., Walker, K. D., and Kan, H.: Impacts of shipping on air pollutant emissions, air quality, and health in the Yangtze river delta and Shanghai, China Special Report 22, Heal. Eff. Inst. Spec. Rep., 22, 1–78, 2019.

Appendix

A: Appendix to Chapter 4

A.1: Wind speed in Hamburg

Input data for wind speed were used from Hamburg weather mast, provided by the Integrated Climate Data Center (ICDC) (ICDC, 2022). The weather mast is positioned at a meteorological measurement station in Billwerder, Hamburg (53° 31′ 09.0″ N, 10° 06′ 10.3″ E). Hourly data from the full year 2018 were statistically analyzed at five different measurement heights (Fig. A.1, Table A.1).

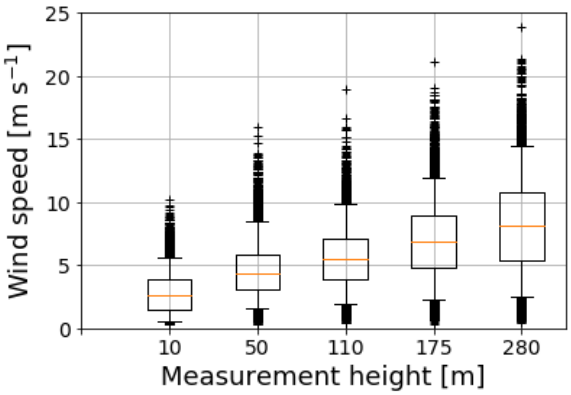

Figure A.1: Boxplots of hourly wind speed data for the year 2018 from Hamburg weather mast. Red lines indicate median values, lower and upper whiskers end at 5th and 95th percentile, respectively.

Table A.1: Statistical data on hourly wind speed values [m s^{-1}] from Hamburg weather mast for the year 2018.

Wind speed [m s^{-1}]	**10 m**	**50 m**	**110 m**	**175 m**	**280 m**
Mean	2.8	4.6	5.6	7.0	8.2
Median	2.6	4.3	5.5	6.9	8.1
5th percentile	0.6	1.6	1.9	2.3	2.5
90th percentile	5.0	7.4	8.7	10.8	13.1
95th percentile	5.7	8.5	9.9	12.0	14.4
99th percentile	7.2	10.8	12.1	14.6	16.9
Maximum	10.2	16.0	18.9	21.1	23.9

A.2: Plume temperature

Figure A.2 presents results for maximum temperatures in the MITRAS domain for one case with the highest temperature (400 °C). Ambient temperatures (15 °C) are reached at a horizontal distance of approximately 100 m from the stack.

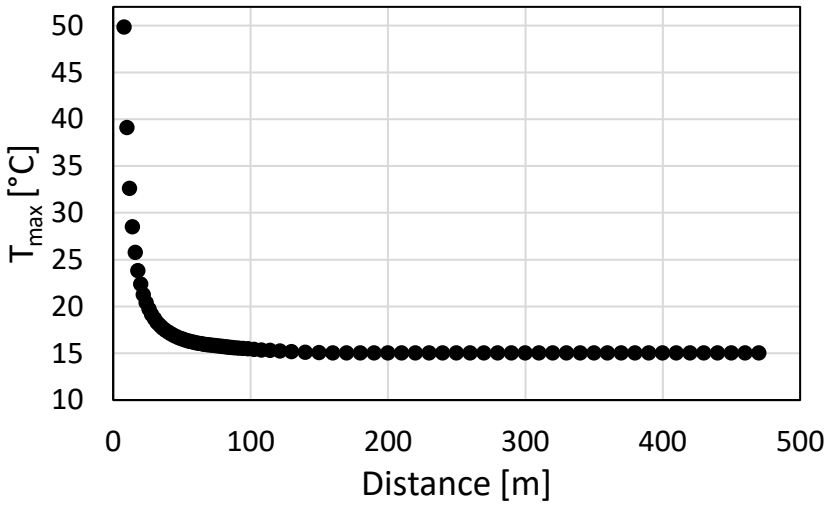

Figure A.2: Results for calculated maximum temperatures in the MITRAS domain in distance downwind from the stack for a case of 400 °C plume with ambient temperature of 15 °C. The values closer to the stack are not shown for clarity. The thermic effect on the plume rise due to the hot exhaust gas vanishes at around 100 m distance from the stack.

A.3: Regressions

This section describes the general application of linear and multiple regression on the model results.

A.3.1: Single linear regression

A simple approach to estimate a target variable Y (e.g., the downward dispersion) from one single independent variable X (e.g., the wind speed) is a linear regression in the form of

$$\hat{Y} = \widehat{\beta_0} + \widehat{\beta_1} X \,, \tag{A.1}$$

where β_0 and β_1 are the ordinate axis intersection and the slope, respectively, and the circumflex (^) describes an estimated parameter. $\widehat{\beta_0}$ and $\widehat{\beta_1}$ are calculated with the least squares method, minimizing the quadratic deviation between model result values Y_i and estimated values $\hat{Y}_i$. The required function Q reads:

$$Q\left(\widehat{\beta_0}, \widehat{\beta_1}\right) = \sum_{i=1}^{n} \left(Y_i - \hat{Y}_i\right)^2 = \sum_{i=1}^{n} \left(Y_i - \widehat{\beta_0} - \widehat{\beta_1} X_i\right)^2 \tag{A.2}$$

Minimizing is done by applying partial derivations from Q to $\widehat{\beta_0}$ and $\widehat{\beta_1}$. This results in

$$\widehat{\beta_0} = \overline{Y} - \widehat{\beta_1}\overline{X}\,, \tag{A.3}$$

$$\widehat{\beta_1} = \frac{\sum_{i=1}^{n}((X_i-\overline{X})(Y_i-\overline{Y}))}{\sum_{i=1}^{n}(X_i-\overline{X})^2}, \tag{A.4}$$

where $\overline{X}$ and $\overline{Y}$ are the mean values of the corresponding dataset.

A.3.2: Multiple regression

The variable Y can depend on more than one independent input variable (X_1, X_2, …, X_p). Then, a multiple regression can be applied and in the case of linear dependencies, the corresponding regression is called multilinear. The multilinear estimation for $\hat{Y}$ reads:

$$\widehat{Y} = \widehat{\beta_0} + \widehat{\beta_1}X_1 + \widehat{\beta_2}X_2 + \ldots + \widehat{\beta_p}X_p \tag{A.5}$$

Again, the minimum distance between Y_i and $\widehat{Y_i}$ can be calculated by the least squares method, similar to the case of linear regression, by minimizing the function Q:

$$Q\left(\widehat{\beta_0}, \widehat{\beta_1}, \widehat{\beta_2}, \ldots \widehat{\beta_p}\right) = \sum_{i=1}^{n}\left(Y_i - \widehat{\beta_0} - \widehat{\beta_1}X_{i,1} - \widehat{\beta_2}X_{i,2} - \ldots - \widehat{\beta_p}X_{i,p}\right)^2 \tag{A.6}$$

However, as this can lead to complicated expressions of $\hat{\beta}$, one can make use of a matrix representation.

$$\begin{pmatrix} \widehat{Y_1} \\ \widehat{Y_2} \\ \vdots \\ \widehat{Y_n} \end{pmatrix} = \begin{pmatrix} 1 & X_{11} & X_{12} & \cdots & X_{1p} \\ 1 & X_{21} & X_{22} & \cdots & X_{2p} \\ \vdots & \vdots & \vdots & \ddots & \vdots \\ 1 & X_{n1} & X_{n2} & \cdots & X_{np} \end{pmatrix} \cdot \begin{pmatrix} \widehat{\beta_0} \\ \widehat{\beta_1} \\ \vdots \\ \widehat{\beta_p} \end{pmatrix} \tag{A.7}$$

By using both the transpose (^{T}) and the invert ($^{-1}$) operator, the equations can be transformed to a general solution for $\hat{\beta}$:

$$\begin{pmatrix} \widehat{\beta_0} \\ \widehat{\beta_1} \\ \vdots \\ \widehat{\beta_p} \end{pmatrix} = (\mathbf{X}^T\mathbf{X})^{-1} \cdot \mathbf{X}^T \cdot \begin{pmatrix} \widehat{Y_1} \\ \widehat{Y_2} \\ \vdots \\ \widehat{Y_n} \end{pmatrix} \tag{A.8}$$

Table A.2 presents an overview on the results of the multiple regression.

Table A.2: Data table for regression analyses. $v_{wind,\ in}$ refers to the input wind speed at the top model layer, $v_{wind,\ stack}$ refers to the wind speed at stack height. Further input data are exit velocity (v_{exit}), exhaust temperature (T_{exh}), wind direction (ϕ) with 0° referring to frontal and 90° to lateral wind. Results are given for downward dispersion with and without obstacle effect (D and $D_{stack\text{-}only}$). D_{para} refers to results of the parameterization. The bold values in line number 8 corresponds to the default settings. Values in brackets in $D_{para,\ stack\text{-}only}$ were not included in the multiple regression, because in these cases only the wind direction was changed, which does not affect stack-only results.

No.	$v_{wind,\ in}$ [m s^{-1}]	$v_{wind,\ stack}$ [m s^{-1}]	v_{exit} [m s^{-1}]	T_{exh} [°C]	ϕ [°]	Γ [K · 100 m^{-1}]	D [%]	$D_{stack\text{-}only}$ [%]	D_{para} [%]	$D_{para,\ stack\text{-}only}$ [%]
1	2.0	2.0	10.0	200	0	-0.65	0.0	0.0	0.0	-0.4
2	2.0	2.0	10.0	300	0	-0.65	0.0	0.0	-2.6	-2.2
3	2.0	2.0	10.0	400	0	-0.65	0.0	0.0	-5.2	-4.0
4	2.0	2.0	10.0	200	90	-0.65	1.0	0.0	6.2	(-0.4)
5	2.0	2.1	10.0	300	90	-0.65	0.7	0.0	3.6	(-2.2)
6	2.0	2.1	10.0	400	90	-0.65	0.6	0.0	0.9	(-4.0)
7	5.0	4.7	10.0	200	0	-0.65	11.2	3.9	10.4	4.9
8	**5.0**	**4.7**	**10.0**	**300**	**0**	**-0.65**	**7.0**	**2.3**	**7.7**	**3.2**
9	5.0	4.7	10.0	400	0	-0.65	4.3	1.1	5.1	1.4
10	5.0	4.8	10.0	200	90	-0.65	19.1	3.7	16.5	(4.9)
11	5.0	4.8	10.0	300	90	-0.65	16.6	3.1	13.9	(3.2)
12	5.0	4.8	10.0	400	90	-0.65	13.6	2.1	11.3	(1.4)
13	8.0	6.9	4.0	200	0	-0.65	32.1	14.8	26.8	14.1
14	8.0	6.9	4.0	300	0	-0.65	24.7	10.8	24.2	12.3
15	8.0	6.9	4.0	400	0	-0.65	19.7	8.6	21.6	10.5
16	8.0	7.3	4.0	200	90	-0.65	34.6	16.9	32.9	(14.1)
17	8.0	7.3	4.0	300	90	-0.65	30.8	12.4	30.3	(12.3)
18	8.0	7.3	4.0	400	90	-0.65	27.6	9.9	27.7	(10.5)
19	5.0	4.7	10.0	250	0	-0.65	8.9	3.3	9.1	4.1
20	5.0	4.7	10.0	350	0	-0.65	5.4	1.6	6.4	2.3
21	4.0	3.9	10.0	300	0	-0.65	2.2	0.3	4.3	1.4
22	6.0	5.4	10.0	300	0	-0.65	11.8	4.9	11.2	5.0
23	8.0	6.9	10.0	300	0	-0.65	20.9	9.0	18.1	8.5
24	10.0	8.3	10.0	300	0	-0.65	28.0	12.8	25.0	12.1
25	5.0	4.7	4.0	300	0	-0.65	9.8	3.9	13.8	6.9
26	5.0	4.7	8.0	300	0	-0.65	7.8	2.8	9.8	4.4
27	5.0	4.7	12.0	300	0	-0.65	6.1	1.8	5.7	1.9
28	5.0	5.2	10.0	300	0	0.50	4.4	0.4	5.2	0.9
29	5.0	5.0	10.0	300	0	0.10	4.9	0.6	6.1	1.7
30	5.0	5.0	10.0	300	0	0.00	5.0	0.8	6.1	1.7
31	5.0	4.7	10.0	300	0	-0.50	6.5	1.9	7.1	2.6
32	5.0	4.7	10.0	300	0	-0.98	9.2	3.2	9.8	5.0
33	5.0	4.9	10.0	300	0	-1.20	11.0	4.2	11.6	6.6
34	10.0	9.2	4.0	200	90	-0.98	44.8	20.8	41.9	19.5
35	15.0	11.8	10.0	300	0	-0.65	40.3	21.1	42.2	21.0
36	15.0	13.3	4.0	200	90	-1.20	54.9	31.1	60.9	30.0
37	5.0	4.7	10.0	300	45	-0.65	8.7	2.3	9.6	(3.2)
38	5.0	4.7	10.0	300	60	-0.65	11.5	2.3	10.8	(3.2)
39	5.0	4.7	10.0	300	30	-0.65	7.1	2.3	8.5	(3.2)

A.4: Comparative assessment of the model results

To get an impression on similarities and differences of MITRAS results with a common dispersion model, the results are compared under similar conditions with results from the integral plume model IBJPluris (Janicke and Janicke, 2001), which can be used to describe the plume dispersion in the momentum-driven regime. IBJPluris calculates average plume properties like concentration and temperature along the plume centerline and applies a circular Gaussian dispersion around this central axis. IBJPluris does not account for obstacle-induced turbulence effects and is therefore only compared to stack-only conditions in MITRAS.

Since the primary output of IBJPluris is the plume centerline and not the downward dispersion, a similar centerline height for MITRAS was calculated to compare the plume behavior. Therefore, the centerline in MITRAS $h_{center,\ MITRAS}$ is defined as the median height of the plume mass (i.e., 50% of the plume mass lies below and 50% lies above). It is calculated at the same distance as downward dispersion for a column of 100 m × 100 m (see Fig. 4.4). Since this is an average of values between a distance of 100 m to 200 m, IBJPluris centerline heights were calculated at a distance of 100 m to 200 m as well ($h_{center,\ Pluris}$). Table A.3 gives an overview of the comparison. Δh_{MITRAS} and Δh_{Pluris} are the differences between plume height (52 m) and centerline height for MITRAS and IBJPluris calculations, respectively. Their minimum difference is given by $\min(|\Delta h_{MITRAS} - \Delta h_{Pluris}|)$ in Table A.3, which represents the closest similarity of both models. Results are given at default settings and selected conditions to compare effects of input parameters.

For all selected cases, MITRAS calculates larger centerline height values than IBJPluris. The lowest differences occur at low wind speed, low exhaust temperature and very stable conditions. The strongest differences of over 20 m occur for cases of low exit velocity and high exhaust temperature.

By calculating effective ranges, $r_i = \Delta|\min(|\Delta h_{MITRAS} - \Delta h_{Pluris}|)_{i,\ max} - \min(|\Delta h_{MITRAS} - \Delta h_{Pluris}|)_{i,\ min}|$ for a certain input parameter i, one can evaluate which input parameter causes the highest discrepancy between the models. For example, changing the wind speed only results in an effective range of 1 m, while temperature and stability changes both show effective ranges of 10 m.

The higher plume rise in MITRAS is consistent with the interaction of the hot plume with the ambient air. MITRAS accounts for the change in the thermodynamic field and the heat balance equation creates an additional buoyancy which is not considered in simpler approaches. This explains the high effective range for temperature and stability changes.

This shows that the results for stack-only conditions are reasonable and that MITRAS provides a more complex improvement over simple Gaussian approaches in the near field.

Table A.3: Comparison of results of plume center heights h_{center} for MITRAS and IBJPluris for different selected cases (case numbers based on Table A.2). This table is part of the Supplement of Chapter 4.

Case name & number	v_{wind} [m s^{-1}]	v_{exit} [m s^{-1}]	T_{exh} [°C]	Γ [K · 100 m^{-1}]	$h_{center, MITRAS}$ [m]	Δh_{MITRAS} [m]	$h_{center, Pluris}$ [m]	Δh_{Pluris} [m]	min($\lvert\Delta h_{MITRAS} - \Delta h_{Pluris}\rvert$) [m]
Default (8)	5	10	300	-0.65	110	58	76 – 92	24 – 40	18
Low v_{wind} (2)	2	10	300	-0.65	160	108	117 – 151	65 – 99	9
High v_{wind} (36)	15	10	300	-0.65	76	24	61 – 66	9 – 14	10
Low v_{exit} (25)	5	4	300	-0.65	104	52	71 – 82	19 – 30	22
High v_{exit} (27)	5	12	300	-0.65	112	60	79 – 95	27 – 43	17
Low T_{exh} (7)	5	10	200	-0.65	102	50	77 – 91	25 – 39	11
High T_{exh} (9)	5	10	400	-0.65	116	64	79 – 95	27 – 43	21
Unstable (33)	5	10	300	-1.2	112	60	78 – 93	26 – 41	19
Stable (28)	5	10	300	+0.5	100	48	77 – 91	25 – 39	9

Table A.4: Exemplary comparison of MITRAS results for two different ship types. This table is part of the Supplement of Chapter 4.

Parameter	Cruise Ship	Container Ship
Length	246 m	168 m
Width	30 m	27 m
Height stack	52 m	38 m
Wind speed at stack height	5 m s^{-1}	
Wind direction	frontal	
Exit velocity	10 m s^{-1}	
Exhaust temperature	15 °C	
Stability	-0.65 K · 100 m^{-1}	
Downward Dispersion in 100 m distance	43%	33%

B: Appendix to Chapter 5

B.1: Plume evaluation schemes

Figure B.1 describes the scheme after which vertical concentration profiles from MITRAS have been derived. These concentration profiles were later normalized and used as vertical emission profiles in EPISODE-CityChem.

Figure B.2 describes the scheme for deriving ground-level concentration versus distance plots.

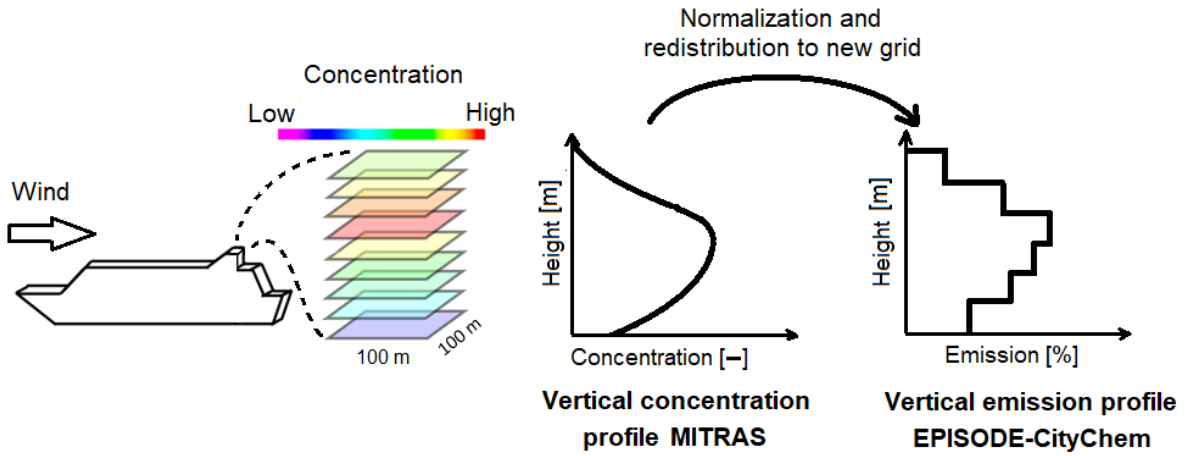

Figure B.1: Scheme for deriving the vertical plume concentration profile from MITRAS and transformation into emission profiles in EPISODE-CityChem. Dimensionless concentration values are derived from mean column values of 100 m × 100 m horizontal and 10 m vertical size in a distance of 100 m downwind from the ship to include plume rise and obstacle-induced turbulence. Normalization of the concentration profile and redistribution into the coarser EPISODE-CityChem grid is done to derive the vertical emission profile in EPISODE-CityChem.

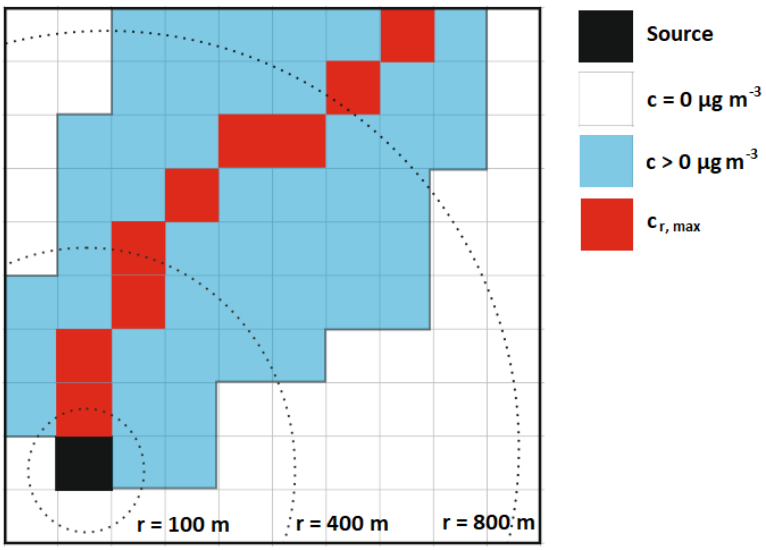

Figure B.2: Scheme for deriving ground-level concentration versus distance plots. Top view of the lowest model layer grid. The grid has a resolution of 100 m × 100 m. Blue cells are affected by the plume concentration, while white cells are not. For every radius of r = 100 m to r = 4000 m a circular function is applied to determine the highest concentration value along the perimeter. This is exemplarily shown for r = 100 m, 400 m and 800 m. Red cells show the resulting path of highest ground-level concentration.

B.2: Gauss and Expgauss statistics

Tables B.1 and B.2 present the results of the Gaussian and Expgauss regression analyses, based on which Eq. (5.2), (5.3) and (5.6)−(5.9) have been derived.

Table B.1: Data table for Gaussian regression analyses. Input data are wind speed at stack height of 50 m (v_{wind}), exit velocity (vexit), exhaust temperature (T_{exh}) and wind direction (ϕ), with 0° referring to frontal and 90° to lateral wind, and atmospheric stability (Γ). Results are mean (μ), standard deviation (σ) and regression coefficient (R^2) for the regression analysis of MITRAS results against the fitted Gaussian functions and regression of fit against parameterization. The bold values in line no. 8 correspond to the default settings.

Case no.	v_{wind} [m s^{-1}]	v_{exit} [m s^{-1}]	T_{exh} [°C]	ϕ [°]	Γ [K · 100 m^{-1}]	μ_{fit}	σ_{fit}	R^2_{fit}	μ_{para}	σ_{para}	$R^2_{fit\ vs.\ para}$
1	2.0	10	200	0	-0.65	143	63.1	0.88	144	63.6	1.00
2	2.0	10	300	0	-0.65	156	73.6	0.85	152	68.9	0.99
3	2.0	10	400	0	-0.65	165	85.3	0.8	159	74.2	0.98
4	2.0	10	200	90	-0.65	141	61.8	0.89	140	68.6	0.99
5	2.0	10	300	90	-0.65	154	72.3	0.86	147	73.9	0.99
6	2.0	10	400	90	-0.65	162	83.4	0.81	155	79.2	0.99
7	5.0	10	200	0	-0.65	98	48.3	0.94	97	47.3	1.00
8	**5.0**	**10**	**300**	**0**	**-0.65**	**106**	**53.7**	**0.90**	**104**	**52.6**	**1.00**
9	5.0	10	400	0	-0.65	112	56.7	0.88	112	57.9	1.00
10	5.0	10	200	90	-0.65	89	53.9	0.96	92	52.3	1.00
11	5.0	10	300	90	-0.65	95	59.4	0.94	100	57.6	1.00
12	5.0	10	400	90	-0.65	101	62.4	0.93	107	62.9	0.99
13	8.0	4	200	0	-0.65	68	38.9	0.97	69	36.5	1.00
14	8.0	4	300	0	-0.65	78	41.8	0.97	76	41.8	1.00
15	8.0	4	400	0	-0.65	84	43.7	0.97	84	47.1	1.00
16	8.0	4	200	90	-0.65	65	40.2	0.99	64	41.5	1.00
17	8.0	4	300	90	-0.65	70	43.8	0.99	72	46.8	1.00
18	8.0	4	400	90	-0.65	75	47.4	0.98	79	52.1	0.99
19	5.0	10	250	0	-0.65	102	50.5	0.91	101	50.0	1.00
20	5.0	10	350	0	-0.65	110	54.8	0.89	108	55.3	1.00
21	4.0	10	300	0	-0.65	115	55.9	0.86	116	56.6	1.00
22	6.0	10	300	0	-0.65	96	49	0.93	95	49.4	1.00
23	8.0	10	300	0	-0.65	83	43.1	0.97	80	44.2	1.00
24	10.0	10	300	0	-0.65	73	42.4	0.97	68	40.3	0.99
25	5.0	4	300	0	-0.65	100	50.1	0.91	101	50.2	1.00
26	5.0	8	300	0	-0.65	104	52.3	0.90	103	51.8	1.00
27	5.0	12	300	0	-0.65	108	54.1	0.89	106	53.4	1.00
28	5.0	10	300	0	0.50	97	35.9	0.93	104	37.4	0.97
29	5.0	10	300	0	0.10	100	40.4	0.93	104	42.7	0.99
30	5.0	10	300	0	0.00	102	41.8	0.92	104	44.0	1.00
31	5.0	10	300	0	-0.50	105	50.2	0.91	104	50.6	1.00
32	5.0	10	300	0	-0.98	96	50.1	0.84	104	57.0	0.97
33	5.0	10	300	0	-1.20	93	50.0	0.85	104	59.9	0.95
34	10.0	4	200	90	-0.98	49	45.2	0.98	52	41.9	1.00
35	15.0	10	300	0	-0.65	58	37.7	0.96	47	33.0	0.93
36	15.0	4	200	90	-1.20	40	40.2	0.99	31	37.5	0.97
37	5.0	10	300	45	-0.65	102	53.1	0.88	103	54.1	1.00
38	5.0	10	300	60	-0.65	98	55.8	0.90	102	55.1	1.00
39	5.0	10	300	30	-0.65	103	51.8	0.88	104	53.3	1.00

Table B.2: Data table for Expgauss regression analyses. Input data are wind speed at stack height of 50 m (v_{wind}), exit velocity (v_{exit}), exhaust temperature (T_{exh}) and wind direction (ϕ), with 0° referring to frontal and 90° to lateral wind, and atmospheric stability (Γ). Results are upper plume boundary height (h_{up}), shape parameters for the Expgauss function (λ_1, λ_2, λ_3) and regression coefficient (R^2) for the regression analysis of MITRAS results against the fitted Expgauss functions and regression of fit against parameterization. The bold values in line no. 8 correspond to the default settings.

Case No.	v_{wind} [m s^{-1}]	v_{exit} [m s^{-1}]	T_{exh} [°C]	ϕ [°]	Γ [K · 100 m^{-1}]	h_{up} [m]	$\lambda_{1, fit}$	$\lambda_{2, fit}$	$\lambda_{3, fit}$	R^2_{fit}	$h_{up, para}$ [m]	$\lambda_{1,para}$	$\lambda_{2, para}$	$\lambda_{3, para}$	R^2_{fit} vs. para
1	2.0	10	200	0	-0.65	229	0.0037	67.40	7.97	1.00	232	0.0033	66.69	13.32	0.99
2	2.0	10	300	0	-0.65	261	0.0037	70.64	9.10	1.00	249	0.0033	68.99	11.97	0.99
3	2.0	10	400	0	-0.65	298	0.0040	71.45	9.24	1.00	265	0.0033	71.29	10.62	0.99
4	2.0	10	200	90	-0.65	229	0.0042	69.52	8.30	1.00	232	0.0033	63.83	21.60	0.94
5	2.0	10	300	90	-0.65	261	0.0041	71.88	8.99	1.00	249	0.0033	66.13	20.25	0.95
6	2.0	10	400	90	-0.65	298	0.0044	72.26	9.43	1.00	265	0.0033	68.43	18.90	0.96
7	5.0	10	200	0	-0.65	170	0.0069	44.38	12.89	0.99	187	0.0093	45.72	13.32	0.99
8	5.0	10	300	0	-0.65	186	0.0065	47.26	8.53	0.99	203	0.0093	48.02	11.97	0.97
9	5.0	10	400	0	-0.65	200	0.0067	50.44	7.71	0.99	220	0.0093	50.32	10.62	0.97
10	5.0	10	200	90	-0.65	170	0.0100	38.17	22.62	0.99	187	0.0093	42.86	21.60	0.96
11	5.0	10	300	90	-0.65	186	0.0081	37.76	19.32	1.00	203	0.0093	45.16	20.25	0.96
12	5.0	10	400	90	-0.65	200	0.0101	43.48	20.53	0.96	220	0.0093	47.46	18.90	0.97
13	8.0	4	200	0	-0.65	160	0.0203	35.07	22.18	0.95	164	0.0153	34.96	13.32	0.93
14	8.0	4	300	0	-0.65	180	0.0222	44.83	27.57	0.95	180	0.0153	37.26	11.97	0.88
15	8.0	4	400	0	-0.65	200	0.0196	48.01	26.54	0.96	197	0.0153	39.56	10.62	0.86
16	8.0	4	200	90	-0.65	160	0.0340	41.13	32.31	0.98	164	0.0153	32.10	21.60	0.92
17	8.0	4	300	90	-0.65	180	0.0249	39.42	31.09	0.98	180	0.0153	34.40	20.25	0.94
18	8.0	4	400	90	-0.65	200	0.0143	33.43	25.32	0.99	197	0.0153	36.70	18.90	0.98
19	5.0	10	250	0	-0.65	178	0.0067	45.52	9.49	0.99	195	0.0093	46.87	12.65	0.98
20	5.0	10	350	0	-0.65	192	0.0065	48.94	7.93	0.99	212	0.0093	49.17	11.29	0.97
21	4.0	10	300	0	-0.65	202	0.0061	52.65	5.38	1.00	215	0.0073	53.12	11.97	0.97
22	6.0	10	300	0	-0.65	180	0.0084	44.24	13.51	1.00	194	0.0113	43.84	11.97	0.96
23	8.0	10	300	0	-0.65	170	0.0139	41.17	21.32	0.97	180	0.0153	37.26	11.97	0.90
24	10.0	10	300	0	-0.65	160	0.0147	33.76	19.98	0.96	169	0.0193	32.15	11.97	0.90
25	5.0	4	300	0	-0.65	178	0.0069	44.62	9.69	1.00	203	0.0093	48.02	11.97	0.98
26	5.0	8	300	0	-0.65	182	0.0067	46.44	8.87	0.99	203	0.0093	48.02	11.97	0.98
27	5.0	12	300	0	-0.65	190	0.0063	48.17	8.17	0.99	203	0.0093	48.02	11.97	0.96
28	5.0	10	300	0	0.50	144	0.0038	51.29	6.51	1.00	76	0.0027	52.45	5.07	0.99
29	5.0	10	300	0	0.10	160	0.0056	50.69	7.19	0.99	122	0.0050	50.91	7.47	1.00
30	5.0	10	300	0	0.00	160	0.0046	49.92	6.63	1.00	124	0.0056	50.52	8.07	1.00
31	5.0	10	300	0	-0.50	180	0.0058	47.76	7.87	1.00	171	0.0084	48.59	11.07	0.98
32	5.0	10	300	0	-0.98	300	0.0110	45.59	9.28	0.99	305	0.0112	46.74	13.95	0.99
33	5.0	10	300	0	-1.20	400	0.0112	44.00	10.61	1.00	396	0.0125	45.89	15.27	0.99
34	10.0	4	200	90	-0.98	260	0.0227	19.24	26.65	1.00	254	0.0212	25.72	23.58	0.97
35	15.0	10	300	0	-0.65	150	0.0180	25.48	16.36	0.99	149	0.0293	22.87	11.97	0.82
36	15.0	4	200	90	-1.20	400	0.0343	17.80	30.34	1.00	325	0.0325	15.59	24.90	0.99
37	5.0	10	300	45	-0.65	186	0.0076	45.65	7.90	1.00	203	0.0093	47.16	14.45	0.97
38	5.0	10	300	60	-0.65	186	0.0085	43.08	13.41	0.99	203	0.0093	46.59	16.11	0.98
39	5.0	10	300	30	-0.65	186	0.0067	45.22	5.25	1.00	203	0.0093	47.64	13.05	0.94

B.3: Single regression range-table

Table B.3 presents a quantitative comparison of how strong the different input parameters affect the shape parameters for Gaussian and Expgauss fits.

Table B.3: Quantitative representation of how strong input parameters affect the shape parameters for Gaussian and Expgauss fits. Values in the table indicate the possible change that an input variable could cause on the concentration profile shape parameters (while all other inputs remained at default conditions, comparable to effective ranges in Chapter 4. Bold values were used for the parameterization as they had both a strong impact and a clear correlation.

Input variable	**Range**	**Gaussian Fit**		**Expgauss Fit**			
		μ	σ	λ_1	λ_2	λ_3	h_{up}
Wind Speed	2–15 m s^{-1}	**98.0**	**35.9**	**0.0145**	**45.16**	15.94	**110 m**
Wind direction	0–90° (frontal to lateral)	**11.0**	**7.6**	0.0020	9.50	**14.07**	0 m
Exit velocity	4–12 m s^{-1}	**8.0**	**4.0**	0.0006	**3.55**	1.52	12 m
Exhaust temperature	200–400 °C	**14.0**	**8.4**	0.0006	**6.06**	**5.18**	**30 m**
Stability	-1.2–0.5 K · 100 m^{-1}	13.0	**17.8**	**0.0074**	**7.29**	**4.10**	**257 m**

B.4: Comparison of parameterizations

Figure B.3 presents different input profiles for the EPISODE-CityChem simulation part of this study and the effect of atmospheric stability and wind speed on the profile shape. Figure B.4 compares ground-level concentration values depending on the distance to the source for different settings and initial profiles. Table B.4 summarizes the results of Chapters 5.2 to 5.4 and allows a comparison of the effect of different input variables on the ground-level concentration. Maximum absolute concentration differences (Δc_{max}) for the individual variable (surface roughness, stability, wind speed) and initial emission profile (Gauss, SCE, Expgauss) are presented.

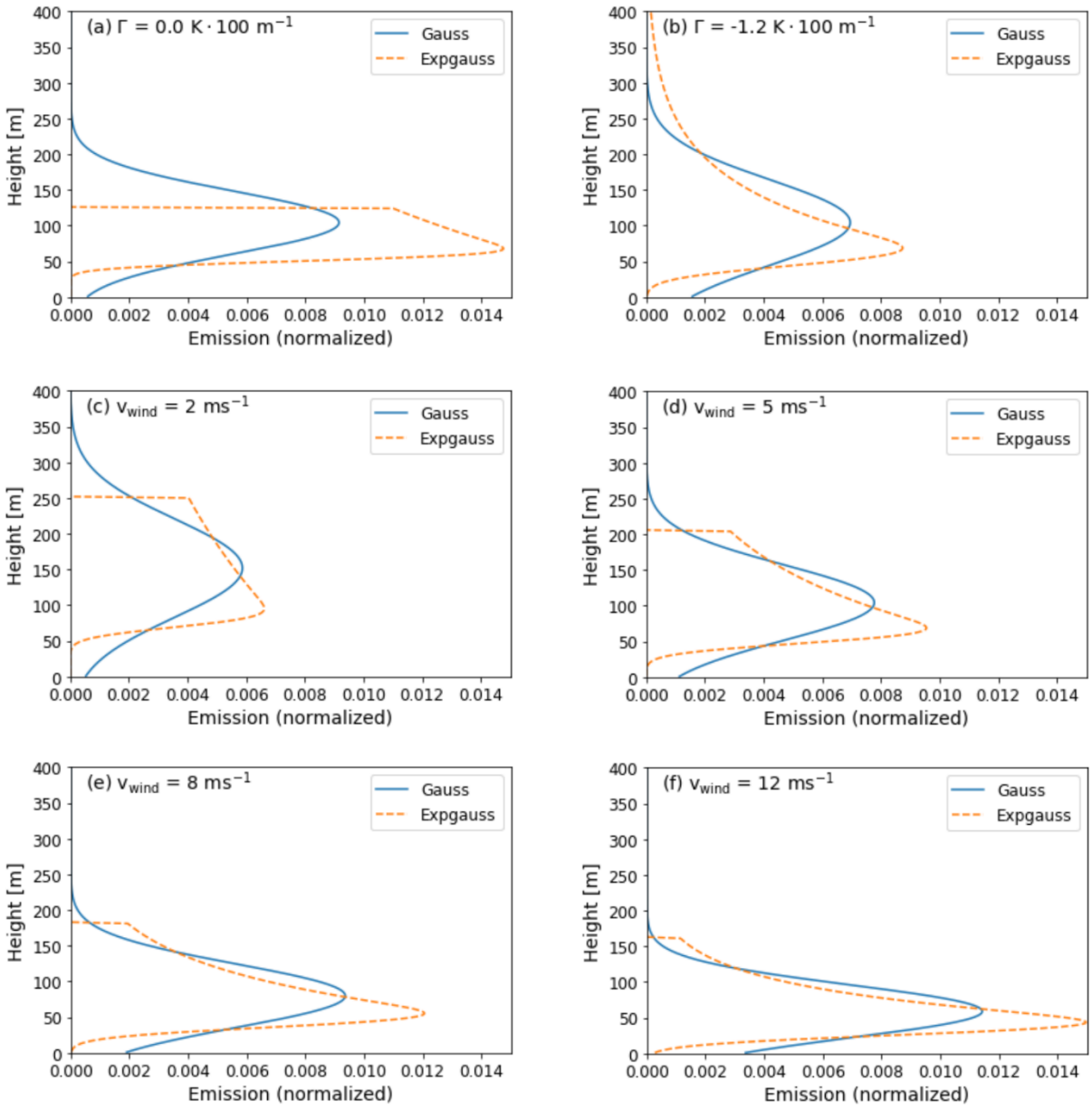

Figure B.3: Initial EPISODE-CityChem emission profiles under default input settings (v_{wind} = 5 m s^{-1}, v_{exit} = 10 m s^{-1}, T_{exh} = 300 °C, Γ = -0.65 K · 100 m^{-1}, ϕ = 0° and $z_{0,\,land}$ = 1 m) for all but one parameter. Panels (a) and (b) show effects of varying the stability while panels (c)−(f) show effects of varying the wind speed. Panel (d) represents full default conditions.

Table B.4: Comparison of effects of different input variables and initial emission profiles on the ground-level concentration. Values of Δc_{max} correspond to the highest absolute differences. Their corresponding relative difference is added in parenthesis and the distance of Δc_{max} is given as well.

Variable	**Variable range**	**$\Delta c_{max,\ Gauss}$**	**$\Delta c_{max,\ SCE}$**	**$\Delta c_{max,\ Expgauss}$**
Roughness length	0.1 m−1.0 m	0.1 m: 2.72 µg m^{-3} (113%) higher than 1.0 m at 700 m distance	0.1 m: 1.26 µg m^{-3} (88%) higher than 1.0 m at 1400 m distance	0.1 m: 2.29 µg m^{-3} (128%) higher than 1.0 m at 700 m distance
Stability	-1.2 K · 100 m^{-1} −0.0 K · 100 m^{-1}	-1.2 K · 100 m^{-1}: 3.16 µg m^{-3} (241%) higher than 0.0 K · 100 m^{-1} at 200 m distance	-1.2 K · 100 m^{-1}: 1.45 µg m^{-3} (302%) higher than 0.0 K · 100 m^{-1} at 900 m distance	-1.2 K · 100 m^{-1}: 2.0 µg m^{-3} (378%) higher than 0.0 K · 100 m^{-1} at 200 m distance
Wind speed	1 m s^{-1}−12 m s^{-1}	1 m s^{-1}: 9.12 µg m^{-3} (374%) higher than 3 m s^{-1} at 200 m distance	1 m s^{-1}: 9.63 µg m^{-3} (1095%) higher than 5 m s^{-1} at 600 m distance	1 m s^{-1}: 9.73 µg m^{-3} (506%) higher than 5 m s^{-1} at 600 m distance

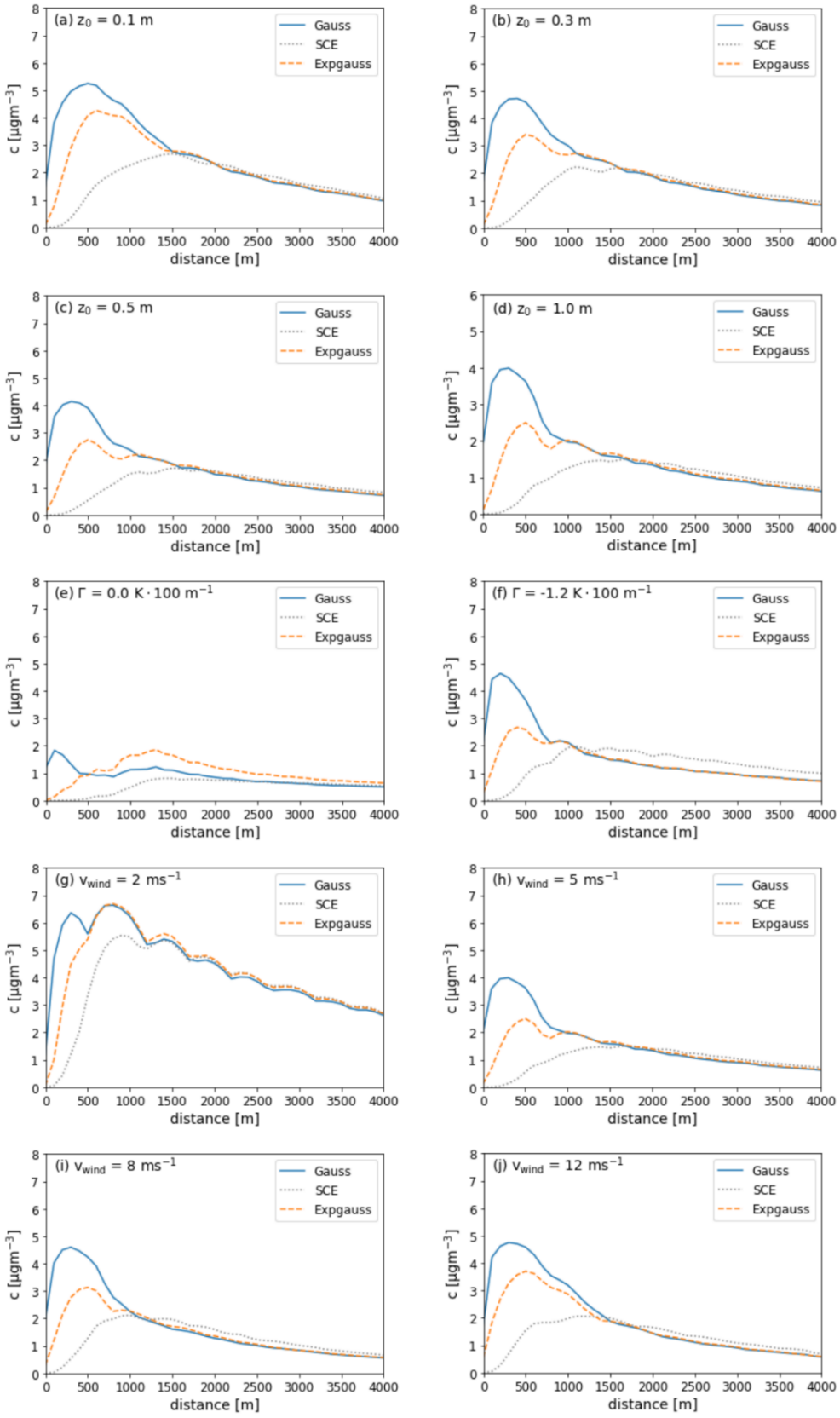

Figure B.4: Comparison for ground-level concentration values depending on the distance to the source for different settings and initial profiles. Default input settings (v_{wind} = 5 m s^{-1}, v_{exit} = 10 m s^{-1}, T_{exh} = 300 °C, Γ = -0.65 K · 100 m^{-1}, ϕ = 0° and $z_{0,\,land}$ = 1.0 m) were used for all but one parameter. Panels (a)−(d) vary roughness lengths over land, panels (e) and (f) vary atmospheric stability. Panels (g)−(j) vary wind speed. Panel (h) represents full default conditions.

C: Appendix to Chapter 6

C.1: Statistical evaluation of TAPM

The suitability of the TAPM meteorology for the correct modeling of the wind fields in EPISODE-CityChem and thus the dispersion of pollutants was checked by a statistical comparison with measurement data from the Hamburg weather mast.

Since wind direction is given as an angle, simple regressions between observation and model need a correction for the transition for the matching of 0° and 360°. Therefore, it is easier to evaluate wind direction by representing it with the wind vectors $\vec{u}$ and $\vec{v}$.

$$\vec{u} = -v_{wind} \cdot \sin(dd) \quad \text{(C.1)}$$

$$\vec{v} = -v_{wind} \cdot \cos(dd), \quad \text{(C.2)}$$

where v_{wind} is the wind speed and dd is the wind direction as radians.

Wind speed is compared at ground level, to investigate, if the source-near dispersion is represented correctly. Wind direction is compared at 280 m height to see if the model can represent the large-scale movement of air masses.

The statistical indicators presented in Chapter 6.1.8 are used to evaluate the TAPM performance in Table C.1. An overall good agreement was found, e.g., with regression values between 0.76 and 0.98. The differences for $\vec{v}$ (north-south component) tend to be larger than for $\vec{u}$, therefore, performance of north-south wind predictions are slightly less accurate.

Table C.1: Statistical indicators for comparison of TAPM modeled wind vectors and wind speed with measured values at the Hamburg weather mast.

	January			**August**		
	$\vec{u}$ (280 m)	**$\vec{v}$ (280 m)**	**v_{wind} (10 m)**	**$\vec{u}$ (280 m)**	**$\vec{v}$ (280 m)**	**v_{wind} (10 m)**
$Mean_{model}$ [m s^{-1}]	4.26	5.13	3.71	3.83	1.15	2.58
$Mean_{obs}$ [m s^{-1}]	3.45	3.40	3.43	3.68	0.93	2.70
Bias [m s^{-1}]	0.81	1.73	0.28	0.18	0.22	-0.12
NMB [%]	23	51	8	4	24	-4
RMSE [m s^{-1}]	1.95	2.44	0.91	1.75	1.79	0.99
STD_{model} [m s^{-1}]	8.96	5.20	1.61	4.9	4.9	1.3
STD_{obs} [m s^{-1}]	8.61	4.65	1.79	4.69	4.51	1.47
R [-]	0.98	0.94	0.88	0.93	0.93	0.76
IOA [-]	0.90	0.72	0.75	0.83	0.82	0.67
FAC2 [-]	0.87	0.72	0.93	0.79	0.74	0.83

C.2: Ship height in MoSES

Several new options for determining the individual ship height in MoSES have been added to the modular system, based on the IHS Markit 2020 ship database information. If information on the draught and the keel-to-mast height are available, the ship height over sea surface is calculated according to Eq. (6.2).

However, if data for an individual ship are missing, they can be calculated with parameterization formulae derived from information of the part of the fleet, which has complete data.

The parameterizations have been derived by linear regression analysis. The best linear dependency was found for a regression between ship height and keel-to-mast height ($R^2 = 0.96$, Fig. C.1a). The derived linear regression formula is:

$$h_{ship} = 0.788 + 0.747\, h_{keel\text{-}to\text{-}mast} \qquad (C.3)$$

This is the preferred option if only the draught information is missing.

If both draught and keel-to-mast height are missing, ship height is parameterized based on regressions with length (l_{ship}) and width (w_{ship}). Single regressions of ship height with length and width show a good linear dependency (Fig. C.1b and C.1c).

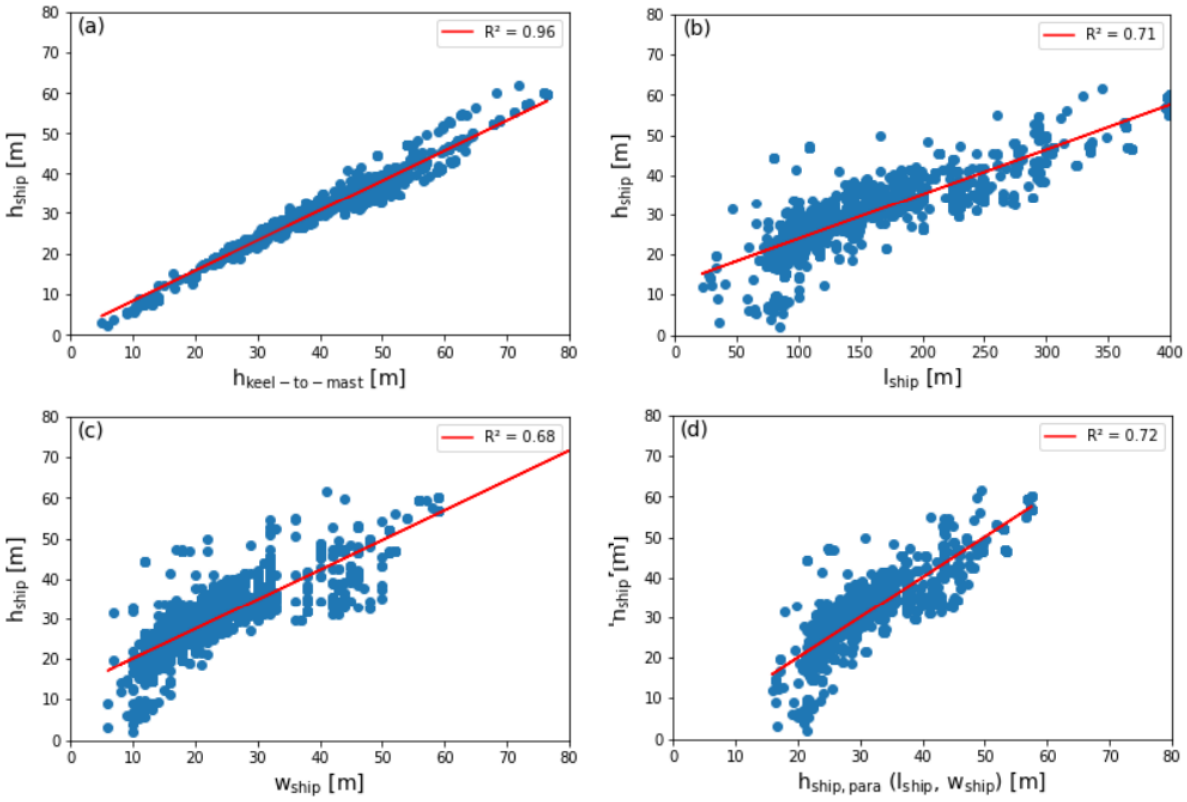

Figure C.1: Regression plots for single regressions of ship heights with (a) keel-to-mast height, (b) length and (c) width of the ship. Panel (d) shows the regression of the ship height with a parameterized height based on ship length and width.

From this information, a multiple linear regression formula has been derived (similar to A.3.2) and reads:

$$h_{ship,para} = 12.46 + 0.084\ l_{ship} + 0.195\ w_{ship} \quad \text{(C.4)}$$

The correlation of the parameterized heights and the given heights has an R^2 value of 0.72 (Fig. C.1d). Based on this formula, an average ship height of ~25 m was derived as input value for Chapter 6.

If only length and width of the ship are available, this is the preferred method to derive the height. If only the length is given, the single linear regression with the length is used to derive the height ($R^2 = 0.71$):

$$h_{ship} = 12.77 + 0.11\ l_{ship} \quad \text{(C.5)}$$

There have been no cases where only the width and not the length were given. The formula for this case would be

$$h_{ship} = 12.69 + 0.74\ w_{ship} \quad \text{(C.6)}$$

It has an R^2 value of 0.68.

If all information (draught, keel-to-mast height, length and width) of the ship are missing, then no value for the individual ship height was added to the fleet information. This was the case for approximately 9% of the ships. With the parameterization formulae, approximately 57% of ship height information could be added.

C.3: Statistical comparison of Flexplume and Fixplume results

Tables C.2 to C.7 give a comprehensive overview of the statistical differences between Flexplume and Fixplume model results compared to measurements at different measurement station positions in the inner-city of Hamburg.

Figure C.2 provides information on the EPISODE-CityChem model performance depending on the wind sector based on the Fixplume approach (for comparisons with Fig. 6.9).

Table C.2: Statistical indicators for comparison of modeled NO concentrations in January with observations at different measurements stations for hourly and daily means and different wind sectors. Station names have been abbreviated according to Table 6.3.

	Flexplume						Fixplume					
80KT	**hourly**	**daily**	**NE**	**SE**	**SW**	**NW**	**hourly**	**daily**	**NE**	**SE**	**SW**	**NW**
$Mean_{model}$ [µg m^{-3}]	15.00	13.24	21.72	23.26	11.66	7.57	24.78	19.31	22.13	36.42	21.59	14.57
$Mean_{obs}$ [µg m^{-3}]	13.43	12.04	13.90	18.62	11.73	9.10	13.43	12.04	13.90	18.62	11.73	9.10
Bias [µg m^{-3}]	1.57	1.20	7.82	4.64	-0.07	-1.53	11.35	7.27	8.23	17.80	9.87	5.48
NMB [%]	12	10	56	25	-1	-17	85	60	59	96	84	60
RMSE [µg m^{-3}]	19.99	8.32	33.98	25.47	14.74	14.45	45.34	18.44	33.93	62.75	39.17	25.76
STD_{model} [µg m^{-3}]	20.99	16.13	25.05	27.15	16.10	13.06	47.35	24.81	25.25	62.35	42.19	32.04
STD_{meas} [µg m^{-3}]	20.05	13.33	35.06	20.79	16.77	17.36	20.05	13.33	35.06	20.79	16.77	17.36
IOA [-]	0.55	0.71	0.50	0.35	0.63	0.61	0.22	0.47	0.49	-0.11	0.27	0.45
R [-]	0.53	0.86	0.43	0.48	0.60	0.59	0.38	0.76	0.44	0.27	0.44	0.62
R^2 [-]	0.28	0.74	0.19	0.23	0.36	0.34	0.14	0.58	0.20	0.07	0.19	0.39
FAC2 [-]	0.47	0.84	0.38	0.37	0.57	0.39	0.44	0.61	0.30	0.32	0.54	0.43
	Flexplume						**Fixplume**					
72FI	**hourly**	**daily**	**NE**	**SE**	**SW**	**NW**	**hourly**	**daily**	**NE**	**SE**	**SW**	**NW**
$Mean_{model}$ [µg m^{-3}]	13.10	11.75	23.03	31.39	5.28	1.96	31.61	26.47	32.77	67.18	18.92	9.60
$Mean_{obs}$ [µg m^{-3}]	9.47	8.34	20.53	15.42	6.04	5.22	9.47	8.34	20.53	15.42	6.04	5.22
Bias [µg m^{-3}]	3.64	3.42	2.50	15.97	-0.76	-3.27	22.14	18.14	12.24	51.76	12.88	4.38
NMB [%]	38	41	12	104	-13	-63	234	218	60	336	213	84
RMSE [µg m^{-3}]	19.96	9.52	34.92	28.39	11.25	14.48	58.18	40.55	41.87	85.02	47.08	33.58
STD_{model} [µg m^{-3}]	26.13	20.64	28.06	35.93	15.87	3.38	63.90	49.70	35.28	83.44	53.61	30.46
STD_{meas} [µg m^{-3}]	22.05	15.75	37.20	28.10	14.62	16.57	22.05	15.75	37.20	28.10	14.62	16.57
IOA [-]	0.61	0.73	0.63	0.45	0.70	0.63	-0.09	0.06	0.46	-0.34	-0.13	0.14
R [-]	0.68	0.92	0.46	0.76	0.73	0.78	0.59	0.90	0.39	0.68	0.66	0.09
R^2 [-]	0.46	0.84	0.21	0.57	0.54	0.60	0.35	0.80	0.15	0.47	0.44	0.01
FAC2 [-]	0.39	0.58	0.31	0.32	0.46	0.36	0.33	0.45	0.22	0.10	0.41	0.51
	Flexplume						**Fixplume**					
82HF	**hourly**	**daily**	**NE**	**SE**	**SW**	**NW**	**hourly**	**daily**	**NE**	**SE**	**SW**	**NW**
$Mean_{model}$ [µg m^{-3}]	13.24	12.68	18.39	13.21	9.79	23.01	20.70	18.68	15.80	17.19	17.50	40.87
$Mean_{obs}$ [µg m^{-3}]	22.23	20.43	25.34	25.62	18.12	28.83	22.23	20.43	25.34	25.62	18.12	28.83
Bias [µg m^{-3}]	-8.99	-7.75	-6.95	-12.41	-8.33	-5.82	-1.53	-1.75	-9.54	-8.43	-0.62	12.03
NMB [%]	-40	-38	-27	-48	-46	-20	-7	-9	-38	-33	-3	42
RMSE [µg m^{-3}]	35.79	14.74	55.27	35.62	27.74	47.71	40.26	18.75	54.86	35.86	30.73	63.15
STD_{model} [µg m^{-3}]	19.19	14.02	25.21	21.02	11.37	28.21	32.93	21.78	21.87	24.51	23.84	60.20
STD_{meas} [µg m^{-3}]	37.07	19.48	56.62	36.83	27.51	50.97	37.07	19.48	56.62	36.83	27.51	50.97
IOA [-]	0.59	0.62	0.67	0.59	0.54	0.62	0.51	0.52	0.69	0.56	0.45	0.44
R [-]	0.38	0.77	0.29	0.44	0.30	0.40	0.34	0.60	0.31	0.41	0.29	0.39
R^2 [-]	0.15	0.59	0.09	0.19	0.09	0.16	0.12	0.35	0.10	0.17	0.08	0.15
FAC2 [-]	0.33	0.45	0.28	0.32	0.35	0.37	0.31	0.42	0.26	0.25	0.37	0.28

Table C.2: continued.

	Flexplume						Fixplume					
13ST	**hourly**	**daily**	**NE**	**SE**	**SW**	**NW**	**hourly**	**daily**	**NE**	**SE**	**SW**	**NW**
$Mean_{model}$ [µg m^{-3}]	10.84	9.41	23.29	14.34	8.19	7.43	11.65	9.76	23.29	14.36	9.31	9.03
$Mean_{obs}$ [µg m^{-3}]	8.32	7.25	13.37	8.93	8.04	5.68	8.32	7.25	13.37	8.93	8.04	5.68
Bias [µg m^{-3}]	2.53	2.16	9.92	5.41	0.15	1.75	3.34	2.50	9.92	5.43	1.28	3.35
NMB [%]	30	30	74	61	2	31	40	34	74	61	16	59
RMSE [µg m^{-3}]	16.48	5.67	31.68	17.94	13.33	12.36	18.04	5.74	31.68	17.94	14.59	20.03
STD_{model} [µg m^{-3}]	17.76	12.48	29.05	22.26	12.49	11.82	19.61	12.62	29.05	22.25	15.05	20.04
STD_{meas} [µg m^{-3}]	14.74	9.24	26.57	13.90	13.54	11.29	14.74	9.24	26.57	13.90	13.54	11.29
IOA [-]	0.54	0.73	0.41	0.48	0.61	0.50	0.51	0.72	0.41	0.48	0.58	0.35
R [-]	0.51	0.93	0.42	0.64	0.48	0.44	0.50	0.93	0.42	0.64	0.49	0.31
R^2 [-]	0.26	0.86	0.17	0.41	0.23	0.19	0.25	0.87	0.17	0.41	0.24	0.09
FAC2 [-]	0.51	0.71	0.35	0.59	0.51	0.49	0.51	0.71	0.35	0.59	0.50	0.50
	Flexplume						**Fixplume**					
70MB	**hourly**	**daily**	**NE**	**SE**	**SW**	**NW**	**hourly**	**daily**	**NE**	**SE**	**SW**	**NW**
$Mean_{model}$ [µg m^{-3}]	56.93	56.39	73.42	45.77	59.06	63.04	59.54	58.29	73.42	48.01	62.53	64.58
$Mean_{obs}$ [µg m^{-3}]	35.28	34.79	54.90	31.59	35.59	31.96	35.28	34.79	54.90	31.59	35.59	31.96
Bias [µg m^{-3}]	21.65	21.60	18.52	14.18	23.47	31.08	24.26	23.50	18.52	16.42	26.94	32.62
NMB [%]	61	62	34	45	66	97	69	68	34	52	76	102
RMSE [µg m^{-3}]	38.72	27.29	48.89	30.34	38.28	48.04	44.62	29.51	48.89	37.68	45.6	50.87
STD_{model} [µg m^{-3}]	46.42	28.86	62.03	44.36	41.38	53.33	51.36	30.75	62.03	50.26	48.06	55.02
STD_{meas} [µg m^{-3}]	34.56	22.77	60.09	32.70	30.47	31.58	34.56	22.77	60.09	32.7	30.47	31.58
IOA [-]	0.44	0.30	0.58	0.54	0.41	0.23	0.40	0.24	0.58	0.50	0.35	0.20
R [-]	0.72	0.82	0.73	0.80	0.68	0.74	0.68	0.82	0.73	0.74	0.64	0.72
R^2 [-]	0.52	0.67	0.53	0.64	0.47	0.55	0.47	0.67	0.53	0.55	0.41	0.52
FAC2 [-]	0.54	0.65	0.59	0.57	0.57	0.36	0.53	0.65	0.59	0.56	0.55	0.36
	Flexplume						**Fixplume**					
17SM	**hourly**	**daily**	**NE**	**SE**	**SW**	**NW**	**hourly**	**daily**	**NE**	**SE**	**SW**	**NW**
$Mean_{model}$ [µg m^{-3}]	37.94	38.22	45.86	39.35	35.67	39.36	38.99	39.19	45.86	39.74	37.20	40.55
$Mean_{obs}$ [µg m^{-3}]	30.72	29.20	49.98	47.44	21.51	21.48	30.72	29.20	49.98	47.44	21.51	21.48
Bias [µg m^{-3}]	7.22	9.02	-4.12	-8.08	14.17	17.87	8.27	9.99	-4.12	-7.70	15.70	19.07
NMB [%]	23	31	-8	-17	66	83	27	34	-8	-16	73	89
RMSE [µg m^{-3}]	35.42	21.00	43.71	41.21	30.03	36.36	36.47	21.66	43.71	41.17	31.92	37.94
STD_{model} [µg m^{-3}]	33.47	22.60	48.23	37.87	27.76	33.30	35.03	23.27	48.23	38.33	30.63	34.80
STD_{meas} [µg m^{-3}]	41.48	28.32	60.20	48.7	32.04	29.71	41.48	28.32	60.20	48.70	32.04	29.71
IOA [-]	0.57	0.58	0.71	0.65	0.43	0.30	0.56	0.56	0.71	0.64	0.41	0.26
R [-]	0.59	0.74	0.70	0.59	0.62	0.50	0.58	0.74	0.70	0.59	0.61	0.49
R^2 [-]	0.35	0.55	0.49	0.35	0.38	0.25	0.34	0.55	0.49	0.35	0.37	0.24
FAC2 [-]	0.42	0.58	0.47	0.60	0.35	0.36	0.42	0.58	0.47	0.59	0.34	0.35

Table C.3: Statistical indicators for comparison of modeled NO concentrations in August with observations at different measurements stations for hourly and daily means and different wind sectors. Station names have been abbreviated according to Table 6.3.

	Flexplume						Fixplume					
80KT	**hourly**	**daily**	**NE**	**SE**	**SW**	**NW**	**hourly**	**daily**	**NE**	**SE**	**SW**	**NW**
$Mean_{model}$ [µg m^{-3}]	13.76	9.01	50.50	14.68	12.73	9.38	20.23	12.59	51.06	30.63	20.14	11.24
$Mean_{obs}$ [µg m^{-3}]	6.87	4.85	3.32	6.06	10.35	4.06	6.87	4.85	3.32	6.06	10.35	4.06
Bias [µg m^{-3}]	6.89	4.16	47.18	8.62	2.38	5.32	13.36	7.74	47.74	24.57	9.79	7.18
NMB [%]	100	86	1423	142	23	131	195	160	1440	405	95	177
RMSE [µg m^{-3}]	36.88	7.15	130.7	27.92	26.20	13.86	49.51	11.91	136.2	53.46	46.49	19.14
STD_{model} [µg m^{-3}]	34.13	5.51	121.8	24.24	19.82	13.08	46.2	9.98	127.5	45.49	42.16	18.67
STD_{meas} [µg m^{-3}]	12.96	5.59	3.79	11.27	17.58	6.09	12.96	5.59	3.79	11.27	17.58	6.09
IOA [-]	0.10	0.07	-0.91	-0.09	0.38	-0.01	-0.25	-0.28	-0.91	-0.59	0.07	-0.20
R [-]	0.02	0.45	0.01	0.02	0.03	0.28	0.03	0.44	0.01	-0.06	0.01	0.31
R^2 [-]	0.00	0.20	0.00	0.00	0.00	0.08	0.00	0.19	0.00	0.00	0.00	0.10
FAC2 [-]	0.38	0.45	0.21	0.36	0.39	0.41	0.35	0.39	0.18	0.28	0.37	0.39
	Flexplume						**Fixplume**					
72FI	**hourly**	**daily**	**NE**	**SE**	**SW**	**NW**	**hourly**	**daily**	**NE**	**SE**	**SW**	**NW**
$Mean_{model}$ [µg m^{-3}]	14.38	6.01	24.05	36.93	13.72	3.37	35.1	17.66	127.1	73.96	24.52	15.87
$Mean_{obs}$ [µg m^{-3}]	3.16	2.40	3.87	4.91	2.71	2.72	3.16	2.40	3.87	4.91	2.71	2.72
Bias [µg m^{-3}]	11.22	3.62	20.18	32.02	11.00	0.65	31.94	15.27	123.2	69.05	21.8	13.14
NMB [%]	355	151	522	652	406	24	1012	637	3185	1405	804	483
RMSE [µg m^{-3}]	46.97	8.70	69.76	66.14	54.51	5.70	156.2	24.77	516.1	115.7	65.7	133.0
STD_{model} [µg m^{-3}]	45.56	8.47	67.04	57.06	53.25	5.24	153.1	20.16	501.1	93.43	62.18	132.3
STD_{meas} [µg m^{-3}]	4.67	1.07	5.13	7.58	3.94	3.10	4.67	1.07	5.13	7.58	3.94	3.10
IOA [-]	-0.68	-0.69	-0.70	-0.73	-0.80	0.10	-0.87	-0.92	-0.95	-0.87	-0.88	-0.80
R [-]	0.04	0.57	0.09	-0.04	0.00	0.16	0.06	0.64	-0.02	0.13	0.08	0.00
R^2 [-]	0.00	0.33	0.01	0.00	0.00	0.02	0.00	0.41	0.00	0.02	0.01	0.00
FAC2 [-]	0.45	0.58	0.45	0.24	0.43	0.57	0.35	0.29	0.21	0.05	0.42	0.43
	Flexplume						**Fixplume**					
82HF	**hourly**	**daily**	**NE**	**SE**	**SW**	**NW**	**hourly**	**daily**	**NE**	**SE**	**SW**	**NW**
$Mean_{model}$ [µg m^{-3}]	10.92	7.18	10.01	7.68	10.76	12.72	23.5	12.40	33.67	20.66	19.52	27.71
$Mean_{obs}$ [µg m^{-3}]	10.85	8.30	8.89	14.35	10.63	9.71	10.85	8.30	8.89	14.35	10.63	9.71
Bias [µg m^{-3}]	0.07	-1.13	1.12	-6.66	0.13	3.01	12.65	4.10	24.78	6.32	8.89	18.00
NMB [%]	1	-14	13	-46	1	31	117	49	279	44	84	185
RMSE [µg m^{-3}]	24.97	5.86	21.66	31.09	23.08	24.12	55.37	11.07	81.87	59.41	49.51	54.86
STD_{model} [µg m^{-3}]	22.30	5.94	19.71	21.35	22.7	22.45	52.89	11.12	76.56	53.74	49.5	51.54
STD_{meas} [µg m^{-3}]	15.27	4.40	13.65	21.19	12.52	14.59	15.27	4.40	13.65	21.19	12.52	14.59
IOA [-]	0.41	0.41	0.43	0.38	0.45	0.37	-0.12	0.01	-0.41	-0.06	0.03	-0.24
R [-]	0.16	0.41	0.20	-0.02	0.25	0.22	0.08	0.38	-0.02	-0.07	0.19	0.12
R^2 [-]	0.02	0.17	0.04	0.00	0.06	0.05	0.01	0.14	0.00	0.00	0.04	0.01
FAC2 [-]	0.37	0.71	0.16	0.20	0.49	0.35	0.33	0.52	0.26	0.21	0.42	0.30

Table C.3: continued.

	Flexplume						Fixplume					
13ST	**hourly**	**daily**	**NE**	**SE**	**SW**	**NW**	**hourly**	**daily**	**NE**	**SE**	**SW**	**NW**
$Mean_{model}$ [µg m^{-3}]	8.65	5.79	23.33	6.35	7.57	8.85	9.20	6.07	23.32	6.51	8.67	9.05
$Mean_{obs}$ [µg m^{-3}]	3.51	2.40	2.26	4.07	4.21	2.66	3.51	2.40	2.26	4.07	4.21	2.66
Bias [µg m^{-3}]	5.14	3.39	21.07	2.28	3.36	6.19	5.69	3.67	21.06	2.44	4.46	6.39
NMB [%]	147	141	931	56	80	232	162	153	930	60	106	240
RMSE [µg m^{-3}]	18.23	4.19	53.16	9.92	11.44	17.69	18.84	4.58	53.16	10.04	13.38	17.91
STD_{model} [µg m^{-3}]	17.30	2.48	48.77	8.85	10.11	17.12	17.92	2.77	48.77	8.91	12.39	17.28
STD_{meas} [µg m^{-3}]	4.96	0.67	0.78	5.38	6.09	3.32	4.96	0.67	0.78	5.38	6.09	3.32
IOA [-]	-0.25	-0.70	-0.96	0.27	0.17	-0.64	-0.30	-0.72	-0.96	0.24	0.05	-0.65
R [-]	0.11	0.16	-0.04	0.15	0.16	0.26	0.13	0.17	-0.04	0.14	0.21	0.26
R^2 [-]	0.01	0.03	0.00	0.02	0.03	0.07	0.02	0.03	0.00	0.02	0.04	0.07
FAC2 [-]	0.42	0.39	0.34	0.50	0.43	0.39	0.41	0.29	0.34	0.48	0.42	0.39
	Flexplume						**Fixplume**					
70MB	**hourly**	**daily**	**NE**	**SE**	**SW**	**NW**	**hourly**	**daily**	**NE**	**SE**	**SW**	**NW**
$Mean_{model}$ [µg m^{-3}]	71.31	71.18	102.1	56.97	71.62	73.42	72.24	71.81	102.1	58.98	72.95	73.51
$Mean_{obs}$ [µg m^{-3}]	23.48	23.29	18.50	21.69	22.98	25.55	23.48	23.29	18.5	21.69	22.98	25.55
Bias [µg m^{-3}]	47.83	47.89	83.56	35.28	48.63	47.87	48.76	48.51	83.55	37.29	49.97	47.97
NMB [%]	204	206	452	163	212	187	208	208	452	172	217	188
RMSE [µg m^{-3}]	66.88	52.53	125.3	50.26	62.1	67.06	67.73	52.98	125.31	52.43	63.46	67.19
STD_{model} [µg m^{-3}]	53.33	25.29	99.04	37.34	45.84	55.96	53.56	24.88	99.13	37.78	46.48	56.03
STD_{meas} [µg m^{-3}]	17.13	7.26	13.29	21.26	15.92	16.42	17.13	7.26	13.29	21.26	15.92	16.42
IOA [-]	-0.46	-0.74	-0.76	-0.19	-0.49	-0.49	-0.47	-0.74	-0.76	-0.23	-0.50	-0.49
R [-]	0.52	0.62	0.48	0.36	0.59	0.65	0.52	0.60	0.49	0.32	0.60	0.65
R^2 [-]	0.27	0.38	0.23	0.13	0.35	0.42	0.27	0.37	0.24	0.11	0.36	0.42
FAC2 [-]	0.25	0.13	0.13	0.23	0.21	0.32	0.24	0.10	0.13	0.22	0.20	0.32
	Flexplume						**Fixplume**					
17SM	**hourly**	**daily**	**NE**	**SE**	**SW**	**NW**	**hourly**	**daily**	**NE**	**SE**	**SW**	**NW**
$Mean_{model}$ [µg m^{-3}]	47.63	46.30	70.21	53.48	44.79	44.79	48.37	46.68	70.47	54.79	45.86	44.97
$Mean_{obs}$ [µg m^{-3}]	12.98	11.46	15.18	21.28	10.44	11.48	12.98	11.46	15.18	21.28	10.44	11.48
Bias [µg m^{-3}]	34.65	34.84	55.03	32.20	34.35	33.31	35.38	35.22	55.29	33.5	35.42	33.49
NMB [%]	267	304	362	151	329	290	273	307	364	157	339	292
RMSE [µg m^{-3}]	49.20	37.43	91.09	48.62	42.58	47.8	49.9	37.77	91.21	49.97	43.68	48.00
STD_{model} [µg m^{-3}]	40.08	16.81	80.62	37.59	30.12	40.81	40.42	16.69	80.58	37.86	30.94	40.92
STD_{meas} [µg m^{-3}]	14.31	6.86	12.09	19.78	13.01	10.98	14.31	6.86	12.09	19.78	13.01	10.98
IOA [-]	-0.44	-0.69	-0.67	-0.19	-0.52	-0.53	-0.45	-0.69	-0.67	-0.22	-0.53	-0.53
R [-]	0.52	0.62	0.71	0.32	0.57	0.68	0.52	0.61	0.71	0.30	0.59	0.68
R^2 [-]	0.27	0.38	0.50	0.10	0.32	0.46	0.27	0.37	0.50	0.09	0.35	0.46
FAC2 [-]	0.15	0.03	0.26	0.30	0.12	0.09	0.14	0.03	0.26	0.28	0.11	0.09

Table C.4: Statistical indicators for comparison of modeled NO_2 concentrations in January with observations at different measurements stations for hourly and daily means and different wind sectors. Station names have been abbreviated according to Table 6.3.

	Flexplume						Fixplume					
80KT	**hourly**	**daily**	**NE**	**SE**	**SW**	**NW**	**hourly**	**daily**	**NE**	**SE**	**SW**	**NW**
$Mean_{model}$ [µg m^{-3}]	21.83	21.68	12.28	19.88	25.66	16.35	23.36	23.27	12.44	21.40	27.34	17.95
$Mean_{obs}$ [µg m^{-3}]	33.00	33.11	20.92	31.83	36.72	27.57	33.00	33.11	20.92	31.83	36.72	27.57
Bias [µg m^{-3}]	-11.2	-11.4	-8.64	-12.0	-11.2	-11.2	-9.65	-9.84	-8.48	-10.4	-9.39	-9.61
NMB [%]	-34	-35	-41	-38	-30	-41	-29	-30	-41	-33	-26	-35
RMSE [µg m^{-3}]	16.07	13.12	10.58	17.81	15.91	15.16	15.3	11.86	10.41	17.68	14.76	14.07
STD_{model} [µg m^{-3}]	11.16	6.75	5.72	9.00	11.12	11.12	12.36	7.88	5.68	10.65	12.15	12.49
STD_{meas} [µg m^{-3}]	13.45	8.95	8.79	10.32	13.86	13.63	13.45	8.95	8.79	10.32	13.86	13.63
IOA [-]	0.40	0.21	0.32	0.16	0.41	0.48	0.44	0.31	0.33	0.17	0.46	0.53
R [-]	0.57	0.70	0.72	0.07	0.60	0.68	0.58	0.70	0.73	0.07	0.62	0.69
R^2 [-]	0.33	0.48	0.52	0.00	0.36	0.46	0.34	0.49	0.53	0.01	0.39	0.48
FAC2 [-]	0.69	0.94	0.54	0.63	0.79	0.57	0.72	0.94	0.56	0.64	0.83	0.62
	Flexplume						**Fixplume**					
72FI	**hourly**	**daily**	**NE**	**SE**	**SW**	**NW**	**hourly**	**daily**	**NE**	**SE**	**SW**	**NW**
$Mean_{model}$ [µg m^{-3}]	12.50	12.05	11.42	22.25	9.52	5.34	15.34	14.61	13.51	25.97	12.18	7.53
$Mean_{obs}$ [µg m^{-3}]	18.63	18.37	22.51	27.37	14.74	14.29	18.63	18.37	22.51	27.37	14.74	14.29
Bias [µg m^{-3}]	-6.14	-6.32	-11.09	-5.12	-5.22	-8.95	-3.30	-3.77	-9.00	-1.40	-2.56	-6.76
NMB [%]	-33	-34	-49	-19	-35	-63	-18	-21	-40	-5	-17	-47
RMSE [µg m^{-3}]	11.11	8.37	13.30	11.73	10.14	12.05	10.40	6.02	11.35	10.71	10.15	10.22
STD_{model} [µg m^{-3}]	9.37	7.84	4.42	8.85	7.01	3.88	12.01	9.41	6.47	10.59	10.70	6.93
STD_{meas} [µg m^{-3}]	12.35	10.49	8.61	13.09	10.25	10.03	12.35	10.49	8.61	13.09	10.25	10.03
IOA [-]	0.58	0.61	0.17	0.56	0.55	0.45	0.62	0.72	0.29	0.61	0.56	0.55
R [-]	0.67	0.86	0.52	0.60	0.55	0.65	0.67	0.89	0.61	0.62	0.56	0.65
R^2 [-]	0.45	0.74	0.27	0.36	0.30	0.42	0.45	0.80	0.38	0.38	0.32	0.42
FAC2 [-]	0.67	0.81	0.49	0.88	0.67	0.37	0.73	0.90	0.65	0.88	0.71	0.58
	Flexplume						**Fixplume**					
82HF	**hourly**	**daily**	**NE**	**SE**	**SW**	**NW**	**hourly**	**daily**	**NE**	**SE**	**SW**	**NW**
$Mean_{model}$ [µg m^{-3}]	17.91	17.59	9.69	12.85	17.83	31.58	20.19	19.79	9.62	14.31	20.69	34.5
$Mean_{obs}$ [µg m^{-3}]	31.91	32.38	23.32	27.29	33.25	39.94	31.91	32.38	23.32	27.29	33.25	39.94
Bias [µg m^{-3}]	-14.0	-14.8	-13.6	-14.4	-15.4	-8.37	-11.7	-12.6	-13.7	-13.0	-12.6	-5.45
NMB [%]	-44	-46	-58	-53	-46	-21	-37	-39	-59	-48	-38	-14
RMSE [µg m^{-3}]	19.93	17.51	17.54	20.12	20.30	19.25	18.75	15.92	17.51	19.20	18.90	17.90
STD_{model} [µg m^{-3}]	9.96	7.52	4.85	4.79	8.00	11.67	12.07	9.31	4.78	6.13	11.13	12.70
STD_{meas} [µg m^{-3}]	15.18	10.96	10.27	14.94	14.8	14.01	15.18	10.96	10.27	14.94	14.8	14.01
IOA [-]	0.37	0.16	0.12	0.39	0.32	0.35	0.41	0.26	0.12	0.41	0.38	0.39
R [-]	0.43	0.54	0.07	0.35	0.46	0.10	0.44	0.55	0.09	0.33	0.44	0.19
R^2 [-]	0.18	0.29	0.00	0.12	0.21	0.01	0.20	0.30	0.01	0.11	0.19	0.04
FAC2 [-]	0.55	0.58	0.38	0.53	0.52	0.80	0.59	0.68	0.34	0.59	0.57	0.82

Table C.4: continued.

	Flexplume						Fixplume					
13ST	**hourly**	**daily**	**NE**	**SE**	**SW**	**NW**	**hourly**	**daily**	**NE**	**SE**	**SW**	**NW**
$Mean_{model}$ [µg m^{-3}]	17.40	17.29	12.89	14.89	20.41	13.85	17.55	17.45	12.89	14.90	20.65	13.98
$Mean_{obs}$ [µg m^{-3}]	27.43	27.39	19.73	24.52	30.83	24.83	27.43	27.39	19.73	24.52	30.83	24.83
Bias [µg m^{-3}]	-10.0	-10.1	-6.84	-9.63	-10.4	-11.0	-9.89	-9.94	-6.84	-9.61	-10.2	-10.9
NMB [%]	-37	-37	-35	-39	-34	-44	-36	-36	-35	-39	-33	-44
RMSE [µg m^{-3}]	13.70	11.25	9.94	12.54	14.47	14.56	13.56	11.06	9.94	12.53	14.27	14.42
STD_{model} [µg m^{-3}]	10.17	6.44	6.18	6.14	11.42	9.99	10.32	6.63	6.18	6.17	11.60	10.12
STD_{meas} [µg m^{-3}]	13.32	8.46	8.79	10.90	14.43	11.79	13.32	8.46	8.79	10.90	14.43	11.79
IOA [-]	0.49	0.27	0.44	0.45	0.49	0.38	0.49	0.28	0.44	0.45	0.50	0.38
R [-]	0.72	0.81	0.58	0.69	0.72	0.63	0.72	0.82	0.58	0.69	0.73	0.63
R^2 [-]	0.51	0.66	0.34	0.47	0.52	0.39	0.52	0.67	0.34	0.47	0.53	0.40
FAC2 [-]	0.67	0.84	0.65	0.77	0.68	0.48	0.67	0.84	0.65	0.76	0.68	0.48
	Flexplume						**Fixplume**					
70MB	**hourly**	**daily**	**NE**	**SE**	**SW**	**NW**	**hourly**	**daily**	**NE**	**SE**	**SW**	**NW**
$Mean_{model}$ [µg m^{-3}]	37.12	36.74	35.37	29.75	41.70	36.01	37.44	37.01	35.37	30.00	42.15	36.15
$Mean_{obs}$ [µg m^{-3}]	39.90	40.39	36.02	34.83	44.32	35.95	39.9	40.39	36.02	34.83	44.32	35.95
Bias [µg m^{-3}]	-2.78	-3.65	-0.65	-5.07	-2.62	0.05	-2.46	-3.38	-0.65	-4.82	-2.17	0.20
NMB [%]	-7	-9	-2	-15	-6	0	-6	-8	-2	-14	-5	1
RMSE [µg m^{-3}]	15.67	8.98	19.83	14.01	15.09	18.28	15.67	8.80	19.83	13.96	15.12	18.25
STD_{model} [µg m^{-3}]	23.17	12.67	22.61	17.13	23.44	28.12	23.35	12.78	22.61	17.28	23.69	28.12
STD_{meas} [µg m^{-3}]	17.59	10.91	13.6	13.63	19.18	16.07	17.59	10.91	13.6	13.63	19.18	16.07
IOA [-]	0.59	0.55	0.30	0.53	0.63	0.52	0.59	0.56	0.30	0.53	0.63	0.52
R [-]	0.75	0.77	0.49	0.66	0.77	0.79	0.75	0.78	0.49	0.66	0.78	0.79
R^2 [-]	0.56	0.59	0.24	0.44	0.60	0.63	0.56	0.60	0.24	0.44	0.60	0.63
FAC2 [-]	0.89	1.00	0.73	0.89	0.93	0.82	0.89	1.00	0.73	0.89	0.94	0.82
	Flexplume						**Fixplume**					
17SM	**hourly**	**daily**	**NE**	**SE**	**SW**	**NW**	**hourly**	**daily**	**NE**	**SE**	**SW**	**NW**
$Mean_{model}$ [µg m^{-3}]	29.48	29.74	23.10	26.35	32.70	27.23	29.67	29.95	23.10	26.46	33.00	27.34
$Mean_{obs}$ [µg m^{-3}]	37.66	38.58	33.78	38.4	38.16	36.33	37.66	38.58	33.78	38.4	38.16	36.33
Bias [µg m^{-3}]	-8.18	-8.85	-10.7	-12.1	-5.45	-9.10	-7.99	-8.63	-10.69	-11.9	-5.15	-8.99
NMB [%]	-22	-23	-32	-31	-14	-25	-21	-22	-32	-31	-14	-25
RMSE [µg m^{-3}]	16.14	12.63	18.15	20.21	12.91	16.47	16.08	12.50	18.15	20.19	12.81	16.37
STD_{model} [µg m^{-3}]	17.59	10.53	15.65	15.31	17.60	20.08	17.73	10.67	15.65	15.37	17.81	20.08
STD_{meas} [µg m^{-3}]	16.26	10.57	15.64	17.45	15.91	15.00	16.26	10.57	15.64	17.45	15.91	15.00
IOA [-]	0.54	0.44	0.45	0.48	0.60	0.45	0.54	0.45	0.45	0.48	0.61	0.46
R [-]	0.66	0.64	0.56	0.52	0.76	0.73	0.67	0.64	0.56	0.51	0.76	0.73
R^2 [-]	0.44	0.40	0.31	0.27	0.58	0.53	0.44	0.41	0.31	0.26	0.58	0.54
FAC2 [-]	0.79	0.94	0.59	0.73	0.89	0.71	0.79	0.94	0.59	0.73	0.90	0.71

Table C.5: Statistical indicators for comparison of modeled NO_2 concentrations in August with observations at different measurements stations for hourly and daily means and different wind sectors. Station names have been abbreviated according to Table 6.3.

	Flexplume						Fixplume					
80KT	**hourly**	**daily**	**NE**	**SE**	**SW**	**NW**	**hourly**	**daily**	**NE**	**SE**	**SW**	**NW**
$Mean_{model}$ [µg m^{-3}]	28.55	26.75	35.82	35.32	29.97	22.90	31.31	29.19	36.74	40.94	33.51	23.74
$Mean_{obs}$ [µg m^{-3}]	25.50	23.89	20.61	34.97	30.32	16.66	25.5	23.89	20.61	34.97	30.32	16.66
Bias [µg m^{-3}]	3.05	2.86	15.21	0.35	-0.35	6.24	5.81	5.30	16.14	5.97	3.19	7.08
NMB [%]	12	12	74	1	-1	37	23	22	78	17	11	42
RMSE [µg m^{-3}]	19.24	7.26	24.93	25.78	18.49	15.10	20.78	9.13	26.05	28.43	20.26	15.65
STD_{model} [µg m^{-3}]	17.28	8.33	23.37	16.74	17.18	14.64	19.49	10.38	24.24	19.14	19.31	15.97
STD_{meas} [µg m^{-3}]	17.13	9.76	12.56	20.28	15.57	12.75	17.13	9.76	12.56	20.28	15.57	12.75
IOA [-]	0.48	0.59	0.05	0.36	0.48	0.44	0.44	0.52	0.01	0.27	0.43	0.43
R [-]	0.39	0.74	0.53	0.04	0.37	0.50	0.41	0.73	0.54	0.01	0.36	0.55
R^2 [-]	0.15	0.55	0.29	0.00	0.13	0.25	0.17	0.53	0.29	0.00	0.13	0.30
FAC2 [-]	0.68	0.94	0.58	0.64	0.77	0.62	0.67	0.90	0.55	0.60	0.75	0.63
	Flexplume						**Fixplume**					
72FI	**hourly**	**daily**	**NE**	**SE**	**SW**	**NW**	**hourly**	**daily**	**NE**	**SE**	**SW**	**NW**
$Mean_{model}$ [µg m^{-3}]	22.24	18.53	27.32	49.06	18.38	13.30	28.58	24.92	37.4	62.49	23.19	17.47
$Mean_{obs}$ [µg m^{-3}]	16.31	14.62	22.32	34.27	12.45	11.32	16.31	14.62	22.32	34.27	12.45	11.32
Bias [µg m^{-3}]	5.93	3.91	5.00	14.79	5.94	1.98	12.27	10.31	15.08	28.23	10.75	6.16
NMB [%]	36	27	22	43	48	17	75	71	68	82	86	54
RMSE [µg m^{-3}]	18.14	8.08	12.45	30.25	18.03	9.36	25.76	15.01	47.37	38.77	22.41	15.22
STD_{model} [µg m^{-3}]	23.78	13.74	11.86	30.57	22.01	10.43	28.73	18.18	43.17	27.53	24.73	15.75
STD_{meas} [µg m^{-3}]	15.80	9.49	11.97	22.92	12.09	7.27	15.8	9.49	11.97	22.92	12.09	7.27
IOA [-]	0.50	0.64	0.51	0.42	0.25	0.40	0.32	0.24	0.11	0.19	0.04	0.18
R [-]	0.69	0.88	0.54	0.55	0.64	0.51	0.62	0.87	-0.01	0.46	0.62	0.47
R^2 [-]	0.48	0.77	0.29	0.30	0.41	0.26	0.38	0.76	0.00	0.21	0.39	0.22
FAC2 [-]	0.64	0.90	0.76	0.66	0.57	0.69	0.60	0.71	0.74	0.53	0.59	0.65
	Flexplume						**Fixplume**					
82HF	**hourly**	**daily**	**NE**	**SE**	**SW**	**NW**	**hourly**	**daily**	**NE**	**SE**	**SW**	**NW**
$Mean_{model}$ [µg m^{-3}]	28.16	25.80	33.97	23.84	25.83	31.91	32.08	29.43	37.43	28.32	29.53	35.86
$Mean_{obs}$ [µg m^{-3}]	29.89	28.79	26.13	37.68	29.79	26.85	29.89	28.79	26.13	37.68	29.79	26.85
Bias [µg m^{-3}]	-1.72	-2.99	7.84	-13.85	-3.96	5.06	2.19	0.64	11.30	-9.36	-0.26	9.01
NMB [%]	-6	-10	30	-37	-13	19	7	2	43	-25	-1	34
RMSE [µg m^{-3}]	20.77	10.25	23.31	27.22	17.51	20.12	23.16	10.91	23.8	29.44	20.54	22.37
STD_{model} [µg m^{-3}]	17.24	6.96	16.59	19.19	15.72	16.95	20.25	8.53	15.33	24.31	19.26	18.96
STD_{meas} [µg m^{-3}]	15.97	9.59	15.56	14.98	14.85	16.38	15.97	9.59	15.56	14.98	14.85	16.38
IOA [-]	0.37	0.50	0.26	0.02	0.43	0.41	0.30	0.45	0.17	-0.03	0.36	0.34
R [-]	0.22	0.33	0.07	0.08	0.38	0.32	0.21	0.28	0.08	0.05	0.30	0.34
R^2 [-]	0.05	0.11	0.00	0.01	0.14	0.10	0.04	0.08	0.01	0.00	0.09	0.11
FAC2 [-]	0.64	0.90	0.66	0.38	0.74	0.64	0.61	0.87	0.55	0.43	0.71	0.60

Table C.5: continued.

	Flexplume						Fixplume					
13ST	**hourly**	**daily**	**NE**	**SE**	**SW**	**NW**	**hourly**	**daily**	**NE**	**SE**	**SW**	**NW**
$Mean_{model}$ [µg m^{-3}]	27.84	25.43	42.29	29.63	24.98	28.12	28.11	25.57	42.23	29.84	25.45	28.25
$Mean_{obs}$ [µg m^{-3}]	21.43	19.46	16.87	29.76	23.64	15.88	21.43	19.46	16.87	29.76	23.64	15.88
Bias [µg m^{-3}]	6.41	5.97	25.42	-0.13	1.34	12.24	6.69	6.11	25.36	0.08	1.81	12.38
NMB [%]	30	31	151	0	6	77	31	31	150	0	8	78
RMSE [µg m^{-3}]	18.08	8.62	33.07	17.20	14.55	18.95	18.25	8.71	33.01	17.40	14.78	19.13
STD_{model} [µg m^{-3}]	17.49	7.31	23.50	14.90	16.35	17.68	17.82	7.38	23.46	15.27	16.88	17.98
STD_{meas} [µg m^{-3}]	15.05	7.79	7.61	16.07	16.39	10.91	15.05	7.79	7.61	16.07	16.39	10.91
IOA [-]	0.44	0.44	-0.54	0.48	0.60	0.17	0.44	0.43	-0.54	0.48	0.60	0.16
R [-]	0.47	0.66	0.45	0.38	0.61	0.58	0.48	0.67	0.45	0.38	0.61	0.58
R^2 [-]	0.22	0.44	0.21	0.15	0.37	0.33	0.23	0.44	0.21	0.15	0.37	0.34
FAC2 [-]	0.67	0.84	0.34	0.80	0.82	0.51	0.67	0.84	0.34	0.80	0.82	0.51
	Flexplume						**Fixplume**					
70MB	**hourly**	**daily**	**NE**	**SE**	**SW**	**NW**	**hourly**	**daily**	**NE**	**SE**	**SW**	**NW**
$Mean_{model}$ [µg m^{-3}]	52.70	50.46	72.50	51.37	51.68	51.69	53.24	50.82	72.82	52.39	52.44	51.80
$Mean_{obs}$ [µg m^{-3}]	44.33	43.97	46.53	53.97	43.53	40.40	44.33	43.97	46.53	53.97	43.53	40.40
Bias [µg m^{-3}]	8.38	6.49	25.97	-2.60	8.15	11.29	8.91	6.85	26.30	-1.58	8.91	11.40
NMB [%]	19	15	56	-5	19	28	20	16	57	-3	20	28
RMSE [µg m^{-3}]	26.60	12.50	47.39	30.57	20.94	26.11	26.78	12.62	47.62	30.97	21.03	26.23
STD_{model} [µg m^{-3}]	27.07	14.11	41.83	18.79	24.08	29.63	27.26	14.00	41.97	19.02	24.33	29.79
STD_{meas} [µg m^{-3}]	21.32	11.29	20.18	30.67	19.03	16.60	21.32	11.29	20.18	30.67	19.03	16.60
IOA [-]	0.43	0.50	0.04	0.50	0.47	0.39	0.43	0.48	0.04	0.49	0.47	0.38
R [-]	0.48	0.67	0.35	0.32	0.62	0.61	0.48	0.67	0.35	0.30	0.64	0.61
R^2 [-]	0.23	0.44	0.12	0.10	0.39	0.37	0.23	0.45	0.12	0.09	0.41	0.37
FAC2 [-]	0.87	1.00	0.74	0.84	0.90	0.88	0.87	1.00	0.74	0.84	0.90	0.88
	Flexplume						**Fixplume**					
17SM	**hourly**	**daily**	**NE**	**SE**	**SW**	**NW**	**hourly**	**daily**	**NE**	**SE**	**SW**	**NW**
$Mean_{model}$ [µg m^{-3}]	44.67	41.58	60.52	49.95	41.79	43.08	45.02	41.83	60.73	50.24	42.36	43.24
$Mean_{obs}$ [µg m^{-3}]	39.92	39.18	43.71	64.48	35.47	32.57	39.92	39.18	43.71	64.48	35.47	32.57
Bias [µg m^{-3}]	4.76	2.41	16.81	-14.5	6.33	10.51	5.11	2.65	17.02	-14.2	6.89	10.67
NMB [%]	12	6	38	-23	18	32	13	7	39	-22	19	33
RMSE [µg m^{-3}]	23.87	10.82	35.31	34.40	18.00	21.21	24.12	10.94	35.52	34.54	18.51	21.34
STD_{model} [µg m^{-3}]	24.01	11.48	35.22	19.88	21.65	25.01	24.33	11.56	35.38	20.25	22.09	25.31
STD_{meas} [µg m^{-3}]	23.30	15.33	19.05	29.67	19.67	14.61	23.30	15.33	19.05	29.67	19.67	14.61
IOA [-]	0.54	0.69	0.23	0.45	0.56	0.40	0.53	0.68	0.23	0.45	0.55	0.40
R [-]	0.51	0.73	0.48	0.26	0.67	0.68	0.51	0.72	0.48	0.25	0.67	0.69
R^2 [-]	0.26	0.53	0.23	0.07	0.45	0.47	0.26	0.52	0.23	0.06	0.44	0.48
FAC2 [-]	0.86	1.00	0.76	0.85	0.87	0.88	0.85	1.00	0.76	0.84	0.86	0.88

Table C.6: Statistical indicators for comparison of modeled O_3 concentrations in January at the measurement station Sternschanze (ST) for hourly and daily means and different wind sectors.

	Flexplume						Fixplume					
13ST	**hourly**	**daily**	**NE**	**SE**	**SW**	**NW**	**hourly**	**daily**	**NE**	**SE**	**SW**	**NW**
$Mean_{model}$ [µg m^{-3}]	25.72	26.18	20.14	19.62	26.51	37.28	25.62	26.06	20.14	19.61	26.34	37.23
$Mean_{obs}$ [µg m^{-3}]	31.25	31.54	24.96	23.19	33.8	40.71	31.25	31.54	24.96	23.19	33.80	40.71
Bias [µg m^{-3}]	-5.53	-5.36	-4.82	-3.57	-7.29	-3.43	-5.63	-5.47	-4.82	-3.58	-7.47	-3.47
NMB [%]	-18	-17	-19	-15	-22	-8	-18	-17	-19	-15	-22	-9
RMSE [µg m^{-3}]	12.49	8.72	9.79	9.64	13.85	13.42	12.56	8.78	9.79	9.66	13.94	13.46
STD_{model} [µg m^{-3}]	18.52	15.43	16.52	14.51	18.34	20.76	18.59	15.51	16.52	14.51	18.47	20.83
STD_{meas} [µg m^{-3}]	21.10	17.15	20.93	17.23	20.81	22.76	21.1	17.15	20.93	17.23	20.81	22.76
IOA [-]	0.74	0.78	0.82	0.76	0.70	0.73	0.74	0.77	0.82	0.76	0.70	0.73
R [-]	0.85	0.92	0.92	0.85	0.83	0.83	0.85	0.92	0.92	0.85	0.83	0.83
R^2 [-]	0.72	0.84	0.85	0.73	0.68	0.68	0.72	0.84	0.85	0.73	0.68	0.68
FAC2 [-]	0.68	0.84	0.63	0.69	0.68	0.75	0.68	0.81	0.63	0.69	0.67	0.75

Table C.7: Statistical indicators for comparison of modeled O_3 concentrations in August at the measurement station Sternschanze (ST) for hourly and daily means and different wind sectors.

	Flexplume						Fixplume					
13ST	**hourly**	**daily**	**NE**	**SE**	**SW**	**NW**	**hourly**	**daily**	**NE**	**SE**	**SW**	**NW**
$Mean_{model}$ [µg m^{-3}]	48.63	49.74	48.05	56.66	47.42	46.33	48.37	49.52	48.11	56.46	46.97	46.18
$Mean_{obs}$ [µg m^{-3}]	59.42	60.20	69.68	71.86	54.62	57.46	59.42	60.20	69.68	71.86	54.62	57.46
Bias [µg m^{-3}]	-10.8	-10.5	-21.6	-15.2	-7.20	-11.13	-11.05	-10.7	-21.58	-15.4	-7.6	-11.3
NMB [%]	-18	-17	-31	-21	-13	-19	-19	-18	-31	-21	-14	-20
RMSE [µg m^{-3}]	25.68	15.93	30.99	33.47	21.31	25.04	25.92	16.14	30.92	33.61	21.67	25.28
STD_{model} [µg m^{-3}]	35.18	18.3	34.89	40.50	33.96	33.32	35.37	18.35	34.83	40.70	34.25	33.42
STD_{meas} [µg m^{-3}]	31.70	19.78	38.56	37.55	31.83	25.09	31.70	19.78	38.56	37.55	31.83	25.09
IOA [-]	0.58	0.56	0.59	0.56	0.68	0.44	0.58	0.55	0.59	0.55	0.67	0.43
R [-]	0.76	0.80	0.82	0.71	0.82	0.74	0.76	0.80	0.82	0.71	0.81	0.74
R^2 [-]	0.58	0.65	0.68	0.50	0.67	0.55	0.58	0.64	0.68	0.51	0.66	0.54
FAC2 [-]	0.71	0.97	0.74	0.61	0.75	0.72	0.71	0.97	0.74	0.61	0.74	0.72

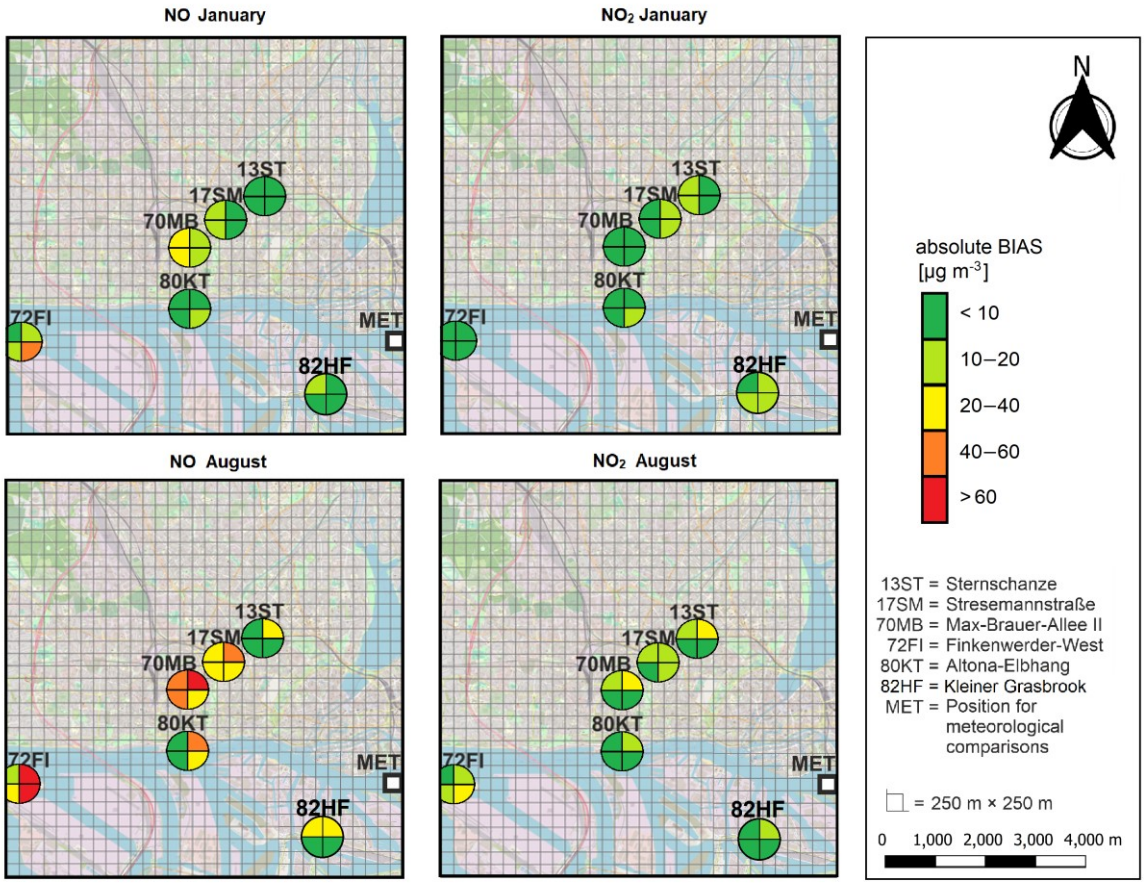

Figure C.2: Overview on the EPISODE-CityChem performance (bias) in NO_2 and NO depending on the wind sector in January and August based on the Fixplume approach. Maps were created using © QGIS-Version 3.22.1-Białowieża with a topographic base map by © OpenStreetMap contributors 2022 and © Copernicus Urban Atlas 2012 land use and land cover data. Distributed under a Creative Commons BY-SA License.

D: Appendix to Chapter 7

Figures D.1 offers a comprehensive overview on the effect of ship emissions on the daily mean concentrations of various atmospheric substances, modeled at the position Altona-Elbhang for the months January and August 2018. Figure D.2 presents corresponding daily mean values for photolysis rate (J_{NO2}), cloud fraction (CLF) and mixing height.

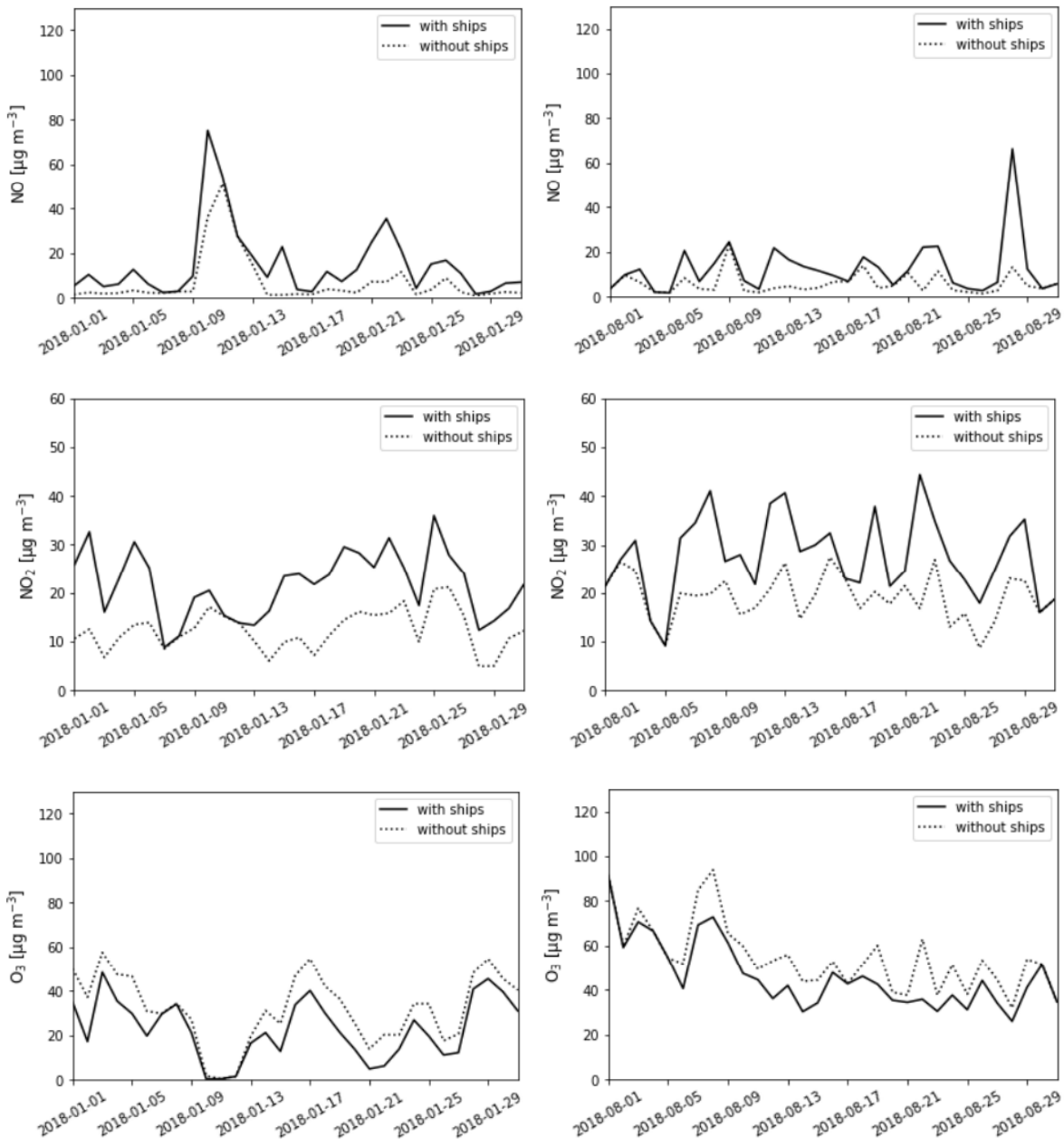

Figure D.1: Daily mean concentrations of different chemical substances modeled at the harbor reference position Altona-Elbhang in January and August 2018. Different model results for calculations with and without ships are shown.

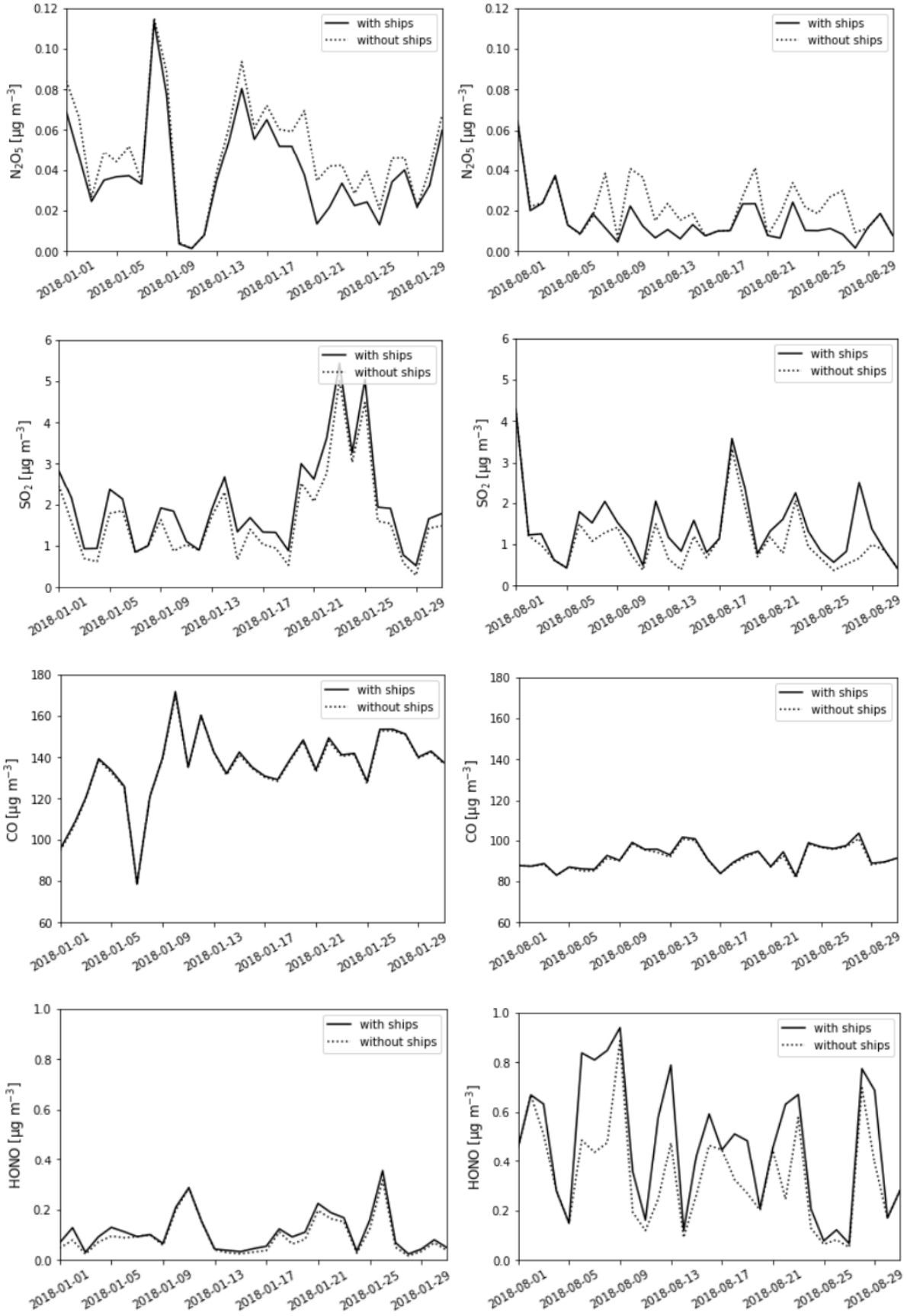

Figure D.1: continued.

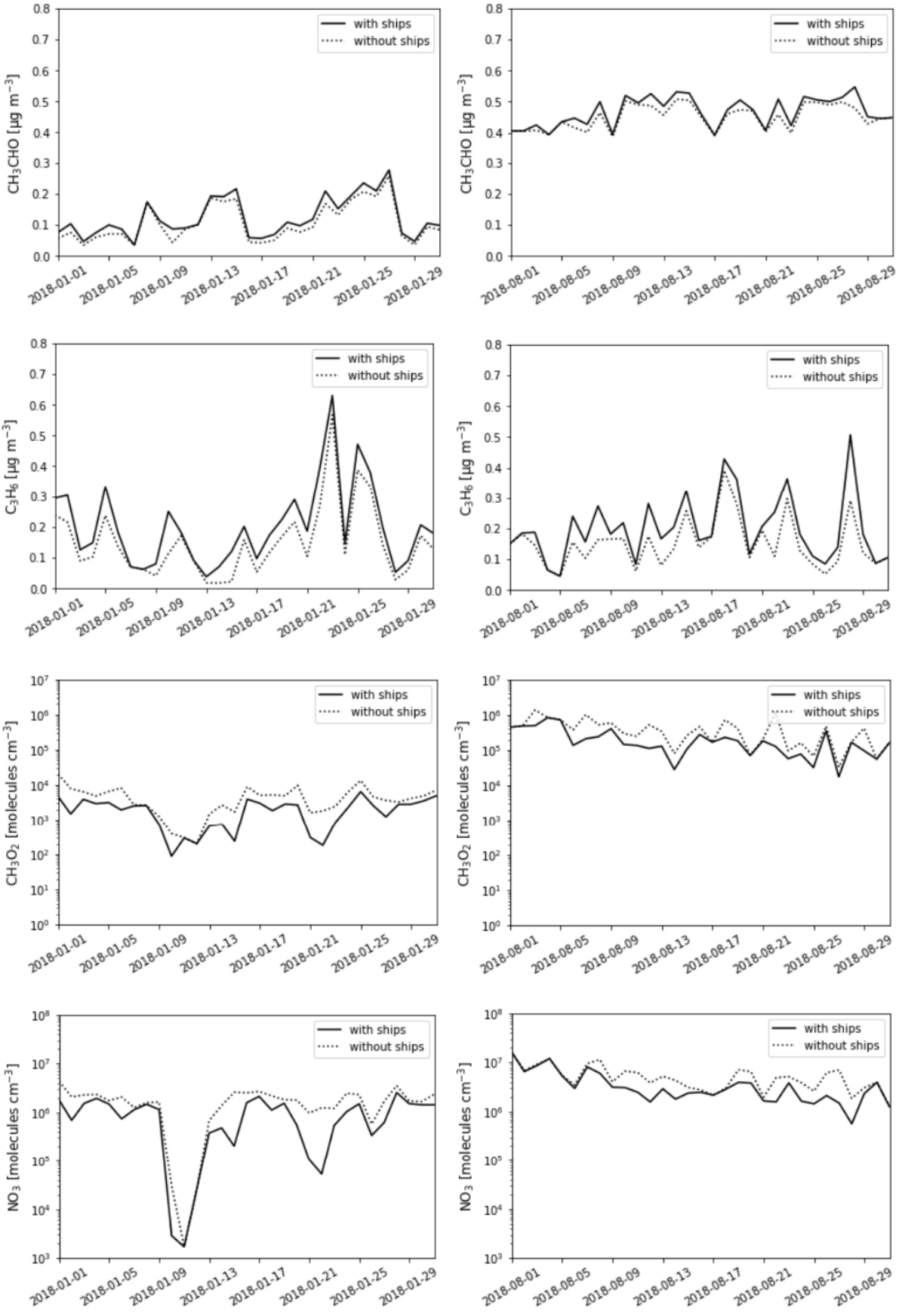

Figure D.1: continued.

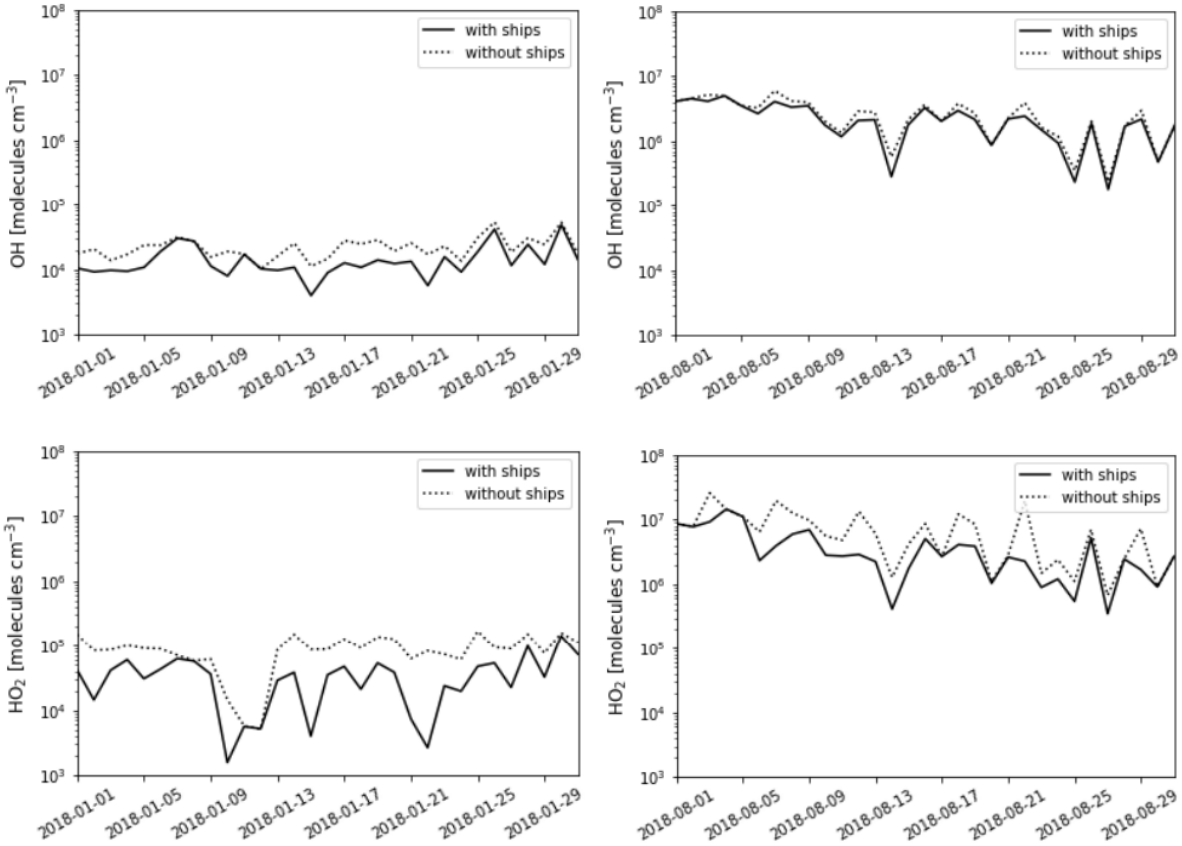

Figure D.1: continued.

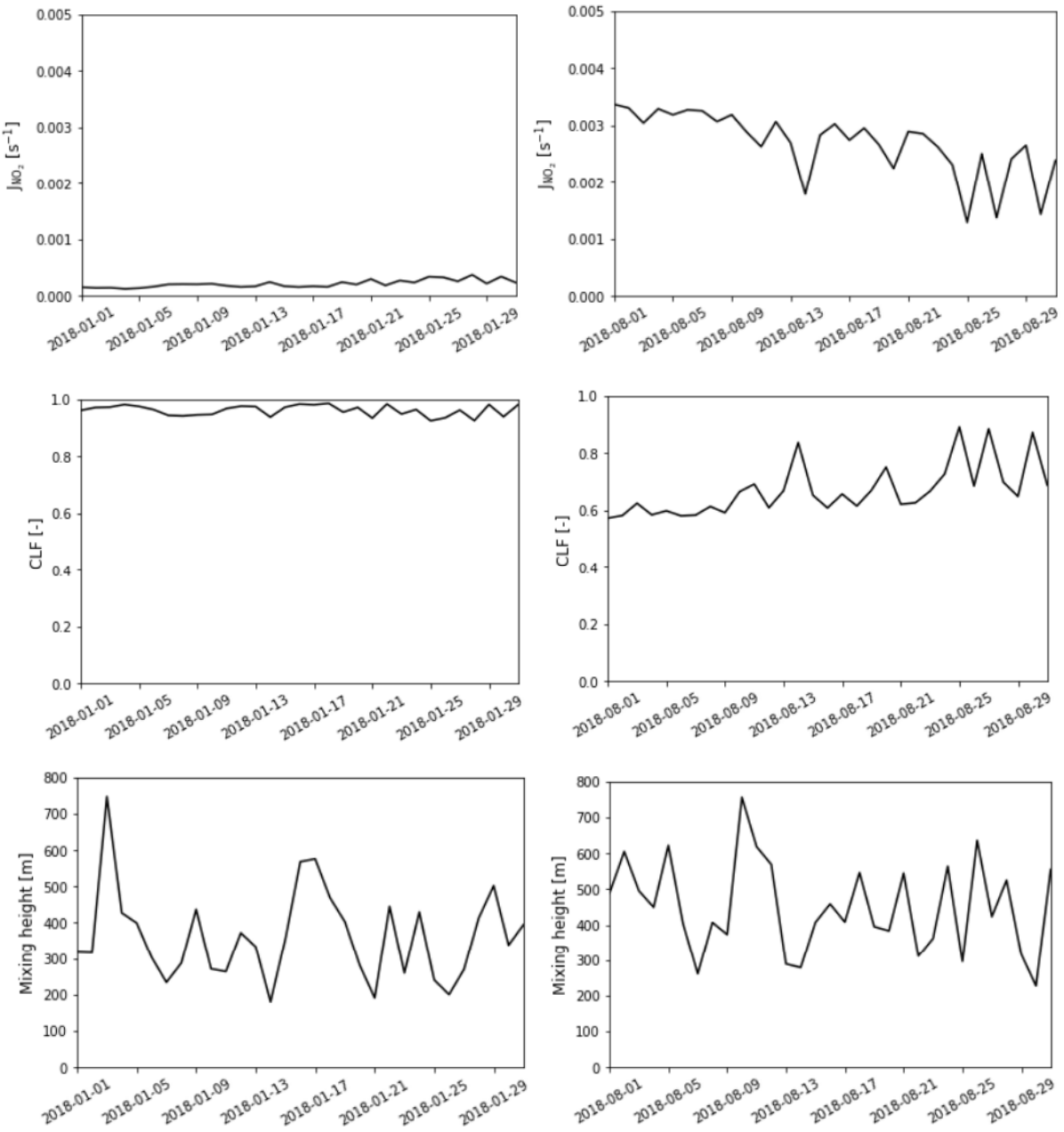

Figure D.2: Daily mean values for photolysis rate (J_{NO2}), cloud fraction (CLF) and mixing height modeled at the harbor reference position Altona-Elbhang in January and August 2018.

Danksagung

Als Hobbyautor erscheint mir der Abschluss dieser Arbeit wie das Ende einer langen Geschichte. Und diese Geschichte hatte wirklich alles: eine abenteuerliche Reise ins ferne Shanghai, viele überraschende Wendungen, sei es bei inhaltlichen Fragen oder der plötzlichen Arbeit im Homeoffice, tiefgründige Dialoge auf zahlreichen Konferenzen und - was mir immer besonders am Herzen liegt - starke Charaktere.

Diesen Charakteren, den Freunden und Kollegen, die den Inhalt meiner Geschichte mit ihren Beiträgen, Ideen und ihrer Kritik, zur finalen Form verholfen haben, möchte ich an dieser Stelle meinen Dank ausdrücken.

Zunächst möchte ich mich bei der Helmholtz-Gemeinschaft, insbesondere dem Helmholtz-Zentrum Hereon und der Deutschen Forschungsgemeinschaft (DFG) für die finanzielle und materielle Ausstattung danken, ohne die eine Bearbeitung dieses Themas nicht möglich gewesen wäre. Weiterhin gilt mein Dank der Universität Hamburg für die Beheimatung des Dissertationsthemas und der Graduiertenschule SICSS für die Vermittlung interessanter Softskills und der organisatorischen Betreuung.

Ein großer Dank gilt meinem Panel: Prof. Dr. Kay-Christian Emeis, Prof. Dr. Bernd Leitl und Dr. Volker Matthias, die mich inhaltlich durch dieses Thema geleitet haben, mir aber gleichzeitig genug Raum zur persönlichen Entfaltung ließen. Mein Dank gilt an dieser Stelle auch Prof. Dr. Markus Quante, der stets ein offenes Ohr für die Belange der Doktoranden zeigte und die Kommunikation zwischen den Arbeitsgruppen förderte.

Ich bedanke mich bei Prof. Yingjun Chen, Prof. Yan Zhang, Dr. Fan Zhang und allen anderen Kollegen von der Fudan Universität Shanghai für ein einmaliges Erlebnis und eine großartige Betreuung während meines achtwöchigen Forschungsaufenthalts in Shanghai. Danke auch an Daniel Schwarzkopf, der ebenfalls an dieser Reise teilgenommen hat - es war eine coole Zeit.

Mein Dank gilt weiterhin sämtlichen Kollegen der Arbeitsgruppe „Chemietransport-modellierung“. Besonders möchte ich mich hier bei Dr. Matthias Karl und Dr. Martin Ramacher bedanken, die mir das Modellsystem EPISODE-CityChem nähergebracht haben. Und ich danke Dr. Jan Arndt für den technischen Support am „Strand“ und die vielen unterhaltsamen Gespräche.

Weiterhin möchte ich mich bei der MeMi-Arbeitsgruppe der Universität Hamburg bedanken, insbesondere bei Dr. David Grawe für die Unterstützung mit MITRAS und sehr viel Geduld bei der Erklärung der feinen Details der mikroskaligen Modellierung.

Dem DKRZ danke ich für die Bereitstellung der Rechenkapazitäten und Dr. Bodo („Alex“) Voigt für neue Einblicke beim Lösen statistischer Probleme. Auch möchte ich Herrn Ingo Lange vom Meteorologischen Institut der Universität Hamburg danken für die Bereitstellung der in dieser Arbeit verwendeten Daten vom Hamburger Wettermast.

Ich danke Kevin Reinck, Eliza-Maria Link und Karl Schneider, die den Abschluss dieser Arbeit im Rahmen ihrer Bachelorarbeiten unterstützten und damit mein Blickfeld auf das Thema der Modellierung von Luftqualitätsproblemen erweiterten.

Meine Freunde haben einen großen Teil dazu geleistet, dass meine Work-Life-Balance in den letzten Jahren im Gleichgewicht blieb. Darum danke ich an dieser Stelle Ulfert, Susi, Nico, Rainer und Luisa. Dazu den Freunden aus fernen Ländern: Mariano, Rémy und Chingiz. Thanks, my buddies. Stay legit!

Auch bei meinen Eltern, Birgit und Rainer Badeke, sowie allen anderen Familienmitgliedern möchte ich mich bedanken. Ihr habt mich stets unterstützt, auch wenn ich inzwischen weit von meiner Heimat Chemnitz weg bin. Mein Vater, der ein großartiger Segler ist, wusste schon früh, dass ich mit der Schifffahrt verbunden bleiben würde. Er sollte Recht behalten. Selbst mein Großvater, Klaus Badeke, ahnte bereits, dass ich ein Wissenschaftler werden würde. Darauf bin ich sehr stolz.

Mein ganz besonderer Dank gilt natürlich meiner Freundin Lisa, die mich auf dieser Reise schon 10 Jahre lang begleitet. Wir haben diese Herausforderung gemeinsam gestemmt, trotz langer Überstunden und Fernbeziehung. Never gonna give you up.